Quantum Dynamics Studies of the Photodissociation of Molecular Systems

by

Simon Peter Neville

A thesis submitted to
the University of Birmingham
for the examination of
DOCTOR OF PHILOSOPHY

School of Chemistry
University of Birmingham
2013

Abstract

The focus of the work presented here is the theoretical description of the photodissociation of molecular systems. Owing to the generally high density of electronically excited states, and in particular intersections between these states, the Born-Oppenheimer approximation, which underpins the majority of our understanding of chemical processes, cannot be invoked in the study of photochemical processes. This, coupled with the large amplitude motion of the nuclei associated with a dissociation process, results in the area of photodissociation dynamics being a rich, but challenging area of research.

The systems studied here are united by the presence of nitrogen-hydrogen bonds, and low-lying, singlet $3s/\pi\sigma^*$ states that are quasi-bound with respect to the dissociation of these bonds. The simplest such system is ammonia, and the photodissociation dynamics of this molecule are studied. The vibronic coupling responsible for the formation of the barrier to dissociation in ammonia's $S_1(3s/\pi\sigma^*)$ state is identified, and two eight-state model Hamiltonians incorporating this coupling are constructed by fitting to the results of MCQDPT2 calculations. Using a transformation of the model Hamiltonians based on a block-diagonalisation scheme, the effect of the coupling of the $S_1(3s\pi\sigma^*)$ state to several higher-lying states on the dissociation dynamics in this state is evaluated. The dynamics of ammonia in its $S_2(3p)$ state are also studied.

The dissociation of 3-pyrroline in its first two excited states are studied using quantum dynamics simulations employing a six-state, eight-mode model Hamiltonian. Using the method of improved relaxation, vibrational eigenstates of the ground electronic state that correspond to the equatorial and axial conformers of 3-pyrroline are calculated. Using these wavefunc-

tions, a conformer-resolved study of 3-pyrroline excited to its $S_1(3s/\pi\sigma^*)$ and $S_2(3p_x)$ states is performed, and the first two bands of its electronic spectrum calculated. Distinct similarities between the photo-induced dynamics of 3-pyrroline and ammonia are found to exist.

Using an eight-state model Hamiltonian fitted to extensive CASPT2 calculations, the photodissociation of pyrrole following excitation to its $A_2(3s/\pi\sigma^*)$, $A_1(\pi\pi^*)$ and $B_2(\pi\pi^*)$ states is investigated. The role played by tunnelling through the barrier to dissociation in the $A_2(3s/\pi\sigma^*)$ state is assessed and found to be significantly underestimated in previous theoretical works. The relaxation of pyrrole from its bright $A_1(\pi\pi^*)$ and $B_2(\pi\pi^*)$ states to the dissociative $A_2(3s/\pi\sigma^*)$ and $B_1(3s/\pi\sigma^*)$ states is studied. The role played by intensity borrowing in the first band of pyrrole's electronic absorption spectrum is analysed, and a re-assignment of much of the structure of this band is made.

An eight-state model Hamiltonian parameterised *via* fitting to EOM-CCSD calculations is constructed and used in the study of the dynamics of aniline following excitation to its first two singlet $\pi\pi^*$ states. Two previously neglected $3p$ Rydberg states are found to play important roles in aniline's excited state dynamics. The first two bands in aniline's electronic absorption spectrum are calculated, and the role played by the Hertzberg-Teller effect in the first band is analysed.

Acknowledgements

Thanks must first, and foremost, go to my supervisor, Graham, without whose support and knowledge the work presented here would not have been possible.

Thanks must also go to the members, past and present, of the Worth group. In particular, Gareth for tolerating many hours of naive questions, and Chris for making me think and laugh in equal amounts.

For the many, many hours spent by her on the aniline work, I am indebted to Fang Wang. Without her contribution the work described in Chapter 7 would not have been possible.

This thesis and the work described in it are entirely my own, except where I have acknowledged *either* help from a named person *or* a reference is given to a published source or a thesis. Text taken from another source will be enclosed in quotation marks and a reference will be given.

September 27, 2013

List of Publications

F. Wang, S. P. Neville, R. Wang and G. A. Worth, "*A Quantum Dynamics Study of Photoexcited Aniline*", J. Phys. Chem. A., **117**, 7298 (2013)

S. P. Neville and G. A. Worth, "*A Reinterpretation of the Electronic Spectrum of Pyrrole: A Quantum Dynamics Study*". Submitted.

S. P. Neville and G. A. Worth, "*A Conformer-Resolved Quantum Dynamics Study of the Photodissociation of 3-Pyrroline*". In preparation.

Contents

List of Figures **xvii**

List of Tables **xxiii**

Glossary **xxv**

1 Introduction **1**

2 Theory **11**

2.1 The Nuclear Schrödinger Equation 11

2.2 Hilbert Subspaces and the Group Born-Oppenheimer Approximation 13

2.3 The Diabatic Representation 16

2.4 Conical Intersections 18

3 Methodology **21**

3.1 Introduction 21

3.2 The Electronic Wavefunction 22

3.2.1 The Hartree-Fock Model 24

3.2.2 The Coupled-Cluster Model 25

3.2.3 The Multiconfigurational Self-Consistent Field Model . 28

3.2.4 Multiconfigurational Perturbation Theory 29

3.3 Representation of the Nuclear Wavefunction 33

3.3.1 The Standard Method 33
3.3.2 The Multiconfigurational Time-Dependent Hartree Method 34
3.4 Calculation of Initial Wavepackets 37
3.4.1 Calculation of the Vibrational Ground State 37
3.4.2 Calculation of Vibrationally Excited States 38
3.5 Evaluation of the Hamiltonian Matrix 40
3.5.1 The Finite Basis Representation 41
3.5.2 The Discrete Variable Representation 42
3.6 Product Representation of the Hamiltonian 43
3.7 The Potfit Algorithm 44
3.8 The Vibronic Coupling Hamiltonian 46
3.9 Complex Absorbing Potentials 49
3.10 Flux, Reaction Probabilities and Diabatic State Populations . 50
3.11 The Calculation of Absorption Spectra 51

4 Ammonia **53**

4.1 Introduction 53
4.2 Evaluation of the Validity of Taking the $\tilde{X}$ and $\tilde{A}(3s)$ States to Form a Hilbert Subspace 56
4.2.1 The Extended Curl Equation 56
4.2.2 Analysis of $\boldsymbol{A}^{(2)}$ 58
4.3 Quantum Dynamics Simulations of Photoexcited Ammonia . . 61
4.3.1 Nuclear Coordinates and Kinetic Energy Operators . . 61
4.3.2 The Model Potentials 66
4.3.3 Product Representation of the Potential 75
4.3.4 Electronic Structure Calculations 75
4.3.5 Block Diagonalisation of the Diabatic Potential 76
4.3.6 Projection Onto the Adiabatic States 79

4.3.7 Preparation of Initial Wavepackets and the Calculation of Spectra . . . 81
4.3.8 The Origin of the Barrier to Dissociation on the S_1 Adiabatic State Surface . . . 83
4.3.9 Quantum Dynamics Simulations Using the Two-Mode Model . . . 84
4.3.10 Quantum Dynamics Simulations Using the Four-Mode Model . . . 92
4.3.11 Electronic Absorption Spectra . . . 103
4.4 Conclusions . . . 106

5 3-Pyrroline 110

5.1 Introduction . . . 110
5.2 Theoretical Framework . . . 112
5.2.1 The Model Hamiltonian . . . 112
5.2.2 Electronic Structure Calculations . . . 118
5.2.3 Calculation of Vibrational Eigenstates: The AX and EQ Conformers . . . 118
5.2.4 Wavepacket Propagations . . . 120
5.3 Results . . . 121
5.3.1 Model Diabatic Potentials . . . 121
5.3.2 Calculation of the $|\Psi_{AX}\rangle$ and $|\Psi_{EQ}\rangle$ Vibrational Eigenstates . . . 124
5.3.3 Excitation to the $\tilde{A}$ State . . . 128
5.3.4 Excitation to the $\tilde{B}$ State . . . 131
5.4 Electronic Absorption Spectra . . . 135
5.5 Discussion and Conclusions . . . 137

6 Pyrrole **141**

6.1 Introduction 141

6.2 Theoretical Framework 144

6.2.1 The Model Hamiltonian 144

6.2.2 Fitting of the Model Potential and Electronic Structure Calculations 148

6.3 Results 151

6.3.1 Electronic Structure Calculations 151

6.3.2 The Model Hamiltonian 152

6.3.3 Dynamics Following Excitation to the $B_2(\pi\pi^*)$ State . 159

6.3.4 Dynamics Following Excitation to the $A_1(\pi\pi^*)$ State . 164

6.3.5 Dynamics Following Excitation to the $A_2(3s)$ State . . 165

6.3.6 Electronic Absorption Spectra 171

6.4 Discussion and Conclusions 178

7 Aniline **182**

7.1 Introduction 182

7.2 Theory 185

7.2.1 The Model Hamiltonian 185

7.2.2 Electronic Structure Calculations 188

7.2.3 Calculation of Absorption Spectra 188

7.3 Results 189

7.3.1 Electronic Structure Calculations 189

7.3.2 The Model Potential 193

7.3.3 Model Spectra 200

7.3.4 Dynamics 203

7.4 Conclusions 207

8 Conclusions **210**

Bibliography **218**

List of Figures

1.1 A so-called Jablonski diagram illustrating the possible relaxation pathways open to a molecular sytem following the absorption of a photon of frequency ν in its singlet ground state. Here, the lables S_n denote the singlet electronic states, and T_n the triplet electronic states. IC, ISC, F, and P denote, respectively, internal conversion, intersystem crossing, flourescence and phosphorescence. 2

1.2 Pictorial representation of the excitation of a system from its ground electronic state $|\psi_i\rangle$ to an excited state $|\phi_i\rangle = \boldsymbol{\mu}|\psi_i\rangle$, a wavepacket that evolves as governed by the time-dependent Schrödinger equation. R here corresponds to a nuclear coordinate. 4

1.3 Energies of the four lowest adiabatic electronic states of indole along the N-H dissociation coordinate (adapted from Ref. [6]), with the geometry of indole at the Franck-Condon point inset. 6

1.4 Potential surfaces yielded by the avoided crossing model given in Equation 1.5 using a coupling function $W_{12}(R_{XH}) = \Delta \tanh(\rho R_{XH})$: (a) model adiabatic surfaces, and; (b) model diabatic surfaces. The labels $3s$ and $\pi\sigma^*$ refer to the characters of the states whose potentials they reside next to. 7

1.5 Calculated adiabatic energies of the first two $\pi\pi^*$ and the first two $3s/\pi\sigma^*$ states of: (a) phenol, and; (b) thiophenol. Adapted from Ref. [9]. 9

4.1 Schematic adiabatic potentials corresponding to the $A_1^{'}(S_0)$ and $A_2(3s)^{''}$ states along the N-H dissociation coordinate starting from: (a) the C_{3v} Franck-Condon point, and; (b) the planar, D_{3h} S_1 minimum energy geometry. 54

4.2 Definition of the effective three-body Jacobi coordinates used in the construction of the two-mode model. 62

4.3 Definition of the three valence vectors and six polyspherical coordinates used in the construction of the four-mode model. . 64

4.4 Model and calculated potentials along the N-H dissociation coordinate R: (a) Model (lines) and MCQDPT2(4,11)/aug (points) adiabatic potentials; (b) Model diabatic potentials, and; (c) Model diabatic coupling between the $\tilde{A}(3s)$ and $\tilde{D}(4s)$ states. 85

4.5 Model and calculated potentials along the inversion coordinate ϕ: (a) Model (lines) and MCQDPT2(4,11)/aug (points) adiabatic potentials; (b) Model diabatic potentials, and; (c) A comparison of the model diabatic, block-diagonalised, and adiabatic ground state potentials. 87

4.6 State population probabilities following vertical excitation to the $\tilde{A}(3s)$ state calculated using the diabatic representation of the nuclear wavefunction and the two-dimensional potential $\boldsymbol{W}(\boldsymbol{q})$. (a) Diabatic state populations, and; (b) adiabatic state populations. 88

4.7 State-resolved N-H dissociation probabilities following vertical excitation to the $\tilde{A}(3s)$ state calculated using the diabatic representation of the nuclear wavefunction and the two-dimensional potential $\boldsymbol{W}(\boldsymbol{q})$. (a) Probabilities of dissociation in the diabatic states, and; (b) probabilities of dissociation in the adiabatic states. 89

4.8 State population probabilities calculated following excitation to the $\tilde{A}(3s)$ state: (a) State population probabilities in the intermediate representation, and; (b) adiabatic populations calculated from both the diabatic and intermediate representations of the nuclear wavepacket. 91

4.9 Model (lines) and calculated (points) potentials along the nuclear degrees of freedom entering into the four-dimensional model. (a) Adiabatic potentials along x. (b) Adiabatic potentials along y (c) Adiabatic potentials along φ. 92

4.10 State population probabilities following vertical excitation to the $\tilde{A}(3s)$ state calculated using the diabatic representation of the nuclear wavefunction and the four-dimensional potential $\boldsymbol{W}(\boldsymbol{r})$. (a) Diabatic state populations, and; (b) adiabatic state populations. 95

4.11 State-resolved N-H dissociation probabilities following vertical excitation to the $\tilde{A}(3s)$ state calculated using the eight-state diabatic representation of the nuclear wavefunction and the four-dimensional potential $\boldsymbol{W}(\boldsymbol{r})$. (a) Probabilities of dissociation in the diabatic states, and; (b) probabilities of dissociation in the adiabatic states. 97

4.12 State population probabilities and probabilities of dissociation following vertical excitation to the $\tilde{A}(3s)$ state calculated using the two-state intermediate representation of the nuclear wavefunction and the four-dimensional potential $\boldsymbol{W}(\boldsymbol{r})$: (a) Adiabtic state population probabilities, and; (b) time-cumulated N-H dissociation probabilities. 99

4.13 State population probabilities and time-cumulated probabilities of dissociation in the diabatic representation following excitation to both components of the doubly-degenerate $\tilde{B}(3p)$ state calculated using the eight-state, four-mode model: (a) diabatic population probabilities, and; (b) time-cumulated probabilities of dissociation in the diabatic states. 100

4.14 State population probabilities and time-cumulated probabilities of dissociation in the adiabatic representation following excitation to both components of the doubly-degenerate $\tilde{B}(3p)$ state calculated using the eight-state, four-mode model and the projected wavefunctions $\boldsymbol{P}_{a,i}^{(d)}|\boldsymbol{\Psi}^{(d)}\rangle$: (a) adiabatic population probabilities, and; (b) time-cumulated probabilities of dissociation in the adiabatic states. 102

4.15 Calculated and experimental spectra corresponding to excitation to the $\tilde{A}(3s)$ state: (a) Spectrum calculated using the two-mode model; (b) spectrum calculated using the four-mode model, and; (c) experimental spectrum adapted from [72]. . . 105

4.16 Spectrum corresponding to vertical excitation to both the $\tilde{B}_y(3p_y)$ and $\tilde{B}_z(3p_z)$ components of the $\tilde{B}(3p)$ state calculated using the four-mode model. 107

5.1 Molecular structure of 3-pyrroline. 111

5.2 Schematic adiabatic potentials corresponding to the $A^{'}(S_0)$, $A^{'}(3s)$, and $A^{'}(3p_x)$ states along the N-H dissociation coordinate for the planar arrangement of the C_4NH unit. 111

5.3 (a) Geometry of the axial conformer; (b) Geometry of the equatorial conformer, and; (c) Geometry of the reference configuration. 112

5.4 Schematic of the ground state adiabatic potential along the reaction coordinate for interconversion of the EQ and AX conformers. 113

5.5 The normal modes of the 3-pyrrolinyl radical important for the description of the photochemistry of 3-pyrroline. (a.) Q_1 (C-N-C out-of-plane bending), (b.) Q_4 (ring stretching and methine wagging), (c.) Q_6 (ring breathing), (d.) Q_{14} (symmetric methyline twisting), (e.) Q_{17} (symmetric methyline wagging), and (f.) Q_{22} (symmetric methyline stretching). . . . 123

5.6 Model diabatic surfaces along the N-H out-of-plane bending mode ϕ and the C-N-C bending mode Q_1: (a) the $\tilde{X}$ state potential; (b) the $\tilde{A}$ state potential, and; (c) the $\tilde{B}$ state potential.125

5.7 Model potential surfaces for the ground and first excited states of 3-pyrroline along the N-H out-of-plane bending mode ϕ and the N-H dissociation coordinate R. (a) Adiabatic surfaces, (b) Diabatic surfaces. 126

5.8 Model adiabatic potentials for the S_0 and S_1 states along the N-H dissociation coordinate plotted for different values of the N-H out-of-plane bending coordinate ϕ: (a) ϕ=0.0 radians, (b) ϕ=0.2 radians, and (c) ϕ=0.7 radians. 127

5.9 The two-dimensional reduced density plotted along the C-N-C inversion coordinate Q_1 and N-H out-of-plane bending coordinate ϕ for: (a) the vibrational eigenstate $|\Psi_{AX}\rangle$ calculated using the method of relaxation, and; (b) the vibrational eigenstate $|\Psi_{EQ}\rangle$ calculated using the method of improved relaxation. 128

5.10 Diabatic population probabilities following excitation to the $\tilde{A}$ state: (a) population probabilities following vertical excitation of the $|\Psi_{AX}\rangle$ state, (b) population probabilities following vertical excitation of the $|\Psi_{EQ}\rangle$ state. 129

5.11 Time-cumulated N-H dissociation probabilities following excitation to the $\tilde{A}$ state: (a) dissociation probabilities following vertical excitation of the $|\Psi_{AX}\rangle$ state, (b) dissociation probabilities following vertical excitation of the $|\Psi_{EQ}\rangle$ state. 131

5.12 Elements of the model diabatic and adiabatic potential matrices along the N-H dissociation coordinate R and the N-H out-of-plane bending mode ϕ. (a) The diabatic potential for the $\tilde{A}$ state, (b) the adiabatic potential for the S_1 state, (c) the diabatic coupling between the $\tilde{X}$ and $\tilde{A}$ states. 132

5.13 Diabatic population probabilities following excitation to the $\tilde{B}$ state: (a) population probabilities following vertical excitation of the $|\Psi_{AX}\rangle$ state, (b) population probabilities following vertical excitation of the $|\Psi_{EQ}\rangle$ state. 134

5.14 Time-cumulated N-H dissociation probabilities following exciation to the $\tilde{B}$ state: (a) dissociation probabilities following vertical excitation of the $|\Psi_{AX}\rangle$ state, (b) dissociation probabilities following vertical excitation of the $|\Psi_{EQ}\rangle$ state. 135

5.15 Spectra calculated from the Fourier transforms of the wavepacket autocorrelation functions following excitation to the $\tilde{A}$ state. (a) Absorption spectrum corresponding to excitation of the AX conformer to the $\tilde{A}$ state, and; (b) Absorption spectrum corresponding to excitation of the EQ conformer to the $\tilde{A}$ state. 136

5.16 Expectation values $\langle Q_1 \rangle$ and $\langle \phi \rangle$ calculated following excitation of the $|\Psi_{AX}\rangle$ conformer to the $\tilde{A}$ state. 137

5.17 (a) Calculated absorption spectrum corresponding to excitation of the AX conformer to the $\tilde{B}$ state. (b) Calculated absorption spectrum corresponding to excitation of the EQ conformer to the $\tilde{B}$ state. 138

5.18 Expectation values $\langle Q_1 \rangle$ and $\langle \phi \rangle$ calculated following excitation of the $|\Psi_{AX}\rangle$ conformer to the $\tilde{B}$ state. 138

5.19 Combined spectrum corresponding to excitation of the AX and EQ eigenstates to both the $\tilde{A}$ and $\tilde{B}$ electronic states. Each contribution is weighted by both the calculated oscillator strength of the electronic state and Boltzmann factors for the vibrational states calculated using the experimentally determined value of ΔE_{EQ-AX}=340 cm^{-1} [75]. For clarity, the combined spectrum is shifted upwards relative to the individual spectra. 139

6.1 Molecular structure of pyrrole. 142

6.2 Schematic adiabatic potentials corresponding to the $A_1(S_0)$, $A_2(3s)$, $B_1(3s)$, $A_1(\pi\pi^*)$, and $B_2(\pi\pi^*)$ states along the N-H dissociation coordinate. 142

6.3 156

6.3 Model (lines) and calculated (points) adiabatic energies along nuclear degrees of freedom important for the description of the dynamics of pyrrole following photoexcitation. 157

6.4 Normal modes of the pyrrolyl radical important for the description of the photoinduced dynamics of the pyrrole molecule: (a) Q_2 (C-N-C out-of-plane bending), (b) Q_3 (C-H out-of-plane bending), (c) Q_7 (C-H out-of-plane bending), (d) Q_{12} (ring breathing), (e) Q_{16} (ring stretching), (f) Q_{17} (C-H stretching), (g) Q_{19} (C-H stretching), and (h) Q_{21} (ring stretching). . 158

6.5 Calculated diabatic state populations following excitation to the $B_2(\pi\pi^*)$ state. (a) State populations calculated using a ten-mode model including the mode Q_2. (b) State populations calculated using a nine-mode model excluding the mode Q_2. . 161

6.6 Calculated probabilities of N-H dissociation following excitation to the $B_2(\pi\pi^*)$ state. (a) Dissociation probabilities calculated using a ten-mode model including the mode Q_2. (b) Dissociation probabilities calculated using a nine-mode model excluding the mode Q_2 161

6.7 The calculated one-dimensional reduced density along the C-N-C out-of-plane bending mode Q_2 at 410 fs following vertical excitation to the $B_2(\pi\pi^*)$ state. 163

6.8 (a) Geometry representative of the location of density in the $B_2(\pi\pi^*)$ state for times greater than 200 fs. (b) Geometry of the ring-puckered conical intersection between the $B_2(\pi\pi^*)$ state and the ground state optimised at the CAS(6,6)/6-311++G** level using an active space comprised of the orbitals $1b_1(\pi)$, $2b_1(\pi)$, $1a_2(\pi)$, $3b_1(\pi^*)$ and $2a_2(\pi^*)$. 163

6.9 (a) Calculated diabatic state populations following excitation to the $A_1(\pi\pi^*)$ state. (b) Calculated probabilities of N-H dissociation following excitation to the $A_1(\pi\pi^*)$ state. 165

6.10 (a) Calculated diabatic state populations following excitation to the $A_2(3s)$ state. (b) Calculated probabilities of N-H dissociation following excitation to the $A_2(3s)$ state. 167

6.11 Fitted values of the tunnelling timescale τ_2 following vertical excitation to the $A_2(3s)$ state using various barriers to dissociation, E_B, on the $A_2(3s)$ state potential surface. 168

6.12 Experimental and calculated spectra corresponding to the first band in the electronic spectrum of pyrrole. Top: experimental electronic absorption spectrum [94] with the envelope of the first band of the photoelectron spectrum [102] inset. Bottom: calculated electronic absorption spectra corresponding to excitation to the $A_1(\pi\pi^*)$, $B_1(3p_y)$ and $B_2(\pi\pi^*)$ states of pyrrole. The combined spectrum corresponds to the oscillator strength-weighted sum of the individual spectra. For clarity, the combined spectrum is shifted upwards relative to the individual spectra. 173

6.13 Calculated spectra corresponding to vertical excitation to the $B_2(\pi\pi^*)$ state using both the full model Hamiltonian and the model Hamiltonian with all interstate coupling constants removed. Overlayed are spectra corresponding to vertical excitation to the $A_2(3p_z)$ and $B_1(3s)$ states calculated using a model Hamiltonian with all interstate coupling constants removed. . 175

6.14 Calculated spectra corresponding to vertical excitation to the $A_1(\pi\pi^*)$ state using both the full model potential and the model potential with all interstate coupling constants removed. 177

7.1 Molecular structure of aniline. 183

7.2 Schematic adiabatic potentials corresponding to the $A_1(S_0)$, $B_2(\pi\pi^*)$, $B_1(3s/\pi\sigma^*)$, and $A_1(\pi\pi^*)$ states along the N-H dissociation coordinate starting from the planar S_1 minimum energy geometry. 183

7.3 Normal modes important for the description of the dynamics of aniline following excitation to the $\tilde{A}(\pi\pi^*)$ and $\tilde{E}(\pi\pi^*)$ states: (a) $\tilde{Q}_1$ 197

7.4 Continued over page. 198

7.4 Model (lines) and calculated (points) adiabatic energies along nuclear degrees of freedom important for the description of the dynamics of aniline following excitation to the $\tilde{A}(\pi\pi^*)$ and $\tilde{E}(\pi\pi^*)$ states. 199

7.5 (a) Absorption spectrum calculated using wavepacket propagations over model potential surfaces representing the sub-Hilbert space spanned by the first six electronic states of aniline. The upper band corresponds to vertical excitation to the $\tilde{E}(\pi\pi^*)$ state and was produced using a fourteen-dimensional model potential. The lower band corresponds to excitation to the $\tilde{A}(\pi\pi^*)$ state, was produced using a twelve-dimensional model including Herzberg-Teller terms. Damping functions have been included in the Fourier transforms of the autocorrelation functions to model the homogeneous broadening due to excluded modes. (b) Experimental spectrum, adapted from Ref 116. 201

7.6 Spectra corresponding to excitation to the $\tilde{A}(\pi\pi^*)$ state, calculated using twelve-dimensional, six-state wavepacket propagations. (a) Spectrum calculated using vertical excitation to the $\tilde{A}(\pi\pi^*)$ state, with assignments of the vibrational progressions given for the first eleven peaks. (b) Spectrum calculated using the linear dipole excitation operator $\hat{O}_{HT}$ to model the Herzberg-Teller effect. 202

7.7 Spectrum corresponding to vertical excitation to the $\tilde{E}(\pi\pi^*)$ state, calculated using a fourteen-dimensional, six-state wavepacket propagation, with assignments of the three dominant vibrational progressions. 204

7.8 Diabatic state population probabilities following excitation to the $\tilde{A}(\pi\pi^*)$ state, calculated using a twelve-dimensional, six-state wavepacket propagation. The corresponding initial state was produced by operation on the ground state wavefunction with the linear dipole excitation operator $\hat{O}_{HT}$. 205

7.9 Diabatic state population probabilities following excitation to the $\tilde{E}(\pi\pi^*)$ state, calculated using a fourteen-dimensional, six-state wavepacket propagation and a vertical excitation of the ground state wavefunction. 206

7.10 Time-resolved photoelectron spectra recorded following photoexcitation of aniline adapted from Ref. [119]: (a) spectrum recored following excitation at 5.17 eV, and; (b) spectrum recorded following excitation at 5.21 eV. The lower peak at $\sim$ 1 eV is attributable to ionisation from the $B_2(\pi\pi^*)$ state. The broad peak seen at $\sim$ 1.3 eV to $\sim$ 1.6 eV has been taken to correspond to ionisation from the $A_1(\pi\pi^*)$ state [119], but at lower excitation energies is found to be composed of two peaks, the lower of which we propose could be due to ionisation from the $\tilde{D}(3p_y)$ and/or $\tilde{C}(3p_z)$ states. 208

List of Tables

4.1 Elements of the tensor $\boldsymbol{A}^{(2)}$ calculated at the FC point using derivative coupling terms calculated at the CAS(8,7)/6-311++G** level. Entries of - denote elements that are zero. All elements are given in atomic units. The numbers indexing the columns and rows correspond to the Cartesian nuclear coordinates ordered x_N, y_N, z_N, x_{H_1}, y_{H_1}, z_{H_1}, x_{H_2}, y_{H_2}, z_{H_2}, x_{H_3}, y_{H_3}, z_{H_3}. 59

4.2 Elements of the tensor $\boldsymbol{A}^{(2)}$ calculated at the D_{3h} $\tilde{A}(3s)$ state minimum using derivative coupling terms calculated at the CAS(8,7)/6-311++G** level. Entries of - denote elements that are zero. All elements are given in atomic units. The numbers indexing the columns and rows correspond to the Cartesian nuclear coordinates ordered x_N, y_N, z_N, x_{H_1}, y_{H_1}, z_{H_1}, x_{H_2}, y_{H_2}, z_{H_2}, x_{H_3}, y_{H_3}, z_{H_3}. 60

4.3 Vertical excitation energies, symmetries and dominant configurations of the first eight singlet excited states of ammonia calculated at the D_{3h} S_1 minimum energy geometry at the MCQDPT2(4,11)/aug level. 76

4.4 Linear interstate coupling coefficients $\lambda^{(i,j)}$ entering into the expansion of the two-dimensional model potential $\boldsymbol{W}(\boldsymbol{q})$. All values are given in eV/radian. 86

4.5 Linear interstate coupling coefficients $\lambda_{\alpha}^{(i,j)}$; $\alpha = x, y, \varphi$, entering into the expansion of the four-dimensional model potential $\boldsymbol{W}(\tilde{\boldsymbol{r}})$. All values are given in eV/radian. 93

4.6 Quadratic interstate coupling coefficients $\mu_{\alpha\beta}^{(i,j)}$ entering into the expansion of the four-dimensional model potential $\boldsymbol{W}(\tilde{\boldsymbol{r}})$. All values are given in eV/radian^2. 94

4.7 Computational details of the wavepacket propagations corresponding to excitation to the $\tilde{A}(3s)$ state using the diabatic and intermediate representations. The DVR types exp and sin correspond to exponential and sine DVRs, respectively. N_i, N_j are the number of primitive DVR functions used to describe each particle. n_i are the number of single-particle functions used for each state. 96

4.8 Comparison of the calculated and measured peak positions (E_n) and spacings (ΔE_n) in the $\tilde{A}(3s) \leftarrow \tilde{X}$ spectrum of ammonia. Both calculated spectra were shifted such that their origins coincided with that of the experimental spectrum. All energies are reported in units of cm^{-1}. † Ref. [25] 104

4.9 Comparison of the calculated and measured peak positions (E_n) and spacings (ΔE_n) in the $\tilde{B} \leftarrow \tilde{X}$ spectrum of ammonia. The calculated spectrum was shifted such that their origins coincided with that of the experimental spectrum. All calculated quantities were computed using the four-mode model. All energies are reported in units of cm^{-1}. †: Ref. [73], ‡: Ref. [74] 107

5.1 Symmetries, dominant configurations and vertical excitation energies of the first six singlet states of 3-pyrroline at the reference point as determined from EOM-CCSD calculations employing the aug-cc-pVDZ basis set. The bracketed numbers displayed alongside the dominant configurations are the corresponding coefficients. $|0\rangle$ denotes the reference (Hartree Fock) configuration. 119

5.2 Linear intrastate coupling constants obtained from the fitting of the model potential to adiabatic energies calculated at the EOM-CCSD/aug-cc-pVDZ level. All quantities are reported in eV. 121

5.3 Linear interstate coupling constants obtained from the fitting of the model potential to adiabatic energies calculated at the EOM-CCSD/aug-cc-pVDZ level. All quantities are reported in eV. 121

5.4 Fitted parameters entering into the expansion of the linear interstate coupling constants $\lambda_\alpha^{(i,j)}$ with respect to the N-H dissociation coordinate R. The terms ${}^1\Lambda_\alpha^{(i,j)}$ are given in eV, all other quantities are dimensionless. 123

5.5 Computational details of the wavepacket propagations corresponding to excitation to the $\tilde{A}$ state. The DVR types exp and HO correspond to exponential and Harmonic oscillator DVRs, respectively. N_i, N_j are the number of primitive DVR functions used to describe each particle. n_i are the number of single-particle functions used for each state. 129

5.6 Computational details of the wavepacket propagations corresponding to excitation to the $\tilde{B}$ state. The DVR types exp and HO correspond to exponential and Harmonic oscillator DVRs, respectively. N_i, N_j are the number of primitive DVR functions used to describe each particle. n_i are the number of single-particle functions used for each state. 133

6.1 Symmetries, dominant configurations and vertical excitation energies E_v of the first seven adiabatic electronic states of pyrrole as obtained from CASPT2(8,8)/aug+ calculations at the FC point. The bracketed numbers displayed alongside the dominant configurations are the corresponding coefficients. All energies are given in units of eV. 150

6.2 A comparison of the calculated CASPT2(8,8)/aug+ vertical excitation with previously reported values determined both experimentally and theoretically.[a]Ref 98, [b]Ref 99, [c]Ref 100, [d]Ref 94, [e]Ref 101. 153

6.3 Normal mode symmetries and frequencies of the pyrrolyl radical calculated calculated at the FC point. Both the nuclear geometry used and the Hessian were calculated using the MP2 method and aug-cc-pVDZ basis. oop: out-of-plane, sym: symmetric, asym: asymmetric. 154

6.4 Linear intrastate coupling constants (eV) determined by fitting to adiabatic energies calculated at the CASPT2(8,8)/aug+ level. 155

6.5 Linear interstate coupling constants (eV) 157

6.6 Computational details of the wavepacket propagations corresponding to excitation to the $B_2(\pi\pi^*)$ state. The DVR types exp and HO correspond to exponential and Harmonic oscillator DVRs, respectively. N_i, N_j are the number of primitive DVR functions used to describe each particle. n_i are the number of single-particle functions used for each state. 159

6.7 Computational details of the wavepacket propagations corresponding to excitation to the $A_1(\pi\pi^*)$ state. The DVR types exp and HO correspond to exponential and Harmonic oscillator DVRs, respectively. N_i, N_j are the number of primitive DVR functions used to describe each particle. n_i are the number of single-particle functions used for each state. 164

6.8 Computational details of the wavepacket propagations corresponding to excitation to the $A_2(3s)$ state. The DVR types exp and HO correspond to exponential and Harmonic oscillator DVRs, respectively. N_i, N_j are the number of primitive DVR functions used to describe each particle. n_i are the number of single-particle functions used for each state. 166

6.9 Fitted parameters entering into the model expression for the N-H dissociation probability calculated following vertical excitation to the $A_2(3s)$ state using various barriers to dissociation, E_B on the $A_2(3s)$ state potential surface. 168

6.10 Parameters entering into the model Hamiltonian $H_{3p_y}(\tilde{\boldsymbol{Q}})$, as defined in Equation 6.22, used to simulate to spectrum corresponding to excitation to the $B_1(3p_y)$ state. All quantities were evaluated from the results of EOM-CCSD calculations using the aug-cc-pVDZ basis. 174

7.1 Frequencies and symmetries of the normal modes calculated at the MP2/aug-cc-pVDZ level at the transition state to NH_2 inversion. ip: in-plane, oop: out-of-plane, sym: symmetric, asym: asymmetric. 191

7.2 Calculated and experimental excitation energies at the reference geometry ($\boldsymbol{Q}_0$) and the FC point ($\boldsymbol{Q}_{min}$). [a]Refs 112 and 113. [b]Ref 115. 192

7.3 Linear intrastate coupling strengths obtained from fitting to the results of EOM-CCSD/aug-cc-pVDZ calculations. 194

7.4 Linear interstate coupling strengths, obtained from fitting to the results of EOM-CCSD/aug-cc-pVDZ calculations. 195

7.5 Details of the MCTDH simulations of excitation to the $\tilde{A}(\pi\pi^*)$ state, for which a propagation time of 300 fs was used. 196

7.6 Details of the MCTDH simulation of excitation to the $\tilde{E}(\pi\pi^*)$ state, for which a propagation time of 300 fs was used. 196

Glossary

ADT Adiabatic-to-diabatic transformation

BF Body-fixed

CAP Complex absorbing potential

CASPT Complete active space perturbation theory

CASPT2 Second-order complete active space perturbation theory

CASSCF Complete active space self-consistent field

CCSD Coupled-cluster singles-and-doubles

CR-EOM-CCSD(T) Completely renormalised equation-of-motion coupled-cluster singles-and-doubles with non-iterative triples corrections

DVR Discrete variable representation

EOM-CC Equation-of-motion coupled-cluster

EOM-CCSD Equation-of-motion coupled-cluster singles-and-doubles

FBR Finite basis representation

FC Franck-Condon

Irrep Irreducible representation

MCQDTP2 Second-order multi-configurational quasi-degenerate pertubation theory

MCSCF Multiconfigurational self-consistent field

MCTDH Multi-configurational time-dependent Hartree

MP2 Second-order Møller-Plesset perturbation theory

NACT Non-adiabatic coupling term

PES Potenital energy surface

RMSD Root mean square deviation

SPF Single-particle function

SPP Single-particle potential

VBR Variational basis representation

VEE Vertical excitation energy

Chapter 1

Introduction

Photochemistry, that is, the area concerned with chemical reactions driven by the interaction of a molecular system with an external electric field, can be considered to be ubiquitous in the natural world. Pertinent examples include the cis/trans isomerisation of the retinal chromophore of the rhodopsin protein, which constitutes the initial step in the process of vision [1], and the efficient radiationless decay mechanisms exhibited by the DNA bases following electronic excitation, which have been posited as constituting possible origins of the photostability of life [2–5].

A qualitative framework in which basic photochemical processes may be cast is as follows. In the presence of an external electric field $\boldsymbol{\epsilon}(t)$, a molecular system experiences a perturbation $\hat{H}_{ML}$ described in the dipole approximation by

$$\hat{H}_{ML} = -\boldsymbol{\mu} \cdot \boldsymbol{\epsilon}(t), \tag{1.1}$$

where $\boldsymbol{\mu}$ denotes the dipole moment of the system. When the frequency of the external field is resonant with a transition between two electronic states, the interaction with the field may result in the transfer of population between the two states in question. Following such an electronic transition, a multitude of possible relaxation pathways may be open, including the radi-

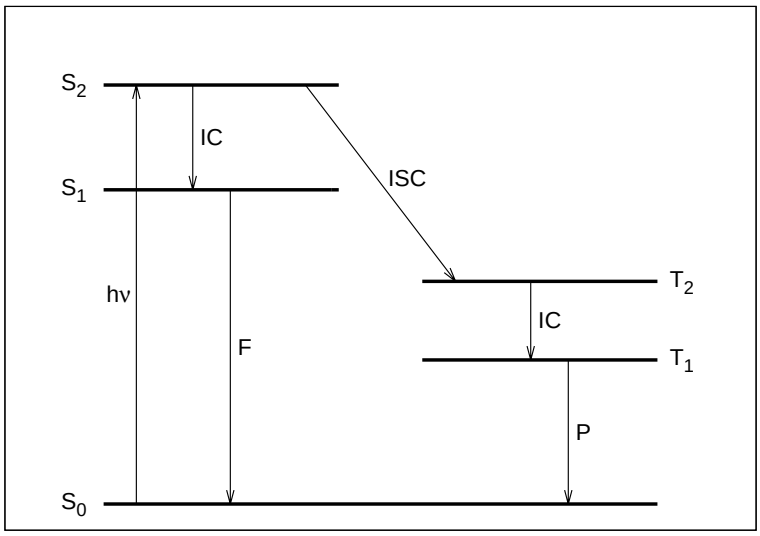

Fig. 1.1: A so-called Jablonski diagram illustrating the possible relaxation pathways open to a molecular sytem following the absorption of a photon of frequency ν in its singlet ground state. Here, the lables S_n denote the singlet electronic states, and T_n the triplet electronic states. IC, ISC, F, and P denote, respectively, internal conversion, intersystem crossing, flourescence and phosphorescence.

ationless transfer of population to energetically proximate electronic states. Such processes are shown schematically in Figure 1.1. Following electronic excitation, the system will typically be at a non-stationary point on the potential surface generated by the electrons of the molecule. Thus, nuclear motion may be driven.

The focus of the work presented here is the photodissociation of molecular systems, that is, the breaking of one or more bonds in a molecule following the absorption of light. Within the framework of non-relativistic quantum mechanics, such a process may be cast in the following form. An initial state $|\psi_i\rangle$ is taken to propagate on the ground state potential until time $t = 0$. Taking $|\psi_i\rangle$ to be an eigenstate of the ground state potential, the initial wavefunction changes only by a phase factor. At time $t = 0$, the absorption of a single photon results in the promotion of the state $|\psi_i\rangle$ to an electronically excited state, which, assuming vertical excitation, is given in

the dipole approximation by

$$|\phi_i(0)\rangle = \boldsymbol{\mu}|\psi_i\rangle, \tag{1.2}$$

where $\boldsymbol{\mu}$ is the corresponding transition dipole moment operator. The initially excited state $|\phi_i(0)\rangle$ consists of a linear combination of the vibrational eigenstates of the excited electronic state

$$\begin{aligned} |\phi_i(0)\rangle &= \sum_n C_n|\psi_n\rangle \\ &= \sum_n \langle\psi_n|\boldsymbol{\mu}\psi_i\rangle\,|\psi_n\rangle, \end{aligned} \tag{1.3}$$

where the $|\psi_n\rangle$ correspond to the eigenstates of the excited state potential. This superposition of eigenstates, a so-called wavepacket, then drives the movement of the excited wavefunction according, in a non-relativistic framework, to the time-dependent Schrödinger equation

$$i\hbar\frac{\partial}{\partial t}|\phi_i\rangle = \hat{H}|\phi_i\rangle, \tag{1.4}$$

with $\hat{H}$ denoting the system Hamiltonian. Pictorially, this process is illustrated in Figure 1.2. Photodissociation may, of course, occur when the excited state potential is unbound with respect to one or more nuclear degrees of freedom.

Photodissociation processes are typically challenging to model in an accurate manner for two primary reasons. Firstly, unlike the preponderance of ground state processes, the excitation of a molecular system to an electronically excited state denies us, in general, the possibility of treating in a satisfactory manner the electronic and nuclear degrees of freedom as being decoupled. Thus, the evolution of the wavepacket $|\phi_i\rangle$ has be considered to occur over a manifold of vibronically coupled electronic states. Secondly, the

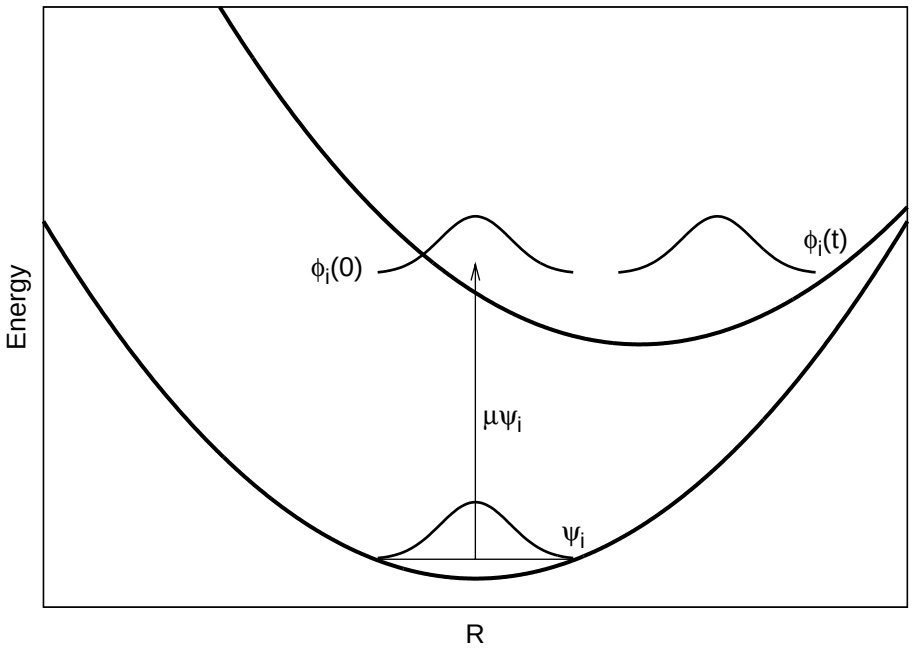

Fig. 1.2: Pictorial representation of the excitation of a system from its ground electronic state $|\psi_i\rangle$ to an excited state $|\phi_i\rangle = \boldsymbol{\mu}|\psi_i\rangle$, a wavepacket that evolves as governed by the time-dependent Schrödinger equation. R here corresponds to a nuclear coordinate.

dissociation of a molecule implies large amplitude motion of the nuclei, rendering necessary the accurate description of the molecular Hamiltonian over a large range of nuclear geometries. This is in particular a challenge for the representation of the potential operator, for which exact analytic expressions do not exist.

One particular class of molecular systems that has attracted much recent attention regarding the photo-induced dissociation of its members are heteroaromatic species containing a heteroatom-hydride bond (denoted X-H), such as phenols, pyrroles and azoles. Many of these species are remarkable for their vanishing fluorescence quantum yields, a phenomenon that is explicable in terms of the existence of efficient radiationless decay mechanisms connecting their excited and ground electronic states. Initial attempts to identify the nature of the operative mechanisms of decay were largely cen-

tred on the observation by Sobolewski and Domcke [6] that common to many heteroaromatic species is the existence of low-lying singlet $3s/\pi\sigma^*$ states that are quasi-bound with respect to an X-H bond. Population of such a state has been posited as providing a mechanism for radiationless decay by means of the accessing of a conical intersection with the ground state situated along the X-H dissociation coordinate R_{XH}. A good example of the roles played by low-lying $3s/\pi\sigma^*$ states in the photochemistry of heteroaromatic molecules is provided by indole. Illustrated in Figure 1.3 are the calculated energies (adapted from Ref. [6]) of the S_0, $S_1(\pi\pi^*)$, $S_2(\pi\pi^*)$ and $S_3(3s/\pi\sigma^*)$ states of indole are shown plotted along the N-H dissociation coordinate. The repulsive nature of the $S_3(3s/\pi\sigma^*)$ state is clearly seen, as is the intersection of this state with the ground state. The mediation of ultrafast N-H dissociation by the $S_3(3s/\pi\sigma^*)$ state has been revealed experimentally, with a timescale of $\sim$ 100 fs for direct N-H dissociation following excitation to the $\pi\pi^*$ states and subsequent internal conversion to the $S_3(3s/\pi\sigma^*)$ state being reported [7], highlighting the efficiency of $3s/\pi\sigma^*$ state-mediated dissociation mechanisms even when the dissociative states under question do not undergo direct excitation.

Before proceeding, clarification of the notation '$3s/\pi\sigma^*$' is sought: the adoption of this label is used to describe the character of the corresponding adiabatic states under question, which typically possess $3s$ Rydberg-type character in the vicinity of the Franck-Condon point, but acquire pronounced $\pi\sigma^*$, valence-type characters as the the X-H dissociation coordinate is traversed. Explanation of this change in character is typically made by taking the adiabatic potential in question to correspond to an avoided crossing between two diabatic states: a lower, bound $3s$ Rydberg state that is vibronically coupled to a higher-lying, purely dissociative $\pi\sigma^*$ state by the X-H

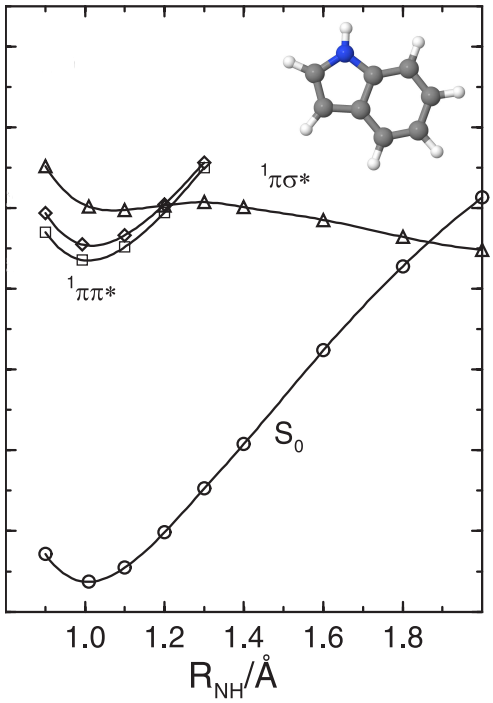

Fig. 1.3: Energies of the four lowest adiabatic electronic states of indole along the N-H dissociation coordinate (adapted from Ref. [6]), with the geometry of indole at the Franck-Condon point inset.

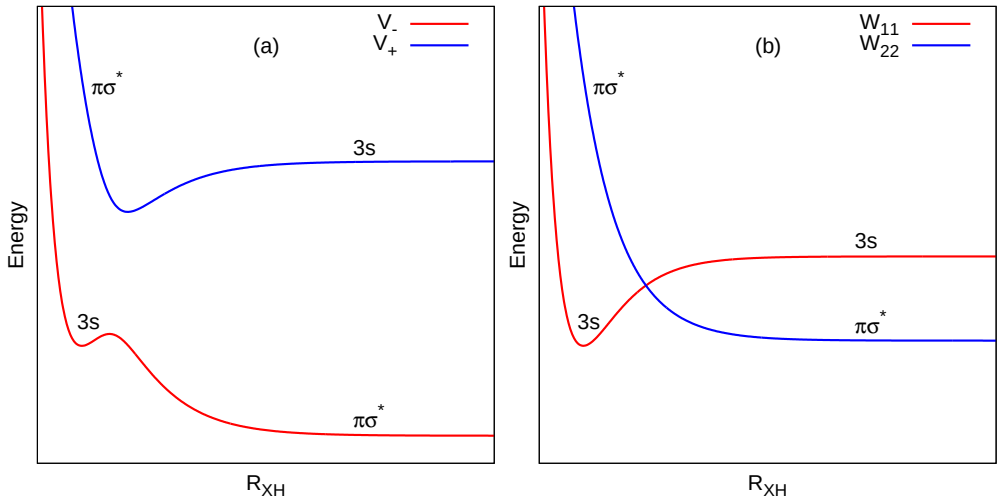

Fig. 1.4: Potential surfaces yielded by the avoided crossing model given in Equation 1.5 using a coupling function $W_{12}(R_{XH}) = \Delta \tanh(\rho R_{XH})$: (a) model adiabatic surfaces, and; (b) model diabatic surfaces. The labels $3s$ and $\pi\sigma^*$ refer to the characters of the states whose potentials they reside next to.

dissociation coordinate. Such an avoided crossing may be modelled by

$$V_{\pm}(R_{XH}) = \frac{1}{2}\Bigg\{ W_{11}(R_{XH}) + W_{22}(R_{XH}) \pm \sqrt{\left(W_{11}(R_{XH}) - W_{22}(R_{XH})\right)^2 + 4W_{12}^2(R_{XH})} \Bigg\}, \tag{1.5}$$

where $V_{-}(R_{XH})$ and $V_{+}(R_{XH})$ denote the lower and upper adiabatic states in question, respectively, $W_{11}(R_{XH})$ and $W_{22}(R_{XH})$ correspond, respectively, to the bound $3s$ Rydberg and dissociative $\pi\sigma^*$ diabatic states, and $W_{12}^2(R_{XH})$ the coupling between the two diabatic states. A pictorial representation of this model is given in Figure 1.4. This model is, of course, an idealisation that neglects the coupling of the states in question to their orthogonal complement, but is still of use in the interpretation of the dissociation dynamics of the molecules under consideration here.

Generally, the oscillator strengths associated with transition from the ground state to the $3s/\pi\sigma^*$ states of heteroaromatic species are either small

or zero, as in the case of indole, with the transition gaining intensity *via* the Herzberg-Teller effect and/or intensity borrowing from nearby optically bright states. The case of a $3s/\pi\sigma^* \leftarrow S_0$ transition mediated by intensity borrowing has typically been viewed as occurring as a result of vibronic coupling of the $3s/\pi\sigma^*$ state to an energetically proximate, optically bright $\pi\pi^*$ state. Depending on the relative energetic spacing and ordering of the low-lying $\pi\pi^*$ and $3s/\pi\sigma^*$ states in these systems, significantly different excited state dynamics may be observed. By way of example, both phenol and thiophenol share in common a bright $\pi\pi^*$ state as their first excited state and a quasi-bound $3s/\pi\sigma^*$ state as their second excited state. Both molecules are found to dissociate following excitation to their first excited states [8]. However, as illustrated in Figure 1.5, the energetic spacing of the $S_1(\pi\pi^*)$ and $S_2(3s/\pi\sigma^*)$ states in thiophenol is greatly reduced in comparison to that in phenol. Consequently, following excitation to the $S_1(\pi\pi^*)$ state of phenol the rate of depopulation of this state is much slower than in the case of thiophenol [8], a result of the hindrance of internal conversion to the $S_2(3s/\pi\sigma^*)$ state owing to the increased energetic separation of the $S_1(\pi\pi^*)$ and $S_2(3s/\pi\sigma^*)$ states.

The aim of the work presented in this thesis is to model at a fully quantum mechanical level the dynamics of $3s/\pi\sigma^*$ state-containing systems following photoexcitation, focussing on the molecules ammonia, 3-pyrroline, pyrrole and aniline. The work is partitioned as follows. In Chapter 2 the theoretical framework underpinning the techniques and methods used is presented, including the definition of the adiabatic and diabatic representations mentioned above. Chapter 3 contains an exposition of the computational methods used in the studies presented in the later chapters.

In Chapter 4 a study of the excited state dynamics of ammonia is pre-

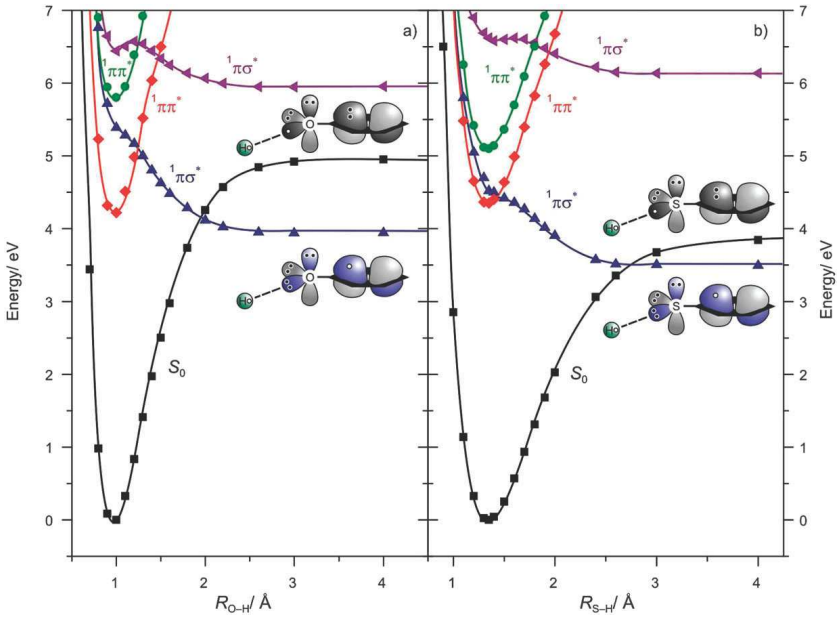

Fig. 1.5: Calculated adiabatic energies of the first two $\pi\pi^*$ and the first two $3s/\pi\sigma^*$ states of: (a) phenol, and; (b) thiophenol. Adapted from Ref. [9].

sented. Ammonia in many ways represents a prototype for the dissociation of molecular systems containing quasi-bound $3s/\pi\sigma^*$ states. As such, numerous studies of its dissociation dynamics following excitation to its $S_1(3s/\pi\sigma^*)$ state have been made over the past few decades. However, no study has yet been made that questions the role played by states higher than the $S_1(3s/\pi\sigma^*)$ state on the dynamics of ammonia following excitation to this state. An estimation of the order of magnitude of the non-adiabatic coupling of the S_0 and $S_1(3s/\pi\sigma^*)$ states of ammonia to their orthogonal complement is made based on an evaluation of the extended Curl equation. Furthermore, two eight-state model Hamiltonians based on different coordinate systems are developed and used in quantum dynamics simulations of ammonia following excitation to its $S_1(3s/\pi\sigma^*)$ and $S_2(3p)$ states. Spectra corresponding to these excitations are calculated and analysed in comparison to the corresponding experimentally determined spectra. An attempt to identify the origin of the barrier to dissociation on the $S_1(3s/\pi\sigma^*)$ state is made, and

a study of effect of the inclusion of the coupling of the $S_1(3s/\pi\sigma^*)$ state to several higher-lying states on the dynamics following excitation to the $S_1(3s/\pi\sigma^*)$ state is performed.

In Chapter 5 a conformer-resolved study of the excited state dynamics of the 3-pyrroline molecule is presented. A model Hamiltonian based on the vibronic coupling Hamiltonian and extended to describe efficiently a dissociation pathway is constructed. Using this model Hamiltonian, quantum dynamics simulations corresponding to the excitation of both ground state conformers of 3-pyrroline to both its $S_1(3s/\pi\sigma^*)$ and $S_2(3p)$ states are performed. Corresponding electronic absorption spectra are calculated and their vibrational structure analysed.

Presented in Chapter 6 are the results of a study of the photoinduced dynamics of pyrrole. Using the methodology outlined in Chapter 5, a model Hamiltonian is constructed to describe the dynamics of pyrrole following excitation to the vibronically coupled manifold of states comprising its first six singlet electronic states. Quantum dynamics simulations of the excitation of pyrrole to its $S_1(3s/\pi\sigma^*)$, $S_4(\pi\pi^*)$ and $S_5(\pi\pi^*)$ states are discussed. The first band in the electronic absorption spectrum of pyrrole is calculated and a comprehensive analysis of its structure is made.

In Chapter 7 a study of the dynamics of aniline following excitation to its first two $\pi\pi^*$ states is made. A vibronic coupling Hamiltonian is constructed and used in subsequent quantum dynamics calculations corresponding to excitation to these two states. An analysis of the role played by two previously neglected $3p$ Rydberg states following excitation to aniline's second $\pi\pi^*$ state is made. The first two bands in aniline's electronic absorption spectrum are calculated and their vibrational structure analysed.

Chapter 2

Theory

2.1 The Nuclear Schrödinger Equation

If one's interest lies in the description of the properties and time-evolution of a molecular system, then, in order to guarantee the generality of an accurate treatment to a large number of situations, the non-relativistic, time-dependent Schrödinger equation,

$$i\dot{\Psi}(\boldsymbol{r},\boldsymbol{R},t) = \hat{H}(\boldsymbol{r},\boldsymbol{R})\Psi(\boldsymbol{r},\boldsymbol{R},t), \tag{2.1}$$

is required to be solved. Here $\Psi(\boldsymbol{r},\boldsymbol{R},t)$ denotes the total wavefunction for a molecular system comprised of electrons and nuclei whose collective coordinates are denoted, respectively, by $\boldsymbol{r}$ and $\boldsymbol{R}$. $\dot{\Psi}(\boldsymbol{r},\boldsymbol{R},t)$ denotes the time-derivative of $\Psi(\boldsymbol{r},\boldsymbol{R},t)$. Here, and in the following, atomic units are used, for which $\hbar$ is equated with unity.

The total Hamiltonian $\hat{H}(\boldsymbol{r},\boldsymbol{R})$ may be partitioned as follows:

$$\hat{H}(\boldsymbol{r},\boldsymbol{R}) = \hat{H}_{el}(\boldsymbol{r};\boldsymbol{R}) + \hat{T}_n(\boldsymbol{R}), \tag{2.2}$$

where $\hat{T}_n(\boldsymbol{R})$ denotes the nuclear kinetic energy operator, and $\hat{H}_{el}(\boldsymbol{r};\boldsymbol{R})$ the electronic Hamiltonian, comprised of the potential and electronic kinetic energy operators:

$$\hat{H}_{el}(\boldsymbol{r};\boldsymbol{R}) = U(\boldsymbol{r},\boldsymbol{R}) + \hat{T}_e(\boldsymbol{r}). \tag{2.3}$$

Expanding the total wavefunction $\Psi(\boldsymbol{r},\boldsymbol{R},t)$ in the basis of the eigenfunctions of the electronic Hamiltonian, $\{\phi_i\}$, we may write

$$\Psi(\boldsymbol{r},\boldsymbol{R},t) = \sum_{i=1}^{\infty} \phi_i(\boldsymbol{r};\boldsymbol{R})\chi_i(\boldsymbol{R},t), \tag{2.4}$$

with

$$\hat{H}_{el}(\boldsymbol{r};\boldsymbol{R})\phi_i(\boldsymbol{r};\boldsymbol{R}) = V_i(\boldsymbol{R})\phi_i(\boldsymbol{r};\boldsymbol{R}). \tag{2.5}$$

Projection onto the Schrödinger equation 2.1 with $\langle\phi_j|$ and subsequent insertion of the expansion 2.4 yields the following set of coupled equations for the time-dependence of the nuclear wavefunctions $\chi_j(\boldsymbol{R},t)$:

$$i\dot{\chi}_j(\boldsymbol{R},t) = \left[\hat{T}_n(\boldsymbol{R}) + V_j(\boldsymbol{R})\right]\chi_j(\boldsymbol{R},t) - \sum_{i=1}^{\infty}\Lambda_{ji}\chi_i(\boldsymbol{R},t), \tag{2.6}$$

where the coupling terms Λ_{ji} describe the coupling of the nuclear and electronic degrees of freedom:

$$\Lambda_{ji} = \delta_{ji}\hat{T}_n(\boldsymbol{R}) - \langle\phi_j|\hat{T}_n|\phi_i\rangle. \tag{2.7}$$

Equation 2.6 corresponds to the nuclear Schrödinger equation in the so-called adiabatic representation. Adopting rectilinear nuclear coordinates and an averaged nuclear mass, M, we may further write

$$\hat{T}_n(\boldsymbol{R}) = -\frac{1}{2M}\boldsymbol{\nabla}\cdot\boldsymbol{\nabla}, \tag{2.8}$$

with

$$\nabla_\alpha = \frac{\partial}{\partial R_\alpha}. \tag{2.9}$$

Using this specific form of the nuclear kinetic energy operator, the coupling terms may be written

$$\Lambda_{ji} = \frac{1}{2M}\left\{2\boldsymbol{\tau}_{ji}\cdot\boldsymbol{\nabla} + \tau_{ji}^{(2)}\right\}. \tag{2.10}$$

Here, the terms $\boldsymbol{\tau}_{ji}$ are the so-called nonadiabatic coupling terms (NACTs),

$$\boldsymbol{\tau}_{ji} = \langle\phi_j|\boldsymbol{\nabla}\phi_i\rangle \tag{2.11}$$

while the scalar coupling terms $\tau_{ji}^{(2)}$ are given by

$$\tau_{ji}^{(2)} = \langle\phi_j|\boldsymbol{\nabla}^2\phi_i\rangle. \tag{2.12}$$

Using this notation, the nuclear Schrödinger equation may be written

$$i\dot{\boldsymbol{\chi}} = \left[-\frac{1}{2M}\left(\boldsymbol{\nabla}+\boldsymbol{\tau}\right)^2 + \boldsymbol{V}\right]\boldsymbol{\chi}, \tag{2.13}$$

with $\boldsymbol{\chi}$ and $\boldsymbol{V}$ denoting, respectively, vectors of the nuclear wavefunctions $\chi_i(\boldsymbol{R})$ and the adiabatic energies $V_i(\boldsymbol{R})$.

The nuclear Schrödinger equation 2.13, as it stands, is intractable, owing to the complete, and in general infinite basis of electronic eigenfunctions $\{\phi_i\}$ used in the expansion of the total wavefunction. Thus, approximations to the nuclear Schrödinger equation as presented above are necessitated.

2.2 Hilbert Subspaces and the Group Born-Oppenheimer Approximation

To render the nuclear Schrödinger equation 2.13 tractable, it is required that we work with only a subspace of the complete Hilbert space of electronic states. We consider the partitioning of the complete Hilbert space into two subspaces: the P-space, spanned by the first N states, and its orthogonal

complement, the Q-space. The nuclear Schrödinger equation is then written such that all quantities now refer only to the P-space states:

$$i\dot{\chi}_j \approx \left[\hat{T}_n(\boldsymbol{R}) + V_i(\boldsymbol{R})\right]\chi_j(\boldsymbol{R},t) - \sum_{i=1}^{N}\Lambda_{ji}\chi_i(\boldsymbol{R},t); \quad j \leq N. \tag{2.14}$$

The question now arises of what criterion for the partitioning of the Hilbert space will not introduce significant errors into the determination of the $\dot{\chi}_j$; $j \leq N$ when using Equation 2.14. For convenience, we introduce the notation ${}^{PP}\Lambda_{ji}$ to denote the term coupling the states $|\phi_j\rangle$, $j \leq N$ and $|\phi_i\rangle$, $i \leq N$, and ${}^{PQ}\Lambda_{ji}$ for the term coupling the states $|\phi_j\rangle$, $j \leq N$ and $|\phi_i\rangle$, $i > N$, with ${}^{QQ}\Lambda_{ji}$ and ${}^{QP}\Lambda_{ji}$ being defined analogously. There are two sources of error introduced from the neglect of the states $|\phi_k\rangle$, $k > N$: (i) the evaluation of the coupling terms ${}^{PP}\Lambda_{ji}$, and; (ii) the neglect of the terms ${}^{PQ}\Lambda_{ji}$.

When working with only the P-space states, the error introduced into the evaluation of the coupling terms ${}^{PP}\Lambda_{ji}$ can be understood most easily by writing

$$\begin{aligned} {}^{PP}\Lambda_{ji} &= \frac{1}{2M}\left\{2{}^{PP}\boldsymbol{\tau}_{ji}\cdot\boldsymbol{\nabla} + {}^{PP}\tau^{(2)}_{ji}\right\} \\ &= \frac{1}{2M}\left\{2{}^{PP}\boldsymbol{\tau}_{ji}\cdot\boldsymbol{\nabla} + \boldsymbol{\nabla}{}^{PP}\boldsymbol{\tau}_{ji} - {}^{PP}(\boldsymbol{\tau}\boldsymbol{\tau})_{ji}\right\} \end{aligned} \tag{2.15}$$

and noting that the terms ${}^{PP}(\boldsymbol{\tau}\boldsymbol{\tau})_{ji}$ can be written as

$${}^{PP}(\boldsymbol{\tau}\boldsymbol{\tau})_{ji} = \sum_{k=1}^{N}{}^{PP}\boldsymbol{\tau}_{jk}{}^{PP}\boldsymbol{\tau}_{ki} + \sum_{k>N}{}^{PQ}\boldsymbol{\tau}_{jk}{}^{QP}\boldsymbol{\tau}_{ki}. \tag{2.16}$$

When working with only the P-space states, the sum over the terms ${}^{PQ}\boldsymbol{\tau}_{jk}{}^{QP}\boldsymbol{\tau}_{ki}$ are neglected. If, however, derivative coupling terms ${}^{PQ}\boldsymbol{\tau}_{ji}$ are of the order of $O(\epsilon)$, then the errors introduced by the neglect of the Q-space states will be of the order of $O(\epsilon^2)$, and, provided ϵ is sufficiently small, the errors introduced will be small enough to warrant their neglect.

The error introduced by the neglect of the coupling terms ${}^{PQ}\Lambda_{ji}$ is less straightforward to determine. We assume that the order of coupling between the P-space and Q-space states, $O(\epsilon)$, is small. The NACTs ${}^{PQ}\boldsymbol{\tau}_{ji}$ entering into ${}^{PQ}\Lambda_{ji}$ can thus be ignored. The scalar coupling terms ${}^{PQ}\tau^{(2)}_{ji}$ contained in ${}^{PQ}\Lambda_{ji}$ can be written

$$ {}^{PQ}\tau^{(2)}_{ji} = \boldsymbol{\nabla}{}^{PQ}\boldsymbol{\tau}_{ji} - \sum_{k=1}^{N} {}^{PP}\boldsymbol{\tau}_{jk}{}^{PQ}\boldsymbol{\tau}_{ki} - \sum_{k>N} {}^{PQ}\boldsymbol{\tau}_{jk}{}^{QQ}\boldsymbol{\tau}_{ki}. \tag{2.17} $$

The term $\boldsymbol{\nabla}{}^{PQ}\boldsymbol{\tau}_{ji}$ may be ignored provided ϵ is small, but there is no reason to assume that the terms ${}^{PP}\boldsymbol{\tau}_{jk}{}^{PQ}\boldsymbol{\tau}_{ki}$ and ${}^{PQ}\boldsymbol{\tau}_{jk}{}^{QQ}\boldsymbol{\tau}_{ki}$ entering into Equation 2.17 should be small. Conversely, near an intersection of the two Q-space states $|\phi_k\rangle$ and $|\phi_i\rangle$ the term ${}^{PQ}\boldsymbol{\tau}_{jk}{}^{QQ}\boldsymbol{\tau}_{ki}$ can be expected to be large. Similarly, the term ${}^{PP}\boldsymbol{\tau}_{jk}{}^{PQ}\boldsymbol{\tau}_{ki}$ can be expected to be large around an intersection of the P-space states $|\phi_j\rangle$ and $|\phi_k\rangle$. To understand how the scalar coupling terms between the P-space and Q-space states may be neglected, we consider a point of intersection between the two Q-space states $|\phi_k\rangle$ and $|\phi_i\rangle$. At this point we have, symbolically,

$$ {}^{PQ}\Lambda_{ji} \ni {}^{PQ}\boldsymbol{\tau}_{jk}{}^{QQ}\boldsymbol{\tau}_{ki}, \tag{2.18} $$

and

$$ {}^{PQ}\Lambda_{jk} \ni {}^{PQ}\boldsymbol{\tau}_{ji}{}^{QQ}\boldsymbol{\tau}_{ik} \tag{2.19} $$

Noting that the NACTs may be written as

$$ \boldsymbol{\tau}_{ji} = \frac{\left\langle \phi_j \middle| \left(\boldsymbol{\nabla} \hat{H}_{el} \right) \middle| \phi_i \right\rangle}{V_i - V_j}, \tag{2.20} $$

it can be seen to be justified to assume that ${}^{PQ}\boldsymbol{\tau}_{jk} \approx {}^{PQ}\boldsymbol{\tau}_{ji}$ at the point of intersection of the states $|\phi_i\rangle$ and $|\phi_k\rangle$. Assuming real, antisymmetric

NACTs, we thus find that

$$ {}^{PQ}\boldsymbol{\tau}_{jk}{}^{QQ}\boldsymbol{\tau}_{ki} \approx -{}^{PQ}\boldsymbol{\tau}_{ji}^{QQ}\boldsymbol{\tau}_{ik}. \tag{2.21} $$

at the point of intersection. Hence, we see that the terms ${}^{PQ}\boldsymbol{\tau}_{jk}{}^{QQ}\boldsymbol{\tau}_{ki}$ appearing in ${}^{PQ}\Lambda_{ji}$ are approximately cancelled by the terms ${}^{PQ}\boldsymbol{\tau}_{ji}{}^{QQ}\boldsymbol{\tau}_{ik}$ appearing in ${}^{PQ}\Lambda_{jk}$. Analogous conclusions hold near an intersection of the P-space states $|\phi_j\rangle$ and $|\phi_h\rangle$ for the approximate cancellation of the terms ${}^{PP}\boldsymbol{\tau}_{jh}{}^{PQ}\boldsymbol{\tau}_{hi}$ appearing in ${}^{PQ}\Lambda_{ji}$ by the terms ${}^{PP}\boldsymbol{\tau}_{hj}{}^{PQ}\boldsymbol{\tau}_{ji}$ appearing in ${}^{PQ}\Lambda_{hi}$. Away from intersections within the P- and Q-spaces these approximations do not hold. However, at such points the terms ${}^{PP}\boldsymbol{\tau}_{jk}{}^{PQ}\boldsymbol{\tau}_{ki}$ and ${}^{PQ}\boldsymbol{\tau}_{jk}{}^{QQ}\boldsymbol{\tau}_{ki}$ should be small if the NACTs ${}^{PQ}\boldsymbol{\tau}_{jk}$ are sufficiently small.

The use of only the P-space states in the evaluation of the nuclear Schrödinger equation is known as the group Born-Oppenheimer approximation. From the above considerations, it is seen that this may be considered a valid approximation so long as the NACTs coupling the P-space and Q-space states are sufficiently small.

2.3 The Diabatic Representation

Writing the NACT $\boldsymbol{\tau}_{ij}$ as

$$ \boldsymbol{\tau}_{ij} = \frac{\langle\phi_i|(\boldsymbol{\nabla}\hat{H}_{el})|\phi_j\rangle}{V_j - V_i} \tag{2.22} $$

it is seen that at an intersection between the adiabatic states $|\phi_i\rangle$ and $|\phi_j\rangle$ $\boldsymbol{\tau}_{ij}$ will become singular. Due to the singular nature of the NACTs $\boldsymbol{\tau}$ at the intersections between the adiabatic potentials, it is desirable to consider the use of a basis in which the NACTs are eliminated. That is, a new set of basis functions $\{\tilde{\phi}_a\}$ are defined that are related to the adiabatic basis by a unitary transformation

$$\tilde{\phi}_a = \sum_{i=1}^{N} \phi_i S_{ia}, \tag{2.23}$$

such that the NACTs in the new basis,

$$\tilde{\boldsymbol{\tau}}_{ab} = \left\langle \tilde{\phi}_a \middle| \boldsymbol{\nabla} \tilde{\phi}_b \right\rangle, \tag{2.24}$$

are zero. Such a basis is termed a diabatic basis, and the transformation matrix the adiabatic-to-diabatic transformation (ADT) matrix.

Rewriting $\tilde{\boldsymbol{\tau}}$ in terms of the adiabatic basis,

$$\tilde{\boldsymbol{\tau}} = \boldsymbol{S}^{\dagger} \boldsymbol{\tau} \boldsymbol{S} + \boldsymbol{S}^{\dagger} \left(\boldsymbol{\nabla} \boldsymbol{S} \right), \tag{2.25}$$

it is clear that the ADT matrix must satisfy the relation

$$\boldsymbol{\tau} \boldsymbol{S} + \boldsymbol{\nabla} \boldsymbol{S} = \mathbf{0}. \tag{2.26}$$

An ADT matrix that fulfils Equation 2.26 exactly yields a so-called strictly diabatic basis, in which the NACTs are truly eliminated. The necessary and sufficient condition for Equation 2.26 having a solution is

$$\frac{\partial^2 \boldsymbol{S}}{\partial R_\alpha \partial R_\beta} - \frac{\partial^2 \boldsymbol{S}}{\partial R_\beta \partial R_\alpha} = \mathbf{0}, \tag{2.27}$$

leading to the condition

$$\frac{\partial \boldsymbol{\tau}_\alpha}{\partial R_\beta} - \frac{\partial \boldsymbol{\tau}_\beta}{\partial R_\alpha} - [\boldsymbol{\tau}_\alpha, \boldsymbol{\tau}_\beta] = \mathbf{0}. \tag{2.28}$$

Equation 2.28, known as the extended Curl equation, is only satisfied for the complete Hilbert space of electronic states. Thus, for all practical purposes, for which a finite Hilbert subspace must be considered, a strictly diabatic basis does not exist. Instead we concern ourselves with a so-called quasi-diabatic basis for which the NACTs $\tilde{\boldsymbol{\tau}}$ are rendered sufficiently small

to be neglected without significant consequence. Setting the NACTs in the quasi-diabatic representation to zero and defining the quasi-diabatic nuclear wavefunctions

$$\tilde{\chi}_a = \sum_{i=1}^{N} S^{\dagger}_{ai} \chi_i, \tag{2.29}$$

yields the following nuclear Schrödinger equation:

$$i\dot{\tilde{\chi}}_j = \hat{T}_n \tilde{\chi}_j + \sum_{i=1}^{N} W_{ji} \tilde{\chi}_i, \tag{2.30}$$

where

$$W_{ji} = \left\langle \tilde{\phi}_j \middle| \hat{H}_{el} \middle| \tilde{\phi}_j \right\rangle. \tag{2.31}$$

It remains to note that Equation 2.26 defines the ADT matrix only up to a constant unitary transformation. That is, if $\boldsymbol{T}$ is a constant, nuclear coordinate-independent, unitary matrix, then the matrix

$$\boldsymbol{S}' = \boldsymbol{S}\boldsymbol{T} \tag{2.32}$$

will also satisfy Equation 2.26. By choosing $\boldsymbol{T} = \boldsymbol{S}^{\dagger}(\boldsymbol{Q}_e)$, we may choose the adiabatic and diabatic representations to be equivalent at the single, arbitrary nuclear geometry $\boldsymbol{Q}_e$.

2.4 Conical Intersections

The points of intersection of two adiabatic potentials are of great importance with regard to the excited state dynamics of a molecular system, owing to the fact that the NACTs $\boldsymbol{\tau}_{ij}$ scale with the inverse of the energetic separation $V_j - V_i$. Hence, at a point of intersection, denoted $\boldsymbol{R}_I$, between the two

states $|\phi_i\rangle$ and $|\phi_j\rangle$ an efficient, ultrafast radiationless transfer of population between the two states is mediated.

Considering a two state system, the adiabatic energies, denoted $V_-(\boldsymbol{R})$ and $V_+(\boldsymbol{R})$, may be written in terms of the diabatic potential

$$\boldsymbol{W}(\boldsymbol{R}) = \begin{pmatrix} W_{11}(\boldsymbol{R}) & W_{12}(\boldsymbol{R}) \\ W_{22}(\boldsymbol{R}) & W_{22}(\boldsymbol{R}) \end{pmatrix} \tag{2.33}$$

as

$$V_\pm(\boldsymbol{R}) = \frac{1}{2}\left\{W_{11}(\boldsymbol{R}) + W_{22}(\boldsymbol{R}) \pm \sqrt{(W_{11}(\boldsymbol{R}) - W_{12}(\boldsymbol{R}))^2 + 4W_{12}(\boldsymbol{R})^2}\right\}. \tag{2.34}$$

Expanding $\boldsymbol{W}(\boldsymbol{R})$ about the point of intersection $\boldsymbol{R}_I$ then gives to first-order

$$\begin{aligned} \Delta V &= V_+ - V_- \\ &= \sqrt{(\boldsymbol{g}\boldsymbol{R})^2 + 4(\boldsymbol{h}\boldsymbol{R})^2}, \end{aligned} \tag{2.35}$$

with

$$\boldsymbol{g} = \boldsymbol{\nabla}(W_{11}(\boldsymbol{R}_I) - W_{22}(\boldsymbol{R}_I)) \tag{2.36}$$

and

$$\boldsymbol{h} = \boldsymbol{\nabla}W_{12}(\boldsymbol{R}_I). \tag{2.37}$$

Defining the intersection-adapted coordinates

$$\boldsymbol{x} = \frac{\boldsymbol{g}}{||\boldsymbol{g}||}, \tag{2.38}$$

$$\boldsymbol{y} = \frac{\boldsymbol{h}}{||\boldsymbol{h}||}, \tag{2.39}$$

and $\boldsymbol{w}_i$, $i = 1, \ldots, 3N-8$ (for N atoms), we see that to first-order the degeneracy is lifted along only the gradient difference vector $\boldsymbol{x}$ and the derivative

coupling vector $\boldsymbol{y}$, which together form the so-called branching space. The remainder of the intersection adapted coordinates, $\boldsymbol{w}$, form the $(3N-8)$-dimensional seam space, in which the degeneracy is lifted quadratically. Such an intersection, for which $\boldsymbol{g} \neq 0$ and $\boldsymbol{h} \neq 0$, is termed a conical intersection. If, by symmetry, $\boldsymbol{g} = \boldsymbol{h} = 0$, but $\boldsymbol{\nabla}^2(W_{11}(\boldsymbol{R}_I) - W_{22}(\boldsymbol{R}_I)) \neq 0$ and $\boldsymbol{\nabla}^2 W_{12}(\boldsymbol{R}_I) \neq 0$, the degeneracy is lifted quadratically and the intersection belongs to a class that includes the so-called Renner-Teller intersection.

Chapter 3

Methodology

3.1 Introduction

In order to evaluate the nuclear Schrödinger equation (as defined in Chapter 2), two principal steps are required to be taken: (i) the determination of the matrix representation of the system Hamiltonian and; (ii) the adoption of a numerical representation of the nuclear wavefunction.

With regards to the evaluation of the Hamiltonian, it is usually possible to express analytically and exactly the kinetic energy operator, but generally the required *a priori* knowledge of the exact potential is not possible. To proceed, then, a model diabatic potential matrix $\boldsymbol{W}(\boldsymbol{R})$ is required to be determined. The construction of the diabatic potential is commonly achieved by one of two procedures: either through the calculation of the adiabatic potential and the ADT matrix [10, 11], or through an assumption of analytic forms of the elements of the diabatic potential and subsequent fitting to calculated adiabatic energies [12, 13]. The latter strategy, commonly referred to as 'diabatisation by *ansatz*', has the advantage of obviating the requirement of calculating the NACTs $\boldsymbol{\tau}$, and is the diabatisation scheme adopted here. In either case, however, an evaluation of the electronic Schrödinger equation must be made at nuclear geometries of interest with regards the dynamics of the system under consideration. To this end, a numerical representation

of the electronic wavefunction must be adopted, and those methods used in this work are described in Section 3.2.

In Section 3.3, methods for the numerical representation of the nuclear wavefunction are discussed. Once a given representation of the nuclear wavefunction has been adopted, the integration of the time-dependent Schrödinger equation requires the specification of an initial wavepacket, and methods for achieving this are discussed in Section 3.4. Sections 3.5 and 3.6 detail the methods used in the evaluation of the Hamiltonian matrix, a core procedure in the integration of the time-dependent Schrödinger equation. The remaining sections of this chapter are concerned with the analysis of a propagated wavepacket and the methods used to fit a diabatic potential to a given set of calculated adiabatic energies.

3.2 The Electronic Wavefunction

We consider a system comprised of N electrons, and assign to each a composite coordinate $\boldsymbol{x}_\alpha$ comprising both the spatial and spin coordinate of the αth electron. The wavefunction $\Psi(\boldsymbol{x}_1, \ldots, \boldsymbol{x}_N)$ for the system may be written as a direct product expansion in terms of a set of one-electron basis functions $\{\phi_i\}$:

$$\Psi(\boldsymbol{x}_1, \ldots, \boldsymbol{x}_N) = \sum_{i,j,\ldots,n} C_{ij\cdots n}\phi_i(\boldsymbol{x}_1)\phi_j(\boldsymbol{x}_2)\cdots\phi_n(\boldsymbol{x}_N). \tag{3.1}$$

Now, as we are considering a system of fermions, we require that the wavefunction be antisymmetric with respect to the interchange of the coordinates of any two electrons, which implies that $C_{ij\cdots kl\cdots n} = -C_{ij\cdots lk\cdots n}$. Thus, we may write

$$\Psi(\boldsymbol{x}_1, \ldots, \boldsymbol{x}_N) = \sum_{i,j,\ldots,n}{}' C_{ij\cdots n} \sum_{\alpha,\beta,\ldots,\nu=1}^{N} \epsilon_{\alpha,\beta,\ldots,\nu} \phi_{\alpha i} \phi_{\beta j} \cdots \phi_{\nu n}, \tag{3.2}$$

where $\phi_{\alpha i} = \phi_i(\boldsymbol{x}_\alpha)$, the primed summation implies summation over unique N-tuples $i, j, \ldots, n$ only, and $\epsilon_{\alpha,\beta,\ldots,\nu}$ is the Levi-Civita symbol:

$$\epsilon_{\alpha,\beta,\ldots,\nu} = \begin{cases} 1, & \text{if } (\alpha, \beta, \ldots, \nu) \text{ is an even permutation of } (1, 2, \ldots, N) \\ -1, & \text{if } (\alpha, \beta, \ldots, \nu) \text{ is an odd permutation of } (1, 2, \ldots, N) \\ 0, & \text{otherwise} \end{cases} \tag{3.3}$$

Hence we may write

$$\begin{aligned} \Psi(\boldsymbol{x}_1, \ldots, \boldsymbol{x}_N) &= \sum_{i,j,\ldots,n} C_{ij\cdots n} \det\left(\boldsymbol{\Phi}_{ij\cdots n}\right) \\ &= \sum_{\mu} C_\mu |\mu\rangle \end{aligned} \tag{3.4}$$

with

$$\boldsymbol{\Phi}_{ij\cdots n} = \begin{pmatrix} \phi_i(\boldsymbol{x}_1) & \phi_j(\boldsymbol{x}_1) & \cdots & \phi_n(\boldsymbol{x}_1) \\ \phi_i(\boldsymbol{x}_2) & \phi_j(\boldsymbol{x}_2) & \cdots & \phi_n(\boldsymbol{x}_2) \\ \vdots & \vdots & \ddots & \vdots \\ \phi_i(\boldsymbol{x}_N) & \phi_j(\boldsymbol{x}_N) & \cdots & \phi_n(\boldsymbol{x}_N) \end{pmatrix}. \tag{3.5}$$

For a complete set of basis functions $\{\phi_i\}$, Equation 3.4 corresponds the exact non-relativistic electronic wavefunction. For all practical implementations, an incomplete, finite basis must, of course, be used. Further, for a set of M one-electron basis functions the number of configurations $|\mu\rangle$ (each corresponding to a single so-called Slater determinant $\det\left(\boldsymbol{\Phi}_{ij\cdots n}\right)$) that exist is given by the binomial coefficient $\begin{pmatrix} M \\ N \end{pmatrix}$. A truncation of the expansion 3.4 is thus enforced. The task at hand, then, is to adopt a suitable criterion for the selection of configurations to enter into an approximate electronic wavefunction.

3.2.1 The Hartree-Fock Model

The *ansatz* for the Hartree-Fock wavefunction reads

$$|\Psi_{HF}\rangle = \left[\prod_{i=1}^{N} a_i^\dagger\right] |vac\rangle, \tag{3.6}$$

where the $a_i^\dagger$ correspond to the elementary creation operators and $|vac\rangle$ the vacuum state. That is, the Hartree-Fock state corresponds to a set of N independent electrons subject to Fermi correlation. As such, the one-electron basis functions $\{\phi_i\}$ (that is, molecular orbitals) of the Hartree-Fock wavefunction are determined as the eigenfunctions of a one-electron operator, the so-called Fock operator $\hat{f}$. Through the minimisation of the expectation value

$$E = \frac{\left\langle \Psi_{HF} \middle| \hat{H} \middle| \Psi_{HF} \right\rangle}{\langle \Psi_{HF} | \Psi_{HF} \rangle}, \tag{3.7}$$

the Fock operator can be determined to take the following form:

$$\hat{f} = h(\boldsymbol{x}_\alpha) + \sum_j \mathcal{J}_j(\boldsymbol{x}_\alpha) - \mathcal{K}_j(\boldsymbol{x}_\alpha), \tag{3.8}$$

with the core Hamiltonian $h(\boldsymbol{x}_\alpha)$, the Coulomb operator $\mathcal{J}_j(\boldsymbol{x}_\alpha)$ and the exchange operator $\mathcal{K}_j(\boldsymbol{x}_\alpha)$ being given by

$$h(\boldsymbol{x}_\alpha) = -\frac{1}{2}\frac{\partial^2}{\partial \boldsymbol{x}_\alpha^2} - \sum_A \frac{Z_A}{r_{\alpha A}}, \tag{3.9}$$

$$\mathcal{J}_j(\boldsymbol{x}_\alpha) = \left\langle \phi_j(\boldsymbol{x}_\beta) \middle| r_{\alpha\beta}^{-1} \middle| \phi_j(\boldsymbol{x}_\beta) \right\rangle, \tag{3.10}$$

and

$$\mathcal{K}_j(\boldsymbol{x}_\alpha)\phi_k(\boldsymbol{x}_\alpha) = \left\langle \phi_j(\boldsymbol{x}_\beta) \middle| r_{\alpha\beta}^{-1} \middle| \phi_k(\boldsymbol{x}_\beta) \right\rangle \phi_j(\boldsymbol{x}_\alpha). \tag{3.11}$$

Here, the core Hamiltonian $h(\boldsymbol{x}_\alpha)$ is defined as the sum of the kinetic energy operator of the αth electron and the Coulombic interaction of the αth electron with the nuclei (indexed by A) of charge Z_A. $r_{\alpha\beta}^{-1}$ denotes the inverse distance between the αth and βth electrons, and $r_{\alpha A}^{-1}$ the inverse distance between the αth electron the the Ath nucleus.

3.2.2 The Coupled-Cluster Model

The *ansatz* for the coupled-cluster wavefunction may be written

$$|\Psi_{CC}\rangle = \left[\prod_\mu (1 + t_\mu \hat{\tau}_\mu)\right] |\Psi_{HF}\rangle, \tag{3.12}$$

where the $\hat{\tau}_\mu$ are excitation operators with corresponding amplitudes t_μ, $|\Psi_{HF}\rangle$ denotes the Hartree-Fock state, and the product is over all excitations, including the identity operator. Noting that the excitation operators $\hat{\tau}_\mu$ are nilpotent,

$$\hat{\tau}_\mu^2 = 0, \tag{3.13}$$

we may write

$$1 + t_\mu \hat{\tau}_\mu = \exp(t_\mu \hat{\tau}_\mu). \tag{3.14}$$

Thus, the coupled-cluster wavefunction may be written

$$|\Psi_{CC}\rangle = \left[\prod_\mu \exp(t_\mu \hat{\tau}_\mu)\right] |\Psi_{HF}\rangle = \exp(\hat{T})|\Psi_{HF}\rangle. \tag{3.15}$$

Here, the cluster operator $\hat{T}$ is given by

$$\hat{T} = \sum_\mu t_\mu \hat{\tau}_\mu = \hat{T}_1 + \hat{T}_2 + \cdots, \tag{3.16}$$

with, for example,

$$\hat{T}_1 = \sum_{A,I} t_I^A a_A^\dagger a_I \tag{3.17}$$

and

$$\hat{T}_2 = \sum_{\substack{A>B \\ I>J}} t_{IJ}^{AB} a_A^\dagger a_I a_B^\dagger a_J, \tag{3.18}$$

where A, B, ... and I, J, ... index, respectively, spin orbitals that are unoccupied and occupied in the Hartree-Fock reference state, and $a_A^\dagger$ and a_I denote the elementary creation and annihilation operators, respectively.

As it stands, the coupled-cluster wavefuction $|\Psi_{CC}\rangle$ as written in Equation 3.15 corresponds to the full direct product expansion of the electronic wavefunction 3.4 for a given spin orbital basis. To introduce a tractable approximation to the wavefunction 3.4, a truncation of the cluster operator $\hat{T}$ must be introduced. Equation 3.16 suggests a convenient way to do so: writing the cluster operator as

$$\hat{T} = \sum_{i=1}^{N} \hat{T}_i \tag{3.19}$$

a hierachy of approximations may be defined by truncating the summation in Equation 3.19 to run over only $i = 1, \ldots, n$, $n \leq N$. By way of example, in the coupled-cluster singles-and-doubles (CCSD) model, the cluster operator is truncated at the level of single and double excitations, and the CCSD wavefunction may be written

$$|\Psi_{CCSD}\rangle = \exp(\hat{T}_1 + \hat{T}_2)|\Psi_{HF}\rangle. \tag{3.20}$$

Extension to Excited States: The Equation-of-Motion Coupled-Cluster Model

The equation-of-motion coupled-cluster (EOM-CC) model corresponds to a method for the calculation of excited states within the coupled-cluster framework. Specifically, the EOM-CC *ansatz* for the ith electronic state, $|\Psi_i^{EOM}\rangle$, corresponds to a linear, configuration-interaction-type parameterisation of the state based upon a coupled-cluster reference state:

$$|\Psi_i^{EOM}\rangle = \sum_\mu c_{\mu,i}\hat{\tau}_\mu|\Psi_{CC}\rangle = \exp(\hat{T})\sum_\mu c_{\mu,i}\hat{\tau}_\mu|\Psi_{HF}\rangle, \tag{3.21}$$

with the summation being over all excitation operators, including the identity operator. The second equality in Equation 3.21 holds as the excitation operators $\hat{\tau}_\mu$ commute amongst each other, and emphasises that the EOM-CC states may be regarded as being generated from a linearly-parameterised configuration interaction state by the application of the exponential operator $\exp(\hat{T})$ containing the ground state amplitudes t_μ. Thus, for a given excited state i, the coefficients $c_{\mu,i}$ can be seen, roughly, to describe the static correlation specific to the ith state and the exponential operator the dynamic correlation common to all states.

Truncating both the cluster operator $\hat{T}$ and the linear excitations $\hat{\tau}_\mu$ appearing in Equation 3.21 to the level of single and double excitations furnishes the commonly used equation-of-motion coupled-cluster singles and doubles (EOM-CCSD) model:

$$|\Psi_i^{EOM-CCSD}\rangle = \exp(\hat{T}_1+\hat{T}_2)\left(\sum_{A,I} c_{I,i}^A a_A^\dagger a_I + \sum_{\substack{A>B\\I>J}} c_{IJ,i}^{AB} a_A^\dagger a_I a_B^\dagger a_J\right)|\Psi_{HF}\rangle \tag{3.22}$$

It remains to note that the CC and EOM-CC models are based on cor-

rections to a single-determinant reference wavefunction, and as such may fail to represent accurately the electronic wavefunction in regions of nuclear configuration space for which the true wavefunction becomes dominated by multiple configurations, such as, for example, dissociation limits. In such situations a method based upon a multi-configurational reference wavefunction is required to be adopted, the most commonly used variant being the so-called multiconfigurational self-consistent field model.

3.2.3 The Multiconfigurational Self-Consistent Field Model

The *ansatz* for the Multiconfigurational Self-Consistent Field (MCSCF) wavefunction corresponds to an orbital-optimised configuration interaction-type expansion:

$$|\Psi_{MCSCF}\rangle = \exp(-\hat{\kappa}) \sum_i C_i |i\rangle, \tag{3.23}$$

with the $|i\rangle$ being the configurations admitted into the MCSCF wavefunction. Here, $\exp(-\hat{\kappa})$ corresponds to the orbital rotation operator [14]:

$$\hat{\kappa} = \sum_{p>q} \kappa_{pq} \left(a_p^\dagger a_q - a_q^\dagger a_p \right). \tag{3.24}$$

The expansion coefficients C_i and orbital rotation parameters κ_{pq} are determined variationally through the minimisation of the expectation value of the Hamiltonian:

$$E = \min_{\boldsymbol{\kappa}, \boldsymbol{C}} \frac{\left\langle \Psi_{MCSCF} \middle| \hat{H} \middle| \Psi_{MCSCF} \right\rangle}{\langle \Psi_{MCSCF} | \Psi_{MCSCF} \rangle}. \tag{3.25}$$

A method for the selection of the configurations $|i\rangle$ entering into the MCSCF wavefunction must be adopted. One particular configuration selection scheme that has seen widespread and successful use is the so-called Complete Active Space Self-Consistent Field (CASSCF) method. In the

CASSCF method the orbital space is partitioned into three classes: the inactive orbitals, the active orbitals and the virtual orbitals. The inactive and virtual orbitals remain, respectively, doubly occupied and unoccupied in all configurations. The CASSCF configurations are generated by distributing the electrons amongst the active orbitals.

The MCSCF method represents a successful way in which to describe electronic wavefunctions dominated by more than one electronic configuration, and is thus of much use in the description of electronically excited states and of bond breaking. The non-linear optimisation of both the orbitals and configurations of the MCSCF wavefunction, however, represents a computationally demanding problem. Consequently, the number of configurations $|i\rangle$ that can be admitted into the MCSCF wavefunction is limited. Hence, whilst important static correlation effects may effectively be accounted for, the description of the dynamic electron correlation required for the calculation of quantitatively accurate energies may not be sufficient. To recover the dynamic correlation missing from a given MCSCF wavefunction, it may be used as the zero-order wavefunction in a subsequent perturbative calculation.

3.2.4 Multiconfigurational Perturbation Theory

The most widely used multiconfigurational perturbation theory method is the so-called Complete Active Space Perturbation Theory (CASPT) method. Here, a CASSCF wavefunction is used as the zero-order wavefunction in a Rayleigh-Schrödinger perturbation theory calculation. Thus the total Hamiltonian $\hat{H}$ is partitioned into two parts

$$\hat{H} = \hat{H}_0 + \hat{V}, \tag{3.26}$$

where $\hat{H}_0$ is a zero-order Hamiltonian with known eigenfunctions $|i^{(0)}\rangle$ and

eigenvalues $E_i^{(0)}$, and $\hat{V}$ is the perturbation. The CASSCF wavefunction is the eigenfunction $|0^{(0)}\rangle$ of the zero-order Hamiltonian with the corresponding eigenvalue $E^{(0)}$.

The eigenfunction $|0\rangle$ and eigenvalue E of the exact Hamiltonian are expanded in terms of the eigenfunctions of the zero-order Hamiltonian. To this end, the differences $|0\rangle - |0^{(0)}\rangle$ and $E - E^{(0)}$ are expanded in terms of the perturbation $\hat{V}$, and we write

$$|0\rangle = \sum_{k=0}^{\infty} |0^{(k)}\rangle \tag{3.27}$$

$$E = \sum_{k=0}^{\infty} E^{(k)}, \tag{3.28}$$

where $|0^{(k)}\rangle$ and $|E^{(k)}\rangle$ denote the kth-order corrections to the wavefunction and energy, respectively. Insertion of these expansions into the Schrödinger equation

$$\hat{H}|0\rangle = E|0\rangle \tag{3.29}$$

yields

$$\left(\hat{H}_0 + \hat{V}\right) \sum_{k=0}^{\infty} |0^{(k)}\rangle = \sum_{k=0}^{\infty} E^{(k)} \sum_{k=0}^{\infty} |0^{(k)}\rangle. \tag{3.30}$$

Collecting terms of the same order then gives an expression for the nth order correction $|0^{(n)}\rangle$ in terms of all lower-order corrections:

$$\left(\hat{H}_0 - E^{(0)}\right) |0^{(n)}\rangle = -\hat{V}|0^{(n-1)}\rangle + \sum_{k=1}^{n} E^{(k)}|0^{(n-k)}\rangle. \tag{3.31}$$

Through the imposition of intermediate normalisation,

$$\langle 0^{(0)}|0^{(n)}\rangle = 0; \quad n > 0, \tag{3.32}$$

the corrections to the zero-order energy are found to be given by

$$E^{(n)} = \langle 0^{(0)}|\hat{V}|0^{(n-1)}\rangle, \tag{3.33}$$

and the corrections to the zero-order wavefunction by

$$|0^{(n)}\rangle = -\left(\hat{H}_0 - E^{(0)}\right)^{-1}\left(\hat{V}|0^{(n-1)}\rangle + \sum_{k=1}^{n} E^{(k)}|0^{(n-k)}\rangle\right) \tag{3.34}$$

To obviate problems arising from the operation of $\left(\hat{H}_0 - E^{(0)}\right)^{-1}$ on the zero-order wavefunction (which would result in a singularity), and noting that neither the left- or right-hand sides of Equation 3.31 contains any component of $|0^{(0)}\rangle$, the projector $\hat{Q} = 1 - |0^{(0)}\rangle\langle 0^{(0)}|$ is introduced into Equation 3.34 as follows

$$\begin{aligned} |0^{(n)}\rangle &= -\hat{Q}\left(\hat{H}_0 - E^{(0)}\right)^{-1}\hat{Q}\left(\hat{V}|0^{(n-1)}\rangle + \sum_{k=1}^{n} E^{(k)}|0^{(n-k)}\rangle\right) \\ &= -\hat{Q}\left(\hat{H}_0 - E^{(0)}\right)^{-1}\hat{Q}\left(\hat{V}|0^{(n-1)}\rangle + \sum_{k=1}^{n-1} E^{(k)}|0^{(n-k)}\rangle\right), \end{aligned} \tag{3.35}$$

which defines the CASPT working equations for the wavefunction corrections.

In the commonly used CASPT2 model, the corrections to the zero-order CASSCF wavefunction $|0^{(0)}\rangle$ and energy $E^{(0)}$ are taken to second order, and the zero-order Hamiltonian is taken as

$$\hat{H}_0 = \langle 0^{(0)}|\hat{f}|0^{(0)}\rangle\hat{P} + \hat{Q}\hat{f}\hat{Q}, \tag{3.36}$$

where $\hat{f}$ is the CASSCF Fock operator [14], and $\hat{P}$ is the projector onto the CASSCF state, $\hat{P} = |0^{(0)}\rangle\langle 0^{(0)}|$. It remains to note that the CASPT2 method is commonly afflicted by poor convergence when their exists an eigenfunction $|i^{(0)}\rangle$, $i > 0$ of the zero-order Hamiltonian that is coupled and quasi-degenerate to the zero-order CASSCF wavefunction $|0^{(0)}\rangle$. Such states are

commonly termed 'intruder states', and their effect on the convergence of a CASPT2 calculation may be understood through a consideration of the second-order correction to the energy, $E^{(2)}$:

$$\begin{aligned} E^{(2)} &= \left\langle 0^{(0)} \middle| \hat{V} \middle| 0^{(1)} \right\rangle \\ &= -\left\langle 0^{(0)} \middle| \hat{V}\hat{Q}\left(\hat{H}_0 - E^{(0)}\right)^{-1} \hat{Q}\hat{V} \middle| 0^{(0)} \right\rangle \\ &= -\sum_i \left\langle 0^{(0)} \middle| \hat{V}\hat{Q}\left(\hat{H}_0 - E^{(0)}\right)^{-1} \middle| i^{(0)} \right\rangle \left\langle i^{(0)} \middle| \hat{Q}\hat{V} \middle| 0^{(0)} \right\rangle \\ &= -\sum_{i>0} \frac{\left| \left\langle 0^{(0)} \middle| \hat{V} \middle| i^{(0)} \right\rangle \right|^2}{E_i^{(0)} - E^{(0)}}, \end{aligned} \tag{3.37}$$

where in the third step the resolution of the identity has been inserted. From Equation 3.37 it can be seen that the existence of an intruder state $|i^{(0)}\rangle$ will result in the second-order correction to the energy to become singular in the limiting case of $E_i^{(0)} = E^{(0)}$. In order to obviate the problems arising from the presence of such a state, the technique of level-shifting may be used [15]. Here, the separation of the eigenvalues of $E_i^{(0)}$ and $E^{(0)}$ of the zero-order Hamiltonian is increased through the addition of a parameter ϵ to the zero-order Hamiltonian:

$$\hat{H}_0 \rightarrow \hat{H}_0 + \epsilon, \tag{3.38}$$

resulting in a modified second-order energy correction $\tilde{E}^{(2)}$:

$$\tilde{E}^{(2)} = -\sum_{i>0} \frac{\left| \left\langle 0^{(0)} \middle| \hat{V} \middle| i^{(0)} \right\rangle \right|^2}{E_i^{(0)} + \epsilon - E^{(0)}}. \tag{3.39}$$

Through the use of an approximate back-transformation [15], the second-order energy unshifted zero-order Hamiltonian may then be obtained.

3.3 Representation of the Nuclear Wavefunction

3.3.1 The Standard Method

Taking the nuclear degrees of freedom to be distinguishable, we may write the nuclear wavefunction for f degrees of freedom q_κ, $\boldsymbol{\Psi}(\boldsymbol{q},t)$, as a direct product expansion in terms of a time-independent basis:

$$\begin{aligned}\Psi(\boldsymbol{q},t) &= \sum_{j_1=1}^{N_1}\cdots\sum_{j_f=1}^{N_f} C_{j_1,\ldots,j_f}(t)\prod_{\kappa=1}^{f}\chi_{j_\kappa}^{(\kappa)}(q_\kappa) \\ &= \sum_{J} C_J(t)\Phi_J,\end{aligned} \tag{3.40}$$

where, due to the distinguishability of the nuclear degrees of freedom, a different set of basis functions $\{\chi_j^{(\kappa)}(q_\kappa)\}$ may be used for each degree of freedom, $J = j_1\cdots j_f$ denotes a composite index, and $\Phi_J = \chi_{j_1}^{(1)}\cdots\chi_{j_f}^{(p)}$. Typically, the basis functions chosen correspond to a discrete variable representation (see Section 3.5.2).

Equations of motion for the time-dependent expansion coefficients C_J may be derived by the insertion of the wavefunction *ansatz* 3.40 into the Dirac-Frenkel variational principle

$$\left\langle \delta\Psi \middle| \hat{H} - i\partial_t \middle| \Psi \right\rangle = 0. \tag{3.41}$$

Doing so results in the set of equations

$$i\dot{C}_J = \sum_L \left\langle \Phi_J \middle| \hat{H} \middle| \Phi_L \right\rangle C_L. \tag{3.42}$$

The representation of the nuclear wavefunction 3.40 and the resulting equations of motion 3.42 are collectively known commonly as the 'standard method'. Whilst the equations of motion furnished by the standard method are readily solved, the applicability of the method is severely limited by the

exponential scaling of the number of configurations Φ_J the with the number of nuclear degrees of freedom. At most, systems comprised of no more than 4 to 6 degrees of freedom may be described in a tractable manner by the standard method, thus excluding from study the vast majority of systems of interest.

3.3.2 The Multiconfigurational Time-Dependent Hartree Method

The basis of the multiconfigurational time-dependent Hartree (MCTDH) method is the use of a wavefunction *ansatz* corresponding to a direct product expansion in terms of a *time-dependent* basis:

$$\Psi(\boldsymbol{Q},t) = \sum_{j_1=1}^{n_1} \cdots \sum_{j_p=1}^{n_p} A_{j_1,\ldots,j_p}(t) \prod_{\kappa=1}^{p} \varphi_{j_\kappa}^{(\kappa)}(Q_\kappa,t). \tag{3.43}$$

Here the p logical coordinates Q_κ correspond each to a composite of d_κ physical coordinates q_ν:

$$Q_\kappa = (q_{\kappa_1},\ldots,q_{\kappa_{d_\kappa}}). \tag{3.44}$$

The time-dependent basis function $\varphi_j^{(\kappa)}$, termed single-particle functions (SPFs), are in turn expanded in terms of sets of time-independent primitive basis functions $\{\chi_k^{(\kappa)}\}$, typically chosen as a DVR:

$$\varphi_j(Q_\kappa,t) = \sum_{k_1=1}^{N_1} \cdots \sum_{k_{d_\kappa}=1}^{N_{d_\kappa}} a_{k_1,\ldots,k_{d_\kappa}}^{(\kappa)}(t) \prod_{\nu=1}^{d_\kappa} \chi_{k_\nu}^{(\nu)}(q_\nu). \tag{3.45}$$

Whilst the exponential scaling of the standard method is retained by the MCTDH approach, the latter is advantageous over the former for the description of larger systems for two primary reasons: (i) the expansion orders n_κ of the MCTDH wavefunction are generally much smaller than those of the

standard method, owing to the use of optimal, time-dependent basis functions, and; (ii) the use of combined modes Q_κ allows for a further reduction of number of coefficients A_J entering into the wavefunction expansion.

Considering the transformed SPFs and coefficients

$$\tilde{\varphi}_{j_\kappa}^{(\kappa)} = \sum_{l_\kappa=1}^{n_\kappa} U_{j_\kappa l_\kappa} \varphi_{l_\kappa}^{(\kappa)} \tag{3.46}$$

and

$$\tilde{A}_{j_1,\ldots,j_p} = \sum_{l_1=1}^{n_1} \cdots \sum_{l_p=1}^{n_p} U_{j_1 l_1}^{-1} \cdots U_{j_p l_p}^{-1} A_{l_1,\ldots,l_p}, \tag{3.47}$$

where $\boldsymbol{U}$ is any non-singular matrix, it is apparent that

$$\Psi(\boldsymbol{Q},t) = \sum_J A_J \Phi_J = \sum_J \tilde{A}_J \tilde{\Phi}_J, \tag{3.48}$$

with $\tilde{\Phi}_J = \tilde{\varphi}_{j_1}^{(1)} \cdots \tilde{\varphi}_{j_f}^{(p)}$. Thus, we see that the MCTDH wavefunction *ansatz* is not unique. To remove the redundancies in the MCTDH wavefunction and guarantee unique equations of motion, the constraints

$$i\langle \varphi_i^{(\kappa)} | \dot{\varphi}_j^{(\kappa)} \rangle = \langle \varphi_i^{(\kappa)} | \hat{g}^{(\kappa)} | \varphi_j^{(\kappa)} \rangle = g_{ij}^{(\kappa)} \tag{3.49}$$

are introduced, where $\hat{g}^{(\kappa)}$ is an operator acting on the κth particle Q_κ. By considering the time-derivative of the SPF overlaps

$$\begin{aligned} \partial_t \langle \varphi_i^{(\kappa)} | \varphi_j^{(\kappa)} \rangle &= \langle \dot{\varphi}_i^{(\kappa)} | \varphi_j^{(\kappa)} \rangle + \langle \varphi_i^{(\kappa)} | \dot{\varphi}_j^{(\kappa)} \rangle \\ &= i \left(g_{ij}^{(\kappa)\dagger} - g_{ij}^{(\kappa)} \right), \end{aligned} \tag{3.50}$$

it can be seen that a set of initially orthonormal SPFs will remain orthonormal for all time if the constraint operators $\hat{g}^{(\kappa)}$ are chosen to be Hermitian.

Assuming $\hat{g}^{(\kappa)} = 0$, insertion of the MCTDH wavefunction *ansatz* into the Dirac-Frenkel variational principle yields the following set of equations of motion for the coefficients and SPFs:

$$i\dot{\boldsymbol{A}} = \boldsymbol{\mathcal{K}}\boldsymbol{A} \tag{3.51}$$

$$i\dot{\boldsymbol{\varphi}}^{(\kappa)} = \left[\left(1 - P^{(\kappa)}\right)\left(\boldsymbol{\rho}^{(\kappa)}\right)^{-1}\boldsymbol{\mathcal{H}}^{(\kappa)}\right]\boldsymbol{\varphi}^{(\kappa)}. \tag{3.52}$$

Here, $\boldsymbol{\mathcal{K}}$ denotes the matrix representation of the Hamiltonian in the basis of the Hartree products Φ_J,

$$\mathcal{K}_{JL} = \left\langle \Phi_J \middle| \hat{H} \middle| \Phi_J \right\rangle. \tag{3.53}$$

$P^{(\kappa)}$ is the projector onto the space spanned by the SPFs for the κth degree of freedom,

$$P^{(\kappa)} = \sum_j |\varphi_j^{(\kappa)}\rangle\langle\varphi_j^{(\kappa)}|, \tag{3.54}$$

and the appearance of the operator $\left(1 - P^{(\kappa)}\right)$ in Equation 3.52 ensures that the time derivative of the SPFs is orthogonal to the space spanned spanned by the SPFs. It is also apparent that this operator results in time-independent SPFs in the limit of a complete basis, thus recovering the standard method as a limiting case. The mean-field $\boldsymbol{\mathcal{H}}^{(\kappa)}$ corresponds to on operator on the κth degree of freedom, and is defined as

$$\mathcal{H}_{jl}^{(\kappa)} = \left\langle \Psi_j^{(\kappa)} \middle| \hat{H} \middle| \Psi_l^{(\kappa)} \right\rangle, \tag{3.55}$$

with the single-hole functions $\Psi_j^{(\kappa)}$ being given by

$$\Psi_j^{(\kappa)} = \left\langle \varphi_j^{(\kappa)} \middle| \Psi \right\rangle. \tag{3.56}$$

Finally, the density matrix $\boldsymbol{\rho}^{(\kappa)}$ is given by

$$\rho_{jl}^{(\kappa)} = \left\langle \Psi_j^{(\kappa)} \middle| \Psi_l^{(\kappa)} \right\rangle. \tag{3.57}$$

3.4 Calculation of Initial Wavepackets

The integration of the time-dependent Schrödinger equation is an initial value problem, and as such we are required to first determine an initial wavepacket, $|\Psi(0)\rangle$. For the study of the photoexcitation of a system, $|\Psi(0)\rangle$ can be taken as

$$|\Psi(0)\rangle = \mu|\Psi_{GS}\rangle, \tag{3.58}$$

where μ denotes the corresponding transition operator, and $|\Psi_{GS}\rangle$ a vibrational eigenfunction of the ground electronic state. We here make the distinction between situation for which $|\Psi_{GS}\rangle$ corresponds to the ground vibrational state and those for which it corresponds to a vibrationally excited state.

3.4.1 Calculation of the Vibrational Ground State

The generation of the vibrational ground state may be simply achieved using the method of relaxation [16]. Here, an initial wavepacket is propagated in negative imaginary time and subsequently renormalised:

$$|\Psi(\tau)\rangle = \frac{\exp(-H\tau)|\Psi(0)\rangle}{||\exp(-H\tau)|\Psi(0)\rangle||}, \tag{3.59}$$

where $\tau = -it$. Expanding the initial wavefunction in the eigenfunctions ψ_n of the Hamiltonian,

$$|\Psi(\tau)\rangle = \sum_n c_n \exp(-E_n\tau)\psi_n(0), \tag{3.60}$$

we see that each eigenfunction ψ_n is annihilated at a rate that is proportional to it's eigenvalue E_n. Thus, as $t \to \infty$, $|\Psi(\tau)\rangle$ will converge to the ground state.

3.4.2 Calculation of Vibrationally Excited States

In order to obtain vibrationally excited states within the MCTDH framework, the method of improved relaxation may be used [17]. Here, a time-independent variational principle is employed to determine the optimal coefficients and SPFs for a given vibrational state,

$$\delta\Bigg\{ \langle\Psi|H|\Psi\rangle - E\left(\sum_J A_J^* A_J - 1\right) - \sum_{\kappa=1}^{p}\sum_{j,l=1}^{n_\kappa} \epsilon_{jl}^{(\kappa)} \left(\left\langle \varphi_j^{(\kappa)} \middle| \varphi_l^{(\kappa)} \right\rangle - \delta_{jl}\right) \Bigg\} = 0. \tag{3.61}$$

The Lagrange multipliers E and $\epsilon_{jl}^{(\kappa)}$ are introduced to keep, respectively, the A-vector (with elements A_J) normalised and the SPFs orthonormal. Variation with respect to the coefficients gives

$$\sum_L \langle\Phi_L|H|\Phi_J\rangle A_J = E A_J, \tag{3.62}$$

whilst variation with respect to the SPFs is found to yield

$$\left(1 - P^{(\kappa)}\right) \sum_{l=1}^{n_\kappa} \mathcal{H}_{jl}^{(\kappa)} \varphi_l^{(\kappa)} = 0. \tag{3.63}$$

The variationally optimal solution is furnished when the Equations 3.62 and 3.63 are simultaneously satisfied.

Through the use of the constant mean-field integration scheme [18], a decoupling of the propagation of the A-vector and that of the SPFs is afforded. From Equation 3.62, we see that the A-vector can be obtained as an eigenvector of the matrix representation of the Hamiltonian in the basis of the configurations Φ_J. The determination the optimum set of SPFs is achieved *via* noting that Equation 3.63 implies that

$$\sum_{j=1}^{n_\kappa} C_j \left(1 - P^{(\kappa)}\right) \sum_{l=1}^{n_\kappa} \mathcal{H}_{jl}^{(\kappa)} \varphi_l^{(\kappa)} = 0, \tag{3.64}$$

for any set of coefficients C_j. Choosing the coefficients C_j to be the negatives of the elements $\left(\boldsymbol{\rho}^{(\kappa)}\right)^{-1}_{k,j}$ of the inverse density matrix, it is found that

$$0 = -\left(1 - P^{(\kappa)}\right) \sum_{j,l=1}^{n_\kappa} \left(\boldsymbol{\rho}^{(\kappa)}\right)^{-1}_{kj} \mathcal{H}^{(\kappa)}_{jl} \varphi^{(\kappa)}_l = \frac{\partial \varphi^{(\kappa)}_k}{\partial \tau}. \tag{3.65}$$

Thus, the variationally optimal set of SPFs may be obtained by relaxing an initial set of SPFs until their derivatives with respect to $\tau = -it$ are sufficiently small.

The improved relaxation algorithm derives from Equations 3.62 and 3.65, and is as follows. The Hamiltonian matrix is first diagonalised in the basis of configurations Φ_J corresponding to an initially chosen state. The thus obtained A-vector is then used to relax the SPFs, which are then used to reconstruct the Hamiltonian matrix. By iterating this process until convergence a variationally optimal wavepacket may be obtained. By choosing the eigenvector of the Hamiltonian matrix with the lowest eigenvalue at each time step, the ground vibrational state is obtained. By choosing at each time step the eigenvector that gives the largest overlap with an appropriately chosen initially defined state, a vibrationally excited state may be obtained. By way of example, for a set of harmonic oscillators defined with respect to the modes $\boldsymbol{Q}$, a vibrational state corresponding to excitation of the mode Q_α may be achieved by choosing the initial wavefunction as

$$|\Psi(\tau = 0)\rangle = \left(b^\dagger_\alpha\right)^n |\Psi_0\rangle, \tag{3.66}$$

where $|\Psi_0\rangle$ corresponds to the ground vibrational state (prepared, for example, by relaxation), $b^\dagger_\alpha$ to the harmonic oscillator creation operator for the αth mode, and n is a positive integer.

3.5 Evaluation of the Hamiltonian Matrix

For the sake of simplicity, we consider in the following a one-dimensional problem defined by the coordinate x and the Hamiltonian $\hat{H} = T(\hat{p}) + V(\hat{x})$, where $\hat{p}$ and $\hat{x}$ denote, respectively, the momentum and position operators. We are tasked with the evaluation of the matrix representation of the Hamiltonian in a chosen basis $\{\phi_n\}$. In general, analytic solutions to the elements of the kinetic energy matrix,

$$T_{mn} = \langle \phi_m | T(\hat{p}) | \phi_n \rangle, \tag{3.67}$$

are known. The evaluation of the elements of the potential matrix,

$$V_{mn} = \langle \phi_m | V(\hat{x}) | \phi_n \rangle, \tag{3.68}$$

is, however, non-trivial.

Acknowledging the necessity of working with a finite subset of N basis functions ϕ_n, we introduce the projector $\hat{P}_N$ onto the desired N-dimensional subspace:

$$\hat{P}_N = \sum_{n=1}^{N} |\phi_n\rangle\langle\phi_n|. \tag{3.69}$$

Then, the potential operator in the so-called variational basis representation (VBR) may be written

$$\hat{V}^{VBR} = \hat{P}_N V(\hat{x}) \hat{P}_N, \tag{3.70}$$

the use of which in the evaluation of the potential matrix will yield a variational upper bound to the energy.

3.5.1 The Finite Basis Representation

In the finite basis representation (FBR) the following approximation is made:

$$\hat{P}_N V(\hat{x}) \hat{P}_N = V(\hat{P}_N \hat{x} \hat{P}_N) = \hat{V}^{FBR}. \tag{3.71}$$

We note the VBR and FBR would be equivalent if the basis set $\{\phi_n\}$ used were complete, for then the following would hold:

$$\hat{P}_N \rightarrow \hat{P} = \sum_{n=1}^{\infty} |\phi_n\rangle\langle\phi_n| = 1, \tag{3.72}$$

$$\hat{P}\hat{x}^j\hat{P} = \prod_{i=1}^{j} \left[\hat{P}\hat{x}\hat{P}\right]. \tag{3.73}$$

Introducing the eigenfunctions θ_α and corresponding eigenvalues x_α of the position operator,

$$\hat{x}\theta_\alpha = x_\alpha \theta_\alpha, \tag{3.74}$$

and the transformation between the original basis $\{\phi_n\}$ and the set of eigenfunctions of $\hat{x}$, $\{\theta_\alpha\}$,

$$\boldsymbol{x} = \boldsymbol{U}^\dagger \boldsymbol{X} \boldsymbol{U}, \tag{3.75}$$

$$x_{\alpha\beta} = x_\alpha \delta_{\alpha\beta}, \tag{3.76}$$

$$X_{mn} = \langle\phi_m|\hat{x}|\phi_n\rangle, \tag{3.77}$$

the advantage of working with the FBR may be understood as follows. In the FBR the elements of the potential matrix may be written

$$\begin{aligned} V_{mn}^{FBR} &= \langle\phi_m|V(\hat{P}_N\hat{x}\hat{P}_N)|\phi_n\rangle \\ &= \sum_{k,l=1}^{N}\langle\phi_m|V(|\phi_k\rangle\langle\phi_k|\hat{x}|\phi_l\rangle\langle\phi_l|)|\phi_n\rangle \\ &= \sum_{k,l=1}^{N}\langle\phi_m|\phi_k\rangle V(\langle\phi_k|\hat{x}|\phi_l\rangle)\langle\phi_l|\phi_m\rangle \\ &= V(\langle\phi_m|\hat{x}|\phi_n\rangle) \\ &= \sum_{\alpha=1}^{N} U_{m\alpha}V(\langle\theta_\alpha|x|\theta_\beta\rangle)U_{\alpha n}^{\dagger} \\ &= \sum_{\alpha=1}^{N} U_{m\alpha}V(x_\alpha)U_{\alpha n}^{\dagger}. \end{aligned} \tag{3.78}$$

Hence, from a knowledge of the value of the potential at the points x_α, corresponding to the eigenvalues of $\hat{x}$, and the eigenfunctions of $\hat{x}$, the potential in the FBR may be easily evaluated.

3.5.2 The Discrete Variable Representation

The discrete variable representation (DVR) corresponds to the representation of the Hamiltonian in the basis of the eigenfunctions of the position operator, $\{\theta_\alpha\}$, with the additional approximation made that $\hat{V} = \hat{V}^{FBR}$. Hence, we write

$$\begin{aligned} H_{\alpha\beta}^{DVR} &= \langle\theta_\alpha|T(\hat{p})|\theta_\beta\rangle + \langle\theta_\alpha|V(\hat{P}_N\hat{x}\hat{P}_N)|\theta_\beta\rangle \\ &= T_{\alpha\beta}^{DVR} + V_{\alpha\beta}^{DVR}. \end{aligned} \tag{3.79}$$

The potential matrix in the DVR is determined by a simple prescription:

$$V_{\alpha\beta}^{DVR} = V(x_\alpha)\delta_{\alpha\beta}. \tag{3.80}$$

The kinetic energy matrix in the DVR is most straightforwardly determined *via* the transformation from the VBR to the DVR:

$$T_{\alpha\beta}^{DVR} = \sum_{m,n=1}^{N} U_{\alpha m}^{\dagger}\langle\phi_m|T(\hat{p})|\phi_n\rangle U_{n\beta}. \tag{3.81}$$

3.6 Product Representation of the Hamiltonian

In order to integrate the MCTDH equations of motion, the Hamiltonian matrix elements $\mathcal{K}_{IJ}$ must be evaluated. Assuming the use of a DVR, we may write

$$\begin{aligned}\mathcal{K}_{IJ} &= \langle \varphi_{i_1}^{(1)} \cdots \varphi_{i_p}^{(p)} | \hat{H} | \varphi_{j_1}^{(1)} \cdots \varphi_{j_p}^{(p)} \rangle \\ &= \sum_{k_1 \ldots k_f} \Bigg[\sum_{l_1 \ldots l_f} a^{(1)*}_{k_1 \ldots k_{d_1}, i_1} \cdots a^{(p)*}_{k_f - d_p + 1 \ldots k_f, i_p} a^{(1)*}_{l_1 \ldots l_{d_1}, j_1} \cdots a^{(p)*}_{l_f - d_p + 1 \ldots l_f, j_p} \\ &\times \langle \chi_{k_1}^{(1)} \cdots \chi_{k_f}^{(f)} | \hat{T} | \chi_{l_1}^{(1)} \cdots \chi_{l_f}^{(f)} \rangle \\ &+ a^{(1)*}_{k_1 \ldots k_{d_1}, i_1} \cdots a^{(p)*}_{k_f - d_p + 1 \ldots k_f, i_p} a^{(1)}_{k_1 \ldots k_{d_1}, j_1} \cdots a^{(p)}_{k_f - d_p + 1 \ldots k_f, j_p} V(q_{k_1}^{(1)}, \ldots, q_{k_f}^{(f)}) \Bigg].\end{aligned} \tag{3.82}$$

Thus, assuming the same number, N, of primitive functions for each degree of freedom, a prohibitive number of multidimensional integral evaluations would have to be made: N^f potential evaluations and $N^f \times N^f$ kinetic energy matrix element evaluations. However, if the Hamiltonian is expressible as a sum of products of monomodal terms,

$$\hat{H}(\boldsymbol{q}) = \sum_{r=1}^{n_s} c_r \prod_{\kappa=1}^{p} \hat{h}_r^{(\kappa)}(Q_\kappa), \tag{3.83}$$

significant gains may be made, for then every multidimensional integral $\mathcal{K}_{IJ}$ may be written

$$\begin{aligned}\mathcal{K}_{IJ} &= \langle \varphi_{i_1}^{(1)} \cdots \varphi_{i_p}^{(p)} | \hat{H} | \varphi_{j_1}^{(1)} \cdots \varphi_{j_p}^{(p)} \rangle \\ &= \sum_{r=1}^{n_s} c_r \prod_{\kappa=1}^{p} \langle \varphi_{i_\kappa}^{(\kappa)} | \hat{h}_r^{(\kappa)} | \varphi_{j_\kappa}^{(\kappa)} \rangle.\end{aligned} \tag{3.84}$$

Thus only $n_s \cdot p$ low-dimensional integrals need be evaluated.

The kinetic energy operator is usually expressible in the product form required for use with MCTDH. In contrast, the potential function is often

not of the required form. In order to recast a given potential function in the desired product form the so-called potfit algorithm may be employed.

3.7 The Potfit Algorithm

The basic idea underlying the potfit algorithm is to express a given potential function $V(\boldsymbol{Q})$ as a direct product expansion in terms of a set of one-particle basis functions. Thus, denoting by $Q^{(\kappa)}$ the κth combined mode, the approximate potential $V^{PF}(\boldsymbol{Q})$ may be written

$$V^{PF}(Q^{(1)},\ldots,Q^{(p)}) = \sum_{j_1=1}^{m_1}\cdots\sum_{j_p=1}^{m_p} C_{j_1,\ldots,j_p}\prod_{\kappa=1}^{p}\nu_{j_\kappa}^{(\kappa)}(Q^{(\kappa)}). \tag{3.85}$$

In order to afford as compact an expansion as possible, both the coefficients $C_{j_1,\ldots,j_p}$ and the so-called single-particle potentials (SPPs) $\nu_{j_\kappa}^{(\kappa)}(Q^{(\kappa)})$ are optimised. Assuming the use of a DVR, the potential need only be known at the corresponding grid points, that is, we only need to determine the finite set of values

$$V^{PF}_{i_1,\ldots,i_p} = V^{PF}(Q^{(1)}_{i_1},\ldots,Q^{(p)}_{i_p}) = \sum_{j_1=1}^{m_1}\cdots\sum_{j_p=1}^{m_p} C_{j_1,\ldots,j_p}\prod_{\kappa=1}^{p}\nu_{i_p j_p}^{(p)}, \tag{3.86}$$

where $Q_i^{(\kappa)}$ denotes the coordinate of the ith grid point of the κth grid, and $\nu_{ij}^{(\kappa)} = \nu_j^{(\kappa)}(Q_i^{(\kappa)})$. The determination of the optimal set of coefficients and SPPs would be achieved through the minimisation of the functional

$$\Delta^2 = \sum_{i_1=1}^{N_1}\cdots\sum_{i_p=1}^{N_p}\left\{V^{PF}_{i_1,\ldots,i_p} - V_{i_1,\ldots,i_p}\right\}^2. \tag{3.87}$$

Taking the SPPs to be orthonormal on the grid,

$$\sum_{i=1}^{N_\kappa}\nu_{ij}^{(\kappa)}\nu_{il}^{(\kappa)} = \delta_{jl}, \tag{3.88}$$

it can be shown that for a given set of SPPs the optimal set of coefficients is given by

$$C_{j_1,\ldots,j_p} = \sum_{i_1=1}^{N_1} \cdots \sum_{i_p=1}^{N_p} \prod_{\kappa=1}^{p} \nu_{i_\kappa j_\kappa}^{(\kappa)} V_{i_1,\ldots,i_p}, \tag{3.89}$$

that is, by the overlap of the SPPs with the potential. Introducing the composite indices I and J to label, respectively, the grid points and configurations (that is, products of SPPs), and letting $\Omega_{I,J} = \prod_{\kappa=1}^{p} \nu_{i_\kappa j_\kappa}^{(\kappa)}$, the functional Δ^2 may be written

$$\begin{aligned} \Delta^2 &= \boldsymbol{V}^T\boldsymbol{V} - \boldsymbol{V}^T\boldsymbol{\Omega}\boldsymbol{\Omega}^T\boldsymbol{V} \\ &= \boldsymbol{V}^T\boldsymbol{V} - \boldsymbol{C}^T\boldsymbol{C}. \end{aligned} \tag{3.90}$$

As such, the optimal set of SPPs would be obtained by the maximisation of the norm of the coefficient vector $\boldsymbol{C}$ under the constraint that the SPPs remain orthonormal. Doing so can be shown to furnish the following set of equations:

$$\sum_k \left(\delta_{k'k} - \sum_l \nu_{k'l}^{(\kappa)} \nu_{kl}^{(\kappa)} \right) \sum_i \tilde{\varrho}_{ki}^{(\kappa)} \nu_{ij}^{(\kappa)} = 0, \tag{3.91}$$

where the so-called modified potential density matrices $\tilde{\varrho}_{ki}^{(\kappa)}$ are defined as

$$\tilde{\varrho}_{ki}^{(\kappa)} = \sum_{j_1=1}^{m_1} \cdots \sum_{j_{\kappa-1}}^{m_{\kappa-1}} \sum_{j_{\kappa+1}}^{m_{\kappa+1}} \cdots \sum_{j_p=1}^{m_p} C^{(\kappa)}_{j_1,\ldots,j_{\kappa-1},k,j_{\kappa+1},\ldots,j_p} C^{(\kappa)}_{j_1,\ldots,j_{\kappa-1},i,j_{\kappa+1},\ldots,j_p}, \tag{3.92}$$

with the partially transformed coefficients $C_{j_1,\ldots,j_{\kappa-1},k,j_{\kappa+1},\ldots,j_p}$ being given by

$$\begin{aligned} C_{j_1,\ldots,j_{\kappa-1},k,j_{\kappa+1},\ldots,j_p} = &\sum_{i_1=1}^{N_1} \cdots \sum_{i_{\kappa-1}=1}^{N_{\kappa-1}} \sum_{i_{\kappa+1}}^{N_{\kappa+1}} \cdots \sum_{i_p=1}^{N_p} \nu_{i_1 j_1}^{(1)} \cdots \nu_{i_{\kappa-1} j_{\kappa-1}}^{(\kappa-1)} \nu_{i_{\kappa+1} j_{\kappa+1}}^{(\kappa+1)} \cdots \nu_{i_p j_p}^{(p)} \\ &\times V_{i_1,\ldots,i_{\kappa-1},k,i_{\kappa+1},\ldots,i_p}. \end{aligned} \tag{3.93}$$

In order to avoid an iterative solution of Equation 3.93, the potfit algorithm proceeds by approximating the modified potential density matrices $\tilde{\boldsymbol{\varrho}}^{(\kappa)}$ by the so-called potential density matrices $\boldsymbol{\varrho}^{(\kappa)}$, defined as

$$\varrho^{(\kappa)}_{k,k'} = \sum_{i_1=1}^{N_1} \cdots \sum_{i_{\kappa-1}=1}^{N_{\kappa-1}} \sum_{i_{\kappa+1}=1}^{N_{\kappa+1}} \cdots \sum_{i_p=1}^{N_p} V_{i_1,\ldots,i_{\kappa-1},k,i_{\kappa+1},\ldots,i_p} V_{i_1,\ldots,i_{\kappa-1},k',i_{\kappa+1},\ldots,i_p}. \tag{3.94}$$

3.8 The Vibronic Coupling Hamiltonian

The vibronic coupling Hamiltonian [19,20] corresponds to a diabatisation by *ansatz* in which an assumed diabatic potential matrix $\boldsymbol{W}(\mathbf{Q})$ is expanded in terms of the ground state normal modes $\boldsymbol{Q}$ about a suitably chosen reference geometry $\boldsymbol{Q}_0$. Collecting terms of the same order, we may write

$$\boldsymbol{H}(\boldsymbol{Q}) = \boldsymbol{H}^{(0)}(\boldsymbol{Q}) + \boldsymbol{W}^{(1)}(\boldsymbol{Q}) + \boldsymbol{W}^{(2)}(\boldsymbol{Q}) + \cdots \tag{3.95}$$

where the zero-order Hamiltonian $\boldsymbol{H}^{(0)}(\boldsymbol{Q})$ corresponds to a set of ground state harmonic oscillators displaced to the vertical excitation energies E_i of the electronic states under consideration:

$$H^{(0)}_{ij}(\boldsymbol{Q}) = \left[E_i + \sum_{\alpha=1}^{3N-6} \frac{\omega_\alpha}{2} \left(Q_\alpha^2 - \frac{\partial^2}{\partial Q_\alpha^2} \right) \right] \delta_{ij}, \tag{3.96}$$

and assumes a diagonal form as the adiabatic and diabatic states are taken to be equivalent at the point of expansion. For a system comprised of N atoms, the first- and second-order potentials $\boldsymbol{W}^{(1)}(\boldsymbol{Q})$ and $\boldsymbol{W}^{(2)}(\boldsymbol{Q})$ may be written

$$W^{(1)}_{ii}(\boldsymbol{Q}) = \sum_{\alpha=1}^{3N-6} \kappa^{(i)}_\alpha Q_\alpha, \tag{3.97}$$

$$W_{ij}^{(1)}(\boldsymbol{Q}) = \sum_{\alpha=1}^{3N-6} \lambda_{\alpha}^{(i,j)} Q_{\alpha}, \quad i \neq j, \tag{3.98}$$

$$W_{ii}^{(2)}(\boldsymbol{Q}) = \frac{1}{2} \sum_{\alpha,\beta=1}^{3N-6} \gamma_{\alpha\beta} Q_{\alpha} Q_{\beta}, \tag{3.99}$$

$$W_{ij}^{(2)}(\boldsymbol{Q}) = \frac{1}{2} \sum_{\alpha,\beta=1}^{3N-6} \mu_{\alpha\beta}^{(i,j)} Q_{\alpha} Q_{\beta}, \quad i \neq j. \tag{3.100}$$

The change in equilibrium geometry and the so-called Duschinsky rotation of the normal modes upon electronic excitation to the state indexed by i are described, respectively, by the parameters $\kappa_{\alpha}^{(i)}$ and $\gamma_{\alpha\beta}^{(i)}$:

$$\begin{aligned} \kappa_{\alpha}^{(i)} &= \frac{\partial}{\partial Q_{\alpha}} \left\langle \Phi_i \middle| \hat{H}_{el} \middle| \Phi_i \right\rangle \Big|_{\boldsymbol{Q}_0} \\ &= \left\langle \Phi_i \middle| \frac{\partial \hat{H}_{el}}{\partial Q_{\alpha}} \middle| \Phi_i \right\rangle \Big|_{\boldsymbol{Q}_0}, \end{aligned} \tag{3.101}$$

$$\gamma_{\alpha\beta}^{(i)} = \frac{\partial^2}{\partial Q_{\alpha} \partial Q_{\beta}} \left\langle \Phi_i \middle| \hat{H}_{el} \middle| \Phi_i \right\rangle \Big|_{\boldsymbol{Q}_0} \tag{3.102}$$

The parameter $\lambda_{\alpha}^{(i,j)}$ describes to first-order the diabatic coupling between the states indexed by i and j, and can be seen to be related to the NACTs $\boldsymbol{\tau}$ by

$$\begin{aligned} \lambda_{\alpha}^{(i,j)} &= \frac{\partial}{\partial Q_{\alpha}} \left\langle \Phi_i \middle| \hat{H}_{el} \middle| \Phi_j \right\rangle \Big|_{\boldsymbol{Q}_0} \\ &= \left\langle \Phi_i \middle| \frac{\partial \hat{H}_{el}}{\partial Q_{\alpha}} \middle| \Phi_j \right\rangle \Big|_{\boldsymbol{Q}_0} \\ &= \left[E_j(\boldsymbol{Q}_0) - E_i(\boldsymbol{Q}_0) \right] \tau_{\alpha ij}(\boldsymbol{Q}_0). \end{aligned} \tag{3.103}$$

Through the use of simple group theoretical arguments it may be determined whether a given parameter of the vibronic coupling Hamiltonian is necessarily zero by symmetry. Specifically, for a parameter to be non-zero it is required that the corresponding integrand belong to a function space that generates the totally symmetric irreducible representation of the point group

of the molecule at its reference geometry $\boldsymbol{Q}_0$. Thus, letting Γ^α denote the representation generated by the coordinate Q_α, Γ^i the representation generated by the diabatic state $|\Phi_i\rangle$, and Γ^1 the totally symmetric irreducible representation, we see, for example, that

$$\kappa_\alpha^{(i)} \neq 0, \quad \Gamma^\alpha \ni \Gamma^1, \tag{3.104}$$

and

$$\lambda_\alpha^{(i,j)} \neq 0, \quad \Gamma^i \otimes \Gamma^j \otimes \Gamma^\alpha \ni \Gamma^1. \tag{3.105}$$

More universally, for a general parameter

$$\eta_{n_1,\ldots,n_{3N-6}}^{(i,j)} = \frac{\partial^m}{\partial Q_1^{n_1} \cdots Q_{3N-6}^{n_{3N-6}}} \left\langle \Phi_i \middle| \hat{H}_{el} \middle| \Phi_j \right\rangle; \quad m = \sum_{\alpha=1}^{3N-6} n_\alpha \tag{3.106}$$

to be non-zero, it can be shown that the necessary, but not sufficient, condition is [21]

$$g^{-1} \sum_a g_a \chi^{red}(C_a) > 0. \tag{3.107}$$

Here, g denotes the order of the point group, g_a is the number of operations of the ath class of the point group, and $\chi^{red}(C_a)$ corresponds to the character of the reducible representation Γ^{red} of the operators of the ath class formed from the direct product

$$\Gamma^{red} = \left[\bigotimes_{\alpha=1}^{3N-6} (\Gamma^\alpha)^{n_\alpha} \right] \otimes \Gamma^i \otimes \Gamma^j \tag{3.108}$$

That is, explicitly,

$$\eta_{n_1,\ldots,n_{3N-6}}^{(i,j)} \neq 0, \quad g^{-1} \sum_a \left\{ g_a \left(\prod_{\alpha=1}^{3N-6} [\chi^\alpha(C_a)]^{n_\alpha} \right) \chi^i(C_a) \chi^j(C_a) \right\} > 0 \tag{3.109}$$

3.9 Complex Absorbing Potentials

Considering a system for which there exists an accessible region for which the potential function is unbound with respect to a degree of freedom r, it may be expected that a prohibitively long grid length for the degree of freedom under question may have to be employed in order to avoid unwanted reflections of the wavepacket from the grid edges. The use of a compact grid may, however, be accommodated if a so-called complex absorbing potential (CAP) is used. The use of a CAP corresponds to the augmentation of the system Hamiltonian H with a negative imaginary potential function:

$$H \to \tilde{H} = H - iW(r). \tag{3.110}$$

Commonly, the potential function $W(r)$ is chosen to assume the following monomial form:

$$W(r) = \eta(r - r_c)^n \Theta(r - r_c), \tag{3.111}$$

where r_c denotes a value of the coordinate r outside of the interaction region, η is a strength parameter, n an integer, typically 2 or 3, and $\Theta(r - r_c)$ denotes the Heaviside step function centred at r_c, defined as

$$\Theta(r - r_c) = \begin{cases} 1, & \text{if } r \geq r_c \\ 0, & \text{otherwise} \end{cases} \tag{3.112}$$

By considering the time-derivative of the square of the norm of the wavepacket, it is found that

$$\begin{aligned} \frac{\partial}{\partial t}||\Psi|| &= \frac{1}{2}\left\{\left\langle \dot{\Psi}\middle|\Psi\right\rangle + \left\langle \Psi\middle|\dot{\Psi}\right\rangle\right\}||\Psi||^{-1} \\ &= \frac{1}{2}\left\{\left\langle \Psi\middle|i\tilde{H}^{\dagger} - i\tilde{H}\middle|\Psi\right\rangle\right\}||\Psi||^{-1} \\ &= -\left\langle \Psi|W(r)|\Psi\right\rangle||\Psi||^{-1}. \end{aligned} \tag{3.113}$$

Hence, the parts of the wavepacket entering into the CAP are annihilated.

3.10 Flux, Reaction Probabilities and Diabatic State Populations

We define dissociation of a given bond to have occurred if the corresponding bond length r exceeds a critical value r_c. The probability of dissociation, $p_{diss}(t)$, may then be defined as the expectation value of the projector onto the subspace for which $r > r_c$:

$$p_{diss}(t) = \langle \Psi(t) | \Theta(r - r_c) | \Psi(t) \rangle \tag{3.114}$$

where $\Theta(r - r_c)$ the Heaviside step function centred at r_c. Similarly, the state-resolved probabilities of dissociation are given by

$$p_{diss,i}(t) = \langle \Psi(t) | P_i \Theta(r - r_c) P_i | \Psi(t) \rangle, \tag{3.115}$$

where P_i denotes the projector onto the ith electronic state. The Equations 3.114 and 3.115 are valid as long as the norm of the wavepacket is conserved. However, as is common practice, a CAP may be used to annihilate the dissociating part of a wavepacket. In this case, a different strategy must be employed to calculate the probabilities of dissociation.

The flux passing through a dividing surface placed at r_c may be written as

$$F(t') = \frac{\partial}{\partial t} \langle \Psi(t') | \Theta(r - r_c) | \Psi(t') \rangle, \tag{3.116}$$

with state-resolved components $F_i(t')$ being given by

$$F_i(t') = \frac{\partial}{\partial t} \langle \Psi(t') | P_i \Theta(r - r_c) P_i | \Psi(t') \rangle. \tag{3.117}$$

Thus, the state-resolved probabilities of dissociation can be written

$$p_{diss,i}(t) = \int_0^t dt^{'} F_i(t^{'}). \tag{3.118}$$

Assuming that the component of the wavepacket leaving the interaction region in a particular electronic state remains in that state as it exits into the reaction asymptote, we may take the population $\rho_i(t)$ of the diabatic state i to be

$$\rho_i(t) = \langle \Psi(t)|P_i\Theta(r_c - r)P_i|\Psi(t)\rangle + \int_0^t dt^{'} F_i(t^{'}). \tag{3.119}$$

Finally, we note that the components $F_i(t^{'})$ may most straightforwardly be calculated using the relationship

$$\begin{aligned} F_i(t) &= i\langle \Psi(t)|P_i\left[H, \Theta(r_c - r)\right]P_i|\Psi(t)\rangle \\ &= i\langle \Psi(t)|P_i\left[T_N, \Theta(r_c - r)\right]P_i|\Psi(t)\rangle. \end{aligned} \tag{3.120}$$

3.11 The Calculation of Absorption Spectra

The absorption spectrum $\sigma(E)$ may be calculated from the Fourier transform of the wavepacket autocorrelation function, that is,

$$\sigma(E) = \frac{1}{2\pi}\int_{-\infty}^{\infty} dt e^{iEt} a(t), \tag{3.121}$$

with

$$a(t) = \langle \Psi(0)|\Psi(t)\rangle\,. \tag{3.122}$$

Taking the Hamiltonian to be Hermitian, we may write

$$\begin{aligned} a(-t) &= \left\langle \Psi(0)\middle| e^{i\hat{H}t}\middle|\Psi(0)\right\rangle \\ &= \left\langle \Psi(0)\middle| \left(e^{-i\hat{H}t}\right)^{\dagger}\middle|\Psi(0)\right\rangle \\ &= a(t)^{*}. \end{aligned} \tag{3.123}$$

Hence, the spectrum may be calculated without recourse to integration over negative time:

$$\begin{aligned}\sigma(E) &= \frac{1}{2\pi}\int_0^\infty dt e^{-iEt}a(-t) + e^{iEt}a(t) \\ &= \frac{1}{2\pi}\int_0^\infty dt \left[e^{iEt}a(t)\right]^* + e^{iEt}a(t) \\ &= \frac{1}{\pi}Re\int_0^\infty dt e^{iEt}a(t).\end{aligned} \tag{3.124}$$

In order to obviate problems arising from a finite wavepacket propagation time T (specifically, issues arising from Gibbs phenomenon), $a(t)$ may be pre-multiplied by a filter function before its Fourier transform is computed such that $a(t)$ is forced to decay smoothly to zero as the time T is approached. One such family of suitable filter functions may be written

$$g_n(t) = \cos^n\left(\frac{\pi t}{2T}\right)\Theta\left(t-T\right); \quad n = 0, 1, 2, \ldots \tag{3.125}$$

with $\Theta\left(t-T\right)$ denoting the Heaviside step function centred at T.

In order to account for homogeneous broadening present in experimentally determined spectra, the autocorrelation function may further be multiplied by a damping function

$$f(t) = \exp\left(\frac{-t^m}{\tau^m}\right), \tag{3.126}$$

which is defined with respect to the free parameters τ and m.

Chapter 4

Ammonia

4.1 Introduction

The photodissociation of ammonia has been subject to many experimental [22–46] and theoretical [47–59] studies during the past few decades, owing to the system being a prototype for non-planar to planar electronic transitions, vibrational predissociation and nonadiabatic dynamics.

In the ground electronic state ($\tilde{X}$, $^1A_1'$), ammonia possesses a pyramidal geometry, with two isoenergetic C_{3v} minima that are connected by a D_{3h} saddle point along the umbrella inversion coordinate. The first excited state ($\tilde{A}(3s)$, $^1A_2''$) possesses a trigonal planar (D_{3h}) minimum and is quasi-bound with respect to N-H dissociation. From the planar $\tilde{A}(3s)$ state minimum, N-H dissociation leads to a conical intersection with the ground electronic state, as illustrated schematically in Figure 4.1. Hence, the N-H dissociation may evolve either diabatically, with the system passing through the conical intersection to form ground state $NH_2(\tilde{X},\ ^2B_1)$, or adiabatically, with the system crossing to the $\tilde{X}$ diabat to form the $NH_2(\tilde{A},\ ^2A_1)$ product, i.e.,

$$\begin{aligned} NH_3(\tilde{A},^1\,A_2'') &\rightarrow NH_2(\tilde{X},^2\,B_1) + H \quad \text{(Diabatic)} \\ &\rightarrow NH_2(\tilde{A},^2\,A_1) + H \quad \text{(Adiabatic).} \end{aligned} \tag{4.1}$$

Following excitation to the ground vibrational state of the $\tilde{A}(3s)$ state, dis-

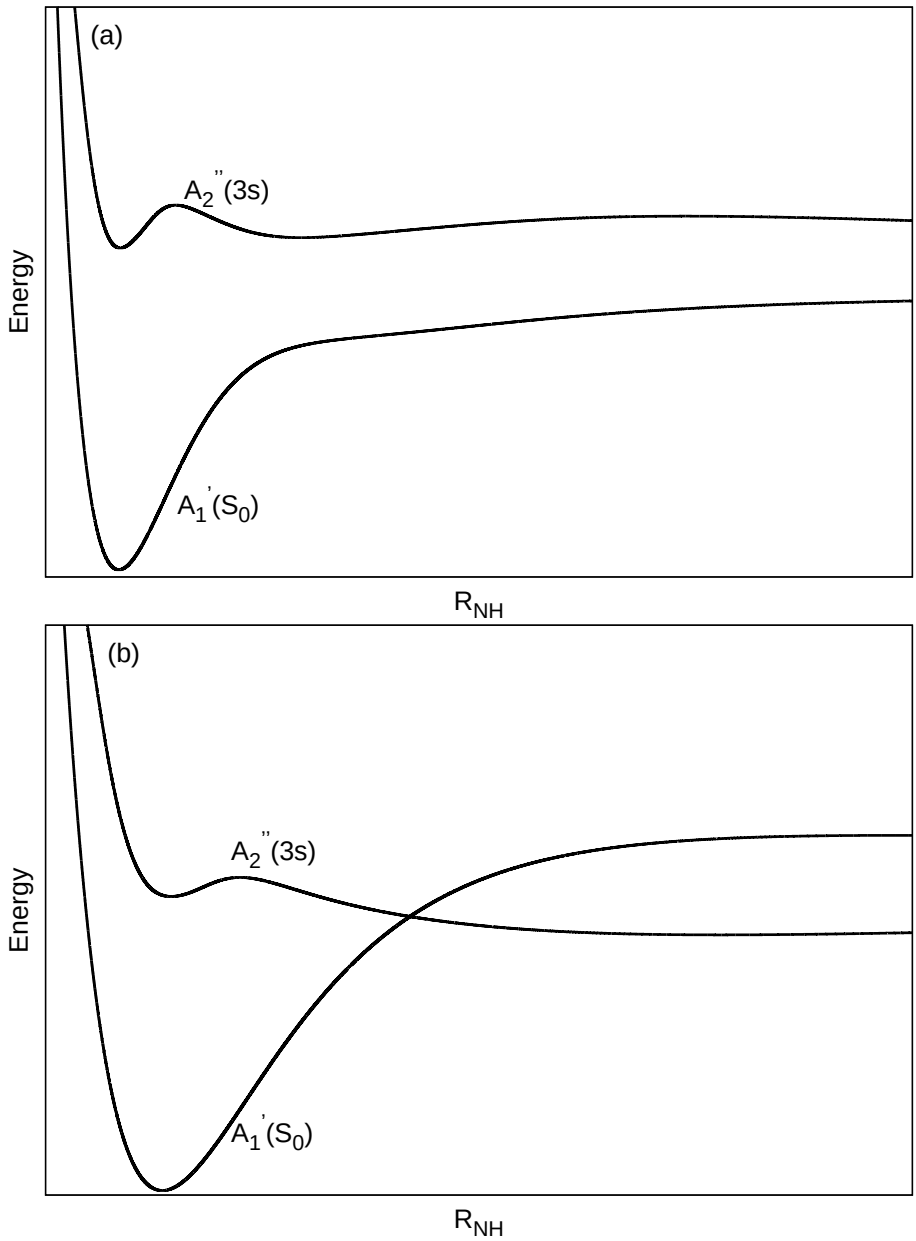

Fig. 4.1: Schematic adiabatic potentials corresponding to the $A_1^{'}(S_0)$ and $A_2(3s)^{''}$ states along the N-H dissociation coordinate starting from: (a) the C_{3v} Franck-Condon point, and; (b) the planar, D_{3h} S_1 minimum energy geometry.

sociation has been observed experimentally to proceed almost entirely diabatically [44]. The branching ratio between the two dissociation channels is, however, found to be dependent upon the excitation wavelength, with excitation of the umbrella inversion mode being found to promote adiabatic dissociation [29, 43]. Theoretically, these observations are supported by recent quantum dynamics simulations [59, 60]. However, the branching ratio is found to be sensitive to the dimensionality of the model used, with models of reduced dimensionality being found to yield a greater amount of adiabatic dissociation [59].

Concomitant with the crossing of the small barrier to dissociation on the $\tilde{A}(3s)$ state surface is a pronounced change in the character of $\tilde{A}(3s)$ state wavefunction; around the minimum point the wavefunction is dominated by excitation to a diffuse $3s$-type Rydberg orbital, whilst a pronounced valence character is acquired once the barrier has been traversed. The barrier to N-H dissociation has thus been viewed as likely being a consequence of an avoided crossing between a lower, bound Rydberg state and a higher-lying, purely dissociative state. No previous theoretical studies have, however, been performed that have sought to identify the origin of the barrier to N-H dissociation in ammonia. Similarly, previous theoretical studies of the photodissociation of ammonia have not been made with the intention of the evaluation the potential importance with respect to the excited state dynamics of ammonia of the nonadiabatic coupling of the $\tilde{A}(3s)$ state to higher-lying states that may give rise to the barrier to dissociation on the $\tilde{A}(3s)$ state surface. It is the intention of this work to address these two points.

In order to evaluate the validity of a two-state model of ammonia, two approaches are used. Firstly, in Section 4.2 a static approach is used whereby an assessment of whether the first two excited states of ammonia are decoupled

to a satisfactory extent from the electronic states forming their orthogonal complement is made. This is achieved through the evaluation of the extended Curl equation at the S_0 and S_1 minima. Secondly, in Section 4.3 a dynamical approach is pursued *via* the construction of two eight-state model Hamiltonians for use in quantum dynamics simulations of the photoexcitation of ammonia to the $\tilde{A}(3s)$ state. By utilising a transformation of the full eight-state Hamiltonians based on a block-diagonalisation of the potential matrix, the coupling of the $\tilde{X}$ and $\tilde{A}(3s)$ states from the higher-lying states may be removed, and a direct evaluation of the effects of this coupling to the higher-lying states made. The two model Hamiltonians constructed are: (i) a two-mode Hamiltonian employing Jacobi coordinates, and; (ii) a four-mode Hamiltonian employing valence coordinates. We note here that the main intention of the present study is to construct qualitatively correct model Hamiltonians that capture only the most essential features of potentials and nonadiabatic coupling terms along the degrees of freedom considered. Other, more recent studies have already successfully sought to derive quantitatively accurate model potentials describing the first two electronic states of ammonia [60, 61], but such a rigorous treatment here is inaccessible, owing to the large number of electronic states considered.

4.2 Evaluation of the Validity of Taking the $\tilde{X}$ and $\tilde{A}(3s)$ States to Form a Hilbert Subspace

4.2.1 The Extended Curl Equation

Previous studies of photoexcited ammonia have not addressed to what extent the $\tilde{X}$ and $\tilde{A}(3s)$ states are, or are not, decoupled from their orthogonal complement. In order to do so, we make use of the concept of a Hilbert

$$\begin{aligned} A^{(N)}_{\alpha\beta ij} &= \nabla_\beta \tau_{\alpha ij} - \nabla_\alpha \tau_{\beta ij} - \sum_{k=1}^{N} \left(\tau_{\alpha ik}\tau_{\beta kj} - \tau_{\beta ik}\tau_{\alpha kj}\right); \quad i,j \leq N \\ &= \sum_{k>N} \left(\tau_{\alpha ik}\tau_{\beta kj} - \tau_{\beta ik}\tau_{\alpha kj}\right), \end{aligned} \tag{4.5}$$

will be of the order of $O(\epsilon^2)$, and by evaluating the tensor $\boldsymbol{A}^{(N)}$ we may calculate the order of magnitude of the nonadiabatic coupling of the subspace of states $\{|\phi_i\rangle\}$; $i = 1, \ldots, N$ to it's orthogonal complement.

With regards to ammonia, the subspace to be considered here is that spanned by the $\tilde{X}$ and $\tilde{A}(3s)$ states, and we denote the tensor to be calculated as $\boldsymbol{A}^{(2)}$:

$$\begin{aligned} A^{(2)}_{\alpha\beta} &= \nabla_\beta \tau_{\alpha 12} - \nabla_\alpha \tau_{\beta 12} - \sum_{k=1}^{2} \left(\tau_{\alpha 1k}\tau_{\beta k2} - \tau_{\alpha 1k}\tau_{\beta k2}\right) \\ &= \nabla_\beta \tau_{\alpha 12} - \nabla_\alpha \tau_{\beta 12}. \end{aligned} \tag{4.6}$$

The last equality in Equation 4.6 holds as the derivative coupling matrix $\boldsymbol{\tau}$ is antisymmetric for the case of a basis of real electronic states. We here, and in the following, term the subspace spanned by the $\tilde{X}$ and $\tilde{A}(3s)$ states as the P-space, and that spanned by it's orthogonal complement the Q-space.

4.2.2 Analysis of $\boldsymbol{A}^{(2)}$

To calculate the tensor $\boldsymbol{A}^{(2)}$, derivative coupling terms $\boldsymbol{\tau}_{12}$ between the $\tilde{X}$ and $\tilde{A}(3s)$ states were calculated analytically at the CASSCF level using a full valence active space and the 6-311++G** basis set, denoted CAS(8,7)/6-311++G**. For the sake of simplicity, $\boldsymbol{A}^{(2)}$ was calculated using Cartesian nuclear coordinates. The derivatives $\nabla_\beta \tau_{\alpha 12}$ were calculated using a three-point finite difference formula and a step size of 0.0001 $\mathring{A}$. All derivative coupling calculations were performed using the Molpro 2009 set of programs [63]. The $\boldsymbol{A}^{(2)}$ tensor was calculated at two nuclear geometries pertinent to

subspace, defined as follows: for a subset of N electronic states $\{|\phi_i\rangle\}$; $i = 1, \ldots, N$ to form a Hilbert subspace it is required that

$$\boldsymbol{\tau}_{ij} \cong O(\epsilon); \quad i \leq N, \ j > N, \tag{4.2}$$

where ϵ is a suitably small number. That is, a subset of electronic states is taken to form a Hilbert subspace if the nonadiabatic coupling of them to the states that form their orthogonal complement is negligible. If the $\tilde{X}$ and $\tilde{A}(3s)$ states are found to form, to a satisfactory extent, a Hilbert subspace in the regions of nuclear configuration space relevant to ammonia's dynamics following excitation to the $\tilde{A}(3s)$ state, then the two-state model may be considered entirely valid.

A rather elegant way in which to evaluate the order of magnitude of the nonadiabatic coupling between a subset of electronic states and its orthogonal complement is by a consideration of the so-called extended Curl equation [11, 62]

$$\begin{aligned} \boldsymbol{A}_{\alpha\beta} &= \frac{\partial \boldsymbol{\tau}_\alpha}{\partial R_\beta} - \frac{\partial \boldsymbol{\tau}_\beta}{\partial R_\alpha} - [\boldsymbol{\tau}_\alpha, \boldsymbol{\tau}_\beta] \\ &= \nabla_\beta \boldsymbol{\tau}_\alpha - \nabla_\alpha \boldsymbol{\tau}_\beta - [\boldsymbol{\tau}_\alpha, \boldsymbol{\tau}_\beta] \,, \end{aligned} \tag{4.3}$$

which defines the gauge field tensor $\boldsymbol{A}$. Here, the R_α refer to the nuclear coordinates. For a complete Hilbert space of electronic states $\boldsymbol{A}$ may be shown to be identically zero. Considering two particular states $|\phi_i\rangle$ and $|\phi_j\rangle$; $i, j \leq N$, we may write

$$\begin{aligned} A_{\alpha\beta ij} &= \nabla_\beta \tau_{\alpha ij} - \nabla_\alpha \tau_{\beta ij} - \sum_{k=1}^{N} \left(\tau_{\alpha ik}\tau_{\beta kj} - \tau_{\beta ik}\tau_{\alpha kj}\right) - \sum_{k>N} \left(\tau_{\alpha ik}\tau_{\beta kj} - \tau_{\beta ik}\tau_{\alpha kj}\right) \\ &= A^{(N)}_{\alpha\beta ij} - \sum_{k>N} \left(\tau_{\alpha ik}\tau_{\beta kj} - \tau_{\beta ik}\tau_{\alpha kj}\right) = 0. \end{aligned} \tag{4.4}$$

Thus, it is found that the elements of the tensor $\boldsymbol{A}^{(N)}$,

Table 4.1: Elements of the tensor $\boldsymbol{A}^{(2)}$ calculated at the FC point using derivative coupling terms calculated at the CAS(8,7)/6-311++G** level. Entries of - denote elements that are zero. All elements are given in atomic units. The numbers indexing the columns and rows correspond to the Cartesian nuclear coordinates ordered x_N, y_N, z_N, x_{H_1}, y_{H_1}, z_{H_1}, x_{H_2}, y_{H_2}, z_{H_2}, x_{H_3}, y_{H_3}, z_{H_3}.

	1	2	3	4
2	0.012	-	-	-
3	0.074	0.011	-	-
4	0.357	-0.026	0.023	-
5	-0.048	0.025	0.001	0.036
6	-0.609	-0.044	-0.060	0.268
7	0.363	0.293	0.033	-0.218
8	0.349	0.507	0.051	-0.175
9	0.156	0.539	-0.005	-0.052
10	0.302	-0.221	0.027	-0.138
11	-0.349	0.469	-0.038	0.125
12	0.388	-0.507	-0.014	-0.197
	5	6	7	8
6	0.025	-	-	-
7	-0.014	0.043	-	-
8	-0.021	-0.042	0.044	-
9	-0.018	-0.085	0.022	-0.037
10	-0.012	0.017	-0.001	-0.044
11	0.011	0.016	-0.024	0.014
12	-0.007	0.050	0.053	0.045
	9	10	11	
10	-0.116	-	-	
11	0.134	0.004	-	
12	-0.062	-0.074	0.113	

Table 4.2: Elements of the tensor $\boldsymbol{A}^{(2)}$ calculated at the D_{3h} $\tilde{A}(3s)$ state minimum using derivative coupling terms calculated at the CAS(8,7)/6-311++G** level. Entries of - denote elements that are zero. All elements are given in atomic units. The numbers indexing the columns and rows correspond to the Cartesian nuclear coordinates ordered x_N, y_N, z_N, x_{H_1}, y_{H_1}, z_{H_1}, x_{H_2}, y_{H_2}, z_{H_2}, x_{H_3}, y_{H_3}, z_{H_3}.

	1	2	3	4
2	-	-	-	-
3	-	0.152	-	-
4	-	-	-	-
5	-	-	0.270	-
6	-	-0.247	-	-
7	-	-0.129	-	-
8	0.141	-	-0.067	0.031
9	-	0.057	-	-
10	-	0.129	-	-
11	-0.141	-	-0.067	-0.031
12	-	0.057	-	-
	5	6	7	8
6	0.304	-	-	-
7	-0.059	-	-	-
8	-	0.047	-0.193	-
9	0.007	-	-	-0.109
10	0.059	-	-	0.027
11	-	0.047	0.027	-
12	0.007	-	-	0.056
	9	10	11	
10	-	-	-	
11	-0.056	0.193	-	
12	-	-	-0.109	

the photoinduced dynamics of ammonia: (i) the C_{3v} FC point, and; (ii) the D_{3h} $\tilde{A}(3s)$ state minimum energy geometry.

The results of the calculation of $\boldsymbol{A}^{(2)}$ at the FC point and the $\tilde{A}(3s)$ state minimum are shown in Tables 4.1 and 4.2, respectively. It is found that at both geometries elements of $\boldsymbol{A}^{(2)}$ are far from zero: the largest calculated $|A^{(2)}_{\alpha\beta}|^{\frac{1}{2}}$ values, which are representative of the order of magnitude of the nonadiabatic coupling of the P-space and Q-space states, at the FC and $\tilde{A}(3s)$ state minimum are, respectively, 0.780 a.u. and 0.551 a.u.. It may thus be seen that the first two electronic states of ammonia do not constitute a Hilbert subspace at these two points, which are certain to be of importance with respect to excitation to the $\tilde{A}(3s)$ state. Further, the calculated $|A^{(2)}_{\alpha\beta}|^{\frac{1}{2}}$ values can be seen to imply that the order of magnitude of the nonadiabatic coupling of the P-space and Q-space states should be large, providing a motivation to pursue further the effect of this coupling on the dynamics of ammonia in its $\tilde{A}(3s)$ state.

4.3 Quantum Dynamics Simulations of Photoexcited Ammonia

4.3.1 Nuclear Coordinates and Kinetic Energy Operators

Our choice of nuclear coordinates is guided by two factors: (i) the coordinates used determine the order of expansion of the model potential required to satisfactorily reproduce the true potential in the regions of interest, and; (ii) the correlation of the particles of an MCTDH calculation, and thus the convergence of it with respect to the numbers of SPFs, is determined by the nuclear coordinates used. Photoexcited ammonia is known to undergo large amplitude motion, and so the use of curvilinear coordinates is desirable

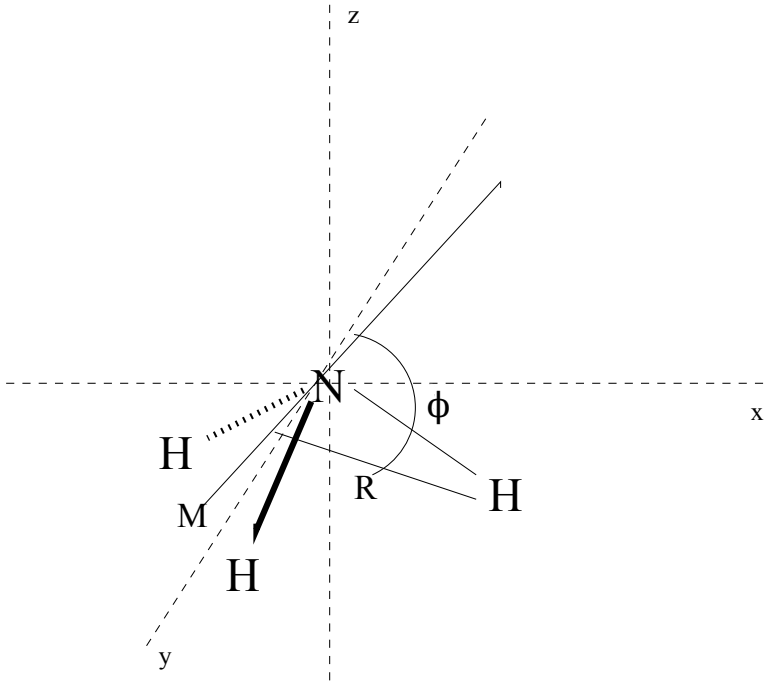

Fig. 4.2: Definition of the effective three-body Jacobi coordinates used in the construction of the two-mode model.

in order to reduce the 'artificial' correlation of the coordinates. Further, owing to our interest in dissociation following excitation to the $\tilde{A}(3s)$ state, a coordinate system that describes efficiently the dissociation of the N-H bonds is required.

Two-Dimensional Model

For the two-dimensional model, we consider the system to be an effective three-body system, composed of a single dissociating hydrogen atom, the nitrogen atom, and the centre of mass of the remaining H_2 unit, denoted by M. To construct the kinetic energy operator, we make use of Jacobi coordinates, as illustrated in Figure 4.2. We denote by R_{MN} the distance between M and the nitrogen atom, which is held constant in our model. R denotes the distance between the dissociating hydrogen atom and the centre of mass of the M-N unit, and ϕ is the out-of-plane angle between $\boldsymbol{R}_{MN}$

and $\boldsymbol{R}$. We denote collectively the coordinates (R, ϕ) as $\boldsymbol{q}$. In terms of the coordinates $\boldsymbol{q}$, the kinetic energy operator may be written, for the case of zero total angular momentum,

$$T(\boldsymbol{q}) = -\frac{1}{2\mu}\frac{\partial^2}{\partial R^2} - \frac{1}{2I}\frac{\partial^2}{\partial \phi^2}, \tag{4.7}$$

with,

$$\frac{1}{I} = \frac{1}{\mu R^2} + \frac{1}{\mu_{MN} R_{MN}^2}, \tag{4.8}$$

where

$$\mu = \frac{m_h(m_{H_2} + m_N)}{m_H + m_{H_2} + m_N}, \tag{4.9}$$

$$\mu_{MN} = \frac{m_{H_2} m_N}{m_{H_2} + m_N}. \tag{4.10}$$

Here, m_H, m_{H_2}, and m_N denote the masses of the hydrogen atom, H_2 unit and nitrogen atoms, respectively.

Four-Dimensional Model

For the four-dimensional model, polyspherical coordinates based on a valence vector parameterisation of the nuclear coordinates are used. The three valence vectors $\boldsymbol{R}_i$ used here are those connecting the nitrogen and three hydrogen atoms, as is depicted in Figure 4.3. Here R_i; $i = 1, 2, 3$ denote the three N-H bond lengths, θ_i; $i = 1, 2$ the planar angles between $\boldsymbol{R}_3$ and the vectors $\boldsymbol{R}_1$ and $\boldsymbol{R}_2$, and φ the dihedral angle between the vectors $\boldsymbol{R}_1$ and $\boldsymbol{R}_2$ and $\boldsymbol{R}_3$. The body-fixed (BF) frame used is defined such that the vector $\boldsymbol{R}_3$ lies along the z-axis of the BF frame, and the vector $\boldsymbol{R}_2$ lies in the x,z-plane of the BF frame. In order to yield a more compact expression of the kinetic energy operator, the coordinates $\zeta_i = \cos\theta_i$ are used in place of θ_i. The four

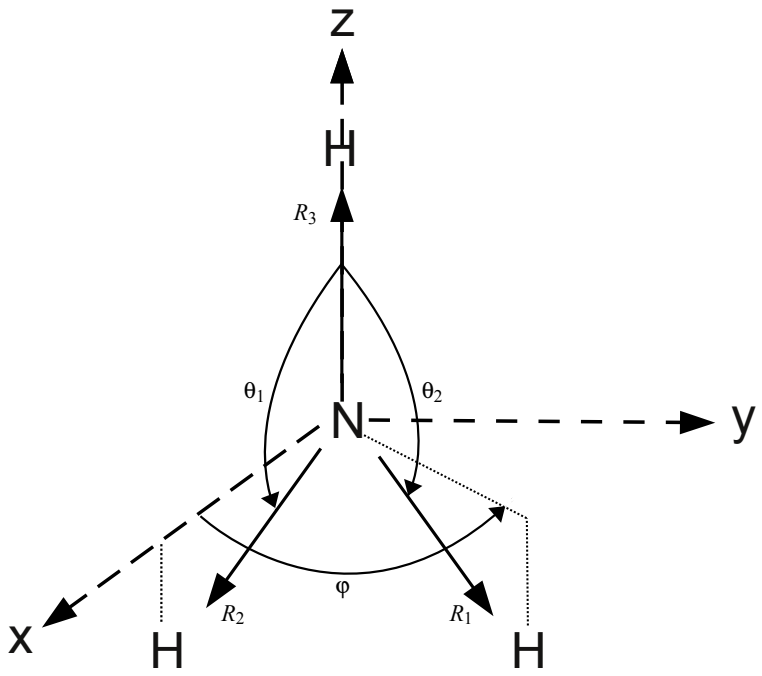

Fig. 4.3: Definition of the three valence vectors and six polyspherical coordinates used in the construction of the four-mode model.

coordinates entering into the reduced-dimensionality model used here are the N-H bond length R_1, the two cosines of the planar angles ζ_i and the dihedral angle φ. We denote collectively by $\boldsymbol{r}$ these four coordinates.

We choose as our reference point the D_{3h} $\tilde{A}(3s)$ state minimum energy geometry. The valence coordinates $\boldsymbol{r}$ do not generate irreducible representations (irreps) of the D_{3h} point group, but are found to generate irreps of the highest Abelian subgroup of the D_{3h} point group, that is, the C_{2v} point group. Specifically, we have $\Gamma^{R_i} = A_1$; $i = 1, 2, 3$, $\Gamma^{\theta_i} = B_2$; $i = 1, 2$, and $\Gamma^{\varphi} = B_1$.

Further, within the space spanned by the two planar angles θ_i lies a pair of Jahn-Teller active coordinates. To see this we perform the transformation

$$\begin{pmatrix} \theta_1 \\ \theta_2 \end{pmatrix} \rightarrow \begin{pmatrix} x \\ y \end{pmatrix} = \begin{pmatrix} \cos(\frac{\pi}{4}) & \sin(\frac{\pi}{4}) \\ -\sin(\frac{\pi}{4}) & \cos(\frac{\pi}{4}) \end{pmatrix} \begin{pmatrix} \theta_1 \\ \theta_2 \end{pmatrix}. \tag{4.11}$$

The new pair of degenerate planar angles, $x = 2^{-\frac{1}{2}}(\theta_1 + \theta_2)$ and $y = 2^{-\frac{1}{2}}(\theta_1 -$

θ_2), together are found to generate the $E^{'}$ irrep of the D_{3h} point group, and in C_{2v} symmetry we have $\Gamma^x = A_1$, $\Gamma^y = B_2$.

In terms of the valence coordinates $\boldsymbol{r}$ the kinetic energy operator may be written [17]

$$
\begin{aligned}
T(\boldsymbol{r}) = &- \frac{M_{11}}{2}\frac{\partial^2}{\partial R_1^2} - \sum_{i=1}^{2}\left[\frac{M_{i3}\zeta_i}{R_3R_i} + \left(\frac{M_{ii}}{2R_i^2} + \frac{M_{33}}{2R_3^2}\frac{\partial^2}{\partial\zeta_i}u_i^2\frac{\partial^2}{\partial\zeta_i}\right)\right] \\
&- \frac{M_{12}\left(\zeta_1\zeta_2 + u_1u_2\cos(\varphi)\right)}{R_1R_2} - \left(\frac{M_{13}}{2R_3}\frac{\partial}{\partial R_1}\right)\left(u_1^2\frac{\partial}{\partial\zeta_1} + \frac{\partial}{\partial\zeta_1}u_1^2\right) \\
&- \frac{M_{13}u_1\cos(\varphi)}{2R_3}\frac{\partial}{\partial R_1}\left(u_2\frac{\partial}{\partial\zeta_2} + \frac{\partial}{\partial\zeta_2}u_2\right) - \frac{M_{12}\zeta_1}{2R_2}\frac{\partial}{\partial R_1}\left(u_2^2\frac{\partial}{\partial\zeta_2} + \frac{\partial}{\partial\zeta_2}u_2^2\right) \\
&- \frac{M_{33}\cos(\varphi)}{2R_3^2}\left(u_1\frac{\partial^2}{\partial\zeta_1\partial\zeta_2}u_2 + u_2\frac{\partial^2}{\partial\zeta_1\partial\zeta_2}u_1\right) \\
&+ \frac{M_{12}}{2R_2}\frac{\partial}{\partial R_1}\left(u_1\cos(\varphi)\right)\left(\zeta_2u_2\frac{\partial}{\partial\zeta_2} + \frac{\partial}{\partial\zeta_2}\zeta_2u_2\right) \\
&+ \sum_{i\neq j=1}^{2}\frac{M_{i3}\cos(\varphi)}{2R_3R_i}\left(u_j\frac{\partial^2}{\partial\zeta_i\partial\zeta_j}\zeta_iu_i + \zeta_iu_i\frac{\partial^2}{\partial\zeta_i\partial\zeta_j}u_j\right) \\
&+ \sum_{i\neq j=1}^{2}\left[\frac{M_{i3}}{R_3R_i}\frac{\partial}{\partial\zeta_i}u_i^2\zeta_i\frac{\partial}{\partial\zeta_i} + \left(\frac{M_{12}}{2R_2} - \frac{M_{13}\zeta_2}{2R_3}\right)\right. \\
&\left.\times\frac{u_1}{u_2}\frac{\partial}{\partial R_1}\left(\sin(\varphi)\frac{\partial}{\partial\varphi} + \frac{\partial}{\partial\varphi}\sin(\varphi)\right)\right] \\
&- \frac{M_{12}}{2R_1R_2}\left[\left(\frac{\partial}{\partial\zeta_1}u_1\zeta_1u_2\zeta_2\frac{\partial}{\partial\zeta_2} + u_1\zeta_1\frac{\partial}{\partial\zeta_1}\frac{\partial}{\partial\zeta_2}u_2\zeta_2\right)\cos\varphi\right. \\
&\left.+ \frac{\partial}{\partial\zeta_1}u_1^2u_2^2\frac{\partial}{\partial\zeta_2} + u_1^2\frac{\partial}{\partial\zeta_1}\frac{\partial}{\partial\zeta_2}u_2^2\right] \\
&+ \sum_{i\neq j=1}^{2}\frac{M_{i3}\zeta_j}{2R_2R_iu_j}\left(\sin\varphi\frac{\partial^2}{\partial\zeta_i\partial\varphi}\zeta_iu_i + \zeta_iu_i\frac{\partial^2}{\partial\zeta_i\partial\varphi}\sin\varphi\right) \\
&- \sum_{i\neq j=1}^{2}\frac{M_{ij}}{2R_iR_ju_j}\left(\frac{\partial}{\partial\zeta_i}u_i\zeta_i\sin\varphi\frac{\partial}{\partial\varphi} + u_i\zeta_i\frac{\partial}{\partial\zeta_i}\frac{\partial}{\partial\varphi}\sin\varphi\right) \\
&- \sum_{i\neq j=1}^{2}\left(\frac{M_{33}\zeta_i}{2R_3^2u_i} - \frac{M_{i3}}{2R_3R_iu_i}\right)\left(\sin\varphi\frac{\partial^2}{\partial\zeta_j\partial\varphi}u_j + u_j\frac{\partial^2}{\partial\zeta_j\partial\varphi}\sin\varphi\right) \\
&- \sum_{i=1}^{2}\left(\frac{M_{ii}}{2R_i^2u_i^2} + \frac{M_{33}\zeta_i^2}{2R_3^2u_i^2} - \frac{M_{i3}\zeta_i}{R_3R_iu_i^2}\right)\frac{\partial^2}{\partial\varphi^2}
\end{aligned}
\tag{4.12}
$$

$$-\sum_{i\neq j=1}^{2}\left[\frac{M_{i3}\zeta_j}{R_3R_iu_ju_i}-\frac{1}{u_2u_1}\left(\frac{M_{12}}{R_1R_2}+\frac{M_{33}\zeta_2\zeta_1}{R_3^2}\right)\right]\frac{\partial}{\partial\varphi}\cos\varphi\frac{\partial}{\partial\varphi},$$

where $u_i = (1-\zeta_i^2)^{\frac{1}{2}}$, and the quantities M_{ij} denote the elements of the inverse-mass matrix

$$\boldsymbol{M} = \begin{pmatrix} \frac{1}{m_H}+\frac{1}{m_n} & \frac{1}{m_N} & \frac{1}{m_N} \\ \frac{1}{m_N} & \frac{1}{m_H}+\frac{1}{m_N} & \frac{1}{m_N} \\ \frac{1}{m_N} & \frac{1}{m_N} & \frac{1}{m_H}+\frac{1}{m_N} \end{pmatrix}, \tag{4.13}$$

with m_H and m_N denoting, respectively, the masses of the hydrogen and nitrogen atoms.

4.3.2 The Model Potentials

The model potential matrices used, $\boldsymbol{W}(\boldsymbol{q})$ and $\boldsymbol{W}(\boldsymbol{r})$, corresponds to the matrix representations of the electronic Hamiltonian in assumed diabatic bases. That is, we adopt diabatizations by *ansatz*, in which the matrix elements $W_{ij}(\boldsymbol{q})$ and $W_{ij}(\boldsymbol{r})$ are taken to assume particular functional forms, which are in turn parameterised such that maximal agreement between the model and calculated adiabatic potentials is found.

We take the adiabatic and diabatic representations to be equal at the D_{3h} reference points, denoted $\boldsymbol{q}_0$ and $\boldsymbol{r}_0$. For both models, the first eight electronic states are considered, that is, $\boldsymbol{W}(\boldsymbol{q})$ and $\boldsymbol{W}(\boldsymbol{r})$ correspond to 8×8 matrices.

The Two-Dimensional Model

We may write the full diabatic potential $\boldsymbol{W}(\boldsymbol{q})$ as a sum of uncorrelated potentials and an interaction potential:

$$\boldsymbol{W}(\boldsymbol{q}) = \boldsymbol{W}^{(0)} + \boldsymbol{W}(R) + \boldsymbol{W}(\phi) + \boldsymbol{W}^{I}(R,\phi), \tag{4.14}$$

where $\boldsymbol{W}^{(0)}$ corresponds to a zero-order term, the uncorrelated potentials $\boldsymbol{W}(R)$ and $\boldsymbol{W}(\phi)$ describe the potentials along the coordinates R and ϕ, and the interaction potential $\boldsymbol{W}^{I}(R,\phi)$ accounts for the correlation of the two coordinates R and ϕ.

The zero-order term $\boldsymbol{W}^{(0)}$ is given by $\boldsymbol{W}^{(0)} = \boldsymbol{W}(\boldsymbol{q}_0)$, with elements

$$W_{ij}^{(0)} = E_i \delta_{ij}, \tag{4.15}$$

where E_i denotes the vertical excitation energy of the state $|\Phi_i\rangle$ at the reference point. The diagonal form of $\boldsymbol{W}^{(0)}$ arises due to the equivalence of the adiabatic and diabatic representations at $\boldsymbol{q}_0$.

The uncorrelated diabatic potentials along the inversion angle ϕ, $W_{ii}(\phi)$, are taken as a set of quartic oscillators:

$$W_{ii}(\phi) = \frac{1}{2}\omega^{(i)}\phi^2 + \frac{1}{24}\epsilon^{(i)}\phi^4. \tag{4.16}$$

The off-diagonal elements $W_{ij}(\phi)$; $i \neq j$, are taken as linear expansions:

$$W_{ij}(\phi) = \lambda^{(i,j)}\phi, \tag{4.17}$$

with the interstate coupling constants $\lambda^{(i,j)}$ being given by

$$\begin{aligned} \lambda^{(i,j)} &= \frac{\partial}{\partial \phi}\langle \Phi_i | H_{el} | \Phi_j \rangle |_{\boldsymbol{q}_0} \\ &= \left\langle \Phi_i \middle| \left(\frac{\partial H_{el}}{\partial \phi} \right) \middle| \Phi_j \right\rangle \Big|_{\boldsymbol{q}_0}, \end{aligned} \tag{4.18}$$

with the last equality holding due to the integral $\langle \Phi_i | H_{el} | \Phi_j \rangle$ being evaluated at the reference point $\boldsymbol{q}_0$, at which the adiabatic and diabatic representations are taken to be equal. From Equation 4.18 we find that for a given interstate coupling constant $\lambda^{(i,j)}$ to be non-zero, the following necessary, but not sufficient, condition has to be met:

$$\lambda^{(i,j)} \neq 0, \quad \Gamma^i \otimes \Gamma^j \ni B_1, \tag{4.19}$$

where Γ^i denotes the symmetry of the diabatic state $|\Phi_i\rangle$ and B_1 is the irrep of the C_{2v} point group generated by the coordinate ϕ.

The uncorrelated diabatic potentials along the N-H dissociation coordinate, $W_{ii}(R)$, are modelled using a set of Morse and exponentially decaying potentials:

$$W_{ii}(R) = D_{0,i}\left(1 - \exp(-\alpha_i(R - R_{0,i}))\right)^2 + E_{0,i}; \quad i \neq 6, \tag{4.20}$$

$$E_{0,i} = -D_{0,i}\left(1 - \exp(\alpha_i R_{0,i})\right)^2, \tag{4.21}$$

and

$$W_{66}(R) = E_\infty\left(\exp(-\rho R) - 1\right). \tag{4.22}$$

The bound/unbound nature of the diabatic potentials $W_{22}(R)/W_{66}$ in contrast to the quasi-bound/bound forms of the corresponding adiabatic potentials $V_2(R)/V_6(R)$ arises as we here take the two diabatic states $|\Phi_2\rangle$ and $|\Phi_6\rangle$ to be coupled strongly by the degree of freedom R, and the barrier to dissociation on the potential $V_2(R)$ to be a consequence of this. Specifically, we model the coupling between these two states as

$$W_{26}(R) = \Lambda_1 \tanh(\Lambda_2 R). \tag{4.23}$$

The reasoning behind this parametrisation of $\boldsymbol{W}(R)$ is expanded upon in Section 4.3.8.

The correlation of the two degrees of freedom R and ϕ is dealt with by taking the parameters $\omega^{(i)}$, $\epsilon^{(i)}$ and $\lambda^{(i,j)}$ entering into the expansion of $\boldsymbol{W}(\phi)$

to be functions of the N-H dissociation coordinate R. Specifically, we choose the elements of the interaction potential $\boldsymbol{W}^I(R,\phi)$ as follows:

$$\begin{aligned} W^I_{ii}(R,\phi) =& \frac{1}{2}\left[-\omega^{(i)}\tanh\left(a_{\omega,i}R\right) + \left(b_{\omega,i}R + c_{\omega,i}R^2\right)\exp\left(-d_{\omega,i}R\right)\right]\phi^2 \\ & - \frac{1}{24}\frac{\epsilon^{(i)}}{2}\left[1+\tanh\left(\frac{R-A_{\epsilon,i}}{B_{\epsilon,i}}\right)\right]\phi^4; \quad i=1,2, \end{aligned} \tag{4.24}$$

$$\begin{aligned} W^I_{ii}(R,\phi) =& -\frac{1}{2}\frac{\omega^{(i)}}{2}\left[1+\tanh\left(\frac{R-A_{\omega,i}}{B_{\omega,i}}\right)\right]\phi^2 \\ & - \frac{1}{24}\frac{\epsilon^{(i)}}{2}\left[1+\tanh\left(\frac{R-A_{\epsilon,i}}{B_{\epsilon,i}}\right)\right]\phi^4; \quad i=3,\ldots,8, \end{aligned} \tag{4.25}$$

$$W^I_{12}(R,\phi) = \left[-\lambda^{(1,2)}\tanh\left(a_{\lambda,1,2}R\right) + \left(b_{\lambda,1,2}R + c_{\lambda,1,2}R^2\right)\exp(-d_{\lambda,1,2}R)\right]\phi, \tag{4.26}$$

$$W^I_{ij}(R,\phi) = -\frac{\lambda^{(i,j)}}{2}\left[1+\tanh\left(\frac{A_{\lambda,i,j}}{B_{\lambda,i,j}}\right)\right]\phi; \quad i,j \neq 1,2. \tag{4.27}$$

The functional forms presented in Equations 4.24 to 4.27 are chosen such that the contribution of ϕ to the potential decays smoothly to zero as the dissociation limit is reached. The parameters $\omega^{(i)}$; $i > 2$, $\epsilon^{(i)}$; $\forall i$, and $\lambda^{(i,j)}$; $i,j \neq 1,2$, are expanded about R_0 such that they remain approximately constant in the interaction region and then decay to zero as the dissociation limit is neared. In order to reproduce correctly the topology of the adiabatic surfaces around the conical intersection between the S_0 and S_1 states that is formed upon extension of the N-H bond, the parameters $\omega^{(i)}$; $i = 1,2$, and $\lambda^{(1,2)}$ were allowed to increase in magnitude in the interaction region before being forced to zero in the dissociation limit.

The Four-Dimensional Model

As mentioned in Section 4.3.1, the pair of symmetrised coordinates $x = 2^{-\frac{1}{2}}(\theta_1 + \theta_2)$ and $y = 2^{-\frac{1}{2}}(\theta_1 - \theta_2)$ are found to constitute a pair of Jahn-Teller active coordinates. As degenerate electronic states are present in the subspace of states considered here, we find it preferential to use the coordinates (x, y) in the parameterisation of the four-dimensional model potential. In the following the set of coordinates (R_1, x, y, φ) are denoted collectively by $\tilde{\boldsymbol{r}}$

As for the two-dimensional model, we write the four-dimensional potential $\boldsymbol{W}(\tilde{\boldsymbol{r}})$ as a sum of zero-order, uncorrelated, and interaction potentials:

$$\begin{aligned}\boldsymbol{W}(\tilde{\boldsymbol{r}}) =& \boldsymbol{W}^{(0)} + \boldsymbol{W}(R_1) + \boldsymbol{W}(x) + \boldsymbol{W}(y) + \boldsymbol{W}(\varphi) + \boldsymbol{W}^I(R_1, \varphi) + \boldsymbol{W}^I(x, y) \\ &+ \boldsymbol{W}^I(x, \varphi) + \boldsymbol{W}^I(y, \varphi) + \boldsymbol{W}^I(R_1, x, \varphi) + \boldsymbol{W}^I(R_1, y, \varphi).\end{aligned} \tag{4.28}$$

The forms of $\boldsymbol{W}^{(0)}$ and $\boldsymbol{W}(R_1)$ are the same as those given in Equations 4.15 and 4.20-4.23, respectively.

With respect to the planar angles x and y, it is convenient to sum the potentials $\boldsymbol{W}(x)$, $\boldsymbol{W}(y)$ and $\boldsymbol{W}^I(x, y)$ to give

$$\boldsymbol{W}(x, y) = \boldsymbol{W}(x) + \boldsymbol{W}(y) + \boldsymbol{W}^I(x, y). \tag{4.29}$$

We take the on-diagonal elements of $\boldsymbol{W}(x, y)$ corresponding to singly-degenerate states as

$$W_{ii}(x, y) = \left[D_{0,x}^{(i)} \left(1 - \exp(-\alpha_x^{(i)}(x - x_0^{(i)})) \right)^2 + E_{0,x}^{(i)} \right] + \frac{1}{2}\gamma_y^{(i)} y^2; \quad i = 1, 2, 5, 6, \tag{4.30}$$

with

$$E_{0,x}^{(i)} = -D_{0,x}^{(i)} \left(1 - \exp(\alpha_x^{(i)} x_0^{(i)})\right)^2 . \tag{4.31}$$

That is the diabatic potentials for the singly degenerate states are taken as Morse potentials along x and as harmonic oscillators along y.

For the two pairs of degenerate states $|\Phi_3\rangle$ and $|\Phi_4\rangle$, and $|\Phi_7\rangle$ and $|\Phi_8\rangle$, the symmetry of the coordinates x and y allows us to write [64]

$$\begin{aligned} \boldsymbol{W}^{(i,j)}(x,y) &= \begin{pmatrix} W_{ii} & W_{ij} \\ W_{ji} & W_{jj} \end{pmatrix}; \quad i,j = (3,4),(7,8) \\ &= \boldsymbol{W}_0^{(i,j)}(x,y) + \begin{pmatrix} -\kappa_x^{(i)} x - \frac{1}{2}\gamma_x^{(i)}(y^2 - x^2) & \kappa_x^{(i)} y + \gamma_x^{(i)} xy \\ \kappa_x^{(i)} y + \gamma_x^{(i)} xy & \kappa_x^{(i)} x + \frac{1}{2}\gamma_x^{(i)}(y^2 - x^2) \end{pmatrix}, \end{aligned} \tag{4.32}$$

where the diagonal matrices $\boldsymbol{W}_0^{(i,j)}(x,y)$, which represent the potentials of the corresponding states in the absence of any coupling, are given by Morse potentials along x and harmonic oscillators along y:

$$\boldsymbol{W}_0^{(i,j)}(x,y) = \left(\left[D_{0,x}^{(i)} \left(1 - \exp(-\alpha_x^{(i)}(x - x_0^{(i)})) - 1\right)^2 + E_{0,x}^{(i)} \right] + \frac{1}{2}\omega_y^{(i)} y^2 \right) \mathbf{1}. \tag{4.33}$$

The off-diagonal elements of $\boldsymbol{W}(x,y)$ that are not contained within the sub-matrices $\boldsymbol{W}_0^{(3,4)}(x,y)$ and $\boldsymbol{W}_0^{(7,8)}(x,y)$ are expanded to second-order with respect to x and to first-order with respect to y:

$$W_{ij}(x,y) = \lambda_x^{(i,j)} x + \frac{1}{2}\mu_x^{(i,j)} x^2 + \lambda_y^{(i,j)} y. \tag{4.34}$$

The diabatic potentials along the dihedral angle φ are taken as quartic oscillators,

$$W_{ii}(\varphi) = \frac{1}{2}\omega_\varphi^{(i)} \varphi^2 + \frac{1}{24}\epsilon_\varphi^{(i)} \varphi^4, \tag{4.35}$$

while the off-diagonal elements $W_{ij}(\varphi)$ are taken as linear expansions,

$$W_{ij}(\varphi) = \lambda_{\varphi}^{(i,j)}\varphi. \tag{4.36}$$

The interstate coupling constants entering into the model potential, that is, $\lambda_x^{(i,j)}$, $\lambda_y^{(i,j)}$, $\lambda_\varphi^{(i,j)}$ and $\mu_x^{(i,j)}$, are determined to be non-zero by symmetry *via* the conditions

$$\lambda_\alpha^{(i,j)} \neq 0, \quad \Gamma^i \otimes \Gamma^j \ni \Gamma^\alpha; \quad \alpha = x, y, \varphi \tag{4.37}$$

$$\mu_x^{(i,j)} \neq 0, \quad \Gamma^i = \Gamma^j. \tag{4.38}$$

The pairwise correlation of the degrees of freedom x and φ, and y and φ, corresponding to the potentials $\boldsymbol{W}^I(x,\varphi)$ and $\boldsymbol{W}^I(y,\varphi)$, is of particular importance for describing correctly the adiabatic potentials along the inversion pathway that connects the two isoenergetic C_{3v} ground state minima. This pairwise correlation is modelled by including in the model potential terms non-zero by symmetry entering into an eighth-order expansion of the elements $W_{11}(\tilde{\boldsymbol{r}})$ and $W_{22}(\tilde{\boldsymbol{r}})$ with respect to only x and φ, and y and φ. Specifically, we take

$$\begin{aligned} W_{ii}^I(x,\varphi) =& \frac{1}{3!}\eta_{x\varphi^2}^{(i)} x\varphi^2 + \frac{1}{4!}\eta_{x^2\varphi^2}^{(i)} x^2\varphi^2 + \frac{1}{5!}\eta_{x^3\varphi^2}^{(i)} x^3\varphi^2 + \frac{1}{5!}\eta_{x\varphi^4}^{(i)} x\varphi^4 + \frac{1}{6!}\eta_{x^2\varphi^4}^{(i)} x^2\varphi^4 \\ &+ \frac{1}{7!}\eta_{x^3\varphi^4}^{(i)} x^3\varphi^4 + \frac{1}{8!}\eta_{x^4\varphi^4}^{(i)} x^4\varphi^4; \quad i = 1, 2, \end{aligned} \tag{4.39}$$

and

$$W_{ii}^I(y,\varphi) = \frac{1}{4!}\eta_{y^2\varphi^2} y^2\varphi^2 + \frac{1}{6!}\eta_{y^2\varphi^4} y^2\varphi^4 + \frac{1}{6!}\eta_{y^4\varphi^2} y^4\varphi^2 + \frac{1}{8!}\eta_{y^4\varphi^4} y^4\varphi^4; \quad i = 1, 2 \tag{4.40}$$

where

$$\eta^{(i)}_{x^m\varphi^n} = \left.\frac{\partial^{(m+n)} W_{ii}}{\partial x^m \partial \varphi^n}\right|_{\tilde{\boldsymbol{r}}_0}, \tag{4.41}$$

and

$$\eta^{(i)}_{y^m\varphi^n} = \left.\frac{\partial^{(m+n)} W_{ii}}{\partial y^m \partial \varphi^n}\right|_{\tilde{\boldsymbol{r}}_0}. \tag{4.42}$$

The parameters $\eta_{x^m\varphi^n}$ and $\eta_{y^m\varphi^n}$ are taken as functions of the N-H dissociation coordinate R_1. We take these parameters to be approximately constant in the interaction region and to decay to zero as the dissociation limit is reached. This is achieved through the use of the interaction potentials

$$W^I_{ii}(R_1, x, \varphi) = \sum_{m,n} -\frac{1}{(m+n)!}\frac{\eta_{x^m\varphi^n}}{2}\left[1 + \tanh\left(\frac{R_1 - A_{x^m\varphi^n}}{B_{x^m\varphi^n}}\right)\right] x^m\varphi^n; \quad i = 1, 2 \tag{4.43}$$

$$W^I_{ii}(R_1, y, \varphi) = \sum_{m,n} -\frac{1}{(m+n)!}\frac{\eta_{y^m\varphi^n}}{2}\left[1 + \tanh\left(\frac{R_1 - A_{y^m\varphi^n}}{B_{y^m\varphi^n}}\right)\right] y^m\varphi^n; \quad i = 1, 2 \tag{4.44}$$

with the sums being taken to run over only the combinations of m and n given in Equations 4.39 and 4.40.

The pairwise correlation of the degrees of freedom R_1 and φ is accounted for through the use of the interaction potential $\boldsymbol{W}^I(R_1, \varphi)$, which is taken to have the following form:

$$\begin{aligned} W^I_{ii}(R_1, \varphi) = &\left[-\frac{1}{2}\omega^{(i)}_{\varphi}\tanh\left(a_{\omega,i}R_1\right) + \left(b_{\omega,i}R_1 + c_{\omega,i}R_1^2\right)\exp(-d_{\omega,i}R_1)\right]\varphi^2 \\ &- \frac{1}{2}\frac{\epsilon^{(i)}_{\varphi}}{2}\left[1 + \tanh\left(\frac{R_1 - A_{\epsilon,i}}{B_{\epsilon,i}}\right)\right]\varphi^4; \quad i = 1, 2 \end{aligned} \tag{4.45}$$

$$W^I_{ii}(R_1,\varphi) = -\frac{1}{2}\frac{\omega^{(i)}_\varphi}{2}\left[1+\tanh\left(\frac{R_1-A_{\omega,i}}{B_{\omega,i}}\right)\right]\varphi^2 - \frac{1}{2}\frac{\epsilon^{(i)}_\varphi}{2}\left[1+\tanh\left(\frac{R_1-A_{\epsilon,i}}{B_{\epsilon,i}}\right)\right],\varphi^4; \quad i=3,\ldots,8, \tag{4.46}$$

$$W^I_{ij}(R_1,\varphi) = \left[-\lambda^{(i,j)}_\varphi \tanh\left(a_{\lambda,i,j}R_1\right) + \left(b_{\lambda,i,j}R_1 + c_{\lambda,i,j}R_1^2\right)\exp(-d_{\lambda,i,j}R_1)\right]\varphi; \quad i,j=1,2, \tag{4.47}$$

$$W^I_{ij}(R_1,\varphi) = -\frac{\lambda^{(i,j)}_\varphi}{2}\left[1+\tanh\left(\frac{R_1-A_{\lambda,i,j}}{B_{\lambda,i,j}}\right)\right]\varphi; \quad i,j\neq 1,2. \tag{4.48}$$

That is, the parameters $\omega^{(i)}_\varphi$; $i>2$, $\epsilon^{(i)}_\varphi$; $\forall i$, and $\lambda^{(i,j)}_\varphi$; $i,j\neq 1,2$ are taken to be approximately constant in the interaction region and decay to zero as the dissociation limit is reached. The parameters $\omega^{(i)}_\varphi$; $i=1,2$, and $\lambda^{(1,2)}_\varphi$ are allowed to vary in magnitude in the interaction region, as is found to be required to reproduce faithfully the topology of the S_0 and S_1 adiabatic potentials in the vicinity of the conical intersection of these two states.

Parameterisation of the Model Potentials

The parameterisation of both model potentials was achieved by minimising the root mean square deviation (RMSD) of the model adiabatic energies, obtained by diagonalising the model diabatic potentials, and adiabatic energies calculated at a large number of points pertinent to the dynamics of ammonia following excitation to the $\tilde{A}(3s)$ state. In order that the model potentials be preferentially accurate in regions of low energy, the actual quantity optimised is the following functional:

$$\Delta = \sum_{s=1}^{\sigma}\sum_{i=1}^{n_\sigma}(V_i^s - V_i^{s,mod})^2\Omega_i^s. \tag{4.49}$$

Here, σ is the number of electronic states, n_σ is the number of points for the state σ, and V_i^s and $V_i^{s,mod}$ are the true and model adiabatic energies at the ith point for the sth state, respectively. Ω_i^s is a weight function, chosen as

$$\Omega_i^s = \exp\left(-(V_i^s - V_0^s)\right), \tag{4.50}$$

where V_0^s is the value of the sth adiabatic potential at the reference point.

4.3.3 Product Representation of the Potential

The low dimensionality of the two-dimensional model is such that the standard wavepacket propagation method, as outlined in Section 3.3.1, may be used. There exists, then, no restriction on the form of the model potential $\boldsymbol{W}(\boldsymbol{q})$. For the four-dimensional model, however, we are forced to resort to the use of the MCTDH method. As such, we require that the model potential $\boldsymbol{W}(\boldsymbol{r})$ be cast in the form of a sum of products of monomodal operators. Although the *ansatz* for the model potential $\boldsymbol{W}(\tilde{\boldsymbol{r}})$ as outlined in Section 4.3.2 is in the required product form, the kinetic energy operator written in terms of the coordinates $\tilde{\boldsymbol{r}}$ is not. We are thus required to transform the model potential $\boldsymbol{W}(\tilde{\boldsymbol{r}})$ to be in terms of the coordinates $\boldsymbol{r}$. To proceed, we make use of the potfit algorithm [65] to expand the model potential $\boldsymbol{W}(\boldsymbol{r})$, as calculated from the parameterised potential $\boldsymbol{W}(\tilde{\boldsymbol{r}})$, in terms of a direct product basis. We note that the smooth form of elements $W_{ij}(\boldsymbol{r})$ results in a very accurate product representation of the potential using only small expansion orders in the potfit procedure.

4.3.4 Electronic Structure Calculations

The adiabatic energies used in the parametrisation of both model potentials were calculated using the second-order Multi-Configurational Quasi-Degenerate Perturbation Theory (MCQDPT2) method [66] as implemented

Table 4.3: Vertical excitation energies, symmetries and dominant configurations of the first eight singlet excited states of ammonia calculated at the D_{3h} S_1 minimum energy geometry at the MCQDPT2(4,11)/aug level.

State	Dominant Configuration	Symmetry: D_{3h} (C_{2v})	ΔE (eV)
$\tilde{X}$	$\|0\rangle$	$A_1^{'}$ (A_1)	0.00
$\tilde{A}$	$2p_x \rightarrow 3s$	$A_2^{''}$ (B_1)	5.19
$\tilde{B}_y$	$2p_x \rightarrow 3p_y$	$E^{''}$ (A_2)	6.67
$\tilde{B}_z$	$2p_x \rightarrow 3p_z$	$E^{''}$ (B_1)	6.67
$\tilde{C}$	$2p_x \rightarrow 3p_x$	$A_1^{'}$ (A_1)	8.59
$\tilde{D}$	$2p_x \rightarrow 4s$	$A_2^{''}$ (B_1)	9.13
$\tilde{E}_y$	$2p_x \rightarrow 4p_y$	$E^{''}$ (A_2)	9.17
$\tilde{E}_z$	$2p_x \rightarrow 4p_z$	$E^{''}$ (B_1)	9.17

in the GAMESS-US software package [67] in conjuction with the aug-cc-pVDZ basis set. The reference wavefunction used corresponds to a CAS(4,11) wavefunction, with an active space formed by the orbitals $1e^{'}(2p_z)$, $1a_2^{''}(2p_x)$, $3a_1^{'}(3s)$, $2e^{'}(3p_y)$, $2e^{'}(3p_z)$, $2a_2^{''}(3p_x)$, $4a_1^{'}(4s)$, $3e^{'}(4p_y)$, $3e^{'}(4p_z)$, $4e^{'}(5p_y)$ and $4e^{'}(5p_z)$. We denote this method of calculation by MCQDPT2(4,11)/aug. At each geometry used in the fitting procedure the first eight adiabatic energies were calculated, the details of which are summarised in Table 4.3. In order to distinguish between the components of the doubly degenerate states, the following convention is used: each state label (either $\tilde{B}$ or $\tilde{E}$) is indexed by either the label y and z, with the labels denoting, respectively, states that are dominated by a configuration corresponding to excitation into an np_y or np_z orbital.

4.3.5 Block Diagonalisation of the Diabatic Potential

We consider a unitary transformation of the diabatic basis $\{\Phi_i\}$ to yield a new basis $\{\Phi_i^{BD}\}$,

$$\Phi_i^{BD} = \sum_{j=1}^{N} S_{ji}\Phi_j, \tag{4.51}$$

such that the matrix representation of the potential in the new basis $\{\Phi_i^{BD}\}$, $\boldsymbol{W}_{BD}$, has a given block diagonal form:

$$\boldsymbol{W}_{BD} = \begin{pmatrix} \boldsymbol{W}_{BD,1} & & & \\ & \boldsymbol{W}_{BD,2} & & 0 \\ & & \ddots & \\ & 0 & & \boldsymbol{W}_{BD,n} \end{pmatrix}, \tag{4.52}$$

where the sub-matrices $\boldsymbol{W}_{BD,i}$ are $N_i \times N_i$ square matrices. That is, the states entering into two different blocks $\boldsymbol{W}_{BD,i}$ and $\boldsymbol{W}_{BD,j}$ are no longer coupled by the electronic Hamiltonian. Correspondingly, the matrix representation of the kinetic energy operator should also be subject to the same transformation, i.e., we should make the transformation

$$\boldsymbol{T} \rightarrow \boldsymbol{T}_{BD} = \boldsymbol{S}^{\dagger}\boldsymbol{T}\boldsymbol{S} \tag{4.53}$$

in order to yield an equivalent representation of the Hamiltonian.

We here, however, consider the use of an intermediate Hamiltonian,

$$\tilde{\boldsymbol{H}} = \boldsymbol{W}_{BD} + \boldsymbol{T}, \tag{4.54}$$

in order to study the effect of the neglect of the coupling of the states entering into the different blocks $\boldsymbol{W}_{BD,i}$ and $\boldsymbol{W}_{BD,j}$, which may be achieved through the use of the two Hamiltonians $\boldsymbol{H}$ and $\tilde{\boldsymbol{H}}$ in separate quantum dynamics simulations. We may consider $\tilde{\boldsymbol{H}}$ to be the matrix representation of the Hamiltonian in the basis $\{\Phi_i^{BD}\}$ with the approximation made that the states entering into different blocks $\boldsymbol{W}_{BD,i}$ and $\boldsymbol{W}_{BD,j}$ are decoupled. In the following, we make this approximation implicitly and term this basis the intermediate basis.

In order to calculate the transformation matrix $\boldsymbol{S}$, we make use of the method developed by Cederbaum *et al.* [68] Within this scheme, the transformation matrix $\boldsymbol{S}$ is constructed such that

$$||\boldsymbol{S}-\boldsymbol{1}|| = minimum, \tag{4.55}$$

where $||\boldsymbol{A}||$ denotes the Euclidean norm of the matrix $\boldsymbol{A}$. That is, the transformation matrix $\boldsymbol{S}$ will bring the potential matrix $\boldsymbol{W}$ into block diagonal form, but beyond this will do nothing else. This constraint is found to be necessary as there exists an infinite number of unitary transformations that will bring the potential matrix into a given block diagonal form. Through the enforcement of this requirement, it can be shown that [68]

$$\boldsymbol{S} = \boldsymbol{U}\boldsymbol{U}_{BD}^{\dagger}\left(\boldsymbol{U}_{BD}\boldsymbol{U}_{BD}^{\dagger}\right)^{-\frac{1}{2}}. \tag{4.56}$$

Here, $\boldsymbol{U}$ denotes the matrix of eigenvectors of the diabatic potential $\boldsymbol{W}$, and $\boldsymbol{U}_{BD}$ the block-diagonal part of $\boldsymbol{U}$.

For the case of ammonia, we wish to determine the effect of the neglect of the coupling of the $\tilde{X}$ and $\tilde{A}(3s)$ states to the six higher-lying states $\tilde{B}$ to $\tilde{E}$. Thus, we take the matrix $\boldsymbol{U}_{BD}$ that enters into the definition of the transformation matrix $\boldsymbol{S}$ to be

$$\boldsymbol{U}_{BD} = \begin{pmatrix} U_{11} & U_{12} & 0 & 0 & 0 & 0 & 0 & 0 \\ U_{21} & U_{22} & 0 & 0 & 0 & 0 & 0 & 0 \\ 0 & 0 & U_{33} & U_{34} & U_{35} & U_{36} & U_{37} & U_{38} \\ 0 & 0 & U_{43} & U_{44} & U_{45} & U_{46} & U_{47} & U_{48} \\ 0 & 0 & U_{53} & U_{54} & U_{55} & U_{56} & U_{57} & U_{58} \\ 0 & 0 & U_{63} & U_{64} & U_{65} & U_{66} & U_{67} & U_{68} \\ 0 & 0 & U_{73} & U_{74} & U_{75} & U_{76} & U_{77} & U_{78} \\ 0 & 0 & U_{83} & U_{84} & U_{85} & U_{86} & U_{87} & U_{88} \end{pmatrix}. \tag{4.57}$$

In order to simplify the discussion of the two model Hamiltonians $\boldsymbol{H}$ and $\tilde{\boldsymbol{H}}$, we introduce the following notation. We denote the total nuclear wavefunction in the diabatic representation by $|\Psi^{(d)}\rangle$:

$$|\Psi^{(d)}\rangle = \sum_{i=1}^{N} |\Psi_i^{(d)}\rangle |i^{(d)}\rangle, \tag{4.58}$$

where the sum is over the diabatic electronic states $|i^{(d)}\rangle$, and $|\Psi_i^{(d)}\rangle$ denotes the nuclear wavefunction for the diabatic electronic state $|i^{(d)}\rangle$. Similarly, we write the nuclear wavefunction in the adiabatic representation as

$$|\Psi^{(a)}\rangle = \sum_{i=1}^{N} |\Psi_i^{(a)}\rangle |i^{(a)}\rangle. \tag{4.59}$$

Finally, we denote by $|\Psi^{(bd)}\rangle$ the nuclear wavefunction in the intermediate representation:

$$|\Psi^{(bd)}\rangle = \sum_{i=1}^{N} |\Psi_i^{(bd)}\rangle |i^{(bd)}\rangle. \tag{4.60}$$

4.3.6 Projection Onto the Adiabatic States

Although allowing for a rigorous decoupling of the $\tilde{X}$ and $\tilde{A}(3s)$ states from their orthogonal complement, the block diagonalisation scheme used here does not allow for a simple comparison of the results of wavepacket propagations performed using the Hamiltonians $\boldsymbol{H}$ and $\tilde{\boldsymbol{H}}$. In the case of using the Hamiltonian $\boldsymbol{H}$, that is, when working in the original, diabatic, representation, dissociation can occur in the three electronic states $|1^{(d)}\rangle$, $|2^{(d)}\rangle$ and $|6^{(d)}\rangle$. When using the intermediate Hamiltonian $\tilde{\boldsymbol{H}}$, however, dissociation may proceed only in the states $|1^{(bd)}\rangle$ and $|2^{(bd)}\rangle$. A direct comparison of the results may, however, be made *via* the transformation of the diabatic and intermediate wavefunctions to the adiabatic representation.

In principle, as the two potentials $\boldsymbol{W}$ and $\boldsymbol{W}_{BD}$, and thus their eigenvectors, are known, the transformation to the adiabatic representation of both wavefunctions is known:

$$\begin{aligned} |\boldsymbol{\Psi}^{(a)}\rangle &= \boldsymbol{U}^{\dagger} |\boldsymbol{\Psi}^{(d)}\rangle \\ &= \boldsymbol{X}^{\dagger} |\boldsymbol{\Psi}^{(bd)}\rangle, \end{aligned} \tag{4.61}$$

where $|\boldsymbol{\Psi}^{(a)}\rangle$ denotes the vector of adiabatic nuclear wavefunctions $|\Psi_i^{(a)}\rangle$, with $|\boldsymbol{\Psi}^{(b)}\rangle$ and $|\boldsymbol{\Psi}^{(bd)}\rangle$ being defined analogously, and

$$\begin{aligned} \boldsymbol{V} &= \boldsymbol{U}^\dagger \boldsymbol{W} \boldsymbol{U} \\ &= \boldsymbol{X}^\dagger \boldsymbol{W}_{BD} \boldsymbol{X}, \end{aligned} \tag{4.62}$$

with $\boldsymbol{V}$ denoting the adiabatic potential matrix. However, as the transformation matrices $\boldsymbol{U}^\dagger$ and $\boldsymbol{X}^\dagger$ are not in the required MCTDH product form, this direct approach cannot be used.

To proceed, we introduce the set of projectors onto the adiabatic states, $P_{a,i}$,

$$P_{a,i}|\Psi^{(a)}\rangle = |\Psi_i^{(a)}\rangle. \tag{4.63}$$

In the adiabatic representation the matrix representation of $P_{a,i}$, $\boldsymbol{P}_{a,i}^{(a)}$, is given by

$$\left(\boldsymbol{P}_{a,i}^{(a)}\right)_{mn} = \delta_{mi}\delta_{ni}. \tag{4.64}$$

In the diabatic and intermediate representations, the matrix representations of $P_i^{(a)}$ are given, respectively, by

$$\begin{aligned} \left(\boldsymbol{P}_{a,i}^{(d)}\right)_{mn} &= \sum_{k,l} U_{mk} \left(\boldsymbol{P}_{a,i}^{(a)}\right)_{kl} U_{ln}^\dagger \\ &= U_{mi}U_{ni}, \end{aligned} \tag{4.65}$$

and

$$\begin{aligned} \left(\boldsymbol{P}_{a,i}^{(bd)}\right)_{mn} &= \sum_{k,l} X_{mk} \left(\boldsymbol{P}_{a,i}^{(a)}\right)_{kl} X_{ln}^\dagger \\ &= X_{mi}X_{ni}. \end{aligned} \tag{4.66}$$

Again, the elements of the projection matrices $\boldsymbol{P}_{a,i}^{(d)}$ and $\boldsymbol{P}_{a,i}^{(bd)}$ are not in product form. We circumvent this problem by making use of the potfit algorithm [65] to expand the elements $\boldsymbol{P}_{a,i}^{(d)}$ and $\boldsymbol{P}_{a,i}^{(bd)}$ in direct product bases

such that they are expressed in the sum-of-products form required for use with the MCTDH method.

Using these projectors the time-evolution of the adiabatic state populations resulting from the use of the Hamiltonians $\boldsymbol{H}$ and $\tilde{\boldsymbol{H}}$ may be calculated, respectively, as the expectation values

$$p_{a,i}^{(d)}(t) = \langle \boldsymbol{\Psi}^{(d)}(t) | \boldsymbol{P}_{a,i}^{(d)} | \boldsymbol{\Psi}^{(d)}(t) \rangle, \tag{4.67}$$

$$p_{a,i}^{(bd)}(t) = \langle \boldsymbol{\Psi}^{(bd)}(t) | \boldsymbol{P}_{a,i}^{(bd)} | \boldsymbol{\Psi}^{(bd)}(t) \rangle. \tag{4.68}$$

Further, the flux passing into the two adiabatic dissociation channels, denoted $F_{a,i}^{(b)}(t)$ and $F_{a,i}^{(bd)}(t)$ $(i = 1, 2)$ for the quantities calculated using, respectively, $\boldsymbol{H}$ and $\tilde{\boldsymbol{H}}$, may be calculated as

$$F_{a,i}^{(d)}(t) = \langle \boldsymbol{\Psi}^{(d)}(t) | \boldsymbol{P}_{a,i}^{(d)} \boldsymbol{F} \boldsymbol{P}_{a,i}^{(d)} | \boldsymbol{\Psi}^{(d)}(t) \rangle, \tag{4.69}$$

and

$$F_{a,i}^{(bd)}(t) = \langle \boldsymbol{\Psi}^{(bd)}(t) | \boldsymbol{P}_{a,i}^{(bd)} \boldsymbol{F} \boldsymbol{P}_{a,i}^{(bd)} | \boldsymbol{\Psi}^{(d)}(t) \rangle, \tag{4.70}$$

where $\boldsymbol{F}$ denotes the appropriately defined flux operator. In this way we may compare in a meaningful manner the differences between the dynamics of ammonia following excitation to the $\tilde{A}(3s)$ state calculated using the Hamiltonians $\boldsymbol{H}$ and $\tilde{\boldsymbol{H}}$.

4.3.7 Preparation of Initial Wavepackets and the Calculation of Spectra

As is well known, the electronic absorption spectrum of ammonia in the region 40000 cm^{-1} to 65000 cm^{-1} contains two progressions in the inversion

mode, corresponding to excitation of the nearly degenerate pair of tunnel-split ground vibrational eigenstates, denoted $|\Psi_g\rangle$ and $|\Psi_u\rangle$. In order to circumvent the propagation of both eigenstates, we make the approximation that the $|\Psi_g\rangle$ and $|\Psi_u\rangle$ eigenstates are isoenergetic. The ground state wavefunction $|\Psi_{GS}\rangle$ may then be written

$$|\Psi_{GS}\rangle = \frac{1}{\sqrt{2}}\left(|\Psi_g\rangle + |\Psi_u\rangle\right). \tag{4.71}$$

Equation 4.71 would be exact if the eigenstates $|\Psi_g\rangle$ and $|\Psi_u\rangle$ were truly isoenergetic, and is considered justifiable as the splitting between the two states is known to be very small ($<1\text{cm}^{-1}$). Further, we assume that the ground state wavefunction $|\Psi_{GS}\rangle$ as written in Equation 4.71 may be obtained as

$$|\Psi_{GS}\rangle = \Theta_{inv}|\Psi_g\rangle, \tag{4.72}$$

where Θ_{inv} denotes the projector onto one of the pair of isoenergetic ground state minima. The assumption of the equality of the expressions for $|\Psi_{GS}\rangle$ given in Equations 4.71 and 4.72 can be taken to be justifiable if the eigenstates $|\Psi_g\rangle$ and $|\Psi_u\rangle$ are approximated to differ only in their parities with respect to the inversion coordinate. The eigenstate $|\Psi_g\rangle$ is calculated using the method of relaxation.

Initial wavepackets $|\Psi(t=0)\rangle$ were produced *via* vertical excitation to the electronic state of interest. We here make the distinction between the initial state used for the study of the dynamics,

$$\begin{aligned} |\Psi(t=0)\rangle &= \left\{|i\rangle\langle 1| + h.c.\right\}|\Psi_g\rangle \\ &= O_v^{(i)}|\Psi_g\rangle, \end{aligned} \tag{4.73}$$

and that used to calculate electronic spectra,

$$\begin{aligned} |\Psi(t=0)\rangle &= \{|i\rangle\langle 1| + h.c.\}\,\Theta_{inv}|\Psi_g\rangle \\ &= O^{(i)}_{v,p}|\Psi_g\rangle, \end{aligned} \tag{4.74}$$

where $|i\rangle$ denotes the excited state of interest.

4.3.8 The Origin of the Barrier to Dissociation on the S_1 Adiabatic State Surface

We here discuss the choice of *ansatz* used for the model potential $\boldsymbol{W}(R)$, which, as detailed in Section 4.3.2, is based on the barrier to dissociation on the S_1 adiabatic surface being a consequence of strong vibronic coupling of the $\tilde{A}(3s)$ and $\tilde{D}(4s)$ states.

Starting from the D_{3h} reference point, movement along a single N-H dissociation coordinate will bring the ammonia molecule into coincidence with a geometry of C_{2v} symmetry. The $\tilde{A}(3s)$ state generates the A_2'' irrep of the D_{3h} point group, and the A_2'' irrep correlates with the B_1 irrep of the C_{2v} point group. Thus for an element W_{2i} $(i \neq 2)$ of the diabatic potential matrix to be nonzero at extended N-H bond lengths, it must be that the state $|\Phi_i\rangle$ generates an irrep of the D_{3h} point group that correlates with the B_1 irrep of the C_{2v} point group. Of the states considered here, only the $\tilde{B}_z(3p_z)$, $\tilde{D}(4s)$ and $\tilde{E}_z(4p_z)$ states generate the B_1 irrep of the C_{2v} point group. Furthermore, we note that adiabatic potentials found in other molecules that are quasi-bound with respect to a heteroatom-hydride bond have been successfully modelled by taking them to correspond to avoided crossings between an upper, dissociative diabatic state and a lower, bound diabatic state [12, 69, 70]. As such we are directed to look for a state that has a significantly large negative gradient with respect to the N-H stretching coordinate R at the D_{3h} reference point, at which our adiabatic and diabatic states are taken to be equivalent. The gradients of the $\tilde{B}_z(3p_z)$, $\tilde{D}(4s)$ and $\tilde{E}_z(4p_z)$ states with respect to R

calculated at the MCQDPT2(4,11)/aug level are +3.02, -4.57, and +1.21 eV/a.u. Additionally, the $\tilde{A}(3s)$ and $\tilde{D}(4s)$ states are found to be strongly coupled with respect to R, with the nonadiabatic coupling term $\tau_{R,2,6}$ calculated at the CAS(4,11)/aug level taking a value of -5.68 eV/a.u. For these reasons we take the coupling of the $\tilde{A}(3s)$ and $\tilde{D}(4s)$ states to be responsible for the formation of barrier to dissociation on the S_1 adiabatic potential.

4.3.9 Quantum Dynamics Simulations Using the Two-Mode Model

The Parameterised Model Potential

The two-dimensional model potential $\boldsymbol{W}(\boldsymbol{q})$ was parameterised *via* fitting a total of 111 parameters non-zero by symmetry to 431 calculated adiabatic energies. An unweighted (weighted) RMSD of the model and calculated adiabatic energies of 0.073 (0.028) eV was attained, indicating that the model potential is capable of faithfully reproducing the calculated adiabatic potentials in the regions of nuclear configuration space considered.

Shown in Figure 4.4 are the elements of the model diabatic and adiabatic potential matrices along the N-H dissociation coordinate R. Overall, good agreement of the model and calculated adiabatic potentials is found. The assumption set forth in Section 4.3.8 that the coupling of the $\tilde{A}(3s)$ and $\tilde{D}(4s)$ states is responsible for the formation of the barrier to dissociation on the S_1 adiabatic potential is further supported through the ability of the simple model potential $\boldsymbol{W}(R)$, that is based on this assumption, to reproduce accurately the calculated adiabatic potentials along the N-H dissociation coordinate.

The model and calculated adiabatic and diabatic potentials along the inversion coordinate ϕ are displayed in Figure 4.5. Given in Table 4.4 are the values of the fitted linear interstate coupling constants $\lambda^{(i,j)}$ that enter into

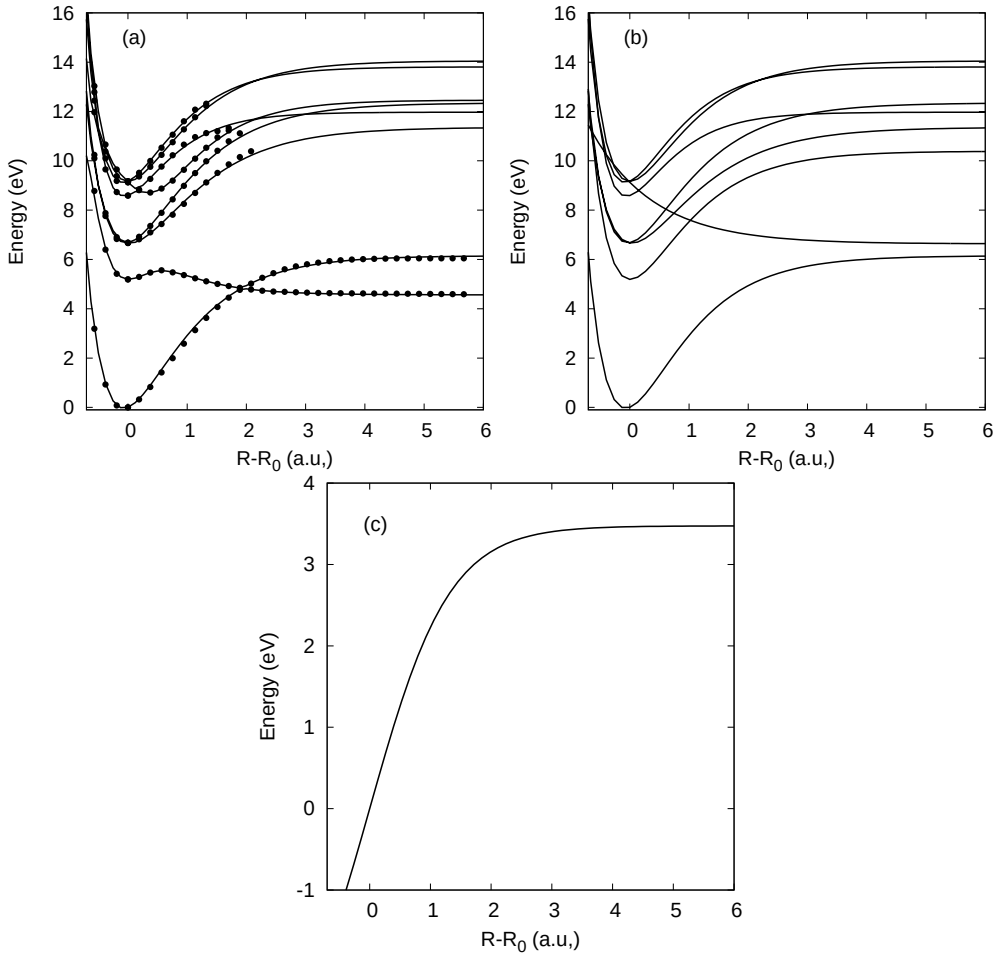

Fig. 4.4: Model and calculated potentials along the N-H dissociation coordinate R: (a) Model (lines) and MCQDPT2(4,11)/aug (points) adiabatic potentials; (b) Model diabatic potentials, and; (c) Model diabatic coupling between the $\tilde{A}(3s)$ and $\tilde{D}(4s)$ states.

Table 4.4: Linear interstate coupling coefficients $\lambda^{(i,j)}$ entering into the expansion of the two-dimensional model potential $\boldsymbol{W}(\boldsymbol{q})$. All values are given in eV/radian.

i, j	$\lambda^{(i,j)}$
1, 2	-1.1025
1, 4	0.9697
1, 6	1.0920
1, 8	1.2921
2, 5	0.2371
4, 5	-0.1916
5, 6	-0.0046
5, 8	0.5414

the off-diagonal elements $W_{ij}(\phi)$ of the model potential. It is found that the ground $\tilde{X}$ state is strongly coupled to the $\tilde{A}(3s)$, $\tilde{B}_z(3p_z)$, $\tilde{D}(4s)$ and $\tilde{E}_z(3p_z)$ states by ϕ. Further, it is this coupling of the ground and excited states by the inversion coordinate that is found to be responsible for the formation of the barrier to inversion on the ground state adiabatic potential. If only the $\tilde{X}$ and $\tilde{A}(3s)$ states are taken to be coupled, then this is not the case. To see this, we consider the block diagonalisation of the diabatic potential as outlined in Section 4.3.5. The thus block-diagonalised ground state potential is shown in Figure 4.5 (c) alongside the corresponding model diabatic and adiabatic potentials. It can be seen that only *via* the inclusion of the coupling of the $\tilde{X}$ and $\tilde{A}(3s)$ states to the higher-lying manifold of electronic states is the origin of the barrier to inversion entirely due to vibronic coupling of the ground state to its orthogonal complement.

Wavepacket Dynamics Following Excitation to the $\tilde{A}(3s)$ State

Owing to its low dimensionality, standard wavepacket propagations employing the full primitive grid were used for the two-dimensional model. For both degrees of freedom, R and ϕ, exponential DVRs were used. For the N-H dissociation coordinate R, a grid of 111 points from -1.0 to 10.0 a.u. was used.

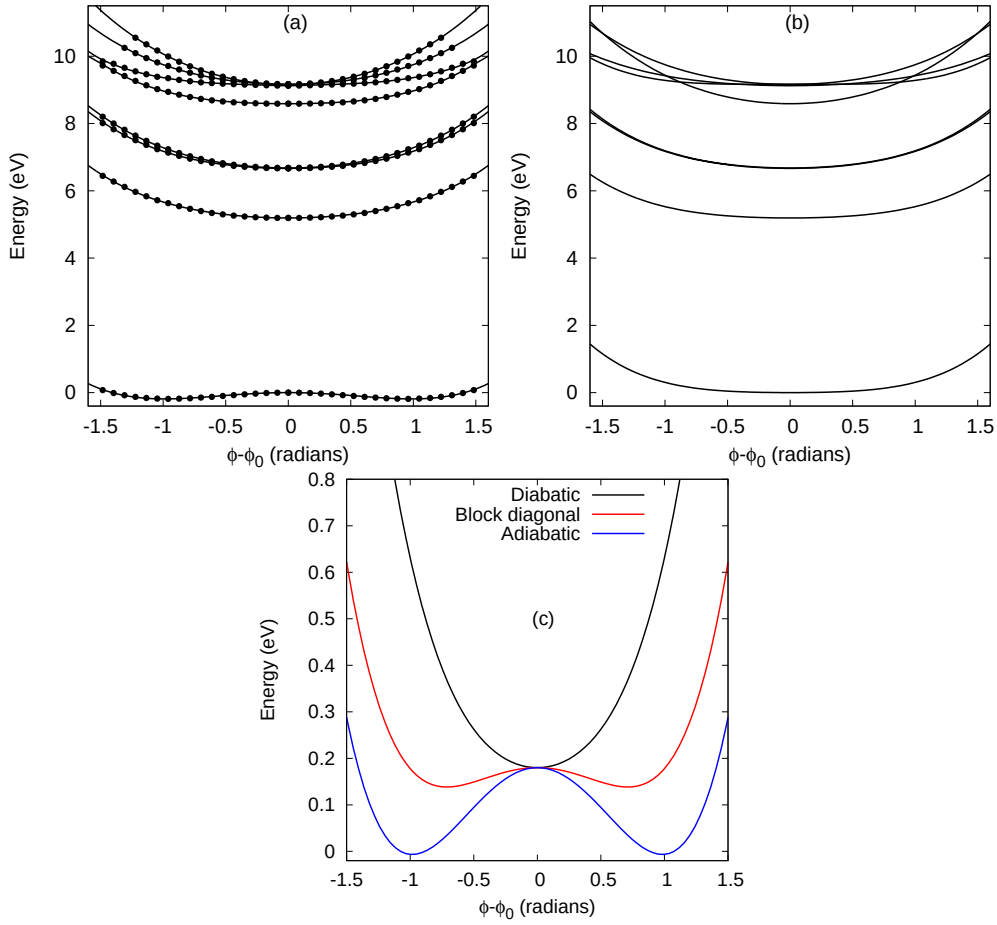

Fig. 4.5: Model and calculated potentials along the inversion coordinate ϕ: (a) Model (lines) and MCQDPT2(4,11)/aug (points) adiabatic potentials; (b) Model diabatic potentials, and; (c) A comparison of the model diabatic, block-diagonalised, and adiabatic ground state potentials.

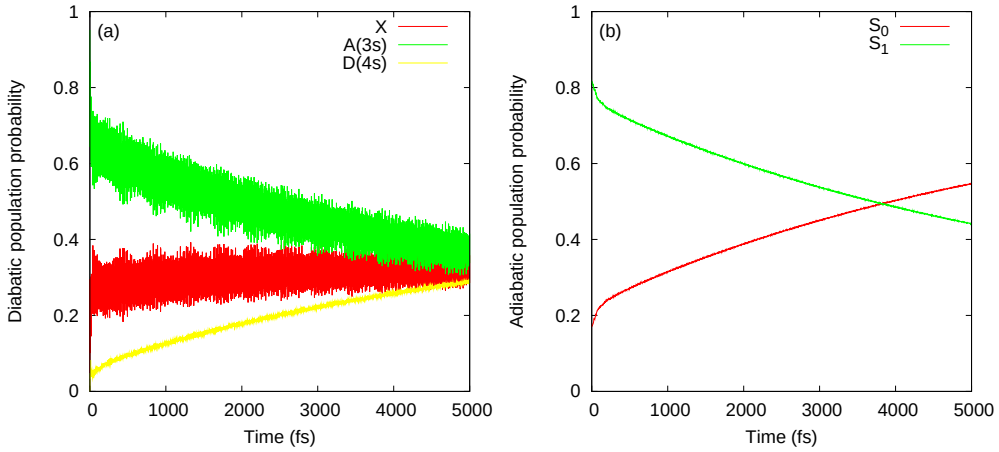

Fig. 4.6: State population probabilities following vertical excitation to the $\tilde{A}(3s)$ state calculated using the diabatic representation of the nuclear wavefunction and the two-dimensional potential $\boldsymbol{W}(\boldsymbol{q})$. (a) Diabatic state populations, and; (b) adiabatic state populations.

For the inversion coordinate ϕ, a grid of 151 points from -3.1 to 3.1 radians was used. All wavepacket propagations were performed for 5000 fs.

Shown in Figure 4.6 are the state populations in the diabatic representation calculated following vertical excitation to the $\tilde{A}(3s)$ state. A strongly driven oscillatory transfer of population between the initially excited $\tilde{A}(3s)$ state and the ground state is found to occur throughout the duration of the simulation. This is presumably a consequence of two factors: (i) the strong coupling of the $\tilde{X}$ and $\tilde{A}(3s)$ states that exits with respect to the inversion mode ϕ, and; (ii) the choice of the planar D_{3h} reference geometry, which results in the value of the diabatic potential element W_{12} being already large in magnitude at the geometries corresponding to the adiabatic ground state minima. Additionally, a slow rise in the population of the $\tilde{D}(4s)$ diabatic state is found to occur, resulting in a slow monotonic rise in the probability of N-H dissociation, as is illustrated in Figure 4.7 (a). In addition to the dissociation on the purely repulsive $\tilde{D}(4s)$ state surface, both the $\tilde{X}$ and $\tilde{A}(3s)$ state dissociation channels are found to be open, a consequence of the strong

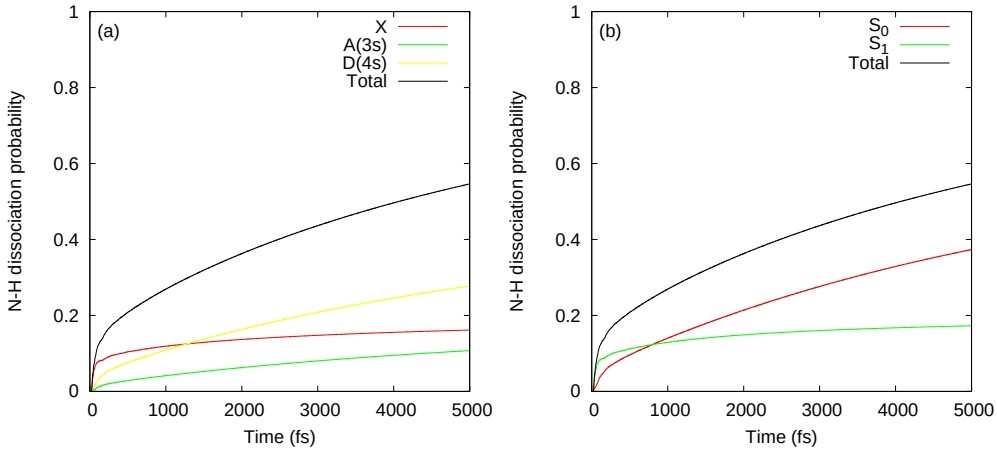

Fig. 4.7: State-resolved N-H dissociation probabilities following vertical excitation to the $\tilde{A}(3s)$ state calculated using the diabatic representation of the nuclear wavefunction and the two-dimensional potential $\boldsymbol{W}(\boldsymbol{q})$. (a) Probabilities of dissociation in the diabatic states, and; (b) probabilities of dissociation in the adiabatic states.

coupling by ϕ of the $\tilde{X}$ and $\tilde{D}(4s)$ states and by R of the $\tilde{A}(3s)$ and $\tilde{D}(4s)$ states.

In order to render the results discussed here more intuitive, we consider the transformation of the nuclear wavefunction to the adiabatic representation. As the standard wavepacket method employing the full primitive grid is used for the two-dimensional model, the elements of the projectors onto the adiabatic states, $\boldsymbol{P}^{(d)}_{a,i}$, can be, and were used directly in the form given in Equation 4.65. The adiabatic state populations calculated using the projected wavefunctions $\boldsymbol{P}^{(d)}_{a,i}|\boldsymbol{\Psi}^{(d)}\rangle$ are shown in Figure 4.6 (b). We note that due to the diabatic nature of the vertical excitation operator $O^{(2)}_{v}$ used, the initial wavepacket corresponds to a linear combination of both the S_0 and S_1 states. The depopulation of the S_1 state following excitation is found to be hindered, a consequence of the inability of the wavepacket to traverse directly the barrier to the conical intersection with the S_0 state. In turn, the hindrance of dissociation can be seen to be a consequence of the modulation of the barrier to dissociation on the S_1 adiabatic state surface by the inver-

sion mode ϕ, with the barrier height being increased at geometries away from the planar arrangement of the molecule. As the initially excited wavepacket is displaced to the repulsive walls of the S_1 state potential, motion along the coordinate ϕ is driven, resulting in a frustration of N-H dissociation by virtue of the evolving wavepacket needing to sample regions of configuration space proximate to the D_{3h} S_1 minimum in order for dissociation to proceed unhindered.

Shown in Figure 4.7 (b) are the time-cumulated probabilities of N-H dissociation in the adiabatic representation. The branching ratio between the two adiabatic state dissociation channels,

$$B_{1,2}^{(d)} = \frac{f_{a,1}^{(d)}}{f_{a,2}^{(d)}}, \tag{4.75}$$

$$f_{a,i}^{(d)} = \int_0^T dt F_{a,i}^{(d)}(t), \tag{4.76}$$

is calculated to take a value of 2.16, corresponding to a dominance of diabatic dissociation. This is in good agreement with the work of Giri *et al.* [59], who reported a branching ratio of 1.98 being obtained from two-state, two-dimensional quantum dynamics. It is found that the preponderance of the dissociation occurring on the S_1 potential occurs within the first 200 fs following excitation.

Shown in Figures 4.8 (a) and 4.8 (b) are, respectively, the state populations in the intermediate representation along with the adiabatic state populations obtained from the projected intermediate wavefunctions $\boldsymbol{P}_{a,i}^{(bd)}|\boldsymbol{\Psi}^{(bd)}\rangle$, both calculated following excitation to the $\tilde{A}(3s)$ state. For reference, the adiabatic state populations calculated from the diabatic representation of the wavepacket are also shown in Figure 4.8 (b). It is found that the vibronic coupling terms neglected upon making the transition from the diabatic rep-

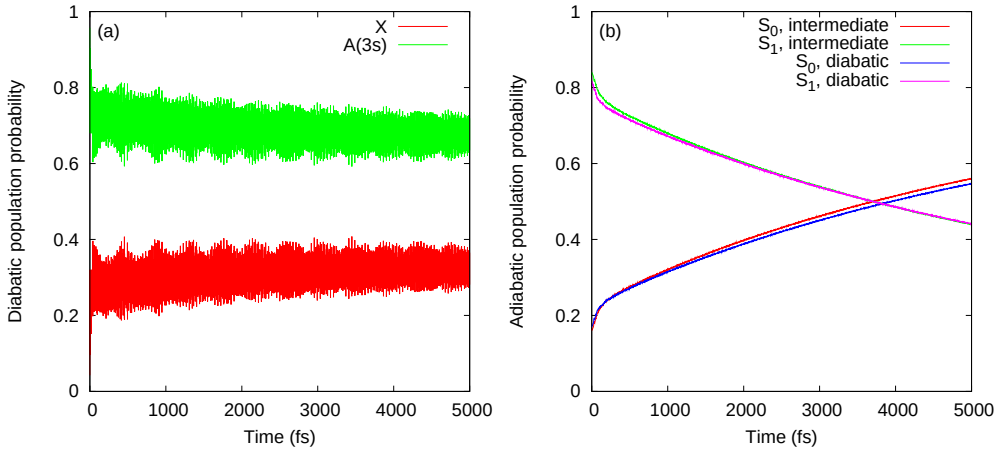

Fig. 4.8: State population probabilities calculated following excitation to the $\tilde{A}(3s)$ state: (a) State population probabilities in the intermediate representation, and; (b) adiabatic populations calculated from both the diabatic and intermediate representations of the nuclear wavepacket.

resentation to the intermediate representation has no significant effect on evolution of the wavepacket in the adiabatic representation. To see this in a quantitative manner, we consider the RMSD of the adiabatic populations calculated using the two representations:

$$\mathcal{D} = \left\{ \frac{1}{2T} \sum_{i=1}^{2} \int_0^T dt \left(p_{a,i}^{(d)} - p_{a,i}^{(bd)} \right)^2 \right\}^{\frac{1}{2}}, \tag{4.77}$$

where T denotes the final propagation time of 5000 fs. $\mathcal{D}$ is found to take a value of 0.0099, that is, the adiabatic populations calculated using the diabatic and intermediate representations differ on average by only $\sim$1%. Finally, we note that the calculated branching ratio

$$B_{1,2}^{(bd)} = \frac{\int_0^T dt F_{a,1}^{(bd)}(t)}{\int_0^T dt F_{a,2}^{(bd)}(t)}, \tag{4.78}$$

takes a value of 2.76, implying that the vibronic coupling terms neglected in the intermediate representation lead to a slight decrease in the propensity for adiabatic dissociation to occur.

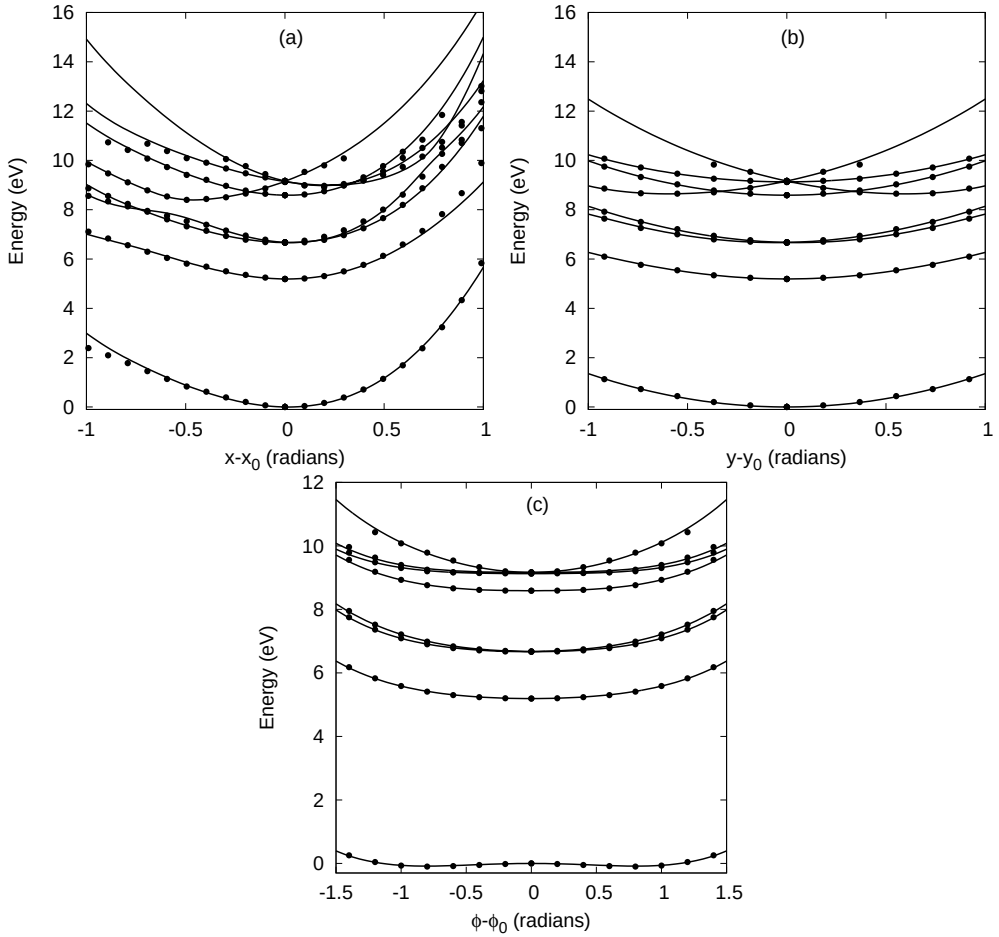

Fig. 4.9: Model (lines) and calculated (points) potentials along the nuclear degrees of freedom entering into the four-dimensional model. (a) Adiabatic potentials along x. (b) Adiabatic potentials along y (c) Adiabatic potentials along φ.

4.3.10 Quantum Dynamics Simulations Using the Four-Mode Model

The Parameterised Model Potential

The four-dimensional model potential $\boldsymbol{W}(\tilde{\boldsymbol{r}})$ was parameterised by fitting a total of 303 parameters non-zero by symmetry to 2424 calculated adiabatic energies. A weighted/unweighted RMSD of the model and calculated adiabatic energies of 0.45/0.16 eV was attained.

The model potentials along the dissociative degree of freedom R_1 are essentially identical, apart from a shift of the origin, to those of the two-

Table 4.5: Linear interstate coupling coefficients $\lambda_\alpha^{(i,j)}$; $\alpha = x, y, \varphi$, entering into the expansion of the four-dimensional model potential $\boldsymbol{W}(\tilde{\boldsymbol{r}})$. All values are given in eV/radian.

α	i	j	$\lambda_\alpha^{(i,j)}$
x	1	5	-3.2017
x	2	4	-1.4856
x	2	6	0.4807
x	2	8	0.7762
x	3	7	0.8528
x	4	6	0.1057
x	4	8	0.4745
x	6	8	2.0120
y	2	3	0.7843
y	2	7	0.5774
y	3	4	-0.1593
y	3	6	0.7799
y	3	8	0.1684
y	4	7	0.5367
y	6	7	0.4668
y	7	8	1.6533
φ	1	2	-0.9910
φ	1	4	1.0306
φ	1	6	0.2810
φ	1	8	-1.7951
φ	2	5	-0.6232
φ	4	5	-0.2138
φ	5	6	0.0808
φ	5	8	-0.5275

Table 4.6: Quadratic interstate coupling coefficients $\mu_{\alpha\beta}^{(i,j)}$ entering into the expansion of the four-dimensional model potential $\boldsymbol{W}(\tilde{\boldsymbol{r}})$. All values are given in eV/radian^2.

α	β	i	j	$\mu_{\alpha\beta}^{(i,j)}$
x	x	1	5	-1.9031
x	x	2	4	-0.7661
x	x	2	6	-0.9282
x	x	2	8	0.4167
x	x	3	7	-1.3561
x	x	4	6	-1.1829
x	x	4	8	2.0129
x	x	6	8	0.3182
x	y	3	4	0.6081
x	y	7	8	3.4888

dimensional potential defined with respect to R, as discussed in Section 4.3.9, and are not discussed further here. The adiabatic potentials along the angular degrees of freedom x, y, and φ are shown in Figure 4.9. Overall good agreement between the calculated and model adiabatic energies is found to be provided by the simple model potential used. Displayed in Tables 4.5 and 4.6 are, respectively, the values of the fitted first- and second-order interstate coupling coefficients. Significant interstate coupling coefficients are found to exist to couple either directly or indirectly all pairs of states considered. Of particular interest is that the $\tilde{A}(3s)$ and $\tilde{B}_z(3p_z)$ states are found to be strongly coupled to both first- and second-orders by the planar angle x. Significant coupling to both first- and second-order of the $\tilde{A}(3s)$ and $\tilde{D}(4s)$ states is also found to exist. Relatively weak coupling of the degenerate states $\tilde{B}_y(3p_y)$ and $\tilde{B}_z(3p_z)$ states by the pair of Jahn-Teller active modes x and y is found to exist, the manifestation of which can be seen in the only modest splitting of the corresponding adiabatic energies by the degrees of freedom x and y. In contrast the pair of degenerate states $\tilde{E}_y(3p_y)$ and $\tilde{E}_z(3p_z)$ are found to be strongly coupled by the degrees of freedom x and y.

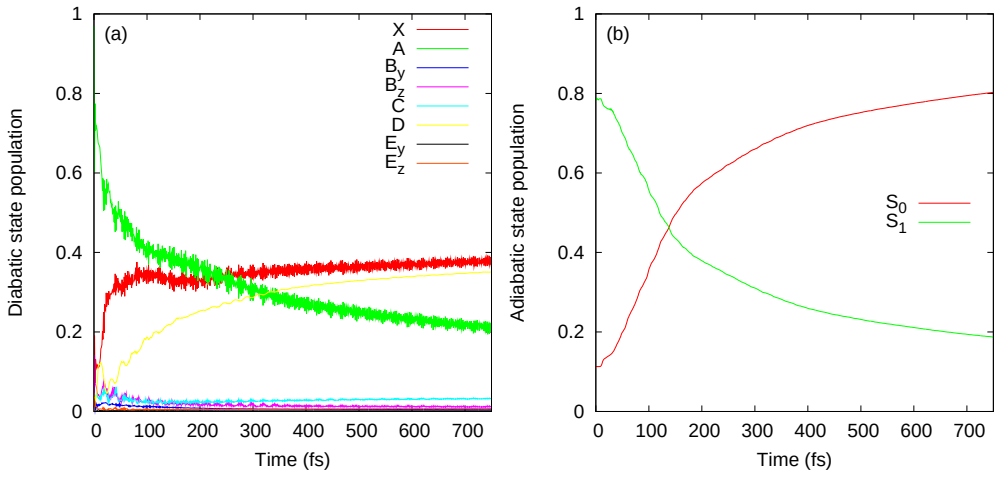

Fig. 4.10: State population probabilities following vertical excitation to the $\tilde{A}(3s)$ state calculated using the diabatic representation of the nuclear wavefunction and the four-dimensional potential $\boldsymbol{W}(\boldsymbol{r})$. (a) Diabatic state populations, and; (b) adiabatic state populations.

Wavepacket Dynamics Following Excitation to the $\tilde{A}(3s)$ State

Four-mode, eight-state wavepacket propagations using both the diabatic and intermediate representations of the nuclear wavepacket were performed using the MCTDH method. Propagation times of 750 fs were used in each case, and all details of the calculations are displayed in Table 4.7.

Shown in Figure 4.10 (a) are the diabatic state populations calculated following excitation to the $\tilde{A}(3s)$ state. As in the case of the two-dimensional model discussed above, significant population of only the diabatic states $\tilde{X}$, $\tilde{A}(3s)$ and $\tilde{D}(4s)$ is found to occur. Correspondingly, as shown in Figure 4.11 (a), dissociation is found to occur in all these three diabatic states, with the majority of the dissociating wavepacket reaching the dissociation limit in the $\tilde{D}(4s)$ state. Illustrated in Figure 4.10 (b) are the adiabatic populations, and in Figure 4.11 (b) the time-cumulated probabilities of N-H dissociation in the adiabatic states, both calculated from the projected diabatic wavefunctions $\boldsymbol{P}_{a,i}^{(d)}|\boldsymbol{\Psi}^{(d)}\rangle$. We note that high expansion orders were required to reproduce

Table 4.7: Computational details of the wavepacket propagations corresponding to excitation to the $\tilde{A}(3s)$ state using the diabatic and intermediate representations. The DVR types exp and sin correspond to exponential and sine DVRs, respectively. N_i, N_j are the number of primitive DVR functions used to describe each particle. n_i are the number of single-particle functions used for each state.

Diabatic Representation	Particle	DVR type	N_i, N_j	Range	n_1, n_2, ..., n_8
	R	exp	81	[-0.8,10.0]	21, 17, 11, 15, 16, 20, 7, 4
	ζ_1, ζ_2	sin	19, 19	[-0.98,0.98], [-0.98,0.98]	17, 17, 12, 15, 13, 18, 7, 4
	φ	exp	51	[-2.5,2.5]	14, 14, 10, 12, 12, 16, 7, 4
Intermediate Representation	Particle	DVR type	N_i, N_j	Range	n_1, n_2
	R	exp	81	[-0.8,10.0]	20, 20
	ζ_1, ζ_2	sin	19, 19	[-0.98,0.98], [-0.98,0.98]	23, 20
	φ	exp	51	[-2.5,2.5]	20, 20

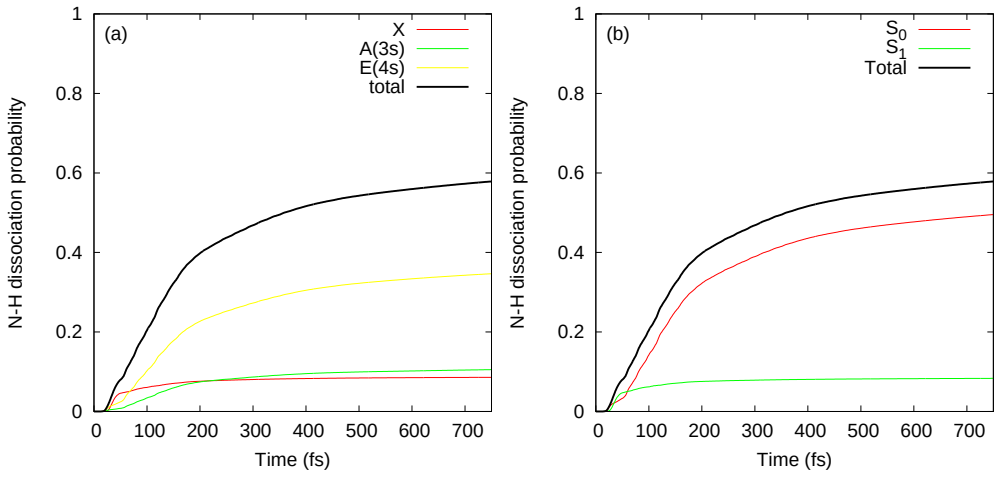

Fig. 4.11: State-resolved N-H dissociation probabilities following vertical excitation to the $\tilde{A}(3s)$ state calculated using the eight-state diabatic representation of the nuclear wavefunction and the four-dimensional potential $\boldsymbol{W}(\boldsymbol{r})$. (a) Probabilities of dissociation in the diabatic states, and; (b) probabilities of dissociation in the adiabatic states.

via the potfit method the elements of the projectors $\boldsymbol{P}_{a,i}^{(d)}$, owing to the discontinuous nature of these functions. A total of 600 terms were admitted into the direct product expansion of each element, a realistic limit considering the linear scaling of the computational effort of the calculation of the expectation values $\langle \boldsymbol{\Psi}^{(d)}(t)|\boldsymbol{O}|\boldsymbol{\Psi}^{(d)}(t)\rangle$ with the number of terms entering into the operator $\boldsymbol{O}$. We note, however, that even with the large expansion orders used the accuracy of the fitted projectors is limited. It is not straightforward to gauge the accuracy of the fitted projectors in a meaningful manner by simply considering the RMSD of the true and fitted elements over all the grid points used. The most meaningful analysis would consist of the calculation of an RMSD weighted by the time-averaged modulus square of the wavepacket at the grid points, which is, however, somewhat complicated. We instead simply consider the requirement that an expectation value be invariant with respect to a unitary transformation of the basis used to represent the wavefunction, and note that the RMSD of the total probabilities of dissociation calculated

using the diabatic and projected wavefunctions,

$$\left\{ \frac{1}{T} \int_0^T dt \left(\int_0^t dt' \left\langle \boldsymbol{\Psi}^{(d)}(t') \middle| \boldsymbol{F} \middle| \boldsymbol{\Psi}^{(d)}(t') \right\rangle - \sum_{i=1}^{N} \left\langle \boldsymbol{\Psi}^{(d)}(t') \middle| \boldsymbol{P}_{a,i}^{(d)} \boldsymbol{F} \boldsymbol{P}_{a,i}^{(d)} \middle| \boldsymbol{\Psi}^{(d)}(t') \right\rangle \right)^2 \right\}^{\frac{1}{2}}, \tag{4.79}$$

takes a value of 0.016. That is, on average the two quantities differ by only 1.6%, which we take to be satisfactory.

It is found that the rate of depopulation of the S_1 state is significantly higher, by approximately an order of magnitude, than that furnished by the two-state model, highlighting the limited use reduced dimensionality models. We note the neglect here of two of the three N-H dissociation coordinates undoubtedly leads to an underestimation of the rate of dissociation yielded by the four-mode model. The construction of a five- or six-dimensional model, however, is not possible here given our requirement of the construction of approximate fitted projectors, the number of terms entering into which scales exponentially with the number of MCTDH particles. The branching ratio $B_{1,2}^{(bd)}$ between the two adiabatic dissociation channels takes a value of 5.94. This result is in agreement with the quantum dynamics calculations of Giri *et al.*, who report a decrease in the amount of adiabatic dissociation seen upon increasing the dimensionality of the model used.

We now consider the effect of the coupling of the $\tilde{X}$ and $\tilde{A}(3s)$ states to their orthogonal complement on the dynamics described using the four-mode model. Shown in Figure 4.12 are the adiabatic state populations and time-cumulated probabilities of N-H dissociation calculated from the intermediate representation of the wavepacket. In contrast with the two-mode model, it is not meaningful to consider the RMSD of the adiabatic populations calculated from the diabatic and intermediate representations of the wavepacket as the stronger coupling of the $\tilde{X}$ and $\tilde{A}(3s)$ states to their orthogonal complement

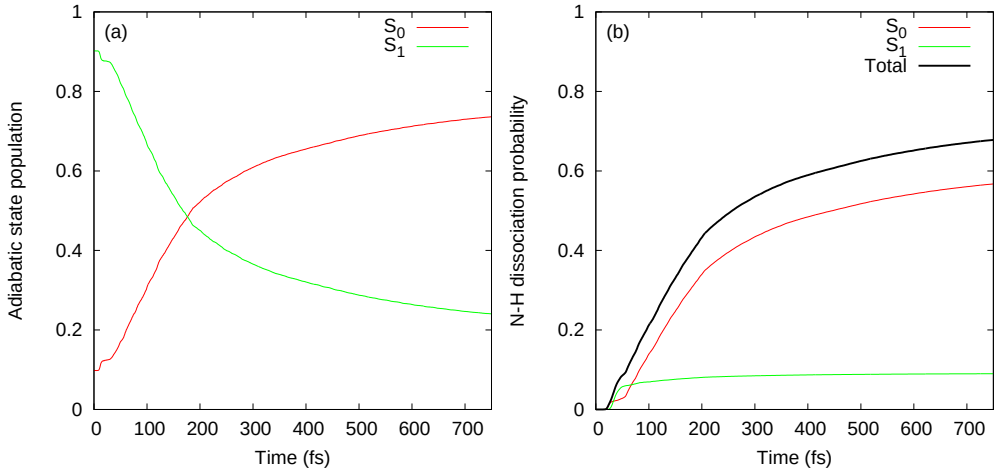

Fig. 4.12: State population probabilities and probabilities of dissociation following vertical excitation to the $\tilde{A}(3s)$ state calculated using the two-state intermediate representation of the nuclear wavefunction and the four-dimensional potential $\boldsymbol{W}(\boldsymbol{r})$: (a) Adiabtic state population probabilities, and; (b) time-cumulated N-H dissociation probabilities.

in the four-mode model and the diabatic nature of the excitation operator used results in markedly different initial adiabatic state populations in the two representations. Instead we focus on the time-cumulated probabilities of dissociation. It is found that the total probability of dissociation by 750 fs in the diabatic and intermediate representations are, respectively, 0.578 and 0.678, implying that dissociation is hindered by the coupling of the $\tilde{X}$ and $\tilde{A}(3s)$ states to their orthogonal complement. By comparison, the rates of dissociation in the two representations obtained using the two-mode model deviate insignificantly. We thus see that the increased hindrance of dissociation in the diabatic representation is predominantly affected by the planar angles ζ_1 and ζ_2. The branching ratio between the two adiabatic dissociation channels calculated from the intermediate representation, $B_{12}^{(bd)}$, is 6.31. Thus, as in the case of the two-mode model, the amount of adiabatic dissociation is increased slightly in the diabatic representation relative to that in the intermediate representation. From the above considerations we

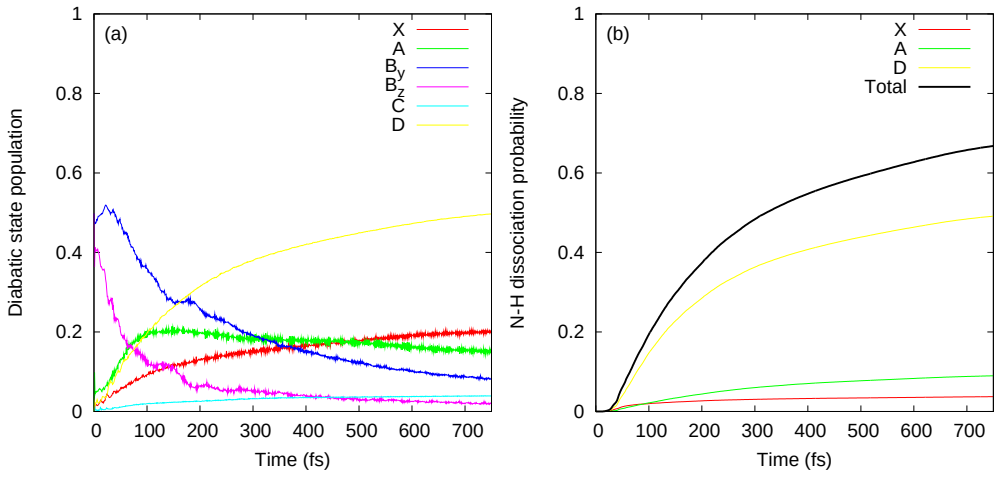

Fig. 4.13: State population probabilities and time-cumulated probabilities of dissociation in the diabatic representation following excitation to both components of the doubly-degenerate $\tilde{B}(3p)$ state calculated using the eight-state, four-mode model: (a) diabatic population probabilities, and; (b) time-cumulated probabilities of dissociation in the diabatic states.

conclude that although the $\tilde{X}$ and $\tilde{A}(3s)$ states do not constitute a Hilbert subspace, the effect on the dynamics following excitation to the $\tilde{A}(3s)$ state of the coupling of these two states to their orthogonal complement is not particularly significant.

Dynamics Following Excitation to the $\tilde{B}(3p)$ State

Neither the two components of the $\tilde{B}(3p)$ state are directly coupled to the $\tilde{A}$ state by the degrees of freedom R and ϕ, and so the two-mode model cannot be used to study the dynamics of ammonia excited to the $\tilde{B}(3p)$ state. Through the inclusion of the planar angles ζ_1 and ζ_2, however, the coupling between both components of the $\tilde{B}(3p)$ state and the $\tilde{A}$ state is included in the four-mode model.

Both components of the $\tilde{B}(3p)$ state are found to be bright, with oscillator strengths for both the $\tilde{B}_y \leftarrow \tilde{X}$ and $\tilde{B}_z \leftarrow \tilde{X}$ transitions of 0.0083 being furnished by MRCI(8,7)/aug-cc-pVDZ calculations. These values are to be compared to the value of 0.0752 for the $\tilde{A} \leftarrow \tilde{X}$ transition calculated at the

same level of theory. As such, the initial state used to study the dynamics of ammonia following excitation to its $\tilde{B}(3p)$ state was chosen as the projection of the ground state onto both components of the $\tilde{B}(3p)$ state:

$$|\Psi(t=0)\rangle = \frac{1}{2}\sum_{i=3}^{4}\{|1\rangle\langle i| + h.c.\}\,|\Psi_g\rangle, \tag{4.80}$$

with $|\Psi_g\rangle$ denoting the ground vibrational eigenstate.

Shown in Figure 4.13 (a) are the calculated diababatic state populations, and in Figure 4.13 (b) the time-cumulated probabilities of dissociation in the diabatic states. We first note that although Figure 4.13 (a) may suggest that the initial population of the $\tilde{B}_z(3p_z)$ state is lower than that of the $\tilde{B}_y(3p_y)$ state, this is not the case: the strong diabatic coupling of the $\tilde{B}_z(3p_z)$ and $\tilde{A}(3s)$ states that exists at the FC point results in an initial loss of ∼10% of the $\tilde{B}_z(3p_z)$ within the first 2 fs. Population from both the $B_y(3p_y)$ and $B_z(3p_z)$ states is found to relax relatively efficiently to the $\tilde{A}(3s)$ state, whereupon the strong coupling of the $\tilde{A}(3s)$ and $\tilde{D}(4s)$ states results in transfer to, and dissociation in, the latter state. By 750 fs the total calculated probability of N-H dissociation stands at 0.67, with dissociation proceeding predominantly in the $\tilde{D}(4s)$ state. The rate of depopulation of the $\tilde{B}_z(3p_z)$ state is found to be markedly faster than that of the $\tilde{B}_y(3p_y)$ state, a consequence of the stronger coupling of the $\tilde{A}(3s)$ state to the $\tilde{B}_z(3p_z)$ state by the planar angles ζ_1 and ζ_2 than of the $\tilde{A}(3s)$ state to the $\tilde{B}_y(3p_y)$ state.

Shown in Figures 4.14 (a) and 4.14 (b) are, respectively, the state populations and time-cumulated probabilities of dissociation in the adiabatic representation calculated using the projected wavefunctions $\boldsymbol{P}^{(d)}_{a,i}|\boldsymbol{\Psi}^{(d)}\rangle$. The interpretation of the dynamics following excitation to the $\tilde{B}(3p)$ state is rather simple and somewhat more intuitive in the adiabatic representation: population is transferred from the initially excited $S_2(3p_y)$ and $S_2(3p_y)$ states

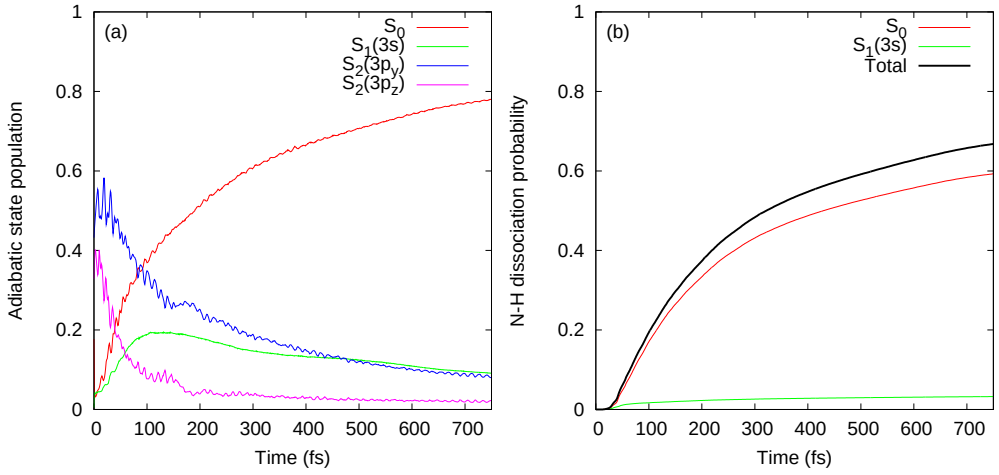

Fig. 4.14: State population probabilities and time-cumulated probabilities of dissociation in the adiabatic representation following excitation to both components of the doubly-degenerate $\tilde{B}(3p)$ state calculated using the eight-state, four-mode model and the projected wavefunctions $\boldsymbol{P}_{a,i}^{(d)}|\boldsymbol{\Psi}^{(d)}\rangle$: (a) adiabatic population probabilities, and; (b) time-cumulated probabilities of dissociation in the adiabatic states.

to the $S_1(3s)$ state, whereupon dissociation in the $S_1(3s)$ state is driven. The propensity for diabatic dissociation following excitation to the $\tilde{B}(3p)$ state is found to be significantly increased relative to the case of excitation to the $\tilde{A}(3s)$ state, with a branching ratio $B_{1,2}^{(d)}$ between the two adiabatic dissociation channels of 18.53 being obtained. As in the case of the diabatic representation, the $3p_z$ component of the S_2 state is found to undergo a more rapid depopulation than the $3p_y$ component.

To date, the most illuminating time-resolved experimental investigation of the dynamics of ammonia following excitation to its $\tilde{B}(3p)$ state have been the pump-probe ionisation measurements of Ritze *et al.* [71]. The reported timescale for relaxation from the $\tilde{B}(3p)$ state were found to be sensitive to the initial vibrational level excited with timescales of 9.5±1.5 ps and 2.5±0.5 ps being reported for excitation to the $2^4 4^1$ and $2^3 3^1$ vibrational levels of the $\tilde{B}(3p)$ state, respectively. The sub-picosecond timescales calculated here for relaxation from both components of the $\tilde{B}(3p)$ state are certainly not

comparable with the experimentally determined values of Ritze *et al.*, but this does not necessarily imply a contradiction. It is evident that the rate of relaxation from the $\tilde{B}(3p)$ state is highly sensitive to the initial vibrational state excited. The initial, vertically displaced, wavepacket used here is comprised of a linear combination of all vibrational states of the $\tilde{B}(3p)$ state and so it may be of little surprise that the rate of depopulation seen in this work is significantly different to those furnished by the excitation of particular vibrational levels.

4.3.11 Electronic Absorption Spectra

Absorption spectra corresponding to excitation to the $\tilde{A}$ and both components of the doubly-degenerate $\tilde{B}(3p)$ state were calculated from the Fourier transforms of the wavepacket autocorrelation functions obtained from wavepacket propagations starting in the respective states. As detailed in Section 4.3.7, the initial wavepackets used correspond to vertical excitation of an approximate linear combination of the two tunnel-split ground vibrational states. All calculations were performed using the diabatic representation of the wavefunction and the full eight-state model Hamiltonians, using both the two- and four-mode models.

Shown in Figure 4.15 are the calculated and experimental $\tilde{A}$ state spectra. Qualitatively, good agreement between the experimental [72] spectrum and the spectra calculated using both the two-dimensional and four-dimensional models is found. As has long been known to be true, both calculated spectra are dominated by a long progression in the umbrella inversion mode, reflecting the pyramidal-to-planar transition that accompanies excitation to the $\tilde{A}$ state. Displayed in Table 4.8 are the calculated and experimentally determined [25] peak positions and spacings. In order to afford an easier comparison to the experimental spectrum, both calculated spectra were shifted

Table 4.8: Comparison of the calculated and measured peak positions (E_n) and spacings (ΔE_n) in the $\tilde{A}(3s) \leftarrow \tilde{X}$ spectrum of ammonia. Both calculated spectra were shifted such that their origins coincided with that of the experimental spectrum. All energies are reported in units of cm^{-1}. † Ref. [25]

n	E_n (2D)	E_n (4D)	E_n (Exp.)†	ΔE (2D)	ΔE (4D)	ΔE (Exp.)†
0	46222	46222	46222			
1	46978	46920	47057	756	698	838
2	47777	47592	47964	799	672	907
3	48601	48293	48869	824	701	905
4	49426	49023	49783	825	730	914
5	50276	49850	50730	850	827	948
6	51125	50707	51656	849	857	926
7	52041	51544	52543	916	837	887
8	52955	52440	53496	914	896	953
9	53883	53375	54454	928	935	958
10	54862	54309	55380	979	934	926
11	55867	55234	56341	1005	945	961
12	56846	56179	57300	979	945	959
13	57845	57172	58285	999	993	985
14	-	58104	59308	-	932	1023

such that their origins were brought into coincidence with that of the experimental spectrum. Overall, particularly considering the simplicity of the model potentials used, good agreement between the calculated and experimental peak spacings is seen, particularly for the two-mode model for which the umbrella inversion is well approximated by the degree of freedom ϕ.

As noted in Section 4.3.10, both components of the doubly-degenerate $\tilde{B}(3p)$ state are bright and share the same oscillator strength. As such, a spectrum corresponding to excitation to the $\tilde{B}(3p)$ state was produced using the initial state

$$|\Psi(t=0)\rangle = \frac{1}{2}\sum_{i=3}^{4}\{|1\rangle\langle i| + h.c.\}\,\Theta_{inv}|\Psi_g\rangle, \tag{4.81}$$

with the quantities Θ_{inv} and $|\Psi_g\rangle$ being defined in Section 4.3.7. That is, the initial state used corresponds to a projection of the approximate linear

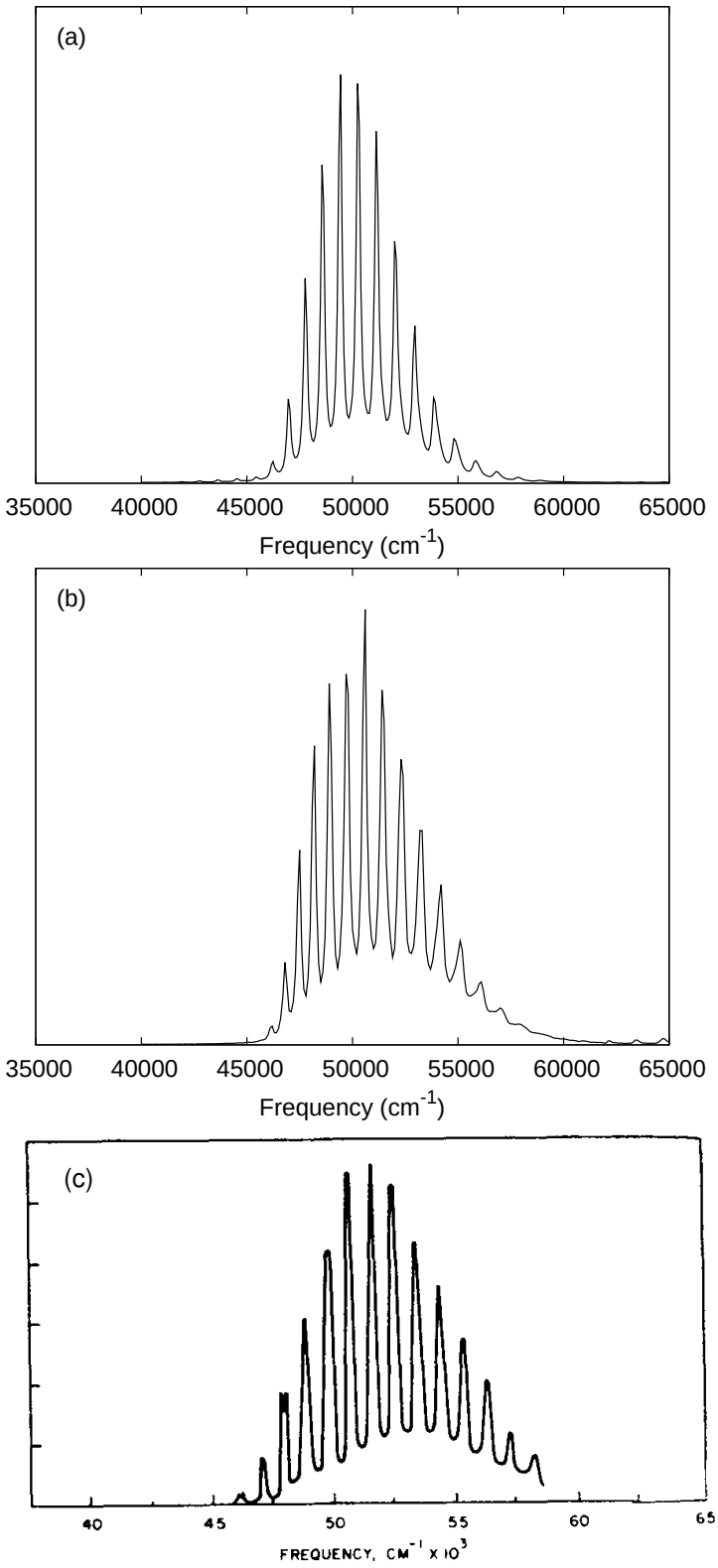

Fig. 4.15: Calculated and experimental spectra corresponding to excitation to the $\tilde{A}(3s)$ state: (a) Spectrum calculated using the two-mode model; (b) spectrum calculated using the four-mode model, and; (c) experimental spectrum adapted from [72].

combination of the two tunnel-split ground vibrational states onto both the $\tilde{B}_y(3p_y)$ and $\tilde{B}_z(3p_z)$ components of the $\tilde{B}(3p)$ state. Shown in Figure 4.16 is the resulting spectrum. As a result of the planar minimum energy geometries of both components of the $\tilde{B}(3p)$ state, the spectrum in dominated by a single progression in the inversion mode. Due to the strong first-order and second-order coupling of the $\tilde{A}(3s)$ and $\tilde{B}_y(3p_z)$ states, a small amount of the intensity seen in the $\tilde{A}(3s) \leftarrow \tilde{X}$ spectrum is found to arise due to borrowing of intensity from the $\tilde{B}(3p_z) \leftarrow \tilde{X}$ transition, as evidenced by intensity in the region 46000 to 57000 cm^{-1} seen in the $\tilde{B}(3p)$ state spectrum. Shown in Table 4.9 is a comparison of the positions and spacings of the peaks of the calculated and experimentally determined $\tilde{B}(3p)$ state spectrum. To aid comparison, the origin of the calculated spectrum was shifted so as to coincide with that of the experimental spectrum. Overall, reasonable agreement of the calculated and experimental spectra if found. The spacings of the peaks is, however, somewhat overestimated in the calculated spectrum. This is presumably a consequence of the the lack of correlation in the model potential of the angular degrees of freedom ζ_1, ζ_2, and φ in the $\tilde{B}_y(3p_y)$ and $\tilde{B}_z(3p_z)$ states.

4.4 Conclusions

In this chapter the effects of the non-adiabatic coupling of the $\tilde{A}(3s)$ and $\tilde{X}$ states of ammonia to a number of higher-lying electronic states have been assessed. By a consideration of the extended Curl equation, the $\tilde{X}$ and $\tilde{A}(3s)$ states have been shown to not constitute a Hilbert subspace at either the FC point or the S_1 minimum energy geometry. The construction of two eight-state model Hamiltonians lends further credence to this proposition, with their existing large diabatic coupling of the $\tilde{X}$ and/or $\tilde{A}(3s)$ states and their orthogonal complement with respect to all degrees of freedom. Most

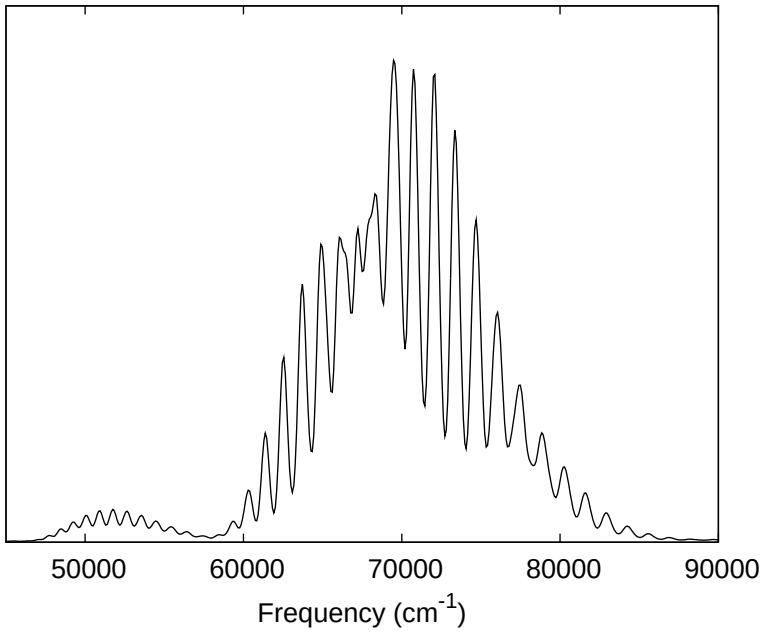

Fig. 4.16: Spectrum corresponding to vertical excitation to both the $\tilde{B}_y(3p_y)$ and $\tilde{B}_z(3p_z)$ components of the $\tilde{B}(3p)$ state calculated using the four-mode model.

Table 4.9: Comparison of the calculated and measured peak positions (E_n) and spacings (ΔE_n) in the $\tilde{B} \leftarrow \tilde{X}$ spectrum of ammonia. The calculated spectrum was shifted such that their origins coincided with that of the experimental spectrum. All calculated quantities were computed using the four-mode model. All energies are reported in units of cm^{-1}. †: Ref. [73], ‡: Ref. [74]

n	E_n (Calc.)	E_n (Exp.)	ΔE_n (Calc.)	ΔE_n (Exp.)
0	59225	59225†		
1	60315	60123†	1090	898
2	61382	61055†	1067	932
3	62451	62015†	1069	960
4	63721	62997†	1270	982
5	64925	63997†	1204	1000
6	66106	65015†	1181	1018
7	67128	66043†	1022	1028
8	68217	67083†	1089	1040
9	69512	-	1295	-
10	70739	69188‡	1227	-
11	72508	70250‡	1769	1062
12	73372	71315‡	864	1065
13	74712	72378‡	1340	1063
14	76029	73455‡	1317	1077
15	77483	74513‡	1454	1058

significantly, the origin of the barrier to dissociation on the S_1 adiabatic potential is posited to result from the strong coupling of the $\tilde{A}(3s)$ and $\tilde{D}(4s)$ states, with a simple model potential based upon this assumption being able to reproduce excellently the topologies of the corresponding adiabatic potentials along the N-H dissociation coordinate. Further validation of the model potentials constructed comes from their ability to reproduce well the experimentally determined $\tilde{A}(3s)$ spectrum.

Through the use of a transformation based on a block-diagonalisation of the model potentials constructed, an assessment of the effect on the dynamics of ammonia in its $\tilde{A}(3s)$ state of the non-adiabatic coupling of the $\tilde{X}$ and $\tilde{A}(3s)$ states to their orthogonal complement has been made. Although the $\tilde{X}$ and $\tilde{A}(3s)$ states manifestly do not constitute a Hilbert subspace, the effect of the neglect of the coupling of these two states to their orthogonal complement is found to be slight: the only discernible effect of the neglect of this coupling appears to be a small increase in the rate of dissociation. In turn, the source of this hindrance of dissociation is found to be the large coupling of the $\tilde{X}$ and $\tilde{A}(3s)$ states to their orthogonal states by the planar angular degrees of freedom.

Using an eight-state, four-mode model, the dynamics of ammonia following excitation to its $\tilde{B}(3p)$ state has been modelled. It is found that, similar to excitation to the $\tilde{A}(3s)$ state, the $\tilde{B}(3p)$ state spectrum is dominated by progressions in the inversion mode, with overlapping contributions from each of the two components of the state. Sub-picosecond timescales for relaxation from both components of the $\tilde{B}(3p)$ state to the $\tilde{A}$ state are found. Unfortunately, the results obtained here are not directly comparable with the sole time-resolved study performed to date of the relaxation of ammonia from its $\tilde{B}(3p)$ state [71], in which the system was prepared in specific vibrationally

excited states. It would, therefore, be desirable to extend the work performed here, in which vertical excitation to the $\tilde{B}(3p)$ state was used, to the preparation of specific initial vibrational states.

Chapter 5

3-Pyrroline

5.1 Introduction

3-pyrroline (C_4H_6NH, see Figure 5.1) is a partially saturated five-membered heterocyclic molecule related to pyrrole by saturation of the carbon atoms adjacent to the N-H bond. The effect of the partial saturation of the 3-pyrroline molecule is to render a planar ground state geometry, as adopted by the pyrrole molecule, inaccessible. Instead, the nitrogen atom lies out of the plane defined by the four carbon atoms, giving rise to two possible conformers, with the N-H bond lying either axial (AX) or equatorial (EQ), as illustrated in Figure 5.3. As shown schematically in Figure 5.4, the AX and EQ conformers are separated by only a modest energy, ΔE_{EQ-AX} =340 ±50 cm^{-1} [75], with the AX conformer lying lowest in energy. Under experimental conditions, 3-pyrroline is found to exist in both conformers [75–78]. The dynamics of 3-pyrroline following electronic excitation has seen little study to date, with a notable exception being the energy-resolved photofragment translational spectroscopy studies of Oliver *et al.* [75], who determined N-H dissociation to occur following excitation to the first excited state of 3-pyrroline.

The electronic spectrum of 3-pyrroline in the region 4.8 to 6.4 eV has previously been reported [75], and has been taken to correspond to excita-

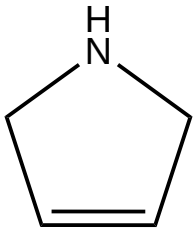

Fig. 5.1: Molecular structure of 3-pyrroline.

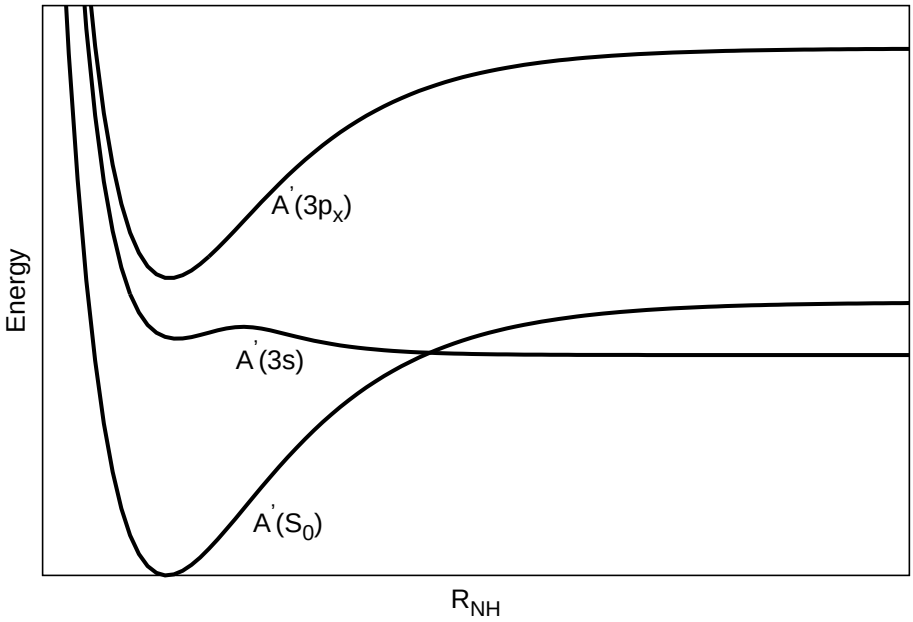

Fig. 5.2: Schematic adiabatic potentials corresponding to the $A^{'}(S_0)$, $A^{'}(3s)$, and $A^{'}(3p_x)$ states along the N-H dissociation coordinate for the planar arrangement of the C_4NH unit.

tion to two states: a lower-lying 3s-type Rydberg state and a higher-lying 3p-type Rydberg state. Using CASPT2 calculations, Oliver and co-workers determined that the $S_1(3s)$ state is quasi-bound with respect to N-H stretching and exhibits a conical intersection with the ground electronic state for a planar arrangement of the C_4NH unit at an elongated N-H bond length. The adiabatic potentials of these states along the N-H dissociation coordinate are shown schematically in Figure 5.2

In this chapter a model Hamiltonian is developed for use in quantum

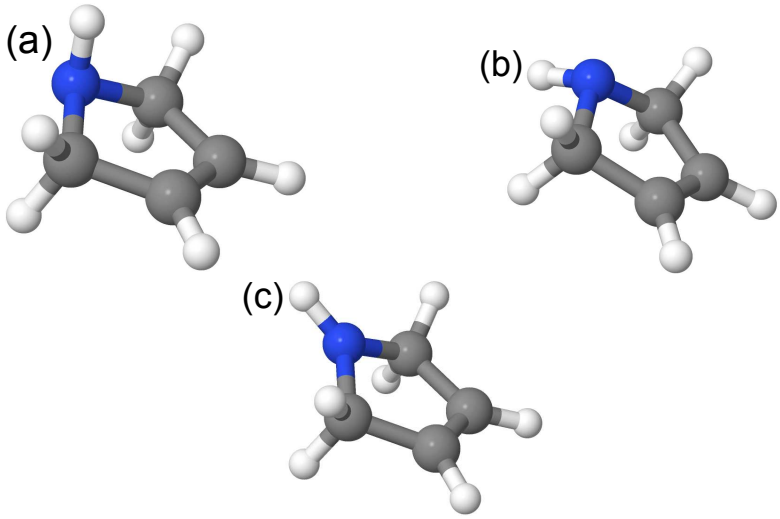

Fig. 5.3: (a) Geometry of the axial conformer; (b) Geometry of the equatorial conformer, and; (c) Geometry of the reference configuration.

dynamics simulations of the excitation of 3-pyrroline to its first two excited states. Through the use of the improved relaxation method, initial states corresponding to both the AX and EQ conformers are prepared, allowing for a conformer-resolved study of the photo-induced dynamics of 3-pyrroline.

5.2 Theoretical Framework

5.2.1 The Model Hamiltonian

We take the photoexcited 3-pyrroline molecule to correspond to a labile, dissociating hydrogen atom, denoted H_d, coupled to a 3-pyrrolinyl radical that undergoes only small displacements. As such, we choose to use as nuclear coordinates the spherical polar coordinates of H_d taken relative to the ground state equilibrium position of the nitrogen atom, denoted $\boldsymbol{r} = (R, \theta, \phi)$. Here, R denotes the distance of H_d from the nitrogen atom, and θ and ϕ the in- and out-of-plane angles of H_d relative to the C-N-C vertex. The remaining $3N - 9$ coordinates are taken to be the dimensionless mass- and frequency-scaled normal modes $\boldsymbol{Q}$ of the pyrrolinyl fragment at the Franck-Condon

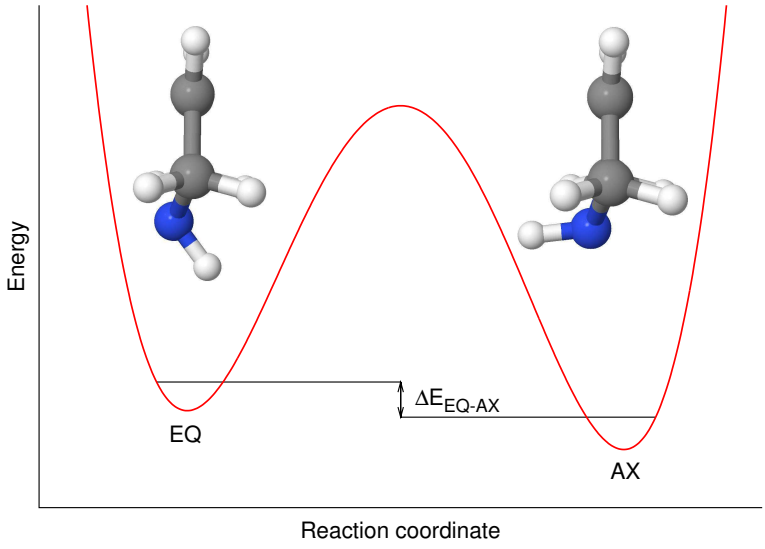

Fig. 5.4: Schematic of the ground state adiabatic potential along the reaction coordinate for interconversion of the EQ and AX conformers.

(FC) point. The potential matrix may thus be written

$$\boldsymbol{W}(\boldsymbol{Q},\boldsymbol{r}) = \boldsymbol{W}(\boldsymbol{Q}) + \boldsymbol{W}(\boldsymbol{r}) + \boldsymbol{W}^{int}(\boldsymbol{Q},\boldsymbol{r}), \tag{5.1}$$

where $\boldsymbol{W}(\boldsymbol{Q})$ and $\boldsymbol{W}(\boldsymbol{r})$ describe the diabatic potential with respect to the uncorrelated pyrrolinyl fragment and H_d nuclear degrees of freedom, respectively, and $\boldsymbol{W}^{int}(\boldsymbol{Q},\boldsymbol{r})$ describes the correlation of the two sets of nuclear degrees of freedom.

$\boldsymbol{W}(\boldsymbol{Q})$ is described using the vibronic coupling Hamiltonian of Köppel *et al* [19, 20]. That is, we take an expansion of $\boldsymbol{W}(\boldsymbol{Q})$ about a reference point. Collecting together terms of the same order, we may write

$$\boldsymbol{W}(\boldsymbol{Q}) = \boldsymbol{W}^{(0)}(\boldsymbol{Q}) + \boldsymbol{W}^{(1)}(\boldsymbol{Q}) + \boldsymbol{W}^{(2)}(\boldsymbol{Q}) + \cdots . \tag{5.2}$$

The zeroth-order potential corresponds to a set of ground state harmonic oscillators displaced at the vertical excitation energies E_i:

$$W_{ij}^{(0)}(\boldsymbol{Q}) = \left(E_i + \sum_{\alpha=1}^{3N-9} \frac{\omega_\alpha}{2} Q_\alpha^2 \right) \delta_{ij}, \tag{5.3}$$

and assumes a diagonal form as we choose the diabatic and adiabatic representations to be equal at the reference point. The first- and second-order potentials may be written

$$W_{ii}^{(1)}(\boldsymbol{Q}) = \sum_{\alpha=1}^{3N-9} \kappa_\alpha^{(i)} Q_\alpha \tag{5.4}$$

$$W_{ij}^{(1)}(\boldsymbol{Q}) = \sum_{\alpha=1}^{3N-9} \lambda_\alpha^{(i,j)} Q_\alpha \tag{5.5}$$

$$W_{ii}^{(2)}(\boldsymbol{Q}) = \sum_{\alpha,\beta=1}^{3N-9} \frac{1}{2} \gamma_{\alpha\beta}^{(i)} Q_\alpha Q_\beta \tag{5.6}$$

In general, a second-order expansion of the diabatic PESs and a linear expansion of the nonadiabatic coupling was found to be sufficient. However, for the accurate description of some important topological features and conical intersections between the states under consideration, the inclusion of certain third-order and fourth-order terms was found to be necessary. The complete third and fourth-order contributions to the diabatic potential, $\boldsymbol{W}^{(3)}$ and $\boldsymbol{W}^{(4)}$, respectively, take the form

$$W_{ii}^{(3)}(\boldsymbol{Q}) = \frac{1}{6} \sum_{\alpha,\beta,\gamma=1}^{3N-9} \iota_{\alpha\beta\gamma}^{(i)} Q_\alpha Q_\beta Q_\gamma, \tag{5.7}$$

$$W_{ii}^{(4)}(\boldsymbol{Q}) = \frac{1}{24} \sum_{\alpha,\beta,\gamma,\delta=1}^{3N-9} = \epsilon_{\alpha\beta\gamma\delta}^{(i)} Q_\alpha Q_\beta Q_\gamma Q_\delta. \tag{5.8}$$

It was, however, found sufficient to use the following truncated expansions:

$$W_{ii}^{(3)}(\boldsymbol{Q}) = \frac{1}{6} \sum_{\alpha,\beta=1}^{3N-9} \iota_{\alpha\beta}^{(i)} Q_\alpha Q_\beta^2, \tag{5.9}$$

$$W_{ii}^{(4)}(\boldsymbol{Q}) = \frac{1}{24}\sum_{\alpha,\beta=1}^{3N-9}\epsilon_{\alpha\beta}^{(i)}Q_\alpha^2 Q_\beta^2. \tag{5.10}$$

The diabatic potentials and nonadiabatic coupling along the in and out-of-plane bending angles θ and ϕ are modelled by low-order Taylor expansions about the FC point:

$$\begin{aligned} W_{ii}(\theta,\phi,R) =& \kappa_\theta^{(i)}(R)\theta + \kappa_\phi^{(i)}(R)\phi + \frac{1}{2}(\gamma_{\theta\theta}^{(i)}(R)\theta^2 \\ &+ \gamma_{\phi\phi}^{(i)}(R)\phi^2) + \frac{1}{6}\iota_\phi^{(i)}(R)\phi^3 + \frac{1}{24}\epsilon_\phi^{(i)}(R)\phi^4 + W_{ii}(R) \end{aligned} \tag{5.11}$$

$$W_{ij}(\theta,\phi,R) = \lambda_\theta^{(i,j)}(R)\theta + \lambda_\phi^{(i,j)}(R)\phi \tag{5.12}$$

That the parameters entering into the expansions 6.3 and 6.4 are written as functions of the N-H dissociation coordinate, R, reflects that as the dissociation limit is reached the contribution of these terms to the potential should decay to zero. This is achieved by expanding these terms about the FC point N-H bond length, R_0 as follows

$$\kappa_a^{(i)}(R) = \kappa_a^{(i)}(R_0)[1 - \tanh(k_a^{(i)}R)], \quad a = \theta,\phi \tag{5.13}$$

$$\gamma_{aa}^{(i)}(R) = \gamma_{aa}^{(i)}(R_0)[1 - \tanh(g_{aa}^{(i)}R)], \quad a = \theta,\phi \tag{5.14}$$

$$\epsilon_a^{(i)}(R) = \epsilon_a^{(i)}(R_0)[1 - \tanh(e_a^{(i)}R)], \quad a = \theta,\phi \tag{5.15}$$

$$\iota_\phi^{(i)}(R) = \iota_\phi^{(i)}(R_0)[1 - \tanh(I_\phi^{(i)}R)] \tag{5.16}$$

$$\lambda_\theta^{(i,j)}(R) = \lambda_\theta^{(i,j)}(R_0)[1 - \tanh(l_\theta^{(i,j)}R)] \tag{5.17}$$

$$\lambda_{\phi}^{(i,j)}(R) = (l_{\phi,1}^{(i,j)} R + l_{\phi,2}^{(i,j)} R^2) \exp(-l_{\phi,3}^{(i,j)} R). \tag{5.18}$$

The anharmonic diabatic potentials along R are described as follows. For states bound with respect to R, we choose to model the diabatic potentials as Morse oscillators:

$$W_{ii}(R) = D_0^i \left[1 - \exp\left(-\alpha_i \left(R - R_0^i\right)\right)\right]^2; \quad i = 1, 3 \tag{5.19}$$

For the dissociative $3s$ state, the diabatic potential is modelled using an avoided crossing model potential:

$$\begin{aligned} W_{22}(R) =& \frac{1}{2}\left(\nu^{bound}(R) + \nu^{diss}(R)\right) \\ & - \frac{1}{2}\left[\left(\nu^{bound}(R) - \nu^{diss}(R)\right)^2 + 4\rho 2\right]^{\frac{1}{2}}, \end{aligned} \tag{5.20}$$

with

$$\nu^{bound}(R) = D_{0,b}\left[1 - \exp\left(-\alpha_b \left(R - R_{0,b}\right)\right)\right]^2 \tag{5.21}$$

$$\nu^{diss}(R) = P\left(\exp\left(-\alpha_d (R - R_{0,d})\right)\right) + D_{0,d}. \tag{5.22}$$

The coupling of the two subsets of nuclear degrees of freedom, $\boldsymbol{r}$ and $\boldsymbol{Q}$, is achieved *via* the use an interaction potential $\boldsymbol{W}^{int}(\boldsymbol{Q}, \boldsymbol{r})$, which we take as

$$\boldsymbol{W}^{int}(\boldsymbol{Q}, \boldsymbol{r}) = \boldsymbol{W}^{int(1)}(\boldsymbol{Q}, \boldsymbol{r}) + \boldsymbol{W}^{int(2)}(\boldsymbol{Q}, \boldsymbol{r}) + \ldots, \tag{5.23}$$

with

$$W_{ii}^{int(1)}(\boldsymbol{Q}, \boldsymbol{r}) = \sum_{\alpha=1}^{3N-9} {}^1K_{\alpha}^{(i)} \tanh({}^2K_{\alpha}^{(i)} R) Q_{\alpha}, \tag{5.24}$$

$$W_{ij}^{int(1)}(\boldsymbol{Q}, \boldsymbol{r}) = \sum_{\alpha=1}^{3N-9} {}^1\Lambda_{\alpha}^{(i,j)} \tanh({}^2\Lambda_{\alpha}^{(i,j)} R) Q_{\alpha}, \tag{5.25}$$

$$W_{ii}^{int(2)}(\boldsymbol{Q},\boldsymbol{r}) = \sum_{\alpha,\beta=1}^{3N-9} {}^{1}\Gamma_{\alpha\beta}^{(i)} \tanh({}^{2}\Gamma_{\alpha\beta}^{(i)} R) Q_\alpha Q_\beta \tag{5.26}$$

The terms ${}^{1}K_{\alpha}^{(i)}$ and ${}^{1}\Gamma_{\alpha\beta}^{(i)}$ correspond to the change in the equilibrium geometry of the pyrrolinyl fragment and the rotation of the normal modes of the pyrrolinyl fragment, respectively, as the H_d atom dissociates. The terms ${}^{1}\Lambda_{\alpha}^{(i,j)}$ describe the corresponding changes in nonadiabatic coupling with respect to the pyrrolinyl normal modes as the dissociation coordinate is traversed.

In the coordinate system used, we may write the kinetic energy T_N operator as

$$\begin{aligned} T_N =& T_X + T_{R_f} + \frac{1}{2}\sum_{\alpha=1}^{3N-9} \omega_\alpha \frac{\partial^2}{\partial Q_\alpha^2} \\ &- \frac{1}{\mu}\left(\frac{1}{R}\frac{\partial^2}{\partial R^2}R + \frac{1}{R^2\sin\phi}\frac{\partial}{\partial\phi}\sin\phi\frac{\partial}{\partial\phi} + \frac{1}{R^2\sin^2\phi}\frac{\partial^2}{\partial\theta^2}\right), \end{aligned} \tag{5.27}$$

where ω_α is the frequency of the pyrrolinyl fragment normal mode Q_α, T_X denotes the centre of mass translational kinetic energy of the whole molecule, T_{R_f} denotes the rotational kinetic energy of the pyrrolinyl fragment, and

$$\frac{1}{\mu} = \frac{1}{m_H} + \frac{1}{m_f}. \tag{5.28}$$

Here, m_h and m_f denote the masses of the hydrogen atom and the pyrrolinyl fragment, respectively. In the following we equate the total rotational kinetic energy and the rotational kinetic energy of the pyrrolinyl fragment, allowing us to ignore the contributions from T_X and T_{R_f}. This approximation is considered justifiable due to the small ratio of m_H/m_f.

All parameters entering into the model potential were determined *via* the minimisation of the weighted root mean square deviation (RMSD) of

the eigenvalues of the model potential and adiabatic energies calculated at a large number of nuclear configurations, as detailed in Section 4.3.2.

5.2.2 Electronic Structure Calculations

The reference geometry chosen was the saddle point connecting the AX and EQ conformers with respect to the N-H out-of-plane bending coordinate ϕ. This geometry was optimised using the CCSD method and aug-cc-pVDZ basis. At this geometry, the 3-pyrroline molecule possesses C_s symmetry, and the irreducible representations of this point group will be used to label the electronic states and nuclear degrees of freedom in the following. All calculations of adiabatic potential energy surfaces were performed using the equation-of-motion coupled cluster single and doubles (EOM-CCSD) method [79]. The six lowest-lying singlet state adiabatic energies were calculated at each geometry considered. At the reference point these correspond to the diabatic states $\tilde{X}$, $\tilde{A}(3s)$, $\tilde{B}(3p_x)$, $\tilde{C}(3p_y)$, $\tilde{D}(n\pi^*)$ and $\tilde{E}(3p_x)$. The symmetries and vertical excitation energies of these states are given in Table 5.1. All calculations were performed using the Molpro 2009 set of programs [63].

5.2.3 Calculation of Vibrational Eigenstates: The AX and EQ Conformers

It is well established that both the AX and EQ conformers exist under experimental conditions [75–78]. The two conformers may be viewed as two different vibrational eigenstates, $|\Psi_{AX}\rangle$ and $|\Psi_{EQ}\rangle$. The eigenstate $|\Psi_{AX}\rangle$ can be taken to correspond to the ground vibrational state. As such, $|\Psi_{AX}\rangle$ may be obtained through the use of the relaxation method, that is, by propagating an initial state in negative imaginary time. The higher-lying eigenstate $|\Psi_{EQ}\rangle$ cannot be calculated so straightforwardly. We here use the method

Table 5.1: Symmetries, dominant configurations and vertical excitation energies of the first six singlet states of 3-pyrroline at the reference point as determined from EOM-CCSD calculations employing the aug-cc-pVDZ basis set. The bracketed numbers displayed alongside the dominant configurations are the corresponding coefficients. $|0\rangle$ denotes the reference (Hartree Fock) configuration.

State	Symmetry	Dominant configurations	Vertical excitation energy (eV)
S_0	$A^{'}$	$\|0\rangle$	0.00
S_1	$A^{'}$	$12a^{'} \rightarrow 13a^{'}$ (0.63)	4.64
		$12a^{'} \rightarrow 14a^{'}$ (0.38)	
		$11a^{'} \rightarrow 14a^{'}$ (0.34)	
S_2	$A^{'}$	$12a^{'} \rightarrow 15a^{'}$ (0.54)	5.45
		$12a^{'} \rightarrow 14a^{'}$ (0.38)	
		$12a^{'} \rightarrow 13a^{'}$ (0.34)	
		$12a^{'} \rightarrow 16a^{'}$ (0.30)	
S_3	$A^{''}$	$12a^{'} \rightarrow 8a^{''}$ (0.59)	5.56
		$12a^{'} \rightarrow 11a^{''}$ (0.30)	
S_4	$A^{''}$	$12a^{'} \rightarrow 12a^{''}$ (0.51)	5.61
		$12a^{'} \rightarrow 8a^{''}$ (0.39)	
		$12a^{'} \rightarrow 17a^{''}$ (0.33)	
		$12a^{'} \rightarrow 11a^{''}$ (0.31)	
S_5	$A^{'}$	$12a^{'} \rightarrow 15a^{'}$ (0.58)	5.68
		$12a^{'} \rightarrow 14a^{'}$ (0.38)	
		$12a^{'} \rightarrow 13a^{'}$ (0.32)	

of improved relaxation to generate a vibrationally excited state that can be taken to correspond to $|\Psi_{EQ}\rangle$. To do so, we make use of the approximation that the AX and EQ conformers are connected by the N-H out-of-plane bending mode ϕ. Doing so, we define an initial state with density localised at $\phi \sim -1$ radians. The A-vector used at each time step in the improved relaxation calculation is then taken as that which gives the greatest overlap with the wavefunction at the previous time step. In this manner, an eigenstate of the Hamiltonian may be obtained that has density localised about $\phi \sim -1$, and as such may be taken to correspond to the EQ conformer.

5.2.4 Wavepacket Propagations

Wavepacket propagations were performed using the MCTDH method. Individual calculations corresponding to excitation of the $|\Psi_{AX}\rangle$ and $|\Psi_{EQ}\rangle$ vibrational states to both the $\tilde{A}$ and $\tilde{B}$ electronic states were performed by vertically displacing the eigenstates to the corresponding electronic states, that is,

$$|\Psi_C(0)\rangle = \{|f\rangle\langle 1| + h.c.\}\,|\Psi_C\rangle; \quad f = 2,3, \;\; C = AX, EQ. \tag{5.29}$$

In order to circumvent the use of prohibitively long grids for the dissociative degree of freedom R, a CAP was placed at a value of R corresponding to an N-H bond length of 6.4 a.u..

State- and conformer-resolved absorption spectra were calculated from the Fourier transforms of the wavepacket autocorrelation functions calculated for each wavepacket propagation.

Table 5.2: Linear intrastate coupling constants obtained from the fitting of the model potential to adiabatic energies calculated at the EOM-CCSD/aug-cc-pVDZ level. All quantities are reported in eV.

Degree of freedom	S_1	S_2
Q_1	-0.0990	-0.0702
Q_3	0.0525	0.0452
Q_4	0.1163	0.0941
Q_6	-0.1703	-0.1230
Q_9	-0.0565	-0.0473
Q_{10}	-0.0934	-0.0817
Q_{12}	-0.0537	-0.0613
Q_{14}	0.0593	0.1503
Q_{17}	-0.0222	-0.0798
Q_{19}	-0.0210	-0.0265
Q_{20}	0.0255	-0.0251
Q_{22}	0.1038	0.1209
Q_{24}	0.0328	0.0161
Q_{26}	-0.0627	-0.0459
ϕ	0.1552	0.1321

Table 5.3: Linear interstate coupling constants obtained from the fitting of the model potential to adiabatic energies calculated at the EOM-CCSD/aug-cc-pVDZ level. All quantities are reported in eV.

Degree of freedom	S_0, S_1	S_0, S_2	S_1, S_2
Q_4	0.0035	0.0000	0.0141
Q_{14}	0.0000	0.0000	-0.0120
Q_{17}	0.0000	0.2410	-0.0336

5.3 Results

5.3.1 Model Diabatic Potentials

A total of 1019 parameters non-zero by symmetry entering the model diabatic potential were determined by fitting to a total of 5322 calculated adiabatic energies. A weighted RMSD of the model and calculated adiabatic energies of 0.067 eV was attained, indicating that the model potential constructed may faithfully reproduce the adiabatic surfaces in the regions of nuclear configuration space of interest.

We are interested in the dynamics of the 3-pyrroline molecule following

excitation to the $\tilde{A}$ and $\tilde{B}$ states, and the first-order terms entering into the expansion of the 3×3 block of $\boldsymbol{W}$ with elements W_{ij}, $i, j = 1, 2, 3$ can be expected to be of greatest importance with respect to this. These parameters are listed in Tables 5.2 and 5.3. We note that as the $\tilde{X}$, $\tilde{A}$ and $\tilde{B}$ states are all of $A^{'}$ symmetry at the point of expansion, they may only be coupled to first-order by the totally symmetric 3-pyrrolinyl modes Q_α, $\Gamma^\alpha = A^{'}$. The first-order intrastate coupling constants, $\kappa_\alpha^{(i)}$, which give the gradients of the ith diabatic state with respect to the modes Q_α, are also non-zero only for totally symmetry degrees of freedom. We thus restrict ourselves to consideration of only the totally symmetric subset of nuclear degrees of freedom. Significant gradients of the $\tilde{A}$ and $\tilde{B}$ state potentials are found for the 3-pyrrolinyl modes Q_1 (C-N-C out-of-plane bending), Q_4 (ring stretching and methine wagging), Q_6 (ring breathing), Q_{14} (symmetric methyline twisting), Q_{17} (symmetric methyline wagging) and Q_{22} (symmetric methyline stretching), and ϕ, the out-of-plane N-H bending coordinate.

At the reference point, the $\tilde{X}$ and $\tilde{B}$ states are coupled strongly to first-order by the mode Q_{17}, while the states $\tilde{A}$ and $\tilde{B}$ are coupled significantly by the modes Q_4, Q_{14} and Q_{17}. Only weak coupling between the $\tilde{X}$ and $\tilde{A}$ states is found to exist at this point. However, a large variation of the first-order interstate coupling constants $\lambda_\alpha^{(1,2)}(R)$ with the N-H bond length is found. Specifically, at the conical intersection between the $\tilde{X}$ and $\tilde{A}$ states (located at R =1.66 a.u., corresponding to an N-H bond length of 3.58 a.u.) the states $\tilde{X}$ and $\tilde{A}$ are found to be coupled strongly by the degrees of freedom Q_4, Q_{17} and ϕ. The parameters entering into the expansion of the first-order interstate coupling constants are displayed in Table 5.4.

From a consideration of the fitted parameters we may isolate a subset of eight nuclear degrees of freedom that can be expected to be of greatest

Table 5.4: Fitted parameters entering into the expansion of the linear interstate coupling constants $\lambda_\alpha^{(i,j)}$ with respect to the N-H dissociation coordinate R. The terms ${}^1\Lambda_\alpha^{(i,j)}$ are given in eV, all other quantities are dimensionless.

Mode	${}^1\Lambda_\alpha^{(1,2)}$	${}^2\Lambda_\alpha^{(1,2)}$	${}^1\Lambda_\alpha^{(1,3)}$	${}^2\Lambda_\alpha^{(1,3)}$	${}^1\Lambda_\alpha^{(2,3)}$	${}^2\Lambda_\alpha^{(2,3)}$
Q_4	0.1193	2.7031	-0.1514	1.1373	0.3603	0.9606
Q_{14}	0.0633	1.4167	0.3738	0.0180	0.0598	0.0192
Q_{17}	0.4104	0.0264	-1.5021	0.0325	-0.0436	0.0277
	$l_{\phi,1}^{(1,2)}$	$l_{\phi,2}^{(1,2)}$	$l_{\phi,3}^{(1,2)}$			
ϕ	-4.5622	0.4309	0.8341			

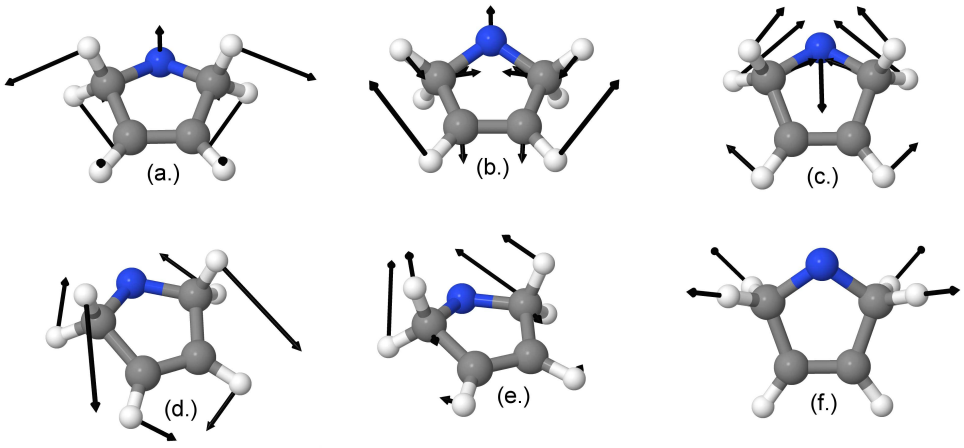

Fig. 5.5: The normal modes of the 3-pyrrolinyl radical important for the description of the photochemistry of 3-pyrroline. (a.) Q_1 (C-N-C out-of-plane bending), (b.) Q_4 (ring stretching and methine wagging), (c.) Q_6 (ring breathing), (d.) Q_{14} (symmetric methyline twisting), (e.) Q_{17} (symmetric methyline wagging), and (f.) Q_{22} (symmetric methyline stretching).

importance for the description of the dynamics of 3-pyrroline following excitation to the $\tilde{A}$ and $\tilde{B}$ states: the 3-pyrrolinyl modes Q_1, Q_4, Q_6, Q_{14}, Q_{17} and Q_{22} (illustrated in Figure 5.5), and R and ϕ, the N-H dissociation and out-of-plane bending coordinates, respectively.

Of particular importance to the photoinduced dynamics of 3-pyrroline are the nuclear degrees of freedom Q_1 and ϕ, which together describe the planarisation of the C_4NH subunit following excitation to both the $\tilde{A}$ and $\tilde{B}$ states. For both the AX and EQ conformers in the $\tilde{X}$ state, both the nitrogen and hydrogen atoms of the N-H unit lie out of the plane defined by

the four carbon atoms. Following excitation to both the $\tilde{A}$ and $\tilde{B}$ states, sp^2 hybridisation of the nitrogen centre occurs for both the AX and EQ conformers, driving a planarisation of the C_4NH unit. The model diabatic potentials for the $\tilde{X}$, $\tilde{A}$ and $\tilde{B}$ states as a function of the Q_1 and ϕ degrees of freedom are shown in Figure 5.6. Through the inclusion of selected second, third and fourth-order terms, namely $\gamma^{(i)}_{\phi,Q_1}$, $\iota^{(i)}_{\phi,Q_1}$ and $\epsilon^{(i)}_{\phi,Q_1}$, a faithful description of the planarisation of the C_4NH unit is found to be given by the model diabatic potential.

Shown in Figure 5.7 are the model adiabatic and diabatic potentials of the first two electronic states of 3-pyrroline in the space spanned by the N-H dissociation coordinate R and the N-H out-of-plane bending coordinate ϕ. It is worth drawing comparison here to the photodissociation of ammonia in its first electronically excited state. As is well known, the planarisation of the ammonia molecule is a prerequisite for unhindered dissociation of the molecule following excitation to its $\tilde{A}$ state, with the barrier to dissociation being modulated accordingly by the umbrella inversion coordinate. Similarly, it is found that for 3-pyrroline the barrier to N-H dissociation is increased for geometries for which the N-H bond lies out of the plane defined by the C-N-C vertex, as illustrated in Figure 5.8.

5.3.2 Calculation of the $|\Psi_{AX}\rangle$ and $|\Psi_{EQ}\rangle$ Vibrational Eigenstates

Using the method of improved relaxation, the eigenstates $|\Psi_{AX}\rangle$ and $|\Psi_{EQ}\rangle$ as defined in Section 5.2.3 were calculated. The two-dimensional reduced density for the degrees of freedom Q_1 and ϕ are shown in Figure 5.9 for the calculated eigenstates $|\Psi_{AX}\rangle$ and $|\Psi_{EQ}\rangle$. It is found that the two eigenstates each have density localised over one, and only one, of the two minima along ϕ, and as such validation of our taking the two states to correspond to the AX

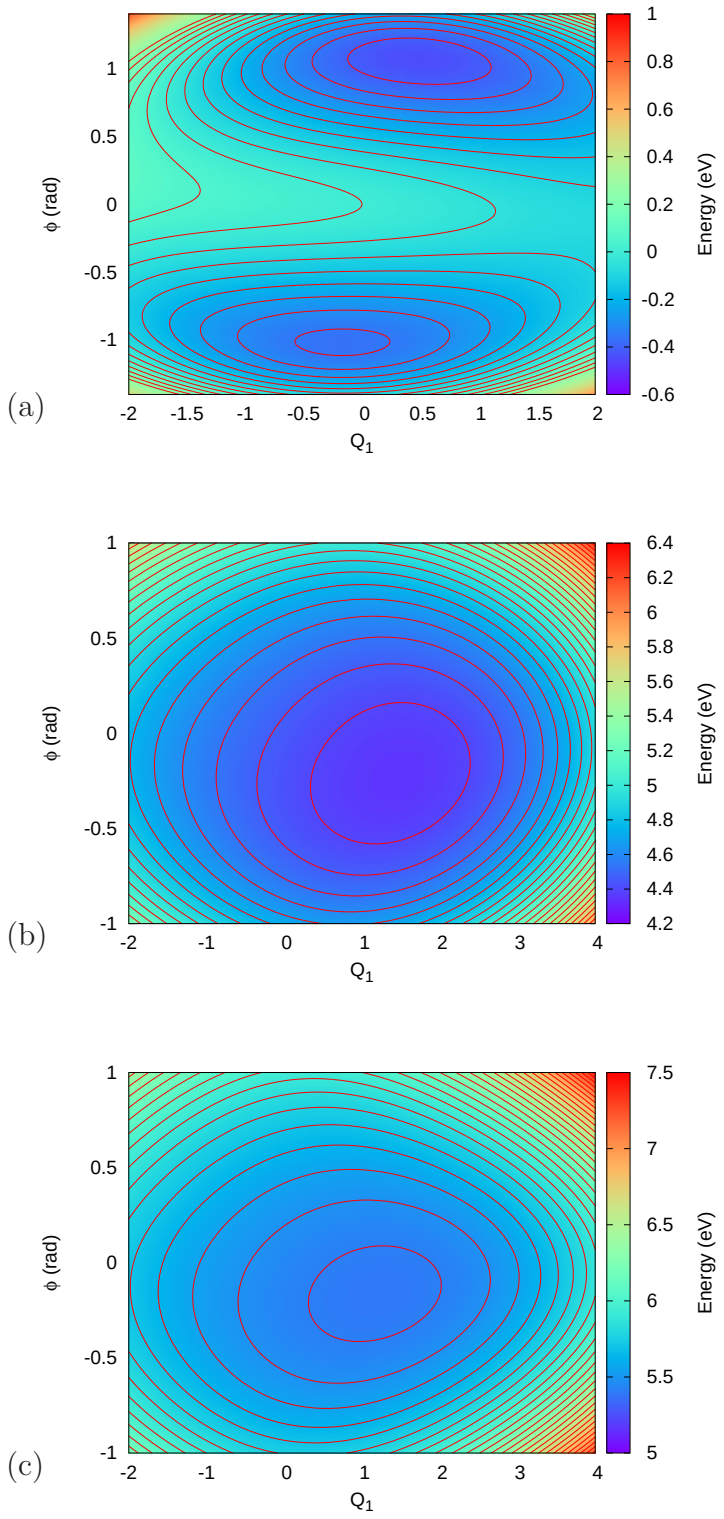

Fig. 5.6: Model diabatic surfaces along the N-H out-of-plane bending mode ϕ and the C-N-C bending mode Q_1: (a) the $\tilde{X}$ state potential; (b) the $\tilde{A}$ state potential, and; (c) the $\tilde{B}$ state potential.

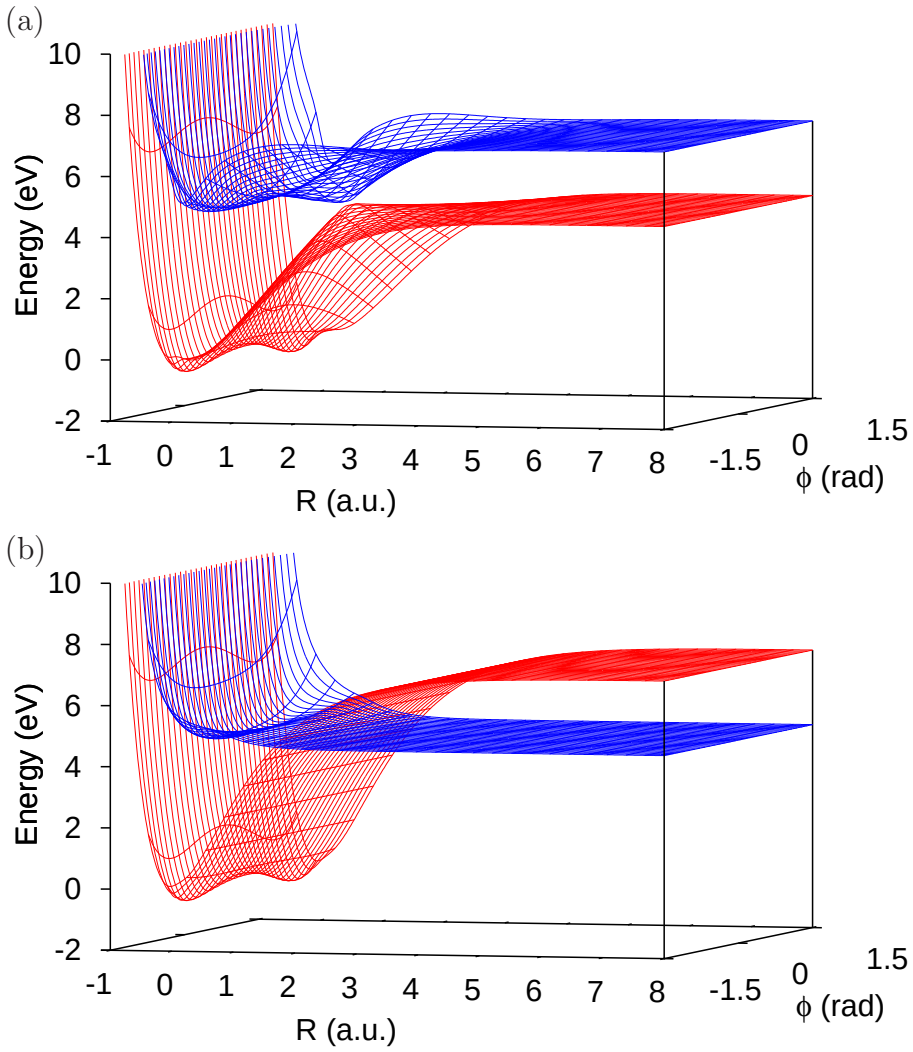

Fig. 5.7: Model potential surfaces for the ground and first excited states of 3-pyrroline along the N-H out-of-plane bending mode ϕ and the N-H dissociation coordinate R. (a) Adiabatic surfaces, (b) Diabatic surfaces.

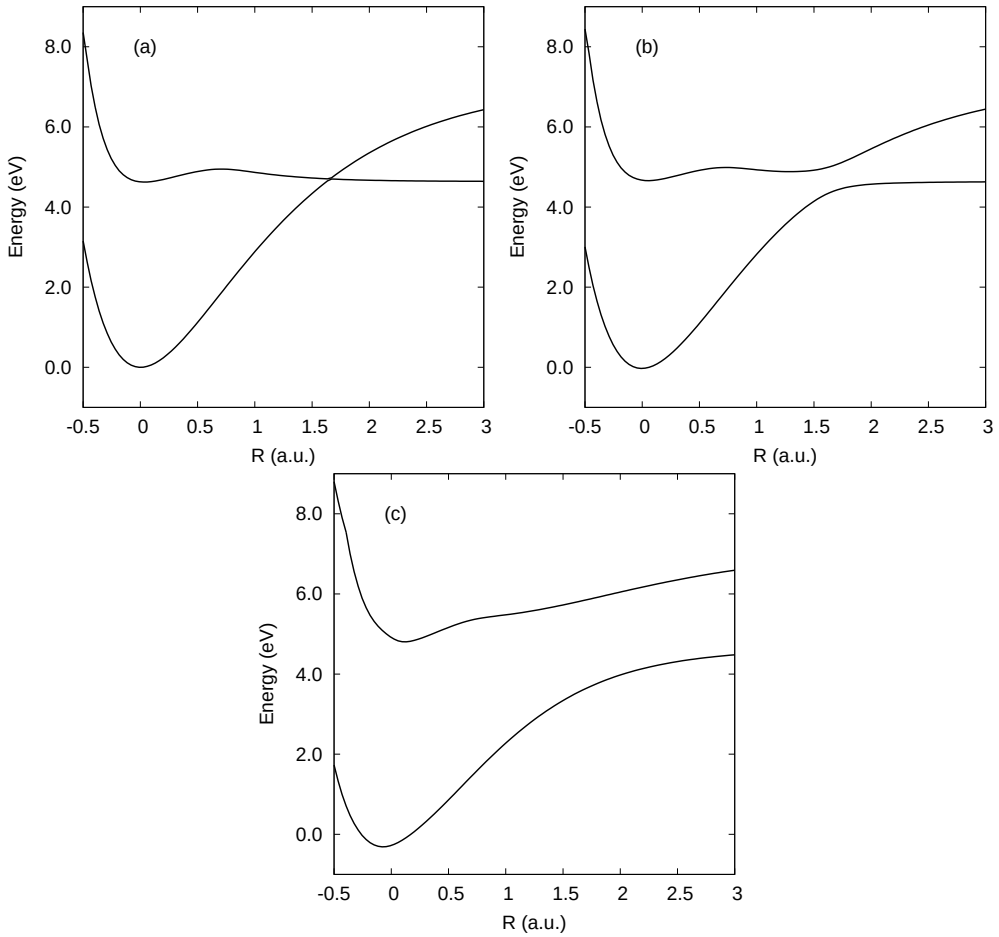

Fig. 5.8: Model adiabatic potentials for the S_0 and S_1 states along the N-H dissociation coordinate plotted for different values of the N-H out-of-plane bending coordinate ϕ: (a) ϕ=0.0 radians, (b) ϕ=0.2 radians, and (c) ϕ=0.7 radians.

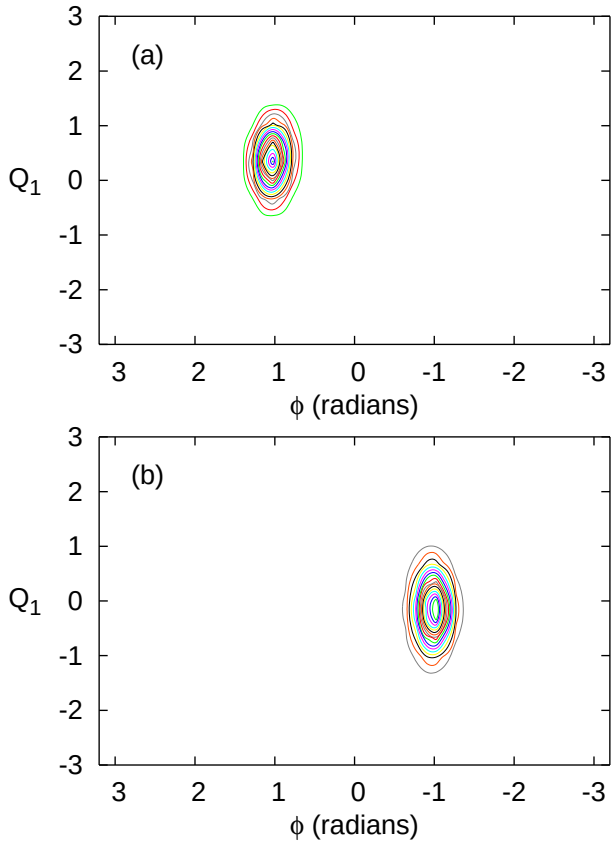

Fig. 5.9: The two-dimensional reduced density plotted along the C-N-C inversion coordinate Q_1 and N-H out-of-plane bending coordinate ϕ for: (a) the vibrational eigenstate $|\Psi_{AX}\rangle$ calculated using the method of relaxation, and; (b) the vibrational eigenstate $|\Psi_{EQ}\rangle$ calculated using the method of improved relaxation.

and EQ conformers is provided. The difference in energy of the eigenstates $|\Psi_{AX}\rangle$ and $|\Psi_{EQ}\rangle$, ΔE_{EQ-AX}, thus obtained is 422.36 cm^{-1}, which compares favourably to an experimentally determined value of 340 $\pm$ 50 cm^{-1} [75].

5.3.3 Excitation to the $\tilde{A}$ State

Quantum dynamics simulations using the $|\Psi_{AX}\rangle$ and $|\Psi_{EQ}\rangle$ eigenstates were performed using the eight nuclear degrees of freedom Q_1, Q_4, Q_6, Q_{14}, Q_{17}, Q_{22}, R and ϕ, and the three electronic states $\tilde{X}$, $\tilde{A}$ and $\tilde{B}$. For both calculations a propagation time of 700 fs was used. All other details of the calculations are summarised in Table 5.5.

Table 5.5: Computational details of the wavepacket propagations corresponding to excitation to the $\tilde{A}$ state. The DVR types exp and HO correspond to exponential and Harmonic oscillator DVRs, respectively. N_i, N_j are the number of primitive DVR functions used to describe each particle. n_i are the number of single-particle functions used for each state.

Particle	DVR type	N_i, N_j	n_1, n_2, n_3
R	exp	81	12, 10, 5
ϕ	exp	101	12, 12, 5
Q_1, Q_6	HO	41, 31	10, 9, 5
Q_4, Q_{14}	HO	31, 41	10, 9, 5
Q_{17}, Q_{22}	HO	31, 31	10, 7, 3

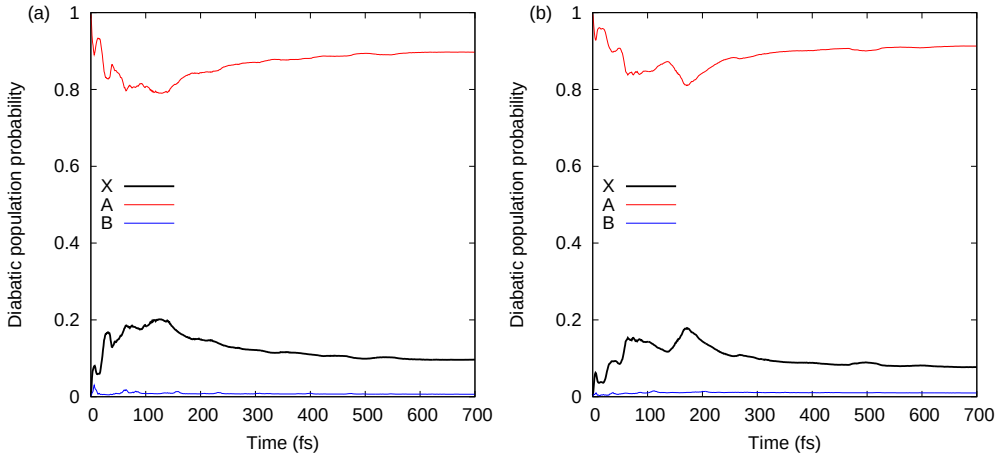

Fig. 5.10: Diabatic population probabilities following excitation to the $\tilde{A}$ state: (a) population probabilities following vertical excitation of the $|\Psi_{AX}\rangle$ state, (b) population probabilities following vertical excitation of the $|\Psi_{EQ}\rangle$ state.

The diabatic electronic state population probabilities following vertical excitation of the $|\Psi_{AX}\rangle$ and $|\Psi_{EQ}\rangle$ eigenstates to the $\tilde{A}$ state are displayed in Figure 5.10. In both cases the evolving wavepacket remains predominantly in the initially excited $\tilde{A}$ state, but with an initial oscillatory transfer of population between the $\tilde{A}$ and $\tilde{X}$ states for the first 250 fs. By 700 fs, the population probabilities of the $\tilde{X}$ and $\tilde{A}$ states following excitation of the $|\Psi_{AX}\rangle$ ($|\Psi_{EQ}\rangle$) eigenstates are, respectively, 0.096 (0.077) and 0.897 (0.091).

The state-resolved, time-cumulated probabilities of N-H dissociation following excitation to the $\tilde{A}$ state are shown in Figure 5.11. These quantities

were calculated by integrating over time the flux passing through a dividing surface placed at an N-H bond length of 6.4 a.u.. We thus define the probability of dissociation as the expectation value of the projector onto the subspace for which the N-H bond length is greater than 6.4 a.u.. For both excitation of the $|\Psi_{AX}\rangle$ and $|\Psi_{EQ}\rangle$ eigenstates, dissociation is found to occur almost entirely diabatically, that is in the $\tilde{A}$ state. The calculated branching ratios for dissociation on the $\tilde{A}$ and $\tilde{X}$ states,

$$\Gamma_{\tilde{X}}^{\tilde{A}} = \frac{P_d^{(2)}(t = 700)}{P_d^{(1)}(t = 700)}, \tag{5.30}$$

are 81.3 and 170.8 for excitation of the $|\Psi_{AX}\rangle$ and $|\Psi_{EQ}\rangle$ eigenstates, respectively. Here $P_d^{(1)}$ and $P_d^{(2)}$ denote, respectively, the probability of dissociation in the $\tilde{A}(3s)$ and $\tilde{B}(3p_x)$ states. The preponderance of the population of the $\tilde{X}$ state is found to remain in the interaction region of this state, with probabilities of forming hot ground state molecules of 0.086 and 0.070 for excitation of the $|\Psi_{AX}\rangle$ and $|\Psi_{EQ}\rangle$ eigenstates, respectively. The calculated branching ratios $\Gamma_{\tilde{X}}^{\tilde{A}}$ are found to compare favourably with the recent energy-resolved photofragment translational spectroscopy study of Oliver *et al.* [75], who observed only the formation of ground state ($\tilde{X}$) 3-pyrrolinyl products following excitation to the $\tilde{A}$ state.

Relatively long timescales for N-H dissociation following excitation of both the $|\Psi_{AX}\rangle$ and $|\Psi_{EQ}\rangle$ eigenstates are found. Hindrance of N-H dissociation in 3-pyrroline may be rationalised by reference to the topology of the diabatic coupling between the $\tilde{X}$ and $\tilde{A}$ states in the space spanned by the N-H stretching coordinate R and the N-H out-of-plane bending coordinate ϕ. As shown in Figure 5.12, the model diabatic coupling of the $\tilde{X}$ and $\tilde{A}$ states is large in magnitude for values of ϕ significantly displaced from its reference value in the sub-volume of nuclear configuration space

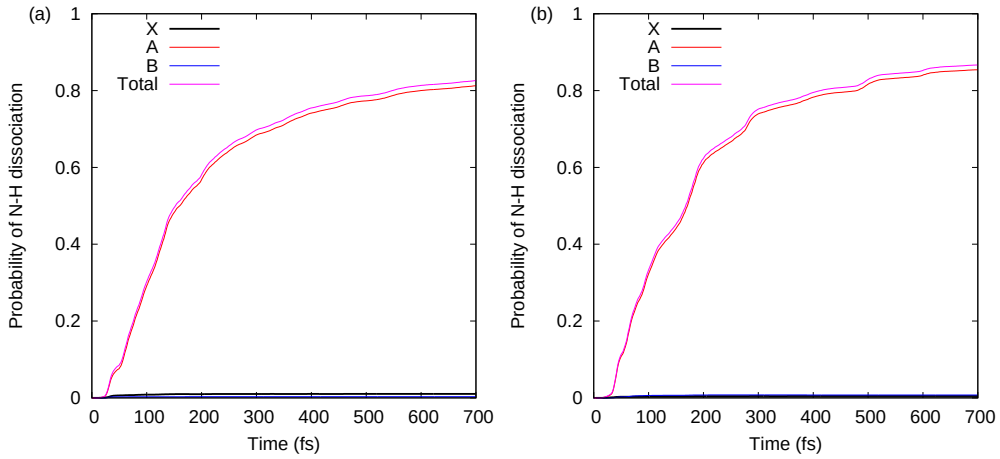

Fig. 5.11: Time-cumulated N-H dissociation probabilities following excitation to the $\tilde{A}$ state: (a) dissociation probabilities following vertical excitation of the $|\Psi_{AX}\rangle$ state, (b) dissociation probabilities following vertical excitation of the $|\Psi_{EQ}\rangle$ state.

spanned by R and ϕ around the barrier to dissociation on the $\tilde{A}$ state diabatic potential. The corresponding adiabatic potential, $S_1(3s)$, thus exhibits an increased barrier to dissociation for displacements along ϕ relative to the reference configuration, for which the C_2NH unit is very almost planar. As illustrated in Figure 5.12, modulation of the height of the barrier to dissociation on the $S_1(3s)$ surface by ϕ results in an adiabatic potential that may effectively funnel the wavepacket to the conical intersection with the ground state only when ϕ is close to its reference value. However, the vertically excited ground state wavepackets (both $|\Psi_{AX}\rangle$ and $|\Psi_{EQ}\rangle$) are initially localised around $\phi_{0,AX} \sim +1$ and $\phi_{0,EQ} \sim -1$, respectively, and are thus initially displaced to the repulsive walls of the $S_1(3s)$ state potential. Oscillatory motion along the degree of freedom ϕ is thus driven, frustrating the passage of the wavepacket over the barrier to dissociation.

5.3.4 Excitation to the $\tilde{B}$ State

Quantum dynamics simulations using the $|\Psi_{AX}\rangle$ and $|\Psi_{EQ}\rangle$ eigenstates were performed using the eight nuclear degrees of freedom Q_1, Q_4, Q_6, Q_{14}, Q_{17},

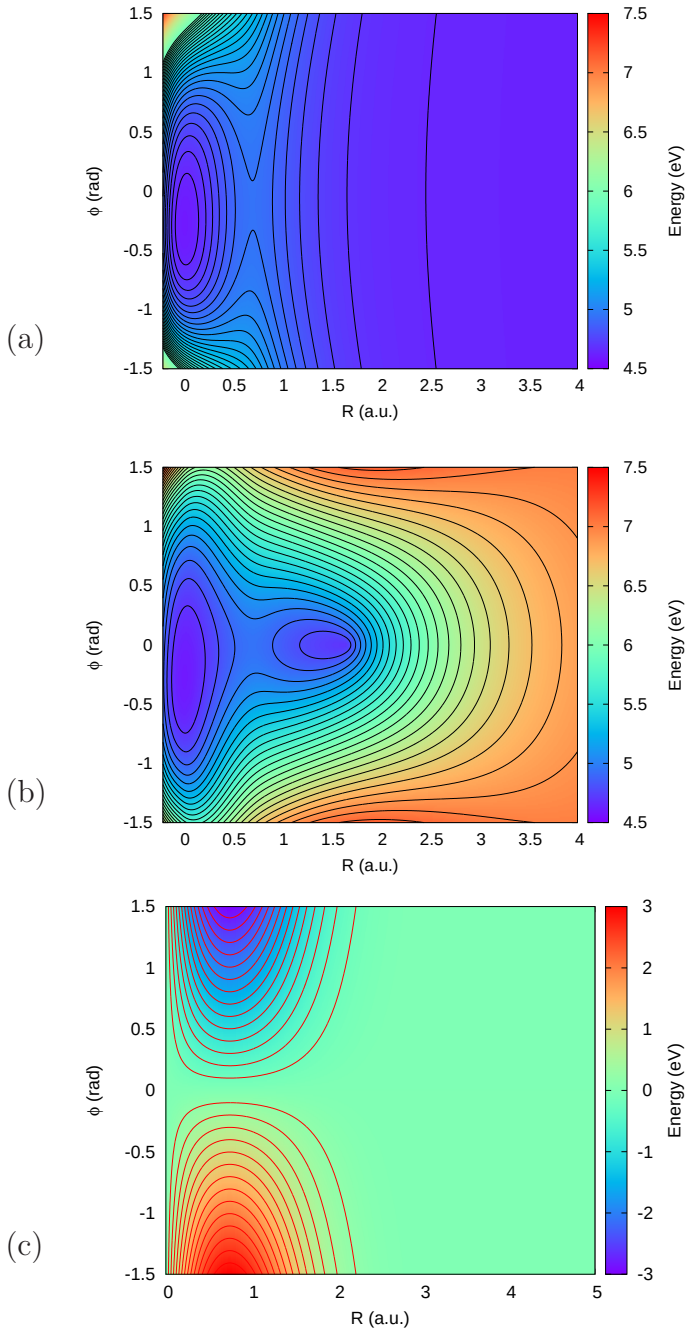

Fig. 5.12: Elements of the model diabatic and adiabatic potential matrices along the N-H dissociation coordinate R and the N-H out-of-plane bending mode ϕ. (a) The diabatic potential for the $\tilde{A}$ state, (b) the adiabatic potential for the S_1 state, (c) the diabatic coupling between the $\tilde{X}$ and $\tilde{A}$ states.

Table 5.6: Computational details of the wavepacket propagations corresponding to excitation to the $\tilde{B}$ state. The DVR types exp and HO correspond to exponential and Harmonic oscillator DVRs, respectively. N_i, N_j are the number of primitive DVR functions used to describe each particle. n_i are the number of single-particle functions used for each state.

Particle	DVR type	N_i, N_j	n_1, n_2, n_3
R	exp	81	12, 10, 5
ϕ	exp	101	12, 12, 12
Q_1, Q_6	HO	41, 31	10, 9, 12
Q_4, Q_{14}	HO	31, 41	10, 9, 5
Q_{17}, Q_{22}	HO	31, 31	10, 7, 3

Q_{22}, R and ϕ, and the three electronic states $\tilde{X}$, $\tilde{A}$ and $\tilde{B}$. A propagation time of 1500 fs was used. The details of these propagations are given in Table 5.6.

The diabatic electronic states populations following vertical excitation of the $|\Psi_{AX}\rangle$ and $|\Psi_{EQ}\rangle$ eigenstates to the $\tilde{B}$ state are displayed in Figure 5.13. For both the $|\Psi_{AX}\rangle$ and $|\Psi_{EQ}\rangle$ eigenstates the relaxation to the $\tilde{A}(3s)$ state is essentially complete by 1.5 ps, at which point the population probabilities of the $\tilde{X}$, $\tilde{A}$ and $\tilde{B}$ states for the $|\Psi_{AX}\rangle$ ($|\Psi_{EQ}\rangle$) eigenstate are 0.028 (0.019), 0.929 (0.937), and 0.042 (0.0434), respectively. The relatively slow timescale for internal conversion from the $\tilde{B}$ state to the $\tilde{A}$ state is attributable to the relatively small first-order intrastate coupling constants that exist to couple these two states, the values of which are given in Table 5.3.

Experimentally, the energy-resolved photofragment translational spectroscopy study of Oliver *et al.* [75] reports an increase in the yield of low kinetic energy H-atoms produced following excitation of 3-pyrroline at wavelengths of less than 230 nm, at which the $\tilde{B}$ state becomes accessible. This rise in the production of slow H-atoms with increasing excitation energy was speculated to arise from either internal conversion from the bound $\tilde{B}$ state to the ground state, or from unimolecular decay following two-photon excitation

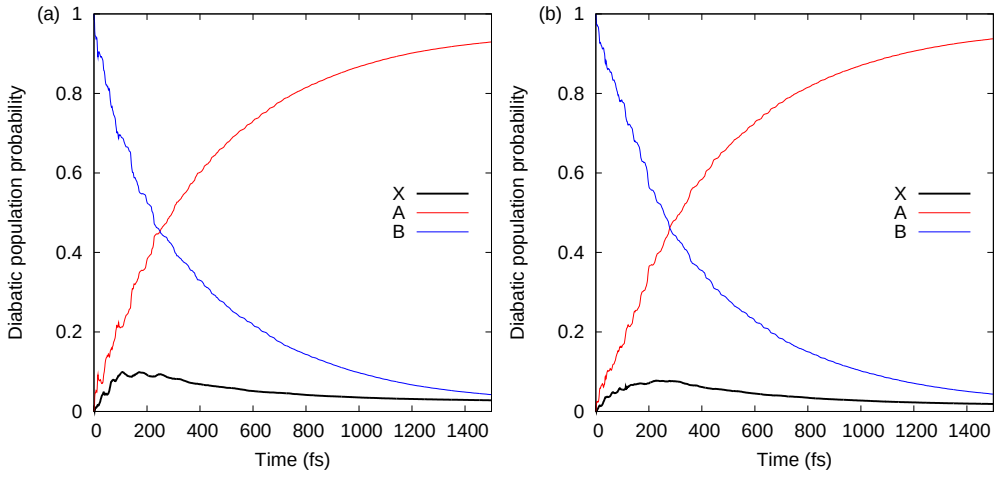

Fig. 5.13: Diabatic population probabilities following excitation to the $\tilde{B}$ state: (a) population probabilities following vertical excitation of the $|\Psi_{AX}\rangle$ state, (b) population probabilities following vertical excitation of the $|\Psi_{EQ}\rangle$ state.

to one of several 'super-excited' states. The results presented here are not consistent with internal conversion from the $\tilde{B}$ state to form vibrationally hot ground state molecules, by virtue of the very small population probabilities of the ground state following excitation of both the $|\Psi_{AX}\rangle$ and $|\Psi_{EQ}\rangle$ eigenstates to the $\tilde{B}$ state. We do note, however, that the model potential presented here is rather simple and as such we cannot definitively rule out the possibility of the existence of an accessible pathway connecting the $\tilde{B}$ and $\tilde{X}$ states.

The state-resolved, time-cumulated probabilities of N-H dissociation following excitation to the $\tilde{B}$ state are shown in Figure 5.14. As in the case of direct excitation to the $\tilde{A}$ state, diabatic N-H dissociation is found to occur almost exclusively, with calculated branching ratios $\Gamma^{\tilde{A}}_{\tilde{X}}$ of 211.7 and 734.4 for the $|\Psi_{AX}\rangle$ and $|\Psi_{EQ}\rangle$ eigenstates, respectively.

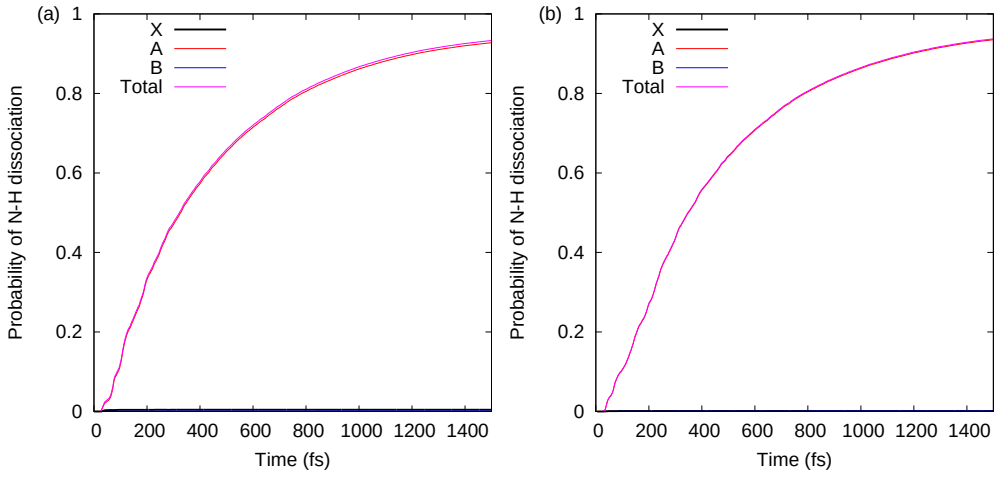

Fig. 5.14: Time-cumulated N-H dissociation probabilities following exciation to the $\tilde{B}$ state: (a) dissociation probabilities following vertical excitation of the $|\Psi_{AX}\rangle$ state, (b) dissociation probabilities following vertical excitation of the $|\Psi_{EQ}\rangle$ state.

5.4 Electronic Absorption Spectra

The only reported experimental electronic absorption spectrum of 3-pyrroline is that of Oliver *et al.* [75]. This spectrum, measured between 4.9 and 6.4 eV, shows no clear vibrational structure and exhibits a long onset, starting from ∼5 ev and reaching a maximum at ∼5.9 eV. We report here calculated spectra corresponding to the excitation of the $|\Psi_{AX}\rangle$ and $|\Psi_{EQ}\rangle$ eigenstates to both the $\tilde{A}$ and $\tilde{B}$ states.

Shown in Figure 5.15 are the calculated spectra corresponding to vertical excitation of the $|\Psi_{AX}\rangle$ and $|\Psi_{EQ}\rangle$ eigenstates to the $\tilde{A}$ state. For both cases, a damping time of 95 fs was used to account for the homogeneous broadening of the spectra due to excluded degrees of freedom. Both spectra appear to be dominated by progressions in modes with frequencies of ∼0.05 eV. We estimate the frequency $\omega_\alpha^{(i)}$ of a mode indexed by α in the electronic state indexed by i from the periodicity of the expectation value $\langle Q_\alpha \rangle(t)$ calculated following excitation to the ith electronic state. In the $\tilde{A}$ state, the modes Q_1 and ϕ are estimated to have frequencies of 0.050 eV and 0.051 eV, respec-

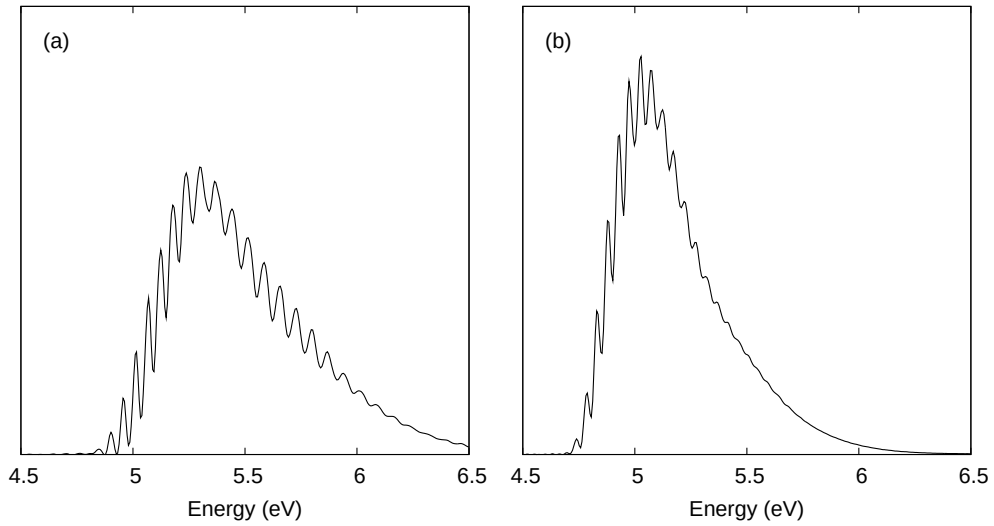

Fig. 5.15: Spectra calculated from the Fourier transforms of the wavepacket autocorrelation functions following excitation to the $\tilde{A}$ state. (a) Absorption spectrum corresponding to excitation of the AX conformer to the $\tilde{A}$ state, and; (b) Absorption spectrum corresponding to excitation of the EQ conformer to the $\tilde{A}$ state.

tively. As such, we determine the dominant features seen in these spectra to be overlapping progressions in these two degrees of freedom. Collectively these two modes describe the planarisation of C_4NH unit upon electronic excitation, which is driven upon excitation to the $\tilde{A}$ state. Shown in Figure 5.16 are the calculated values of $\langle Q_1 \rangle(t)$ and $\langle \phi \rangle(t)$ following excitation to the $\tilde{A}$ state. It is seen that oscillatory motion along both degrees of freedom occurs, with a gradual damping of the amplitude of the motion with time driving the system towards a planar arrangement of the C_4NH unit. A similar evolution of the system is found to occur for following excitation of the $|\Psi_{EQ}\rangle$ eigenstate, owing to the existence of the common minimum in the $\tilde{A}$ state.

Figure 5.17 shows the calculated spectra corresponding the vertical excitation of the $|\Psi_{AX}\rangle$ and $|\Psi_{EQ}\rangle$ eigenstates to the $\tilde{B}$ state. As in the case of excitation to the $\tilde{A}$ state, the spectra are found to be dominated by progressions in modes with frequencies of $\sim$0.05 eV. Again, these progressions are

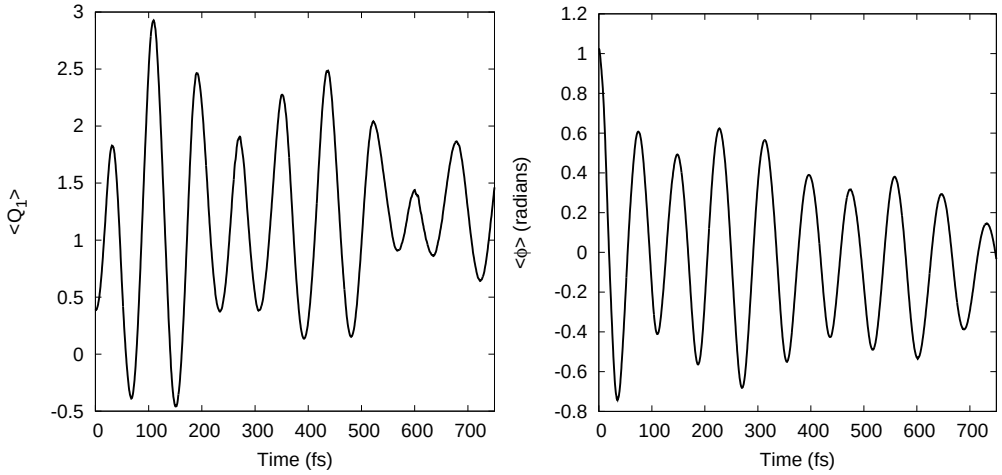

Fig. 5.16: Expectation values $\langle Q_1 \rangle$ and $\langle \phi \rangle$ calculated following excitation of the $|\Psi_{AX}\rangle$ conformer to the $\tilde{A}$ state.

attributed to the modes Q_1 and ϕ. Shown in Figure 5.18 are the expectation values $\langle Q_q \rangle$ and $\langle \phi \rangle$ calculated following excitation of the $|\Psi_{EQ}\rangle$ eigenstate to the $\tilde{B}$ state. Similar to the case of excitation to the $\tilde{A}$ state, a planarisation of the system is found to be driven following excitation to the $\tilde{B}$ state.

Finally, we show in Figure 5.19 the composite spectrum formed from the weighted sum of the four spectra corresponding each to excitation of one of the $|\Psi_{AX}\rangle$ and $|\Psi_{EQ}\rangle$ eigenstates to one of the $\tilde{A}$ and $\tilde{B}$ states, with the weights used being the products of: (i) the calculated oscillator strengths of the electronic states, and; (ii) the Boltzmann coefficient of the vibrational state calculated using the experimentally determined value of ΔE_{EQ-AX} =340 $\pm$50 cm^{-1} [75].

5.5 Discussion and Conclusions

Using the MCTDH method for wavepacket propagation in conjuction with the improved relaxation method for the generation of vibrational eigenstates, it has been possible to perform conformer-resolved quantum dynamics simulations of 3-pyrroline following excitation to its first two electronically excited

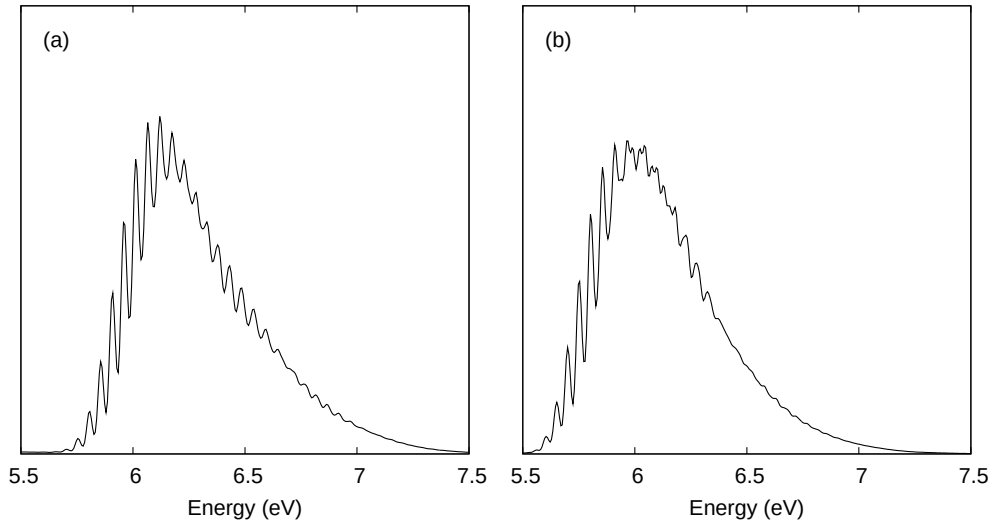

Fig. 5.17: (a) Calculated absorption spectrum corresponding to excitation of the AX conformer to the $\tilde{B}$ state. (b) Calculated absorption spectrum corresponding to excitation of the EQ conformer to the $\tilde{B}$ state.

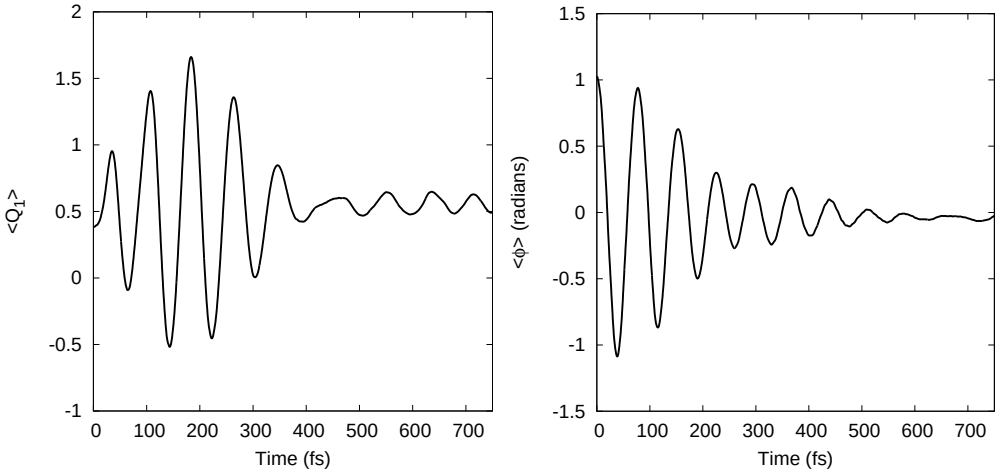

Fig. 5.18: Expectation values $\langle Q_1 \rangle$ and $\langle \phi \rangle$ calculated following excitation of the $|\Psi_{AX}\rangle$ conformer to the $\tilde{B}$ state.

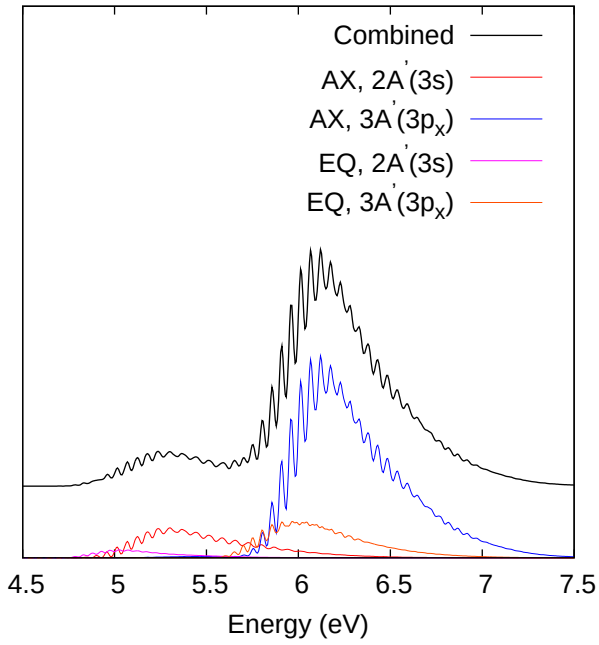

Fig. 5.19: Combined spectrum corresponding to excitation of the AX and EQ eigenstates to both the $\tilde{A}$ and $\tilde{B}$ electronic states. Each contribution is weighted by both the calculated oscillator strength of the electronic state and Boltzmann factors for the vibrational states calculated using the experimentally determined value of ΔE_{EQ-AX}=340 cm^{-1} [75]. For clarity, the combined spectrum is shifted upwards relative to the individual spectra.

states.

Pronounced similarities in the evolution of initial wavepackets corresponding to vertical excitation of the $|\Psi_{AX}\rangle$ and $|\Psi_{EQ}\rangle$ eigenstates to both the $\tilde{A}$ and $\tilde{B}$ states are found, with the calculated rates of N-H dissociation, evolution of state populations and branching ratios between the two N-H dissociation channels being much the same in each case. The similarities regarding the manner in which N-H dissociation proceeds may be rationalised by the common quasi-planar local minima shared by the $|\Psi_{AX}\rangle$ and $|\Psi_{EQ}\rangle$ states in both the electronically excited states $\tilde{A}$ and $\tilde{B}$, and that the planarisation of the C_2NH unit is found to be required for unhindered dissociation to occur in the $\tilde{A}$ state of 3-pyrroline. Both the $|\Psi_{AX}\rangle$ and $|\Psi_{EQ}\rangle$ eigenstates are vertically displaced to the repulsive walls of the $\tilde{A}$ state potential along the N-H out-of-plane bending mode ϕ, resulting in a similar frustration of N-H dissociation in each case. Further, the propensity for dissociation to occur from a planar arrangement of the C_2NH unit efficiently funnels the evolving wavepacket in each case towards the conical intersection with the ground state that is located at an elongated N-H bond length, resulting in a dominance of diabatic dissociation following excitation of both the $|\Psi_{AX}\rangle$ and $|\Psi_{EQ}\rangle$ eigenstates.

The calculated electronic absorption spectra corresponding to excitation of each of the $|\Psi_{AX}\rangle$ and $|\Psi_{EQ}\rangle$ eigenstates to each of the $\tilde{A}$ and $\tilde{B}$ states are all found to be dominated by progressions in the two modes Q_1 and ϕ, which together describe the planarisation of the C_4NH unit. Again, similarities may be drawn with ammonia, whose spectra corresponding excitation to its first excited state is well known to be dominated by progressions in the umbrella inversion mode, owing to the planarisation of the molecule in its $\tilde{A}$ state.

Chapter 6

Pyrrole

6.1 Introduction

The photodissociation of heteroaromatic molecules *via* a $\pi\sigma^*$ state is now well established as an important mechanism by which these molecules may relax following photoexcitation [5, 80]. This process has been the subject of numerous experimental [5, 9] and theoretical [6, 81] studies in recent years, prompted partly as this mechanism is believed to endow a range of biologically important molecules, including aromatic amino acids and the DNA bases, with photostability.

Pyrrole (C_4H_5N, see Figure 6.1), may be considered a prototype for this class of systems, and as such has been the focus of many recent studies [**?**, 69, 82–93]. The electronic spectrum of pyrrole exhibits a broad, intense band centred around 6 eV [94], believed to correspond predominantly to dipole-allowed transitions to the first two $B_2(\pi\pi^*)$ and $A_1(\pi\pi^*)$ valence states [94, 95]. Two $3s$ Rydberg states, $A_2(3s)$ and $B_1(3s)$, are known to exist at lower energies. As a result of strong vibronic coupling to higher lying $\pi\sigma^*$ states, these $3s$ Rydberg states acquire valence $\pi\sigma^*$ character, and consequently become dissociative, along the N-H dissociation coordinate. Illustrated schematically in Figure 6.2 are the topologies of these states along the N-H dissociation coordinate.

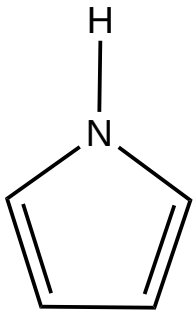

Fig. 6.1: Molecular structure of pyrrole.

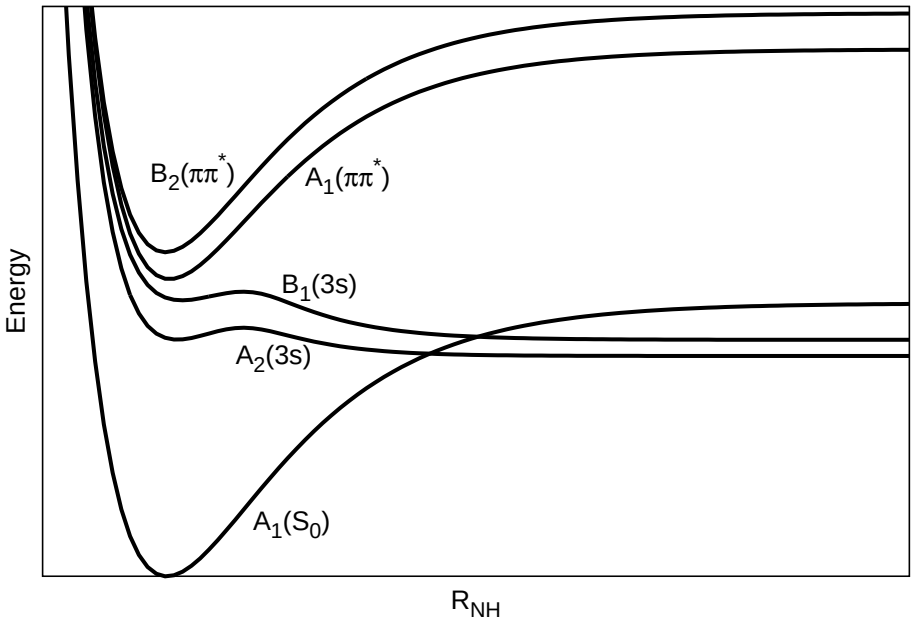

Fig. 6.2: Schematic adiabatic potentials corresponding to the $A_1(S_0)$, $A_2(3s)$, $B_1(3s)$, $A_1(\pi\pi^*)$, and $B_2(\pi\pi^*)$ states along the N-H dissociation coordinate.

The quantum dynamics simulations of Domcke *et al.* [69, 82–84] have established a timescale of ∼30 fs for direct dissociation of the high-energy components of the wavepacket following excitation to the $A_2(3s)$ and $B_1(3s)$ states. Support for this assignment has come from the time-resolved velocity map imaging studies of Stavros *et al.* [96]. However, a second, slower timescale for N-H dissociation of ∼120 fs has also been reported by both Stavros *et al.* and Lippert and co-workers that so far has not been found to be replicable by theoretical means.

The photofragment translational spectroscopy studies of Cronin *et al.* [90] and the photofragment velocity map imaging experiments of Wei and co-workers [92] suggest that following excitation to $B_2(\pi\pi^*)$ direct dissociation on the $A_2(3s)$ state still occurs. However, concomitant with the increase in excitation energy has been found to be an increase in the yield of low kinetic energy H-atoms produced [90], attributed to statistical dissociation following internal conversion to the ground state. It has thus been inferred that an efficient relaxation pathway exists to connect the $B_2(\pi\pi^*)$ and ground states. Identification of potentially accessible pathways that may radiationlessly connect these two states has been provided by the semi-classical surface hopping calculations of Barbatti and co-workers [86–89]. Specifically, essentially barrierless pathways along ring-puckering and ring-opening coordinates were found to connect the Franck-Condon point and conical intersections between the $B_2(\pi\pi^*)$ and ground states.

To date, the only fully quantum mechanical wavepacket propagation simulations of the nuclear dynamics of pyrrole upon excitation to the $B_2(\pi\pi^*)$ state has been conducted by Faraji *et al.* [85]. Ultrafast internal conversion, on a timescale of ∼100 fs, to the dissociative $A_2(3s)$ and $B_1(3s)$ states from the initially excited states was found to occur. However, the model Hamilto-

nian used was acknowledged to be incapable of the description of the origin of the significant yield of low kinetic energy H-atoms observed experimentally.

In this chapter, previous work is built upon through the construction of a model Hamiltonian capable of describing the nuclear dynamics of pyrrole following excitation to a manifold of five excited states, namely the $A_2(3s)$, $B_1(3s)$, $A_2(3p_z)$, $A_1(\pi\pi^*)$ and $B_2(\pi\pi^*)$ states. CASPT2 calculations have been used to construct detailed potential energy surfaces along all nuclear degrees of freedom. A model Hamiltonian based on the vibronic coupling Hamiltonian [19, 20] is developed and parameterised by fitting to this data. The model Hamiltonian constructed is used to simulate the dynamics of pyrrole following excitation to the $A_2(3s)$, $A_1(\pi\pi^*)$ and $B_2(\pi\pi^*)$ states. Further, the electronic absorption spectrum of pyrrole in the region 5.5 to 6.5 eV is calculated and characterised, and comparison to previous experimental and theoretical studies is drawn. It is found that the previously neglected $A_2(3p_z)$ Rydberg state plays an active role following excitation to the $B_2(\pi\pi^*)$ state and is required to reproduce in a satisfactory manner the first band in the electronic absorption spectrum of pyrrole.

6.2 Theoretical Framework

6.2.1 The Model Hamiltonian

The starting point in the construction of our model Hamiltonian is the vibronic coupling Hamiltonian of Köppel *et al* [19, 20]. As is stands, however, this model is not entirely suitable for our needs: a low-order expansion of the diabatic potential matrix will not suffice to describe large amplitude motion such as the N-H dissociation pathways known to be of utmost importance with regard to the photochemistry of pyrrole. We here, however, do take the pyrrolyl radical C_4H_4N to undergo only small amplitude displacements

following electronic excitation. As such, we chose as the first of our $3N$-9 nuclear coordinates the normal modes $\{Q_\alpha\}$; $\alpha = 1, \ldots, 3N-9$, of the pyrrolyl radical at the geometry corresponding to the arrangement of the C_4H_4N moiety at the Franck-Condon point of the parent pyrrole molecule. As the remaining three coordinates we choose the spherical polar coordinates of the hydrogen atom of the N-H bond, denoted H_d, taken relative to the position of the nitrogen atom at the Franck-Condon point, $\boldsymbol{X}_N^{FC}$, of the parent pyrrole molecule, denoted $\boldsymbol{r} = (R, \theta, \phi)$. Here, R denotes the distance of H_d from $\boldsymbol{X}_N^{FC}$, while θ and ϕ correspond, respectively, to the in- and out-of-plane angles formed by the N-H_d bond relative to the plane defined by the C-N-C vertex.

Making use of the division into the two subsets of degrees of freedom $\boldsymbol{Q}$ and $\boldsymbol{r}$, we write the full potential as a sum of three parts,

$$\boldsymbol{W}(\boldsymbol{Q}, \boldsymbol{r}) = \boldsymbol{W}(\boldsymbol{Q}) + \boldsymbol{W}(\boldsymbol{r}) + \boldsymbol{W}^{int}(\boldsymbol{Q}, \boldsymbol{r}). \tag{6.1}$$

where, $\boldsymbol{W}^{int}(\boldsymbol{Q})$ describes the correlation of the two subsets of nuclear degrees of freedom $\boldsymbol{Q}$ and $\boldsymbol{r}$. As alluded to above, we model the model diabatic potential in the space spanned by the degrees of freedom $\boldsymbol{Q}$, $\boldsymbol{W}(\boldsymbol{Q})$, by a vibronic coupling Hamiltonian:

$$\boldsymbol{W}(\boldsymbol{Q}) = \boldsymbol{W}^{(0)}(\boldsymbol{Q}) + \boldsymbol{W}^{(1)}(\boldsymbol{Q}) + \boldsymbol{W}^{(2)}(\boldsymbol{Q}) + \cdots, \tag{6.2}$$

with the terms appearing in Equation 6.2 being given in Chapter 3.8.

The potential in the space spanned by the degrees of freedom $\boldsymbol{r}$ is modelled as follows. The diabatic potentials and nonadiabatic coupling along the in- and out-of-plane bending angles θ and ϕ are modelled by low-order Taylor expansions about the Franck-Condon point:

$$W_{ii}(\theta,\phi,R) = \kappa_{\theta}^{(i)}(R)\theta + \kappa_{\phi}^{(i)}(R)\phi + \frac{1}{2}(\gamma_{\theta\theta}^{(i)}(R)\theta^2 + \gamma_{\phi\phi}^{(i)}(R)\phi^2) + \frac{1}{24}\epsilon_{\phi}^{(i)}(R)\phi^4\delta_{i6} + W_{ii}(R) \tag{6.3}$$

$$W_{ij}(\theta,\phi,R) = \lambda_{\theta}^{(i,j)}(R)\theta + \lambda_{\phi}^{(i,j)}(R)\phi \tag{6.4}$$

That the modelling of the potential along ϕ for the sixth diabatic state, corresponding to the $B_2(\pi\pi^*)$ state, requires the inclusion of a fourth-order term is enforced by the double-well topology of the corresponding adiabatic potential. Whilst it is possible that this feature of the adiabatic potential is the result of the coupling of the $B_2(\pi\pi^*)$ state to a higher-lying state, such a treatment is not within the scope of this work, owing to the need to truncate the subspace of electronic states considered at a tractable level.

The parameters entering into the expansions 6.3 and 6.4 are written as functions of the N-H dissociation coordinate, R. This reflects that as the dissociation limit is reached the contribution of these terms to the potential should decay to zero. This is achieved by expanding these terms about the Franck-Condon N-H bond length, R_0, as follows:

$$\kappa_a^{(i)}(R) = \kappa_a^{(i)}(R_0)[1 - \tanh(k_a^{(i)}R)], \quad a = \theta, \phi \tag{6.5}$$

$$\gamma_{aa}^{(i)}(R) = \gamma_{aa}^{(i)}(R_0)[1 - \tanh(g_{aa}^{(i)}R)], \quad a = \theta, \phi \tag{6.6}$$

$$\epsilon_{\phi}^{(6)}(R) = \epsilon_{\phi}^{(6)}(R_0)[1 - \tanh(e_{\phi\phi}^{(6)}R)] \tag{6.7}$$

$$\lambda_a^{(i,j)}(R) = \lambda_a^{(i,j)}(R_0)[1 - \tanh(l_a^{(i,j)}R)], \quad a = \theta, \phi \tag{6.8}$$

The anharmonic diabatic potentials along R are described as follows. For states bound with respect to R, we choose to model the diabatic potentials

as Morse oscillators:

$$W_{ii}^{bound}(R) = D_0^i \left[1 - \exp\left(-\alpha_i \left(R - R_0^i\right)\right)\right]^2 \tag{6.9}$$

For the dissociative $3s$ states, the diabatic potentials are modelled using avoided crossing model potentials:

$$\begin{aligned} W_{ii}^{diss}(R) = &\frac{1}{2}\left(\nu_i^{bound}(R) + \nu_i^{diss}(R)\right) \\ &- \frac{1}{2}\left[\left(\nu_i^{bound}(R) - \nu_i^{diss}(R)\right)^2 + 4\lambda_i^2\right]^{\frac{1}{2}}, \end{aligned} \tag{6.10}$$

with

$$\nu_i^{bound}(R) = D_{0,b}^i \left[1 - \exp\left(-\alpha_b^i \left(R - R_{0,b}^i\right)\right)\right]^2 \tag{6.11}$$

$$\nu_i^{diss}(R) = P_i \left(\exp\left(-\alpha_d^i (R - R_{0,d}^i)\right)\right) + D_{0,d}^i. \tag{6.12}$$

The coupling of the two subsets of nuclear degrees of freedom, $\boldsymbol{r}$ and $\boldsymbol{Q}$, is achieved *via* the use the interaction potential $\boldsymbol{W}^{int}(\boldsymbol{Q}, \boldsymbol{r})$, which we take as

$$\boldsymbol{W}^{int}(\boldsymbol{Q}, \boldsymbol{r}) = \boldsymbol{W}^{int(1)}(\boldsymbol{Q}, \boldsymbol{r}) + \boldsymbol{W}^{int(2)}(\boldsymbol{Q}, \boldsymbol{r}) + \ldots, \tag{6.13}$$

with

$$W_{ii}^{int(1)}(\mathbf{Q}, \mathbf{r}) = \sum_{\alpha=1}^{3N-9} {}^1K_\alpha^{(i)} \tanh({}^2K_\alpha^{(i)} R) Q_\alpha, \tag{6.14}$$

$$W_{ij}^{int(1)}(\mathbf{Q}, \mathbf{r}) = \sum_{\alpha=1}^{3N-9} {}^1\Lambda_\alpha^{(i,j)} \tanh({}^2\Lambda_\alpha^{(i,j)} R) Q_\alpha, \tag{6.15}$$

$$W_{ii}^{int(2)}(\mathbf{Q}, \mathbf{r}) = \sum_{\alpha,\beta=1}^{3N-9} {}^1\Gamma_{\alpha\beta}^{(i)} \tanh({}^2\Gamma_{\alpha\beta}^{(i)} R) Q_\alpha Q_\beta \tag{6.16}$$

The terms ${}^1K_\alpha^{(i)}$ and ${}^1\Gamma_{\alpha\beta}^{(i)}$ correspond to the change in the equilibrium geometry of the pyrrolyl fragment and the rotation of the normal modes of the pyrrolyl fragment, respectively, as the N-H bond dissociates. The terms ${}^1\Lambda_\alpha^{(i,j)}$ describe the corresponding changes in nonadiabatic coupling with repect to the pyrrolyl normal modes as the dissociation coordinate is traversed.

In the coordinate system used, we may write the kinetic energy T_N operator as

$$\begin{aligned} T_N = &-\frac{1}{2}\sum_{\alpha=1}^{3N-9}\omega_\alpha\frac{\partial^2}{\partial Q_\alpha^2} \\ &-\frac{1}{\mu}\left(\frac{1}{R}\frac{\partial^2}{\partial R^2}R+\frac{1}{R^2\sin\phi}\frac{\partial}{\partial\phi}\sin\phi\frac{\partial}{\partial\phi}+\frac{1}{R^2\sin^2\phi}\frac{\partial^2}{\partial\theta^2}\right), \end{aligned} \tag{6.17}$$

where ω_α is the frequency of the pyrrolyl fragment normal mode Q_α, and

$$\frac{1}{\mu}=\frac{1}{m_H}+\frac{1}{m_f}. \tag{6.18}$$

Here, m_h and m_f denote the masses of the hydrogen atom and the pyrrolyl fragment, respectively.

6.2.2 Fitting of the Model Potential and Electronic Structure Calculations

The parameters entering into the expansion of the model potential were determined through the minimisation of the weighted root mean square deviation (RMSD) of the model and calculated adiabatic energies as described in Section 4.3.2.

The reference geometry used corresponds to the FC point, which was optimised using the MP2 method, employing the aug-cc-pVDZ basis. The normal modes of the pyrrolyl radical in the geometry corresponding to the removal of the active hydrogen atom from the parent pyrrole molecule were

also calculated using this method and basis. Both calculations were made using the GAUSSIAN 03 package [97].

Calculations of the adiabatic potentials were performed using the complete active CASPT2 method. In order to properly describe the $A_2(3s)$, $B_1(3s)$, $A_1(\pi\pi^*)$, and $B_2(\pi\pi^*)$ states, an active space consisting of the $8a_1(\sigma)$, $1b_1(\pi)$, $2b_1(\pi)$, $1a_2(\pi)$, $10a_1(3s/\sigma^*)$, $3b_1(\pi^*)$ and $2a_2(\pi^*)$ orbitals was used. Additionally, the $11a_1(3p_z)$ orbital was included in order to allow for the description of the low-lying $A_2(3p_z)$ state. Thus, an active space consisting of 8 electrons in 8 orbitals was used in all calculations.

In order to attain a balanced description of the calculated potentials, all reference CASSCF calculations were averaged equally over the seven lowest-lying electronic states, corresponding at the FC point, in ascending order, to the adiabatic states $A_1(S_0)$, $A_2(3s)$, $B_1(3s)$, $A_2(3p_z)$, $A_1(\pi\pi^*)$, $B_2(\pi\pi^*)$, and $B_1(3p_z)$. The symmetries and vertical excitation energies of these states are given in Table 6.1. All of the stated states were used in the construction of the model potential, which thus corresponds to an 7×7 matrix representation of the electronic Hamiltonian.

The above mentioned CASPT2 calculations were performed using a basis set based upon the the aug-cc-pVDZ basis. In order to describe correctly the Rydberg character of the $A_2(3s)$ and $B_1(3s)$ states in the vicinity of the Franck-Condon (FC) point, additional diffuse s functions (one centred on the nitrogen atom and two on the active hydrogen atom) and p functions (one set centred on the nitrogen atom and two sets on the active hydrogen atom) were used. Following Vallet *et al.* [69], the exponents of these additional functions were derived in an even-tempered manner *via* the successive division of the exponents of the most diffuse s and p functions in the aug-cc-pVDZ basis by a factor of three. We denote the resulting basis set by aug+.

Table 6.1: Symmetries, dominant configurations and vertical excitation energies E_v of the first seven adiabatic electronic states of pyrrole as obtained from CASPT2(8,8)/aug+ calculations at the FC point. The bracketed numbers displayed alongside the dominant configurations are the corresponding coefficients. All energies are given in units of eV.

State	Symmetry	Character	Dominant configurations	E_v (CASSCF)	E_v (CASPT2)
S_0	A_1		$\|0\rangle$	0.00	0.00
S_1	A_2	$3s$	$1a_2 \rightarrow 10a_1$ (0.94)	4.17	5.06
S_2	B_1	$3s$	$2b_1 \rightarrow 10a_1$ (0.92)	4.87	5.86
S_3	A_2	$3p_z$	$1a_2 \rightarrow 11a_1$ (0.94)	4.91	5.87
S_4	A_1	$\pi\pi^*$	$2b_1 \rightarrow 3b_1$ (0.68) $1a_2 \rightarrow 2a_2$ (0.44)	6.47	6.01
S_5	B_2	$\pi\pi^*$	$1a_2 \rightarrow 3b_1$ (0.90)	7.83	6.24
S_6	B_1	$3p_z$	$2b_1 \rightarrow 11_{a1}$ (0.93)	5.67	6.69

6.3 Results

6.3.1 Electronic Structure Calculations

The quality of the model diabatic potential energy surfaces (PESs) used is dependent upon the accuracy of the adiabatic PESs to which they are fitted. In turn, the accuracy of the adiabatic PESs may be evaluated from comparison of the calculated vertical excitation energies (VEEs) with previously reported experimental and theoretical values. This information is shown in Table 6.2. Overall, no particularly strong consensus on the values VEEs of the states considered here appears to exist in the literature. An exception is the $A_2(3s)$ state, which is generally accepted to lie at around 5.2 eV [94, 98–100]. The value of 5.06 eV furnished by the present CASPT2(8,8)/aug+ calculations for the VEE of the $A_2(3s)$ state, although slightly too low, is in reasonable agreement with previously determined values. Previous theoretical studies have generally placed the VEE of the $B_1(3s)$ state between 5.85 and 6.0 eV, in good agreement with the value reported here. Experimental studies, however, have reported a VEE for this state of ∼6.4 eV [94,101], in stark disagreement to the most generally accepted theoretically determined values. As will be commented on further in Section 6.3.6, we consider these previously reported experimental assignments to be somewhat erroneous. Previous theoretical studies have determined the VEE of the bright $B_2(\pi\pi^*)$ state to lie at around 6.0 eV [98–100]. An experimentally determined value of 5.9 eV has also been reported for the VEE of the $B_2(\pi\pi^*)$ state [101]. The VEE of 6.24 eV yielded by our CASPT2(8,8)/aug+ calculations is significantly higher than these previously reported values. As will be explained more fully in Section 6.3.6, we have confidence in the seemingly high $B_2(\pi\pi^*)$ VEE reported here on account of the utilisation of this value in the model Hamiltonian constructed leading to the correct reproduction of the experimental absorption

spectrum. There exists no conclusive experimentally assigned VEEs for the of the $A_2(3p_z)$ and $A_1(\pi\pi^*)$ states. However, good agreement between the present calculated $A_2(3p_z)$ VEE and previously calculated values is seen.

Together with the VEEs, the zeroth-order Hamiltonian, $\boldsymbol{W}^{(0)}(\boldsymbol{Q})$, is constructed using the frequencies of the normal modes of the pyrrolyl radical. These are displayed in Table 7.1. As the normal modes used are not calculated at the Franck-Condon point of the pyrrolyl radical, but rather at the ground state minimum geometry of the C_4H_4N unit of the parent pyrrole molecule, comparison to experimental values is not made here. In order to aid the interpretation of the symmetry labels shown, it is noted that here the pyrrole molecule is taken to lie in the $y, z-$plane with the N-H bond coincident with the $z-$axis.

6.3.2 The Model Hamiltonian

A total of 2214 parameters entering into the model potential were fitted to 12239 adiabatic energies. A weighted RMSD of the model adiabatic surfaces from the adiabatic energies fitted to of 0.076 eV was obtained, indicating that the model potential is capable of reproducing satisfactorily the adiabatic potentials in the regions of nuclear configuration space considered.

The intrastate linear coupling constants, $\kappa_\alpha^{(i)}$ are listed in Table 7.3. The significance of these terms is that they give the gradients of the diabatic states at the reference point with respect to the totally symmetric modes. Thus, modes Q_α with large corresponding terms $\kappa_\alpha^{(i)}$ can be expected to contribute significantly to the dynamics following excitation to the state indexed by i. For the $B_2(\pi\pi^*)$ and $A_1(\pi\pi^*)$ states, the gradients at the reference point with respect to the ring-stretching mode Q_{12} and the ring-breathing mode Q_{16} are found to be an order of magnitude larger than for those defined with respect to the remaining totally symmetric modes. Barrierless pathways

Table 6.2: A comparison of the calculated CASPT2(8,8)/aug+ vertical excitation with previously reported values determined both experimentally and theoretically.[a]Ref 98, [b]Ref 99, [c]Ref 100, [d]Ref 94, [e]Ref 101.

State	Present work	MR-CASPT2[a]	EOM-CCSD[b]	CCSD[c]	Experimental
$A_2(\pi\sigma^*)$	5.06	5.22	5.18	5.17	5.22[d,e]
$B_1(\pi\sigma^*)$	5.86	6.02	5.84	5.88	6.43[d,e]
$A_2(3p_z)$	5.87	6.01	5.88	5.91	-
$A_1(\pi\pi^*)$	6.01	5.98	6.55	6.55	-
$B_2(\pi\pi^*)$	6.24	5.95	6.02	6.01	5.90[e]

Table 6.3: Normal mode symmetries and frequencies of the pyrrolyl radical calculated calculated at the FC point. Both the nuclear geometry used and the Hessian were calculated using the MP2 method and aug-cc-pVDZ basis. oop: out-of-plane, sym: symmetric, asym: asymmetric.

Mode	Symmetry	Frequency	Description
Q_1	A_2	0.0609	ring twisting
Q_2	B_1	0.0735	C-N-C oop bending
Q_3	B_1	0.0867	C-H oop bending (sym)
Q_4	A_2	0.0990	C-H oop bending (asym)
Q_5	A_1	0.1097	ring breathing
Q_6	B_2	0.1111	ring stretching
Q_7	B_1	0.1118	C-H oop bending (sym)
Q_8	A_2	0.1135	C-H oop bending (asym)
Q_9	B_2	0.1282	ring stretching
Q_{10}	A_1	0.1283	ring breathing
Q_{11}	A_1	0.1366	ring breathing
Q_{12}	A_1	0.1482	ring breathing
Q_{13}	B_2	0.1531	C-H in-plane bending (sym)
Q_{14}	B_2	0.1623	C-H in-plane bending (asym)
Q_{15}	A_1	0.1821	ring stretching
Q_{16}	A_1	0.1885	ring stretching
Q_{17}	B_2	0.4052	C-H stretching (asym)
Q_{18}	A_1	0.4071	C-H stretching (asym)
Q_{19}	B_2	0.4085	C-H stretching (asym)
Q_{20}	A_1	0.4115	C-H stretching (sym)
Q_{21}	B_2	0.5063	ring stretching

Table 6.4: Linear intrastate coupling constants (eV) determined by fitting to adiabatic energies calculated at the CASPT2(8,8)/aug+ level.

Degree of freedom	S_1	S_2	S_3	S_4	S_5
Q_5	0.0381	-0.1390	0.0251	0.0429	0.0395
Q_{10}	-0.0055	0.1270	-0.0339	-0.0369	-0.0348
Q_{11}	-0.1440	-0.0924	0.0440	0.0439	-0.0185
Q_{12}	0.0631	-0.0193	0.0195	-0.2283	-0.1597
Q_{15}	-0.0302	-0.0684	0.0043	-0.0288	0.0655
Q_{16}	-0.1872	0.1435	-0.1521	-0.1270	-0.1489
Q_{18}	-0.0002	0.0077	0.0078	0.0195	0.0060
Q_{20}	0.0113	0.0282	0.0185	0.0790	0.0382

connecting the Franck-Condon point and conical intersections that connect all the excited states considered are also found to exist along Q_{12} and Q_{16}, as illustrated in Figure 6.3. As such, these two totally symmetric modes were chosen for inclusion in the calculations starting from the two $\pi\pi^*$ states considered.

Table 7.4. lists the interstate linear coupling constants, $\lambda_\alpha^{(i,j)}$. These are the terms that enter to first-order in the expansion of the off-diagonal elements W_{ij} of the potential matrix, and are thus the most important with respect to the description of the non-adiabatic coupling present in the subspace of electronic states considered. The calculated values of these terms are, in general, relatively small. However, non-zero terms $\lambda_\alpha^{(i,j)}$ exist to directly or indirectly couple all pairs of states. The antisymmetric C-H stretching modes Q_{17} and Q_{19} are found to couple the $B_2(\pi\pi^*)$ and $A_1(\pi\pi^*)$ states, and also the $A_2(3s)$ and $B_1(3s)$ states. The $A_2(3s)$ and $B_1(3s)$ states are also found to be coupled by the ring stretching mode Q_{21}, which also serves to couple the $A_2(3p_z)$ and $B_1(3s)$ states. The symmetric C-H out-of-plane bending modes Q_3 and Q_7 couple the $B_2(\pi\pi^*)$ and $A_2(3p_z)$ states.

Also worthy of mention is the C-N-C out-of-plane bending mode Q_2, motion along which provides a barrierless pathway from the $B_2(\pi\pi^*)$ state to the

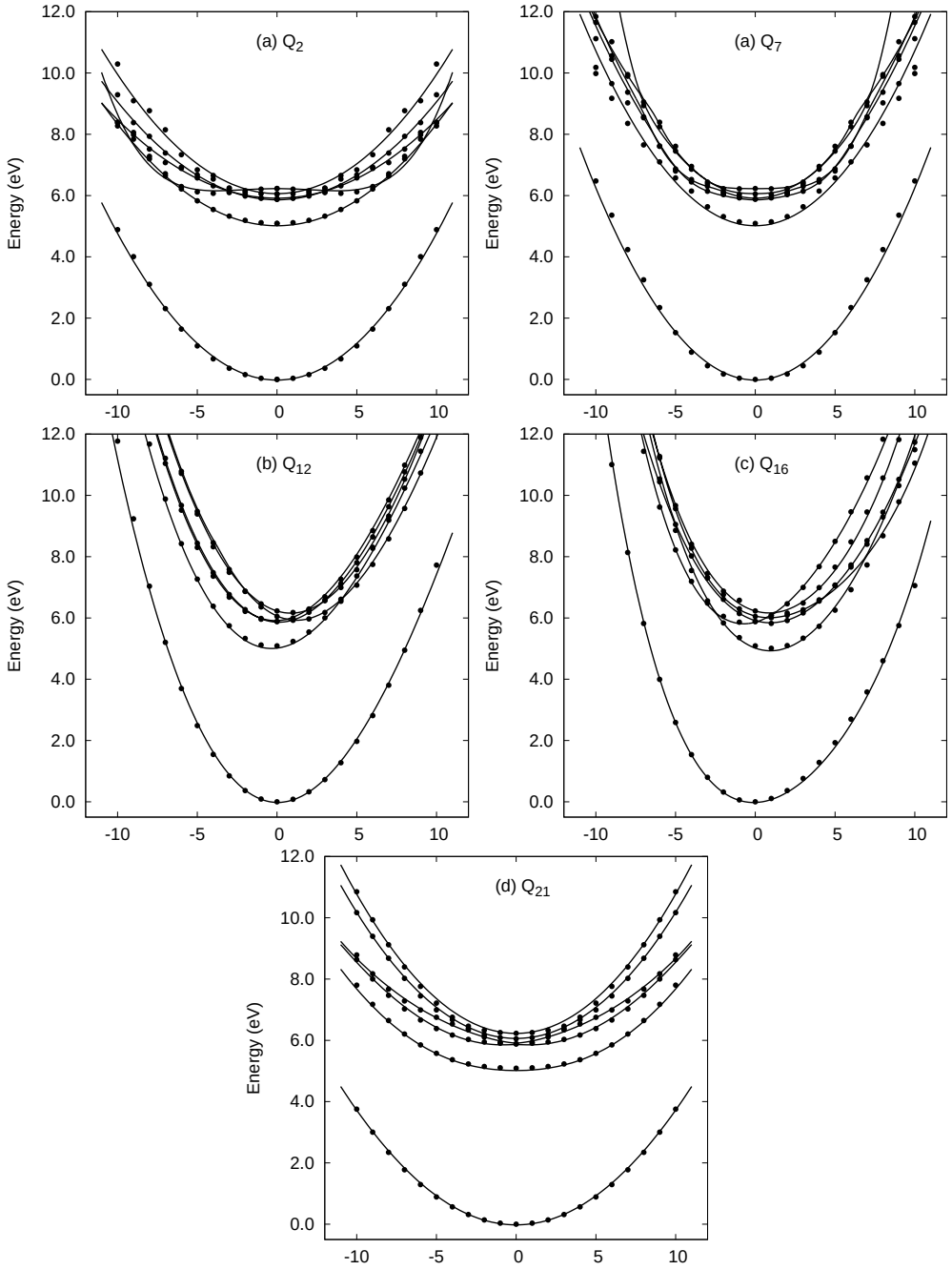

Fig. 6.3:

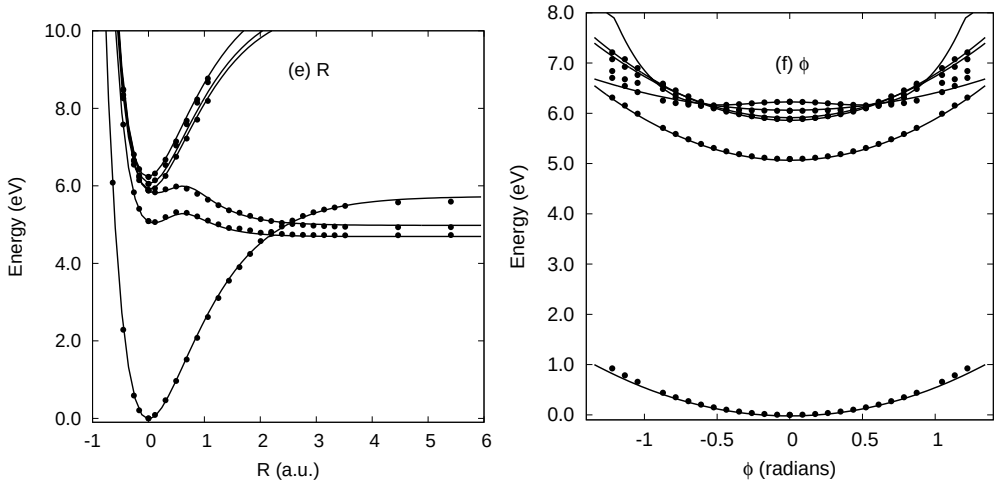

Fig. 6.3: Model (lines) and calculated (points) adiabatic energies along nuclear degrees of freedom important for the description of the dynamics of pyrrole following photoexcitation.

Table 6.5: Linear interstate coupling constants (eV)

Symmetry	Mode	$S_0 - S_4$	$S_1 - S_3$			
A_1	Q_5	0.0000	0.0046			
	Q_{16}	0.0008	-0.0056			
Symmetry	Mode	$S_0 - S_2$	$S_1 - S_5$	$S_2 - S_4$	$S_3 - S_5$	
B_1	Q_3	0.0000	-0.0059	0.0000	0.0293	
	Q_7	-0.0001	0.0000	0.0539	-0.0479	
	ϕ	0.7262	0.0000	0.0000	0.0000	
Symmetry	Mode	$S_0 - S_5$	$S_1 - S_2$	$S_2 - S_3$	$S_4 - S_5$	
B_2	Q_6	0.0000	-0.0056	0.0067	0.0110	
	Q_{13}	0.0000	0.0115	-0.0105	0.0000	
	Q_{17}	-0.1294	0.0322	0.0086	0.0371	
	Q_{19}	-0.0736	0.0533	0.0000	0.0364	
	Q_{21}	0.0000	0.0892	0.0635	0.0000	
Symmetry	Mode	$S_0 - S_1$	$S_0 - S_3$	$S_1 - S_4$	$S_2 - S_5$	$S_3 - S_4$
A_2	Q_4	-0.007	0.0000	0.0330	0.0306	-0.0024

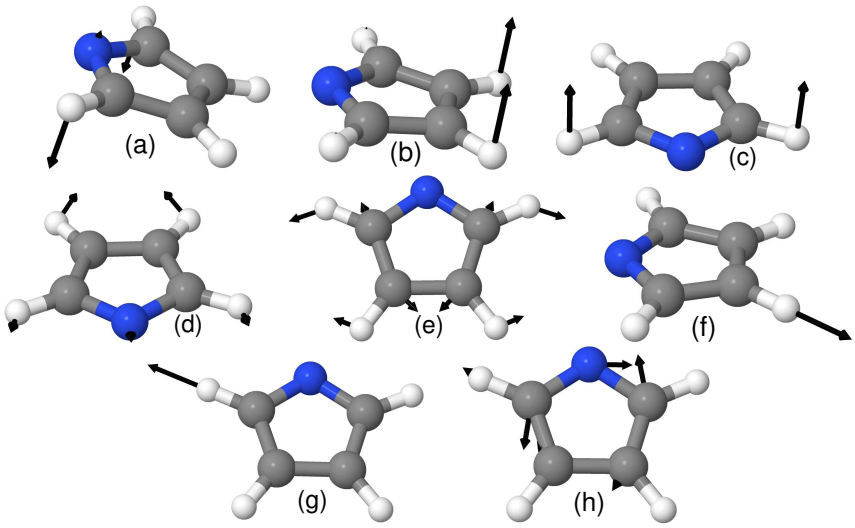

Fig. 6.4: Normal modes of the pyrrolyl radical important for the description of the photoinduced dynamics of the pyrrole molecule: (a) Q_2 (C-N-C out-of-plane bending), (b) Q_3 (C-H out-of-plane bending), (c) Q_7 (C-H out-of-plane bending), (d) Q_{12} (ring breathing), (e) Q_{16} (ring stretching), (f) Q_{17} (C-H stretching), (g) Q_{19} (C-H stretching), and (h) Q_{21} (ring stretching).

$A_2(3s)$ state, as is illustrated in Figure 6.3 (a). Thus, in terms of their impact on the excited state dynamics of pyrrole, the set of eight pyrrolyl normal modes Q_2, Q_3, Q_7, Q_{12}, Q_{16}, Q_{17}, Q_{19}, Q_{21} may be considered to be of most importance, and these are illustrated in Figure 6.4.

Turning our attention to the nuclear coordinates $\boldsymbol{r}$ of the dissociating hydrogen atom, it is found that only the N-H stretching coordinate R and the out-of-plane bending coordinate ϕ are of interest, with the potentials along the non-totally symmetric in-plane bending coordinate θ being rather harmonic and there existing no significant interstate coupling with respect to this coordinate. The model adiabatic potentials along R are shown in Figure 6.3 (e). Overall good agreement between the model and calculated CASPT2 adiabatic energies is found. In particular, we note that the model S_2 adiabatic dissociation limit is reproduced well by the model potential, a consequence of an appropriate choice of nuclear coordinates. Compared to

Table 6.6: Computational details of the wavepacket propagations corresponding to excitation to the $B_2(\pi\pi^*)$ state. The DVR types exp and HO correspond to exponential and Harmonic oscillator DVRs, respectively. N_i, N_j are the number of primitive DVR functions used to describe each particle. n_i are the number of single-particle functions used for each state.

Particle	DVR type	N_i, N_j	n_1, n_2, ..., n_6
R	exp	71	5, 6, 6, 4, 2, 5
ϕ	exp	71	5, 6, 6, 6, 3, 18
Q_{12}, Q_{16}	HO, HO	30, 30	5, 9, 8, 6, 4, 7
Q_2, Q_4	HO, HO	100, 16	7, 7, 8, 11, 5, 18
Q_3, Q_7	HO, HO	50, 70	6, 6, 8, 8, 4, 18
Q_{17}, Q_{21}	HO, HO	16, 70	5, 7, 6, 6, 4, 5

the dissociation energy of 5.6 eV obtained from high-level MRCI+Q calculations by Barbatti and co-workers [88], the value of 5.73 eV furnished by our model potential can be deemed satisfactory. In contrast, the recent quantum dynamics simulations of Faraji *et al.* [85] employed the full set of normal modes of pyrrole, and as such approximated the N-H dissociation coordinate by the N-H stretching normal mode. As a consequence, the model S_2 dissociation energy obtained was rather too high, lying at 6.55 eV. Together with the N-H dissociation coordinate R, the out-of-plane bending coordinate ϕ is of interest due to its significant first-order coupling of the ground and $B_1(3s)$ states. Additionally, as shown in Figure 6.3 (f), starting from the FC point in the $B_2(\pi\pi^*)$ state there exists a barrierless pathway along ϕ to conical intersections with the $A_1(\pi\pi^*)$, $A_2(3p_z)$, and $B_1(3s)$ states.

6.3.3 Dynamics Following Excitation to the $B_2(\pi\pi^*)$ State

To simulate the excitation of pyrrole to the $B_2(\pi\pi^*)$ state, an initial wavepacket was produced by vertical excitation of a ground state wavepacket to the corresponding diabatic state in the model used, that is, state six. In turn, the ground state wavepacket was obtained using the method of relaxation on the ground state potential. Wavepacket propagations were performed using the

ten modes R, ϕ, Q_2, Q_3, Q_4, Q_7, Q_{12}, Q_{16}, Q_{17} and Q_{21}, and employing the six-dimensional manifold of electronic states comprising the ground state and the excited states $A_2(3s)$, $B_1(3s)$, $A_2(3p_z)$, $A_1(\pi\pi^*)$ and $B_2(\pi\pi^*)$. A propagation time of 750 fs was used in all calculations. All other details are given in Table 6.6.

Shown in Figure 6.5 (a) are the calculated diabatic state populations following excitation to the $B_2(\pi\pi^*)$ state. An initial period of rapid transfer of population from the initially excited $B_2(\pi\pi^*)$ state is seen, lasting approximately 50 fs. Proceeding this is a period of hindered transfer of population to the lower-lying states, with a final probability of population of the $B_2(\pi\pi^*)$ state 0.43 being attained after 750 fs. This result is not in accord with the previous wavepacket dynamics calculations of Faraji *et al.* [85] who reported an almost complete depletion of the population of the initially excited $B_2(\pi\pi^*)$ state within 100 fs. The origin of the hindrance of the depopulation of the $B_2(\pi\pi^*)$ state is found to involve the C-N-C out-of-plane bending mode Q_2. Figure 6.5 (b) shows the diabatic state populations following excitation to the $B_2(\pi\pi^*)$ state calculated using a nine-mode model identical to the previously discussed ten-mode model in all aspects expect for the degree of freedom Q_2 being removed. The effect of the removal of this degree of freedom is that the rate of depopulation of the initially excited $B_2(\pi\pi^*)$ state now both begins and remains high.

We note that the present results are in partial agreement with the photofragment translational spectroscopy studies of Cronin *et al.* [90], who reported a rise in the production of low-kinetic energy hydrogen atoms upon increasing the excitation energy used to the point at which excitation to the $B_2(\pi\pi^*)$ state is expected to occur. The production of low-kinetic energy hydrogen atoms may be equated with statistical dissociation in the ground electronic

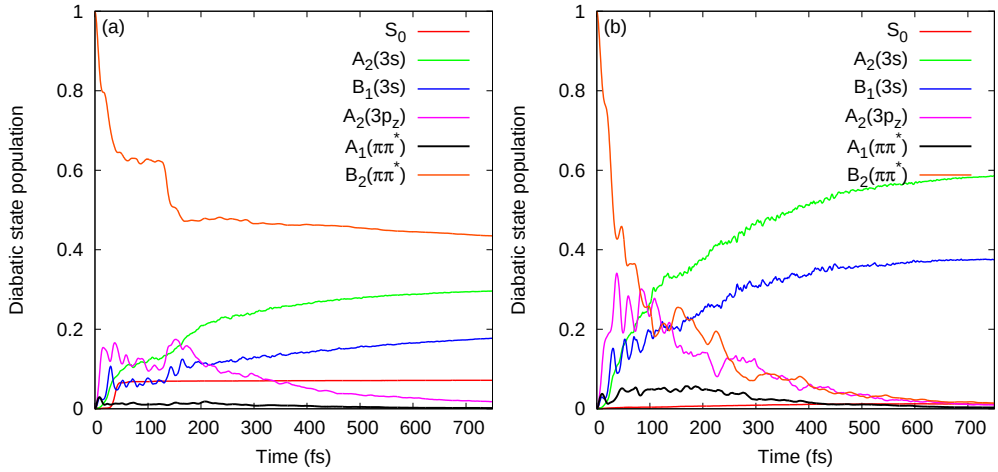

Fig. 6.5: Calculated diabatic state populations following excitation to the $B_2(\pi\pi^*)$ state. (a) State populations calculated using a ten-mode model including the mode Q_2. (b) State populations calculated using a nine-mode model excluding the mode Q_2.

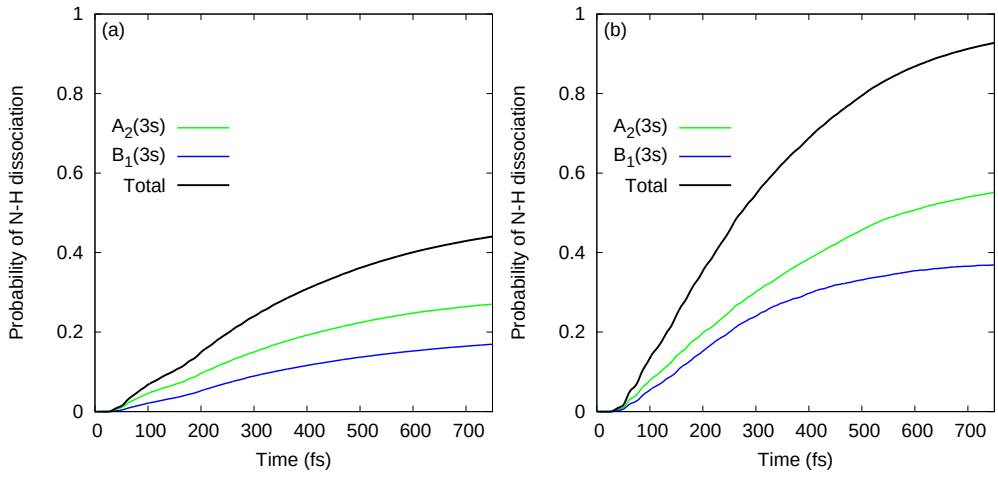

Fig. 6.6: Calculated probabilities of N-H dissociation following excitation to the $B_2(\pi\pi^*)$ state. (a) Dissociation probabilities calculated using a ten-mode model including the mode Q_2. (b) Dissociation probabilities calculated using a nine-mode model excluding the mode Q_2

state, and hence with a hindrance of direct dissociation in the $A_2(3s)$ and $B_1(3s)$ states. We observe a significant decrease in the time-cumulated probability of N-H dissociation for the case in which the mode Q_2 is included in the wavepacket propagation relative to that in which it is not, as illustrated in Figure 6.6. This inhibition of direct dissociation is, of course, a consequence of the diabatic trapping of population in the $B_2(\pi\pi^*)$ state.

Displayed in Figure 6.7 is a representative plot of the one-dimensional reduced density along the mode Q_2 at 410 fs for the component of the wavepacket corresponding to the $B_2(\pi\pi^*)$ state. A significant displacement of the wavepacket along this degree of freedom is found to occur. In Figure 6.8 is shown a geometry representative of the locality of the density in the $B_2(\pi\pi^*)$ state after for times greater than 200 fs together with the geometry of the so-called ring-puckered conical intersection between the $B_2(\pi\pi^*)$ and ground states. We tentatively note the similarity between the two structures, and as such cautiously speculate that within our model the system may be evolving towards the ring-puckered conical intersection, but that at present the limited accuracy of the model potential is such that an accurate description of the potential in the vicinity of this geometry prohibits relaxation to the ground state.

We note that the $A_2(3p_z)$ state, that has been neglected in all previous studies of photoexcited pyrrole, is populated to a significant extent following excitation to the $B_2(\pi\pi^*)$ state. As shown in Figure 6.5 (a), a significant proportion of the population exiting from the $B_2(\pi\pi^*)$ state effectively cascades first into the $A_2(3p_z)$ state, and subsequently from the $A_2(3p_z)$ into the $B_1(3s)$ state, as attested to by the out-of-phase oscillations in the diabatic population probabilities of these two states.

As illustrated in Figure 6.6 (a), dissociation of the N-H bond following

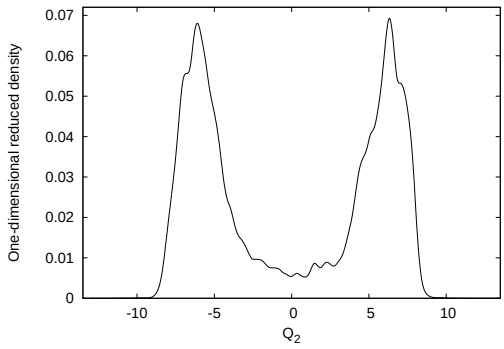

Fig. 6.7: The calculated one-dimensional reduced density along the C-N-C out-of-plane bending mode Q_2 at 410 fs following vertical excitation to the $B_2(\pi\pi^*)$ state.

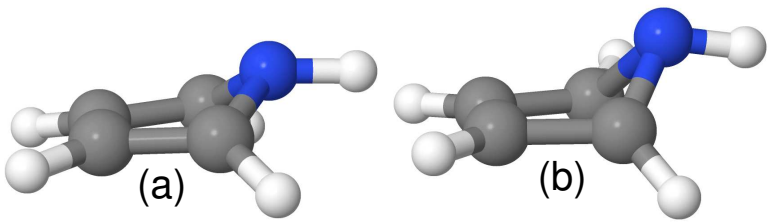

Fig. 6.8: (a) Geometry representative of the location of density in the $B_2(\pi\pi^*)$ state for times greater than 200 fs. (b) Geometry of the ring-puckered conical intersection between the $B_2(\pi\pi^*)$ state and the ground state optimised at the CAS(6,6)/6-311++G** level using an active space comprised of the orbitals $1b_1(\pi)$, $2b_1(\pi)$, $1a_2(\pi)$, $3b_1(\pi^*)$ and $2a_2(\pi^*)$.

Table 6.7: Computational details of the wavepacket propagations corresponding to excitation to the $A_1(\pi\pi^*)$ state. The DVR types exp and HO correspond to exponential and Harmonic oscillator DVRs, respectively. N_i, N_j are the number of primitive DVR functions used to describe each particle. n_i are the number of single-particle functions used for each state.

Particle	DVR type	N_i, N_j	n_1, n_2, ..., n_6
R	exp	71	5, 6, 6, 4, 2, 3
ϕ	exp	71	5, 6, 6, 4, 2, 3
Q_{12}, Q_{16}	HO, HO	30, 30	5, 7, 7, 6, 7, 3
Q_{17}, Q_{19}	HO, HO	20, 20	5, 7, 7, 6, 7, 3
Q_4, Q_{21}	HO, HO	16, 70	5, 7, 6, 6, 7, 3
Q_7, Q_{11}	HO, HO	50, 30	5, 6, 6, 6, 10, 3

excitation to the $B_2(\pi\pi^*)$ state is found to occur only in the $A_2(3s)$ and $B_1(3s)$ states, and the calculated branching ratio

$$\Gamma_{B_1}^{A_2} = \frac{p_{diss,2}(t = 750)}{p_{diss,3}(t = 750)} \tag{6.19}$$

between the two dissociation channels is found to take a value of 1.588.

6.3.4 Dynamics Following Excitation to the $A_1(\pi\pi^*)$ State

The nuclear dynamics of pyrrole following excitation to the $A_1(\pi\pi^*)$ state was simulated using a six-state, ten-mode model comprising the modes R, ϕ, Q_4, Q_7, Q_{11}, Q_{12}, Q_{16}, Q_{17}, Q_{19}, and Q_{21}, and the states $A_1(S_0)$, $A_2(3s)$, $B_1(3s)$, $A_2(3p_z)$, $A_1(\pi\pi^*)$ and $B_2(\pi\pi^*)$. All other details of the calculation are displayed in Table 6.7.

Shown in Figure 6.9 (a) are the calculated diabatic state populations following vertical excitation to the $A_1(\pi\pi^*)$ state. An initial period of rapid depopulation of the initially excited $A_1(\pi\pi^*)$ state is found to occur, lasting $\sim$100 fs, by the end of which $\sim$70% of the population has been transferred to the $A_2(3s)$ and $B_1(3s)$ states. A relatively slow depletion of the $A_1(\pi\pi^*)$ state population is found to follow, with final populations of the $A_1(\pi\pi^*)$,

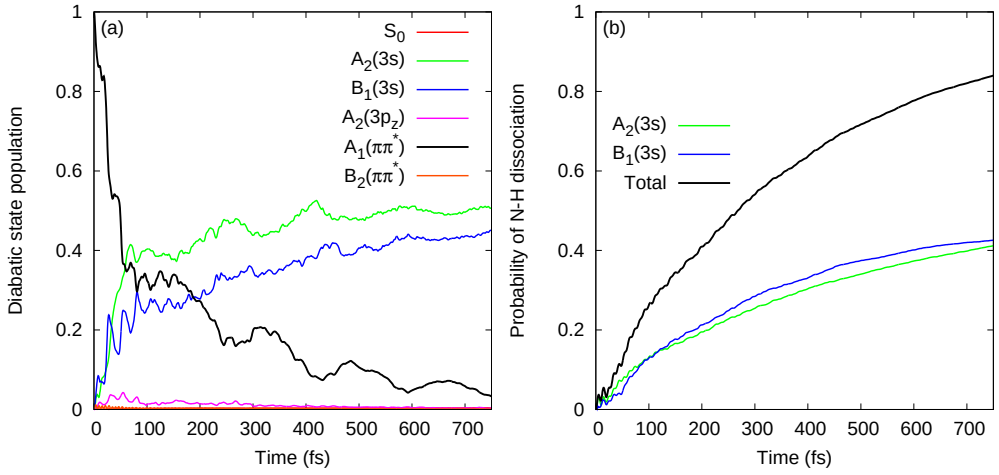

Fig. 6.9: (a) Calculated diababatic state populations following excitation to the $A_1(\pi\pi^*)$ state. (b) Calculated probabilities of N-H dissociation following excitation to the $A_1(\pi\pi^*)$ state.

$A_2(3s)$ and $B_1(3s)$ states of 0.03, 0.45 and 0.51 existing after 750 fs.

Figure 6.9 (b) displays the calculated time-cumulated probabilities of N-H dissociation following vertical excitation to the $A_1(\pi\pi^*)$ state. Dissociation is found to occur essentially entirely in the $A_2(3s)$ and $B_1(3s)$ states, with a probability of dissociation in the ground state of 0.002 after 750 fs. Almost identical probabilities of dissociation in the $A_2(3s)$ and $B_1(3s)$ states are found, with the calculated branching ratio

$$\Gamma_{B_1}^{A_2} = \frac{p_{diss,2}(t = 750)}{p_{diss,3}(t = 750)} \tag{6.20}$$

taking a value of 1.034.

6.3.5 Dynamics Following Excitation to the $A_2(3s)$ State

The dynamics of pyrrole following excitation to the $A_2(3s)$ state was modelled using a seven-mode, six-state model comprising the degrees of freedom R, ϕ, Q_{11}, Q_{16}, Q_{17}, Q_{19} and Q_{21}. All other details of the calculation are displayed in Table 6.8.

Table 6.8: Computational details of the wavepacket propagations corresponding to excitation to the $A_2(3s)$ state. The DVR types exp and HO correspond to exponential and Harmonic oscillator DVRs, respectively. N_i, N_j are the number of primitive DVR functions used to describe each particle. n_i are the number of single-particle functions used for each state.

Particle	DVR type	N_i, N_j	n_1, n_2, ..., n_6
R	exp	71	5, 6, 5, 5, 3, 2
ϕ	fft	80	5, 6, 4, 4, 3, 2
Q_{11}, Q_{16}	HO, HO	30, 30	5, 9, 5, 5, 3, 2
Q_{17}, Q_{19}	HO, HO	16, 16	4, 7, 5, 5, 3, 2
Q_{21}	HO	150	3, 9, 5, 5, 3, 2

Illustrated in Figure 6.10 are the calculated diabatic state populations and time-cumulated N-H dissociation probabilities following vertical excitation to the $A_2(3s)$ state. Population is found to remain predominantly in the initially excited $A_2(3s)$ state. Only negligible transfer of population to the ground state is found to occur. We note that this result is in disagreement with the quantum dynamics calculations of Domcke *et al.* [69, 82, 83], who reported a transfer of ∼10% of the population to the ground diabatic state. Support for the results presented here does, however, arise from the recent TR-VMI studies of Stavros *et al.* [96], who observed no significant contributions from statistical H-atom elimination following excitation to the $A_2(3s)$ state, implying insignificant transfer of population to the ground state interaction region. This result is also in accord with the photofragment translational spectroscopy studies of Cronin *et al.* [90], lending further weight to the results presented here.

The role of tunnelling in the dissociation dynamics of pyrrole following excitation to the $A_2(3s)$ state has received attention recently in the TR-VMI studies of Stavros *et al.* [96]. Following excitation at 4.96 eV, the authors reported a single timescale of 126±28 fs for H-atom elimination which was taken to be attributable to tunnelling through the barrier to N-H dissociation

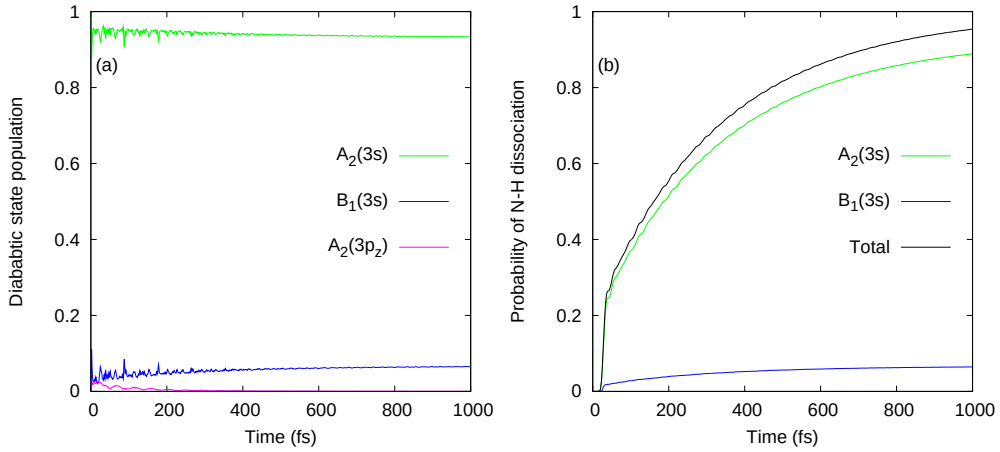

Fig. 6.10: (a) Calculated diababatic state populations following excitation to the $A_2(3s)$ state. (b) Calculated probabilities of N-H dissociation following excitation to the $A_2(3s)$ state.

in the $A_2(3s)$ state. Upon increasing the excitation energy used to 5.21 eV, a decrease in the timescale of H-atom elimination to 46±22 fs was found to occur and was taken to correspond to direct dissociation, rendered possible by excitation above the barrier to dissociation. In order to reconcile the results presented here with these findings, timescales for N-H dissociation were extracted through the fitting of the following simple model to the total calculated time-cumulated probability of N-H dissociation (illustrated in Figure 6.10 (b)):

$$p(t) = \Theta(t - t_c)\left\{1 - a\exp\left(-\frac{t - t_c}{\tau_1}\right) - (1 - a)\exp\left(-\frac{t - t_c}{\tau_2}\right)\right\}. \quad (6.21)$$

Here, the two timescales τ_1 and τ_2 are used to account for the possibility of both direct and tunnelling mechanisms of N-H dissociation being operative. The constant t_c corresponds to the time taken by the wavepacket to first reach the dissociation limit, and $\Theta(t - t_c)$ denotes the Heaviside step function centred at t_c. Using a simple simplex optimiser the following parameter values were determined: a=0.2479, τ_1=7.48 fs, τ_2=339.81 fs, t_c=22.71

Table 6.9: Fitted parameters entering into the model expression for the N-H dissociation probability calculated following vertical excitation to the $A_2(3s)$ state using various barriers to dissociation, E_B on the $A_2(3s)$ state potential surface.

E_B/eV	a	τ_1/fs	τ_2/fs	t_c/fs
0.3508	0.1979	14.55	2234.43	20.39
0.3319	0.2086	12.51	1593.90	21.36
0.3118	0.2166	11.12	1091.83	21.41
0.2915	0.2278	9.36	754.68	22.25
0.2713	0.2383	9.64	511.92	21.70
0.2498	0.2479	7.48	339.81	22.71
0.2285	0.2590	6.43	226.56	23.34
0.2059	0.2724	6.29	152.65	23.41
0.1833	0.2806	6.61	102.43	23.38
0.1610	0.2840	6.85	69.98	23.46

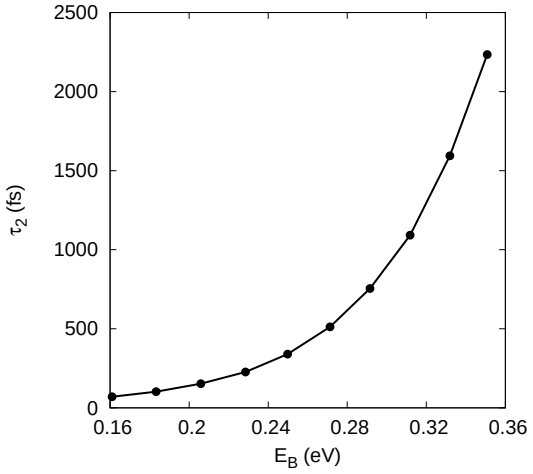

Fig. 6.11: Fitted values of the tunnelling timescale τ_2 following vertical excitation to the $A_2(3s)$ state using various barriers to dissociation, E_B, on the $A_2(3s)$ state potential surface.

fs. The fitted value of a, the coefficient corresponding to direct dissociation, implies that tunnelling through the barrier to dissociation in dominant. Summing the parameters τ_1 and t_c yields a timescale of 30.19 fs that we equate with the experimentally determined timescale of 46±22 fs for direct N-H dissociation. The longer timescale of τ_2=339.81 fs may be attributed to the tunnelling of the wavepacket through the barrier to N-H dissociation. That the two timescales derived here do correspond to direct dissociation and tunnelling through the barrier to dissociation may be verified by recourse to the variation of the barrier to dissociation used in the model Hamiltonian. With reference to Equation 6.10, we note that by varying the parameter P_1 entering into the model potential, modulation of the barrier to dissociation on the $A_2(3s)$ potential may be achieved without significant change of the potential surface either around the FC point or in the dissociation limit. Through the variation of this parameter, modified model potentials were constructed with $A_2(3s)$ barrier heights ranging from 0.16 eV to 0.35 eV. We note that the barrier height of the $A_2(3s)$ diabat obtained using the original model potential takes a value of 0.25 eV. The timescales extracted from wavepacket propagations performed using the modified potentials are displayed in Table 6.9. A profound increase in the slow timescale τ_2 is found to occur upon increasing the barrier to dissociation, as would be expected if this slow timescale did indeed correspond to the tunnelling of the low-energy components of the wavepacket through the barrier to dissociation. In contrast, the fast timescale, τ_1, remains relatively unchanged by the variation in the barrier height, in accord with our assignment to this timescale of direct dissociation of the high-energy components of the wavepacket that lie above the barrier to dissociation. As such, we have confidence in the assignments made here.

Shown in Figure 6.11 are the values of the slow timescale τ_2 plotted against the $A_2(3s)$ barrier height. The near-exponential decrease in the rate of tunnelling upon increasing barrier height serves to emphasise the importance of an accurate representation of the barrier to dissociation in quantum dynamics simulations. The presently reported timescale for tunnelling through the barrier to dissociation of 339.81 fs is not completely satisfactory when compared to the experimentally determined value of 126±28 reported by Stavros *et al.* [96]. However, upon decreasing the barrier height of the model potential by less than 0.05 eV the calculated tunnelling timescale, which now takes a value of 152.65 fs, is bought into excellent agreement with the experimentally-determined value. Finally, we make comment on the impact of the electronic structure calculations underlying the model Hamiltonian on the barrier to dissociation. The CAS(8,8)/aug+ calculations used to generate the reference states for the CASPT2 calculations used here yield a barrier to dissociation in the $A_2(3s)$ state of 0.40 eV. The effect of the dynamic correlation recovered by the CASPT2 calculations is to reduce the barrier to dissociation by 0.15 eV. Assuming an accurate representation of the calculated adiabatic energies to which it is parameterised, we thus see that a model Hamiltonian derived from the results of CASSCF calculations performed using tractable active spaces is likely to massively underestimate the contribution from tunnelling to the dissociation dynamics of pyrrole. Indeed, this is found to be the case with the quantum dynamics calculations of Domcke and co-workers [69, 82, 83], in which the CASSCF calculations underlying the construction of the model potentials used were found to furnish spuriously high barrier heights on the $A_2(3s)$ state potential of ∼0.40 eV, leading to an underestimation of the role played by tunnelling.

6.3.6 Electronic Absorption Spectra

Spectra corresponding to excitation to the $B_2(\pi\pi^*)$ and $A_1(\pi\pi^*)$ states were calculated from the Fourier transforms of the autocorrelation functions calculated from wavepacket propagations performed following vertical excitation of the ground-state wavepacket to the respective states. Both wavepacket propagations were performed using the model Hamiltonian described in Section 6.2.1. Additionally, in order to model the contribution to the first band in the absorption spectrum of pyrrole of the $B_1(3p_y)$ Rydberg state a separate model Hamiltonian was constructed. This is motivated by the general acceptance that this state contributes significantly to the first band in the electronic absorption spectrum of pyrrole [94, 95]. That the $B_1(3p_y)$ state was neglected in the model Hamiltonian used and discussed in the above was dictated by two factors: (i) we are primarily interested in the dynamics of pyrrole following excitation to the bright $B_2(\pi\pi^*)$ state and the subsequent dissociation of the system in the lower-lying $3s$ Rydberg states, and the construction of an active space that was capable of the description of the $B_1(3p_y)$ state was found to render the resulting CASPT2 calculations intractable for our purposes, and; (ii) the feature in the electronic spectrum of pyrrole generally attributed to the $B_1(3p_y)$ state is the sharp, intense peak situated at $\sim$5.85 eV, as illustrated in Figure 6.12, which is likely the consequence of excitation to a state that is not strongly coupled to its neighbouring states. Taking the $B_1(3p_y)$ state to be effectively decoupled from all other electronic states, we write the one-dimensional Hamiltonian used to model excitation to this state, $H_{3p_y}(\tilde{\boldsymbol{Q}})$, as

$$H_{3p_y}(\tilde{\boldsymbol{Q}}) = E_{3p_y} + \sum_{\alpha=1}^{3N-9} \frac{\tilde{\omega}_\alpha}{2}\left(-\frac{\partial^2}{\partial \tilde{Q}_\alpha^2} + \tilde{Q}_\alpha^2\right) + \sum_\alpha \kappa_\alpha^{(3p_y)} \tilde{Q}_\alpha, \qquad (6.22)$$

where E_{3p_y} denotes the vertical excitation energy of the $B_1(3p_y)$ state, and $\tilde{\boldsymbol{Q}}$ denotes the set of normal modes of the pyrrole molecule, that, is $H_{3p_y}(\tilde{\boldsymbol{Q}})$ corresponds to a single-state vibronic coupling Hamiltonian. The normal modes $\tilde{\boldsymbol{Q}}$ and the corresponding frequencies $\tilde{\omega_\alpha}$ were calculated at the MP2 level using the aug-cc-pVDZ basis. The constants E_{3p_y} and $\kappa_\alpha^{(3p_y)}$ entering into Equation 6.22 were determined from EOM-CCSD calculations employing the aug-cc-pVDZ basis. In particular, the intrastate coupling constants $\kappa_\alpha^{(3p_y)}$ were determined from the evaluation of the gradient of the EOM-CCSD energy with respect to all totally symmetric normal modes $\tilde{Q}_\alpha$ using a three-point finite difference formula employing a step size of 0.1. The thus determined constants are displayed in Table 6.10. The calculated vertical excitation energy of the $B_1(3p_y)$ state is 6.00 eV, which compares favourably with the previously reported value of 5.87 eV obtained by Roos *et al.* using MS-CASPT2 calculations. Using the model Hamiltonian $H_{3p_y}(\tilde{\boldsymbol{Q}})$, a spectrum corresponding to excitation to the $B_1(3p_y)$ state was produced from the Fourier transform of the autocorrelation function obtained from a wavepacket propagation performed using the MCTDH method. All nine totally symmetric modes were included in the calculation, and a propagation time of 200 fs was used.

Shown in Figure 6.12 are the calculated and experimental electronic absorption spectra in the region 5.5 to 6.5 eV. Overall, favourable agreement between the calculated and experimental spectra is seen. Excitation to the $B_2(\pi\pi^*)$ state has previously been postulated to dominate the first band in the electronic spectrum of pyrrole [94, 95]. Indeed, the majority of the intensity present in the total calculated spectrum is found to map onto the calculated $B_2(\pi\pi^*)$ state spectrum. We note that the origin of the calculated $B_2(\pi\pi^*)$ spectrum is located at $\sim$ 5.7 eV, whereas the VEE of the

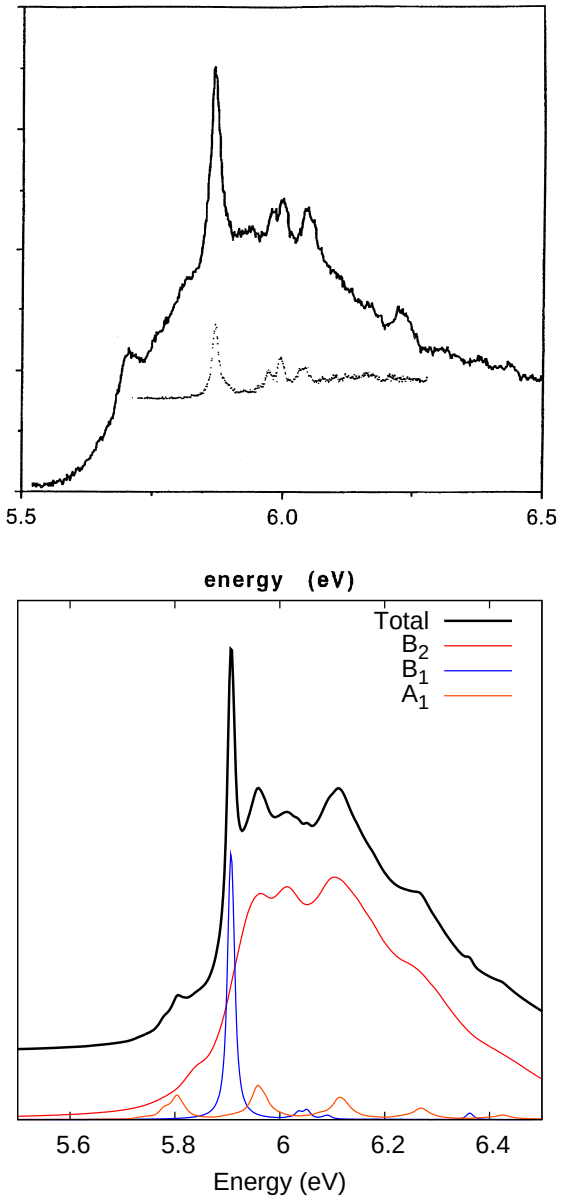

Fig. 6.12: Experimental and calculated spectra corresponding to the first band in the electronic spectrum of pyrrole. Top: experimental electronic absorption spectrum [94] with the envelope of the first band of the photoelectron spectrum [102] inset. Bottom: calculated electronic absorption spectra corresponding to excitation to the $A_1(\pi\pi^*)$, $B_1(3p_y)$ and $B_2(\pi\pi^*)$ states of pyrrole. The combined spectrum corresponds to the oscillator strength-weighted sum of the individual spectra. For clarity, the combined spectrum is shifted upwards relative to the individual spectra.

Table 6.10: Parameters entering into the model Hamiltonian $H_{3p_y}(\tilde{\boldsymbol{Q}})$, as defined in Equation 6.22, used to simulate to spectrum corresponding to excitation to the $B_1(3p_y)$ state. All quantities were evaluated from the results of EOM-CCSD calculations using the aug-cc-pVDZ basis.

Parameter	Parameter value (eV)
E_{3py}	6.0020
$\kappa_9^{(3p_y)}$	-0.0082
$\kappa_{10}^{(3p_y)}$	0.0280
$\kappa_{12}^{(3p_y)}$	-0.0035
$\kappa_{14}^{(3p_y)}$	0.0364
$\kappa_{16}^{(3p_y)}$	-0.0183
$\kappa_{18}^{(3p_y)}$	-0.0272
$\kappa_{21}^{(3p_y)}$	-0.0045
$\kappa_{23}^{(3p_y)}$	-0.0027
$\kappa_{24}^{(3p_y)}$	-0.0994

$B_2(\pi\pi^*)$ state entering into the model Hamiltonian used is 6.24 eV. The rather large difference between the origin of the spectrum and the vertical excitation energy could be attributed to either the shift in the $B_2(\pi\pi^*)$ state minimum relative to the FC point or to the borrowing of intensity from the $B_2(\pi\pi^*) \leftarrow A_1(S_0)$ transition by lower-lying states. Figure 6.13 shows the spectrum corresponding to vertical excitation to the $B_2(\pi\pi^*)$ state calculated using a model Hamiltonian from which all interstate coupling constants had been removed. Non-negligible intensity in the uncoupled spectrum continues down to ∼5.8 eV, indicative of a large shift of the $B_2(\pi\pi^*)$ state minimum away from the FC point. However, the intensity of this spectrum below ∼6 eV is low, suggesting that a significant proportion of the $B_2(\pi\pi^*)$ state spectrum arises due to coupling to lower-lying states. In order to determine the identity of the states to which coupling to the $B_2(\pi\pi^*)$ state gives rise to intensity in the $B_2(\pi\pi^*)$ spectrum, calculations of the $A_2(3p_z)$ and $B_1(3s)$ state spectra were performed with all interstate coupling constants set to zero. The resulting uncoupled spectra are shown in Figure 6.13. It is found

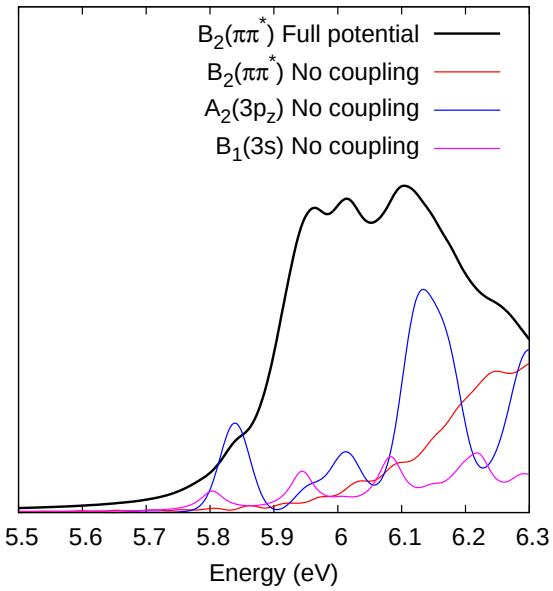

Fig. 6.13: Calculated spectra corresponding to vertical excitation to the $B_2(\pi\pi^*)$ state using both the full model Hamiltonian and the model Hamiltonian with all interstate coupling constants removed. Overlayed are spectra corresponding to vertical excitation to the $A_2(3p_z)$ and $B_1(3s)$ states calculated using a model Hamiltonian with all interstate coupling constants removed.

that through intensity borrowing both the $A_2(3p_z)$ and $B_1(3s)$ states contribute to the $B_2(\pi\pi^*)$ state spectrum. We identify the origin of the shoulder at 5.8 eV as the coupling of the $B_2(\pi\pi^*)$ and $A_2(3p_z)$ states. Further, the coupling of these two states is found to give rise to the prominent peak centred at 6.1 eV. We note that the possibility of the coupling of the $A_1(\pi\pi^*)$ and $B_2(\pi\pi^*)$ states giving rise to the 'missing' intensity in the $B_2(\pi\pi^*)$ spectrum was discounted due to the lack of population of the $A_1(\pi\pi^*)$ state following excitation to the $B_2(\pi\pi^*)$ state, as is illustrated in Figure 6.5.

The peak visible at ∼5.70 eV in the experimental spectrum has previously been assigned to the origin of the $B_2(\pi\pi^*)$ band by both Roos *et al.* [95] and Bavia *at al.* [103]. Palmer *et al.* took this peak to correspond to excitation to the $B_2(3p_x)$ Rydberg state. With reference to the components of the total calculated spectrum (as shown in Figure 6.12), we note that the peak oc-

curring at ∼5.80 eV is a consequence mainly of the $A_1(\pi\pi^*)$ band, with an underlying contribution from the $B_2(\pi\pi^*)$ band. As mentioned above, the contribution from the $B_2(\pi\pi^*)$ band is attributable to intensity borrowing by the $A_2(3p_z)$ state. Shown in Figure 6.14 are the $A_1(\pi\pi^*)$ state spectra calculated both with and without the interstate coupling constants included in the model Hamiltonian. That the peak centred at ∼5.80 eV vanishes upon the removal of the interstate coupling terms implies that this feature arises from intensity borrowing from the $A_1(\pi\pi^*) \leftarrow A_1(S_0)$ transition. As illustrated in Figure 6.9, population originating in the initially populated $A_1(\pi\pi^*)$ state undergoes rapid transfer to the $B_1(3s)$ state, with only a very small population of the $A_2(3p_z)$ state being observed. Thus, we attribute the peak observed experimentally at ∼5.70 eV mainly to intensity borrowing from the $A_1(\pi\pi^*) \leftarrow A_1(S_0)$ transition by the $B_1(3s)$ state, with an underlying contribution arising due to intensity borrowing from the $B_2(\pi\pi^*) \leftarrow A_1(S_0)$ transition by the $A_2(3p_z)$ state. The small discrepancy between the positions of the peaks of the experimental and calculated spectra that are being equated here is presumably due to the limited accuracy of the CASPT2 calculations used in the parameterisation of the model potential.

The most intense feature in the experimental spectrum is the sharp peak centred at ∼5.85 eV. As previously mentioned, this peak has previously been assigned to excitation to the $B_1(3p_y)$ state [94, 95]. Our results are in agreement with this assignment, with the simple model Hamiltonian $H_{3p_y}(\tilde{\boldsymbol{Q}})$ being found to yield a spectrum dominated by a single, intense peak centred at 5.9 eV.

Finally, we comment on the assignment of the peak centred at ∼6.2 eV in the experimental spectrum. Derrick *et al.* [102] first suggested that this peak arises due to excitation to the $B_1(3s)$ Rydberg state. This assignment

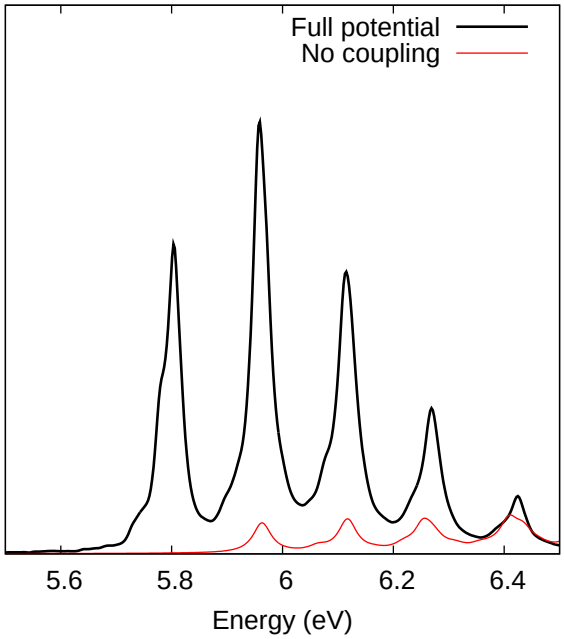

Fig. 6.14: Calculated spectra corresponding to vertical excitation to the $A_1(\pi\pi^*)$ state using both the full model potential and the model potential with all interstate coupling constants removed.

was also favoured by Palmer *et al.* [94]. The spectrum calculated here exhibits a peak situated at around 6.25 eV that arises from contributions from both the $B_2(\pi\pi^*)$ and $A_1(\pi\pi^*)$ bands. The uncoupled $B_2(\pi\pi^*)$ and $A_1(\pi\pi^*)$ spectra retain intensity centred around 6.25 eV. As such, we believe previous assignments made to the $B_1(3s)$ to be incorrect, and that instead most of the intensity of this peak arises due to excitation to the $B_2(\pi\pi^*)$ state, with a significant underlying contribution from excitation to the $A_1(\pi\pi^*)$ state.

We end this section by commenting again on the significant disparity between the start of the calculated $B_2(\pi\pi^*)$ band and the VEE used in the derivation of the model that was used in its production. The extension of this band to energies far below the VEE of the corresponding state has implications for the practice of benchmarking electronic structure calculations against experimentally determined band maxima. Previous joint experimental-theoretical studies [94, 101] have led to an assignment of ∼5.9

eV to the VEE of the $B_2(\pi\pi^*)$ state, based upon a matching of calculated VEEs and observed peak positions in the experimental spectra. Such an approach, however, is not entirely satisfactory in that it neglects the possibility of both intensity borrowing and a shift excited state minima from the FC point resulting in potentially large shifts of band maxima from the corresponding VEEs. In the case of the $B_2(\pi\pi^*)$ state of pyrrole, we have confidence that the true VEE of the state lies significantly higher (at $\sim$6.25 eV) than has previously been postulated, as attested to by the ability of our model Hamiltonian to reproduce satisfactorily the experimental spectrum. This re-assignment has some implications for previously conducted experimental studies of the photoinduced dynamics of pyrrole. By way of example, previous experimental studies have generally taken excitation at energies in the range 5.65 to 6.0 eV to correspond to excitation to the $B_2(\pi\pi^*)$ state [90] on account of a rapid increase in the absorption cross-section in this energy interval. The work presented here, however, offers a new interpretation, namely that excitation in this energy window should result in transition to the $B_1(3s)$ and $A_2(3p_z)$ states, mainly as a result of intensity borrowing from the $A_1(\pi\pi^*) \leftarrow A_1(S_0)$ and $B_2(\pi\pi^*) \leftarrow A_1(S_0)$ transitions, respectively. As such, a reinterpretation of some previously reported experimental observations should, perhaps, be considered.

6.4 Discussion and Conclusions

Through fitting to adiabatic energies resulting from CASPT2 calculations performed at a large number of nuclear geometries, a model Hamiltonian has been parameterised that is capable of the description of the dynamics of the pyrrole molecule in the seven-dimensional manifold of electronic states spanned by the states $A_1(S_0)$, $A_2(3s)$, $B_1(3s)$, $A_2(3p_z)$, $A_1(\pi\pi^*)$, $B_2(\pi\pi^*)$ and

$B_1(3p_z)$. In conjuction with the MCTDH wavepacket propagation algorithm, the model Hamiltonian developed has been used to simulate the dynamics of pyrrole following excitation to the $A_2(3s)$, $A_1(\pi\pi^*)$ and $B_2(\pi\pi^*)$ states.

Excitation to the $A_1(\pi\pi^*)$ state is found to result in prompt and efficient relaxation to the $A_2(3s)$ and $B_1(3s)$ states, resulting in a dominance of direct N-H dissociation in the ensuing dynamics. In contrast, a hindrance of direct N-H dissociation is found to occur following excitation to the $B_2(\pi\pi^*)$ state, with diabatic trapping of the population in the initially excited $B_2(\pi\pi^*)$ state being found to occur. The trapping of the wavepacket in the $B_2(\pi\pi^*)$ state is found to be attributable to the large amplitude displacement of the wavepacket along the C-N-C out-of-plane bending mode Q_2 in the $B_2(\pi\pi^*)$ state. Significantly, this displacement of the evolving wavepacket is found to drive the system towards nuclear geometries that are distinctly similar to that of the ring-puckered conical intersection that is known to exist to connect the ground and $B_2(\pi\pi^*)$ states [88]. At present, however, the simplicity of the model Hamiltonian, and in particular the lack of correlation of the pyrrolyl normal modes $\boldsymbol{Q}$ in the model potential, results in the inability of the model used to describe accurately the pathway connecting the Franck-Condon point and the ring-puckered conical intersection. Clearly, the pursuit in future work of the improvement of the model potential developed here to describe correctly this pathway would be desirable. Such further development is of particular interest as internal conversion to the ground state mediated by an accessible conical intersection connecting the $B_2(\pi\pi^*)$ and ground states, and subsequent statistical dissociation, has been suggested as a plausible explanation for the experimentally observed increase in the yield of low-kinetic energy hydrogen atoms following the decrease of the excitation wavelength used in photofragment translational spectroscopy studies [90].

Following vertical excitation to the $A_2(3s)$ state, we observe both direct dissociation of the high-energy components of the wavepacket and the tunnelling of the low-energy components through the barrier to N-H dissociation. The calculated value of the fast timescale (∼30 fs) is found to be in good agreement with the recently reported experimentally determined value of 46±22 fs [96]. The timescale calculated for the tunnelling of the wavepacket through the barrier to dissociation takes a value of ∼340 fs, comparing not particularly favourably to the experimentally determined value of 126±28 fs [96]. Upon decreasing the barrier to dissociation by less than 0.05 eV, however, the calculated timescale for tunnelling is bought into excellent agreement with the experimentally derived value. This serves to highlight the requirement of using extremely accurate electronic structure calculations in the parameterisation model Hamiltonians for use in the simulation of the excited state dynamics of pyrrole and related systems if accurate appraisals of the role played by tunnelling are to be made.

Electronic absorption spectra corresponding to vertical excitation to the $A_1(\pi\pi^*)$, $B_2(\pi\pi^*)$ and $B_1(3p_y)$ states were calculated from the Fourier transforms of the wavepacket autocorrelation functions obtained from the respective wavepacket propagations. Through intensity borrowing from the bright $B_2(\pi\pi^*) \leftarrow A_1(S_0)$ transition, the $B_1(3s)$ and $A_2(3p_z)$ states are found to contribute significantly to the first band in pyrrole's electronic spectrum, providing much of the intensity at energies below 6 eV. This has consequences for the placement of the $B_2(\pi\pi^*)$ state, the VEE of which has previously been taken to lie at ∼5.9 eV, corresponding to the $B_2(\pi\pi^*)$ band maximum. The results presented here, however, imply that the VEE of the $B_2(\pi\pi^*)$ state may actually lie significantly higher, at ∼6.25 eV, and that excitation at energies around 5.7-6.1 eV should result mainly in transition to the $B_1(3s)$

and $A_2(3p_z)$ states.

Chapter 7

Aniline

7.1 Introduction

Much attention has been paid recently to the photochemistry of small aromatic amines, including the DNA bases adenine [104–106], guanine [107–109] and cytosine [110, 111]. The focus of this chapter is the photoinduced dynamics of the prototypical aromatic amine aniline ($C_6H_5NH_2$, see Figure 7.1). Through a number of experimental [112, 113] and theoretical [114] studies, the electronic spectrum of aniline in the region 4.0 to 6.0 eV is known to be dominated by two bands centred at 4.35 eV and 5.39 eV, corresponding to excitation to the first two $^1\pi\pi^*$ states. Further, a single low-lying $^1 3s/\pi\sigma^*$ state has been identified to exist between these two $^1\pi\pi^*$ states at an energy of ∼4.6 eV by the (2 + 2) resonance enhanced multiphoton ionisation measurements of Ebata *et al.* [115]. The adiabatic potentials of these states along the N-H dissociation coordinate are illustrated schematically in Figure 7.2.

Recent experimental studies of the excited state dynamics of aniline have served to reveal the rich and complex photochemistry of this molecule. Through the use of energy-resolved H (Rydberg) atom photofragment translational spectroscopy measurements, Ashfold *et al.* [116] reasoned that for excitation energies in excess of 4.60 eV, N-H dissociation *via* the $S_2(3s/\pi\sigma^*)$

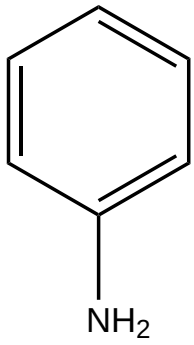

Fig. 7.1: Molecular structure of aniline.

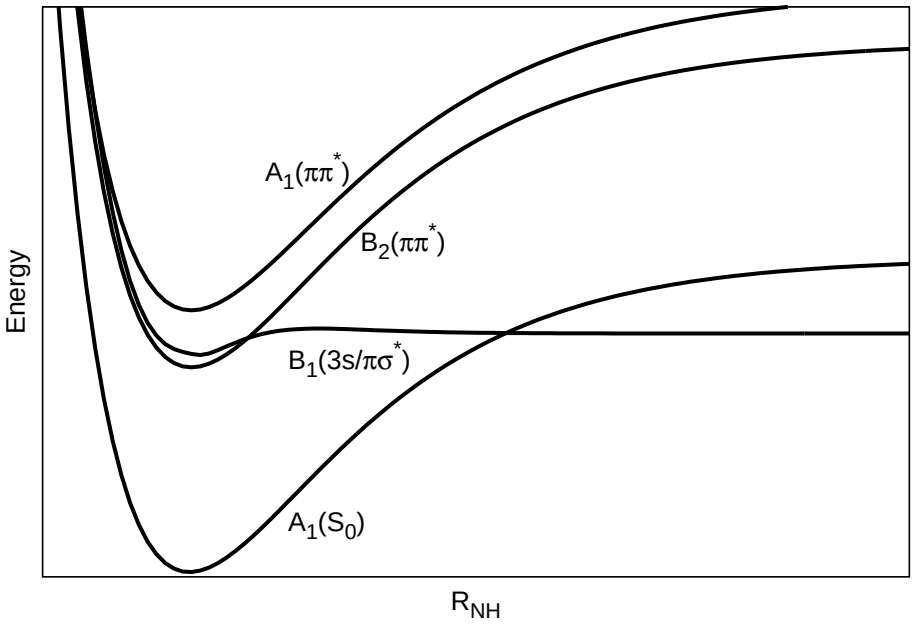

Fig. 7.2: Schematic adiabatic potentials corresponding to the $A_1(S_0)$, $B_2(\pi\pi^*)$, $B_1(3s/\pi\sigma^*)$, and $A_1(\pi\pi^*)$ states along the N-H dissociation coordinate starting from the planar S_1 minimum energy geometry.

state occurs, with the dissociation proceeding diabatically to produce ground state anilino radicals. The time-resolved ion yield studies of Montero and co-workers [117] furnished both short (165 fs) and long (tens of picoseconds to nanoseconds) timescales for relaxation following excitation in the range 4.60 to 5.17 eV. These timescales were attributed, respectively, to dissociation on the $S_2(3s/\pi\sigma^*)$ surface, and sequential transfer of population to the $S_1(\pi\pi^*)$ and S_0 surfaces. Using femtosecond pump-probe velocity map imaging, Stavros *et al.* [118] reported a timescale of 155 fs for the formation of both high and low kinetic energy H-atoms following excitation at 5.17 eV. Further, excitation to the $S_1(\pi\pi^*)$ state was found not to result in direct N-H dissociation. Employing time-resolved photoelectron imaging, Fielding and co-workers find that excitation at energies between 5.17 and 5.21 eV results in a time-scale of decay of <100 fs [119,120]. This is attributed to excitation to the second, bright $^1\pi\pi^*$ state followed by ultrafast internal conversion to the ground state.

In this chapter, the first steps towards performing quantum dynamics simulations of the photo-induced dynamics of aniline are made by the construction of a model Hamiltonian for the description the vibronically-coupled manifold comprised of the first six electronic states of aniline. The model used is the quadratic vibronic coupling Hamiltonian of Köppel *et al.* [19,20], which is parameterised *via* fitting to the results of extensive equation-of-motion coupled-cluster with single and double excitations (EOM-CCSD) calculations. Preliminary calculations are performed whereby the electronic absorption spectrum in the region 4.0 to 6.0 eV is calculated and analysed.

7.2 Theory

7.2.1 The Model Hamiltonian

The model Hamiltonian adopted for the study here of the excited state dynamics of aniline is based on a simple quadratic vibronic coupling Hamiltonian

$$\boldsymbol{H}(\boldsymbol{Q}) = \boldsymbol{H}^{(0)}(\boldsymbol{Q}) + \boldsymbol{W}^{(1)}(\boldsymbol{Q}) + \boldsymbol{W}^{(2)}(\boldsymbol{Q}), \tag{7.1}$$

with all quantities being as defined in Section 3.8. Our choice of reference geometry is guided by the fact that aniline possesses two isoenergetic ground state minima of C_s symmetry connected by the inversion of the amino group. As such, we choose as our reference geometry the transition state for NH_2 inversion. As well as affording a balanced description of the two minima connected by it, this choice of reference geometry renders zero by symmetry a greater number of the parameters of the vibronic coupling Hamiltonian by virtue of the higher (C_{2v}) symmetry of this geometry in comparison to the ground state minima. The nuclear coordinates, $\boldsymbol{Q}$, used are, then, the mass- and frequency-scaled normal mode coordinates of the amino group inversion transition state.

Dissociation of the N-H bond is known to be of importance in the excited state dynamics of aniline. None of the 36 ground-state normal modes describe the N-H stretching motion alone. However, the modes Q_{35} and Q_{36} correspond, respectively, to symmetric and antisymmetric stretching motions of the two N-H bonds. To make the analysis of the bond breaking more straightforward, we therefore make the following coordinate transformation:

$$\boldsymbol{Q} \rightarrow \tilde{\boldsymbol{Q}} = \boldsymbol{D}\boldsymbol{Q}, \tag{7.2}$$

$$\boldsymbol{D} = \mathbf{1} \oplus \begin{pmatrix} \cos\left(\frac{\pi}{4}\right) & \sin\left(\frac{\pi}{4}\right) \\ -\sin\left(\frac{\pi}{4}\right) & \cos\left(\frac{\pi}{4}\right) \end{pmatrix} \tag{7.3}$$

where $\mathbf{1}$ denotes a $(3N-8) \times (3N-8)$ unit matrix. Thus the coordinates $\tilde{Q}_\alpha$; $\alpha \leq 34$ still equate with the ground-state normal modes, while the coordinates $\tilde{Q}_{35}$ and $\tilde{Q}_{36}$ correspond to normalised linear combinations of the symmetric and antisymmetric NH_2 stretching modes (Q_{35} and Q_{36}), respectively, and the N-H dissociation is now well-described by the degree of freedoms $\tilde{Q}_{35}$ and $\tilde{Q}_{36}$.

Using the modified normal modes $\tilde{\boldsymbol{Q}}$, the zeroth-order potential may be written

$$W_{ij}^{(0)}(\tilde{\boldsymbol{Q}}) = \left(E_i + \sum_{\alpha=1}^{3N-8} \frac{\omega_\alpha}{2} \tilde{Q}_\alpha^2 + \frac{\omega^+}{2} \left[\tilde{Q}_{35}^2 + \tilde{Q}_{36}^2 \right] + \omega^- \tilde{Q}_{35} \tilde{Q}_{36} \right) \delta_{ij}, \tag{7.4}$$

where E_i denotes the vertical excitation energy of the ith electronic state at the reference geometry $\tilde{\boldsymbol{Q}}_0$, the quantities ω_α; $\alpha \leq 34$ are the frequencies of the corresponding normal modes $\tilde{Q}_\alpha = Q_\alpha$, and the ω^+ and ω^- are given by

$$\omega^+ = \frac{1}{2} \left(\omega_{35} + \omega_{36} \right) \tag{7.5}$$

$$\omega^- = \frac{1}{2} \left(\omega_{35} - \omega_{36} \right). \tag{7.6}$$

In general, a second-order expansion of the diabatic potential was found to be adequate. However, for a handful of totally-symmetric degrees of freedom the degree of anharmonicity is such that the on diagonal expansions $W_{ii}^{(n)}(\tilde{\boldsymbol{Q}}); \forall n$ were replaced by Morse oscillators:

$$W_{ii}(\tilde{Q}_\alpha) = D_{0,\alpha}^{(i)} \left\{ \exp\left(\delta_\alpha^{(i)} \left(\tilde{Q}_\alpha - \tilde{Q}_{0,\alpha}^{(i)} \right) \right) - 1 \right\}^2 + E_{0,\alpha}^{(i)}; \quad \alpha = 12, 30, 34, \tag{7.7}$$

$$E_{0,\alpha}^{(i)} = -D_{0,\alpha}^{(i)} \left[\exp\left(-\delta_{\alpha}^{(i)} \tilde{Q}_{0,\alpha}^{(i)} \right) - 1 \right]^2 \tag{7.8}$$

For the degree of freedom $\tilde{Q}_{36}$, corresponding to N-H dissociation, the bound state potentials were similarly described by Morse oscillators, whilst the dissociative $\tilde{B}(\pi\sigma^*/3s)$ potential was described by an avoided-crossing model:

$$W_{22}(\tilde{Q}_{36}) = \frac{1}{2} \left\{ \nu_b + \nu_d - \sqrt{(\nu_b - \nu_d)^2 + 4 \left[\Delta \tanh\left(\rho \tilde{Q}_{36} \right) \right]^2} \right\}, \tag{7.9}$$

with

$$\nu_b = D_b \left[\exp(-\alpha_b (\tilde{Q}_{36} - \tilde{Q}_{36,0}^b)) - 1 \right]^2 \tag{7.10}$$

$$\nu_d = A \exp(-\alpha_d (\tilde{Q}_{36} - \tilde{Q}_{36,0}^d)) + D_d. \tag{7.11}$$

The adiabatic potentials correlating with the $\tilde{X}$ and $\tilde{B}(\pi\sigma^*/3s)$ states form avoided crossings along the N-H dissociation coordinate for geometries corresponding to an inverted NH_2 moiety. To account for this, the interstate coupling constants $\lambda_1^{(1,3)}$ and $\lambda_1^{(1,4)}$ are taken as functions of the N-H dissociation coordinate, $\tilde{Q}_{36}$, as follows:

$$\lambda_1^{(i,j)}(\tilde{Q}_{36}) = \lambda_1^{(i,j)}(\tilde{Q}_{36,0}) +^1 \Lambda^{(i,j)} \tanh(^2\Lambda^{(i,j)} \tilde{Q}_{36}); \quad i,j = (1,3),(1,4), \tag{7.12}$$

where $\tilde{Q}_{36,0}$ denotes the reference value of $\tilde{Q}_{36}$.

The matrix representation of the kinetic energy operator in the coordinate system used, $\boldsymbol{T}(\tilde{\boldsymbol{Q}})$, reads

$$T_{ij}(\tilde{\boldsymbol{Q}}) = \left(-\sum_{\alpha=1}^{3N-8} \frac{\omega_\alpha}{2} \frac{\partial^2}{\partial \tilde{Q}_\alpha^2} + \frac{\omega^+}{2} \left[\frac{\partial^2}{\partial \tilde{Q}_{35}^2} + \frac{\partial^2}{\partial \tilde{Q}_{36}^2} \right] + \omega^- \frac{\partial^2}{\partial \tilde{Q}_{35} \partial \tilde{Q}_{36}} \right) \delta_{ij}. \tag{7.13}$$

The parameterisation of the model potential $\boldsymbol{W}(\tilde{\boldsymbol{Q}})$ was achieved by the minimisation of the root mean square deviation of the model and calculated adiabatic energies at a large number of nuclear geometries using the procedure outlined in Section 4.3.2.

7.2.2 Electronic Structure Calculations

There is a preference when excited state potential energy surfaces are to be calculated to use a method employing a multiconfigurational reference function, such as the complete active-space self-consistent field (CASSCF) method, in order to efficiently account for the potentially multiconfigurational characters of excited states considered. Initial attempts to utilise the CASSCF method were made here. However, it was found not to be possible to construct an active space that could simultaneously yield continuous potential surfaces in all regions of nuclear configuration space of interest and also result in the relatively modest computational cost required for the calculation of adiabatic energies at large numbers of nuclear geometries. Instead use was made of the EOM-CCSD [79] method in conjunction with the aug-cc-pVDZ basis set. At each geometry considered, the eight lowest-lying adiabatic energies were computed, corresponding at the Franck-Condon (FC) point to the states $\tilde{X}$, $\tilde{A}(\pi\pi^*)$, $\tilde{B}(\pi\sigma^*/3s)$, $\tilde{C}(3p_z)$, $\tilde{D}(3p_y)$, $\tilde{E}(\pi\pi^*)$, $\tilde{F}(3p_z)$, and $\tilde{G}(3d_{yz})$.

7.2.3 Calculation of Absorption Spectra

Absorption spectra, $\sigma(E)$, corresponding to excitation to the two lowest-lying $^1\pi\pi^*$ states were calculated *via* the Fourier transforms of autocorrelation functions obtained from propagation of wavepackets starting in each of the two states. The initial states, $|\Psi(0)\rangle$, used in the wavepacket propagations were determined by vertically exciting the ground state wavefunction, $|\Psi_{GS}\rangle$,

to the electronic state of interest, that is,

$$|\Psi(0)\rangle = \{|f\rangle\langle 1| + h.c.\}|\Psi_{GS}\rangle, \tag{7.14}$$

where $|f\rangle$ denotes the electronic state of interest and $|\Psi_{GS}\rangle$ is determined by wavepacket relaxation. In addition, it was found that the transition dipole moments corresponding to excitation from the ground state to the $\tilde{A}(\pi\pi^*)$ state have large gradients at the FC point with respect to a number of the degrees of freedom $\tilde{Q}_\alpha$. To assess the effect of the "Herzberg-Teller terms" on excitation to the $\tilde{A}(\pi\pi^*)$ state, the following operator was also used to prepare the initial wavefunction corresponding to excitation to the $\tilde{A}(\pi\pi^*)$ state:

$$\hat{O}_{HT} = \left\{ |2\rangle \left[\boldsymbol{\mu}_{12}(\tilde{\boldsymbol{Q}}_0) + \sum_{\alpha=1}^{3N-6} \frac{\partial \boldsymbol{\mu}_{12}(\tilde{\boldsymbol{Q}}_0)}{\partial \tilde{Q}_\alpha} \tilde{Q}_\alpha \right] \langle 1| \right\} + h.c., \tag{7.15}$$

where $\boldsymbol{\mu}_{12}(\tilde{\boldsymbol{Q}}_0)$ denotes the transition dipole moment for the ground and $\tilde{A}(\pi\pi^*)$ states at the reference point. The gradients $\partial\boldsymbol{\mu}_{12}(\tilde{\boldsymbol{Q}}_0)/\partial\tilde{Q}_\alpha$ were calculated numerically using CASSCF calculations state-averaged over the ground and first excited states and using the 6-311+G(d) basis set. For these calculations, an active space comprising the three π orbitals and the corresponding three π^* orbitals was used.

7.3 Results

7.3.1 Electronic Structure Calculations

The reference geometry used (the transition state along the NH_2 inversion pathway) was optimised using Möller-Plesset second-order perturbation theory (MP2) and the aug-cc-pVDZ basis set as implemented in the Gaussian 03 set of programs [97]. Subsequent normal mode analysis at the same level

of theory confirms that the thus obtained geometry is a stationary point of order one, with the single normal mode of imaginary frequency corresponding to NH_2 inversion. The frequencies and symmetries of these normal modes are listed in Table 7.1.

The vertical excitation energies (VEEs) of the electronic states together with the normal mode frequencies completes the parameterisation of the zero-order potential. The VEEs calculated at the EOM-CCSD/aug-cc-pVDZ level are given in Table 7.2 together with the excitation energies calculated at the ground state minimum energy geometry. In the energy range of interest (4 to 6 eV), interest has generally been devoted to the roles played by the three states $\tilde{A}(\pi\pi^*)$, $\tilde{B}(\pi\sigma^*/3s)$ and $\tilde{E}(\pi\pi^*)$. Although the ordering of the EOM-CCSD VEEs at the FC point is faithfully reproduced, the actual values are all shifted upwards by between 0.3 and 0.4 eV relative to the experimentally determined values. The addition of state-selective non-iterative triples corrections *via* the completely renormalised EOM-CCSD(T) (CR-EOM-CCSD(T)) [121] approach is found to significantly improve the agreement of the calculated and experimental VEEs, as shown in Table 7.2. As the parameters of the quadratic vibronic coupling (QVC) Hamiltonian are predominantly determined by the local topologies of the potential surfaces around the point of expansion and the CR-EOM-CCSD(T) method demands more computational effort than the EOM-CCSD method, we adopt the following strategy: the model Hamiltonian is first parameterised by fitting to EOM-CCSD adiabatic energies, followed by the shifting of the zero-order parameters E_i, corresponding to the VEEs at the point of expansion, by an amount that brings the calculated EOM-CCSD and CR-EOM-CCSD(T) VEEs at the reference point into agreement.

Of interest is the fact that using both the EOM-CCSD and CR-EOM-

Table 7.1: Frequencies and symmetries of the normal modes calculated at the MP2/aug-cc-pVDZ level at the transition state to NH_2 inversion. ip: in-plane, oop: out-of-plane, sym: symmetric, asym: asymmetric.

Mode	Frequency/eV	Symmetry	Description
Q_1	$0.0601i$	B_1	NH_2 inversion
Q_2	0.0265	B_1	Boat
Q_3	0.0394	A_2	NH_2 torsion
Q_4	0.0455	B_2	NH_2 ip bend
Q_5	0.0502	A_2	Boat
Q_6	0.0618	B_1	Boat
Q_7	0.0649	A_1	Ring stretch
Q_8	0.0761	B_2	Ring stretch
Q_9	0.0771	B_1	Chair
Q_{10}	0.0913	B_1	Sym C-H oop bend
Q_{11}	0.1012	A_2	Asym C-H oop bend
Q_{12}	0.1019	A_1	Ring stretch
Q_{13}	0.1058	B_1	Asym C-H oop bend
Q_{14}	0.1122	B_1	Asym C-H oop bend
Q_{15}	0.1138	A_2	Asym C-H oop bend
Q_{16}	0.1231	A_1	Ring stretch
Q_{17}	0.1262	B_2	(N)H_2 ip bend
Q_{18}	0.1290	A_1	C_5H_5 breathing
Q_{19}	0.1374	B_2	Asym C-H ip bend
Q_{20}	0.1439	B_2	Asym C-H ip bend
Q_{21}	0.1470	A_1	Sym C-H ip bend
Q_{22}	0.1629	A_1	Ring breathing
Q_{23}	0.1643	B_2	Asym C-H ip bend
Q_{24}	0.1804	B_2	Ring stretch
Q_{25}	0.1842	B_2	Ring stretch
Q_{26}	0.1870	A_1	Ring stretch
Q_{27}	0.2011	B_2	Ring stretch
Q_{28}	0.2026	A_1	(N)H_2 ip bend
Q_{29}	0.2059	A_1	Ring breathing + (N)H_2 ip bend
Q_{30}	0.3956	A_1	Asym C-H stretch
Q_{31}	0.3957	B_2	Asym C-H stretch
Q_{32}	0.3978	A_1	Sym C-H stretch
Q_{33}	0.3985	B_2	Asym C-H stretch
Q_{34}	0.4008	A_1	Sym C-H stretch
Q_{35}	0.4516	A_1	Sym NH_2 stretch
Q_{36}	0.4692	B_2	Asym NH_2 stretch

Table 7.2: Calculated and experimental excitation energies at the reference geometry ($\boldsymbol{Q}_0$) and the FC point ($\boldsymbol{Q}_{min}$). [a]Refs 112 and 113. [b]Ref 115.

State	Symmetry	EOM, $\boldsymbol{Q}_0$	CR-EOM, $\boldsymbol{Q}_0$	EOM, $\boldsymbol{Q}_{min}$	CR-EOM, $\boldsymbol{Q}_{min}$	Experimental, $\boldsymbol{Q}_{min}$
$\tilde{X}$	$A_1/A^{'}$	0.00	0.00	0.00	0.00	0.00
$\tilde{A}(\pi\pi^*)$	$B_2/A^{''}$	4.55	3.98	4.77	4.21	4.40[a]
$\tilde{B}(\pi\sigma^*/3s)$	$B_1/A^{'}$	4.65	4.31	5.02	4.69	4.60[b]
$\tilde{C}(3p_z)$	$B_1/A^{'}$	5.36	5.00	5.67	5.31	-
$\tilde{D}(3p_y)$	$A_2/A^{''}$	5.37	5.03	5.77	5.42	-
$\tilde{E}(\pi\pi^*)$	$A_1/A^{'}$	5.56	5.11	5.85	5.42	5.39[a]
$\tilde{F}(3p_z)$	$B_1/A^{'}$	6.04	5.70	6.38	6.05	-
$\tilde{G}(3d_{yz})$	$A_2/A^{''}$	6.06	5.71	6.39	6.04	-

CCSD(T) methods two $3p$ Rydberg states ($\tilde{C}(3p_z)$ and $\tilde{D}(3p_y)$) are predicted to exist between the $\tilde{B}(\pi\sigma^*/3s)$ and $\tilde{E}(\pi\pi^*)$ states. At the CR-EOM-CCSD(T) level, the $\tilde{C}(3p_z)$ state is found to lie around 0.1 eV below the $\tilde{E}(\pi\pi^*)$ state, whilst the $\tilde{D}(3p_y)$ state is calculated to be isoenergetic with the $\tilde{E}(\pi\pi^*)$ state at the FC point. The oscillator strengths calculated for these states at the FC point are small: 0.0149 for the $\tilde{C}(3p_z)$ state, and for the and 0.0004 for the $\tilde{D}(3p_y)$ state. To our knowledge, the only other high-level computational study of the excited states of aniline are the calculations of Honda *et al.* [114]. Using the SAC-CI method, the authors determine the VEEs of these states at the FC point to be 5.57 eV ($\tilde{C}(3p_z)$) and 6.06 eV ($\tilde{D}(3p_y)$), in stark disagreement with our CR-EOM-CCSD(T) values. We, however, have confidence in our placing of these states below the $\tilde{E}(\pi\pi^*)$ state, due to the higher level of theory used here. More importantly, the inclusion of these states in the model used is required to reproduce certain features of the experimental spectrum.

7.3.2 The Model Potential

A total of 620 parameters of the model potential non-zero by symmetry were fitted to 4200 adiabatic energies calculated across a wide range of nuclear geometries. A weighted RMSD of the fitted potential of 0.11 eV was attained.

The linear coupling coefficients of the model potential can be expected to have the greatest effect on the excited-state, short-time dynamics. As such, an analysis of the coupling strengths $\kappa_\alpha^{(i)}/\omega_\alpha$ and $\lambda_\alpha^{(i,j)}/\omega_\alpha$ may be used as a measure of the importance of the mode $\tilde{Q}_\alpha$ with respect to its effect on the dynamics of the system. We begin with an analysis of the degrees of freedom important for the description of the nuclear dynamics following excitation to the $\tilde{E}(\pi\pi^*)$ state. By symmetry, intrastate coupling strengths, $\kappa_\alpha^{(i)}/\omega_\alpha$, may be non-zero for only the totally-symmetric subset of degrees of

Table 7.3: Linear intrastate coupling strengths obtained from fitting to the results of EOM-CCSD/aug-cc-pVDZ calculations.

Mode	$\kappa_\alpha^{(2)}/\omega_2$	$\kappa_\alpha^{(3)}/\omega_3$	$\kappa_\alpha^{(4)}/\omega_4$	$\kappa_\alpha^{(5)}/\omega_5$	$\kappa_\alpha^{(6)}/\omega_6$	$\kappa_\alpha^{(7)}/\omega_7$	$\kappa_\alpha^{(8)}/\omega_8$
$\tilde{Q}_7$	-1.0918	-0.7315	-1.1719	-1.2381	-1.0148	-1.0518	-0.5159
$\tilde{Q}_{12}$	0.7309	-0.0059	-0.0285	0.1324	0.4837	0.1030	0.1060
$\tilde{Q}_{16}$	-0.9571	-0.8019	-0.7393	-0.5110	-1.2503	-0.5313	-0.7271
$\tilde{Q}_{18}$	1.0220	0.4505	0.4854	0.3962	0.7428	0.5063	0.5280
$\tilde{Q}_{21}$	-0.2838	0.0660	0.2382	-0.0184	0.3008	0.1048	0.1068
$\tilde{Q}_{22}$	-0.1135	0.1252	0.1307	0.0681	0.2608	0.1056	-0.0012
$\tilde{Q}_{26}$	-0.1417	-0.2059	0.0171	-0.1444	-0.0497	-0.1299	-0.0235
$\tilde{Q}_{28}$	-0.1264	0.4315	0.2651	0.2799	0.7035	0.2587	0.3964
$\tilde{Q}_{29}$	0.4380	-0.3137	-0.2346	-0.1777	-0.1802	-0.1229	-0.1433
$\tilde{Q}_{30}$	0.1026	0.0933	0.1375	0.1211	0.1115	0.1974	0.1317
$\tilde{Q}_{32}$	-0.2004	-0.2424	-0.1146	-0.2901	-0.5720	-0.4287	-0.2207
$\tilde{Q}_{34}$	0.4878	0.2565	0.9182	0.4459	0.2992	0.3600	0.6168

freedom. The frequency-weighted $\kappa_\alpha^{(i)}$ for the totally-symmetric degrees of freedom are listed in Table 7.3. For the $\tilde{E}(\pi\pi^*)$ state significant intrastate coupling strengths are found for the degrees of freedom $\tilde{Q}_7$ (ring stretching), $\tilde{Q}_{12}$ (ring stretching), $\tilde{Q}_{16}$ (ring stretching), $\tilde{Q}_{18}$ (ring breathing), $\tilde{Q}_{21}$ (C-H bending), $\tilde{Q}_{22}$ (ring breathing), $\tilde{Q}_{28}$ ((N)H_2 in-plane bending) and $\tilde{Q}_{32}$ (C-H stretching). The interstate coupling strengths $\lambda_\alpha^{(i,j)}/\omega_\alpha$ are shown in Table 7.4. The $\tilde{E}(\pi\pi^*)$ state is found to be strongly coupled to the $\tilde{D}(3p_y)$ state by the $\tilde{Q}_3$ (NH_2 torsion) mode, to the $\tilde{C}(3p_z)$ state by the $\tilde{Q}_1$ (NH_2 inversion) mode, to the $\tilde{B}(\pi\sigma^*/3s)$ state by the $\tilde{Q}_1$ (NH_2 inversion) and $\tilde{Q}_2$ (boat) modes, and to the $\tilde{A}(\pi\pi^*)$ state by the $\tilde{Q}_4$ (NH_2 in-plane bending) mode. Additionally, the mode $\tilde{Q}_4$ couples strongly the $\tilde{D}(3p_y)$ and $\tilde{B}(\pi\sigma^*/3s)$ states, $\tilde{Q}_{16}$ couples the $\tilde{C}_{3p_z}$ and $\tilde{B}(\pi\sigma^*/3s)$ states, while $\tilde{Q}_3$ couples the $\tilde{C}(3p_z)$ and $\tilde{A}(\pi\pi^*)$ states, and $\tilde{Q}_{11}$ (C-H out-of-plane bending) couples significantly the $\tilde{B}(\pi\sigma^*/3s)$ and $\tilde{A}(\pi\pi^*)$ states. Thus, together with the N-H dissociation coordinate $\tilde{Q}_{36}$ we may identify a total of fourteen nuclear degrees of freedom likely to be important for the description of the nuclear dynamics of aniline following excitation to the $\tilde{E}(\pi\pi^*)$ state.

Table 7.4: Linear interstate coupling strengths, obtained from fitting to the results of EOM-CCSD/aug-cc-pVDZ calculations.

A_1	$\lambda_\alpha^{(1,6)}/\omega_\alpha$	$\lambda_\alpha^{(3,4)}/\omega_\alpha$	$\lambda_\alpha^{(3,7)}/\omega_\alpha$	$\lambda_\alpha^{(4,7)}/\omega_\alpha$	$\lambda_\alpha^{(5,8)}/\omega_\alpha$			
$\tilde{Q}_7$	-0.1294	0.3573	1.1119	0.0708	0.2633			
$\tilde{Q}_{12}$	-0.1413	0.2315	-0.2953	-0.1403	-0.2266			
$\tilde{Q}_{16}$	0.8799	0.7523	0.1495	0.2705	0.2876			
$\tilde{Q}_{18}$	-0.1969	-0.1628	0.0899	-0.1783	-0.0070			
$\tilde{Q}_{21}$	0.7329	0.5110	-0.1497	0.5587	-0.0925			
$\tilde{Q}_{22}$	0.2455	0.1344	0.2136	0.0945	0.0466			
$\tilde{Q}_{26}$	0.2604	0.2198	-0.0551	0.3193	-0.1107			
$\tilde{Q}_{28}$	0.4695	0.2631	-0.2730	0.2069	0.0745			
$\tilde{Q}_{29}$	0.6182	0.3769	0.1515	0.1666	0.1952			
$\tilde{Q}_{30}$	0.0951	-0.1284	0.0344	-0.1115	-0.1782			
$\tilde{Q}_{32}$	0.6155	0.1722	0.2112	0.0219	0.0626			
$\tilde{Q}_{34}$	-0.3366	0.2078	-0.1200	-0.0257	0.2323			
A_2	$\lambda_\alpha^{(1,5)}/\omega_\alpha$	$\lambda_\alpha^{(1,8)}/\omega_\alpha$	$\lambda_\alpha^{(2,3)}/\omega_\alpha$	$\lambda_\alpha^{(2,4)}/\omega_\alpha$	$\lambda_\alpha^{(2,7)}/\omega_\alpha$	$\lambda_\alpha^{(5,6)}/\omega_\alpha$	$\lambda_\alpha^{(6,7)}/\omega_\alpha$	
$\tilde{Q}_3$	-1.6279	-5.2411	-0.0685	-4.3181	-3.2988	-1.6811	-4.2598	
$\tilde{Q}_5$	1.1656	-0.6695	-0.0379	2.5483	-0.8468	-0.1056	-0.3686	
$\tilde{Q}_{11}$	-0.3073	0.7440	-0.3952	-0.7045	-1.4218	-0.0968	-0.9061	
$\tilde{Q}_{15}$	0.8088	0.3279	-0.3780	-0.7666	-0.5626	0.0633	-0.1741	
B_1	$\lambda_\alpha^{(1,3)}/\omega_\alpha$	$\lambda_\alpha^{(1,4)}/\omega_\alpha$	$\lambda_\alpha^{(1,7)}/\omega_\alpha$	$\lambda_\alpha^{(2,5)}/\omega_\alpha$	$\lambda_\alpha^{(2,8)}/\omega_\alpha$	$\lambda_\alpha^{(3,6)}/\omega_\alpha$	$\lambda_\alpha^{(4,6)}/\omega_\alpha$	$\lambda_\alpha^{(6,7)}/\omega_\alpha$
$\tilde{Q}_1$	0.0000	0.0000	0.0000	-1.3616	-2.7632	-0.8223	-0.6225	-0.2447
$\tilde{Q}_2$	0.1281	2.3098	-0.0377	-0.2223	4.0205	1.7634	0.1997	0.2223
$\tilde{Q}_6$	1.0034	-0.2654	0.5211	0.5260	-1.4209	-1.1377	0.4628	0.0259
$\tilde{Q}_9$	0.5723	-0.4308	0.2544	1.0096	-0.0999	0.3880	-0.1596	0.8669
$\tilde{Q}_{10}$	-0.2278	-0.1128	-0.2190	-1.1083	-0.8608	-0.4622	0.1172	-0.7524
$\tilde{Q}_{13}$	-0.2353	0.3733	-0.3582	0.2126	0.2495	-0.0444	-0.2155	-0.5906
$\tilde{Q}_{14}$	-0.0312	0.0606	-0.1756	-0.2987	-0.9165	-0.5198	-0.0508	-0.0437
B_2	$\lambda_\alpha^{(1,2)}/\omega_\alpha$	$\lambda_\alpha^{(2,6)}/\omega_\alpha$	$\lambda_\alpha^{(3,5)}/\omega_\alpha$	$\lambda_\alpha^{(3,8)}/\omega_\alpha$	$\lambda_\alpha^{(4,5)}/\omega_\alpha$	$\lambda_\alpha^{(4,8)}/\omega_\alpha$	$\lambda_\alpha^{(5,7)}/\omega_\alpha$	$\lambda_\alpha^{(7,8)}/\omega_\alpha$
$\tilde{Q}_4$	0.7952	-1.5662	-0.6326	-1.2850	0.2482	1.0939	0.7886	-0.1669
$\tilde{Q}_8$	0.2801	-0.5510	-0.0565	-0.1946	-0.0973	-0.1959	0.1999	0.0092
$\tilde{Q}_{17}$	0.8808	-0.6923	-0.5561	-0.5584	-0.2329	-0.1315	-0.6400	0.1909
$\tilde{Q}_{19}$	0.3807	-0.4047	-0.0262	0.5496	-0.0298	0.1769	0.2715	-0.0116
$\tilde{Q}_{20}$	1.3803	-0.3807	0.1938	0.4113	-0.0424	-0.4064	-0.3404	0.1216
$\tilde{Q}_{23}$	0.3639	-0.3767	-0.0785	-0.6967	0.0189	-0.2282	-0.3596	-0.0268
$\tilde{Q}_{24}$	0.9394	-0.2444	0.1579	-0.1652	0.0737	0.1668	-0.2244	-0.0205
$\tilde{Q}_{25}$	1.7209	-0.0961	0.3431	-0.1965	-0.0521	0.0554	-0.3838	-0.0223
$\tilde{Q}_{27}$	0.0497	0.1437	-0.1099	0.2457	0.0428	0.0836	-0.0139	-0.0124
$\tilde{Q}_{31}$	0.1948	-0.2110	0.0541	-0.3556	-0.0306	-0.1271	-0.2381	0.0081
$\tilde{Q}_{33}$	0.2896	0.0728	-0.0105	-0.3430	0.0296	-0.0858	-0.2288	-0.0141

Table 7.5: Details of the MCTDH simulations of excitation to the $\tilde{A}(\pi\pi^*)$ state, for which a propagation time of 300 fs was used.

Particle	Number of grid points	Grid lengths	Number of SPFs
$\{\tilde{Q}_1, \tilde{Q}_{36}\}$	{20, 71}	[-4.0, 4.0], [-20.0, 3.00]	(4, 3, 3, 3, 3, 2)
$\{\tilde{Q}_7, \tilde{Q}_{12}\}$	{20, 20}	[-7.0, 7.0], [-7.0, 7.0]	(4, 5, 5, 4, 3, 2)
$\{\tilde{Q}_{16}, \tilde{Q}_{18}\}$	{20, 20}	[-7.0, 7.0], [-7.0, 7.0]	(4, 6, 6, 5, 3, 2)
$\{\tilde{Q}_{29}, \tilde{Q}_{34}\}$	{20, 20}	[-7.0, 7.0], [-7.0, 7.0]	(4, 6, 6, 5, 3, 2)
$\{\tilde{Q}_3, \tilde{Q}_5\}$	{20, 20}	[-7.0, 7.0], [-7.0, 7.0]	(4, 6, 6, 6, 4, 2)
$\{\tilde{Q}_{20}, \tilde{Q}_{25}\}$	{20, 20}	[-7.0, 7.0], [-7.0, 7.0]	(4, 5, 3, 3, 3, 2)

Table 7.6: Details of the MCTDH simulation of excitation to the $\tilde{E}(\pi\pi^*)$ state, for which a propagation time of 300 fs was used.

Particle	Number of grid points	Grid lengths	Number of SPFs
$\{\tilde{Q}_1, \tilde{Q}_7\}$	{15, 15}	[-4.0, 4.0],[-7.0, 7.0]	(5, 6, 9, 8, 5, 6)
$\{\tilde{Q}_{21}, \tilde{Q}_{22}\}$	{15, 15}	[-7.0, 7.0], [-7.0, 7.0], [-7.0, 7.0]	(5, 6, 8, 5, 4, 5)
$\{\tilde{Q}_{16}, \tilde{Q}_{18}, \tilde{Q}_{11}\}$	{15, 15, 15}	[-7.0, 7.0], [-7.0, 7.0], [-7.0, 7.0]	(5, 6, 9, 8, 5, 6)
$\{\tilde{Q}_{28}, \tilde{Q}_{32}, \tilde{Q}_4\}$	{15, 15, 15}	[-7.0, 7.0], [-7.0, 7.0], [-7.0, 7.0]	(5, 6, 9, 8, 5, 6)
$\{\tilde{Q}_{12}, \tilde{Q}_2, \tilde{Q}_3\}$	{15, 15, 15}	[-7.0, 7.0], [-7.0, 7.0], [-7.0, 7.0]	(5, 6, 9, 8, 5, 6)
$\{\tilde{Q}_{36}\}$	{71}	[-20.0, 3.00]	(5, 5, 5, 5, 5, 5)

Turning our attention to the excitation to the $\tilde{A}(\pi\pi^*)$ state, we find that significant interstate coupling strengths exist for the degrees of freedom $\tilde{Q}_7$ (ring stretching), $\tilde{Q}_{12}$ (ring stretching), $\tilde{Q}_{16}$ (ring stretching) and $\tilde{Q}_{18}$ (ring breathing). The $\tilde{A}(\pi\pi^*)$ and ground states are found to be very coupled strongly by the degrees of freedom $\tilde{Q}_{20}$ (C-H in-plane bending) and $\tilde{Q}_{25}$ (ring stretching). The modes $\tilde{Q}_3$ (C-H stretching) and $\tilde{Q}_5$ (boat) couple significantly the states $\tilde{A}(\pi\sigma^*/3s)$ and $\tilde{C}_{3p_z}$. Only relatively weak coupling of the $\tilde{A}(\pi\pi^*)$ and $\tilde{B}(\pi\sigma^*/3s)$ states is found to exist.

Illustrated in Figures 7.3 and 7.4 are, respectively, the normal modes most important for the description of the photoinduced dynamics of aniline, and the model and EOM-CCSD adiabatic energies along these degrees of freedom.

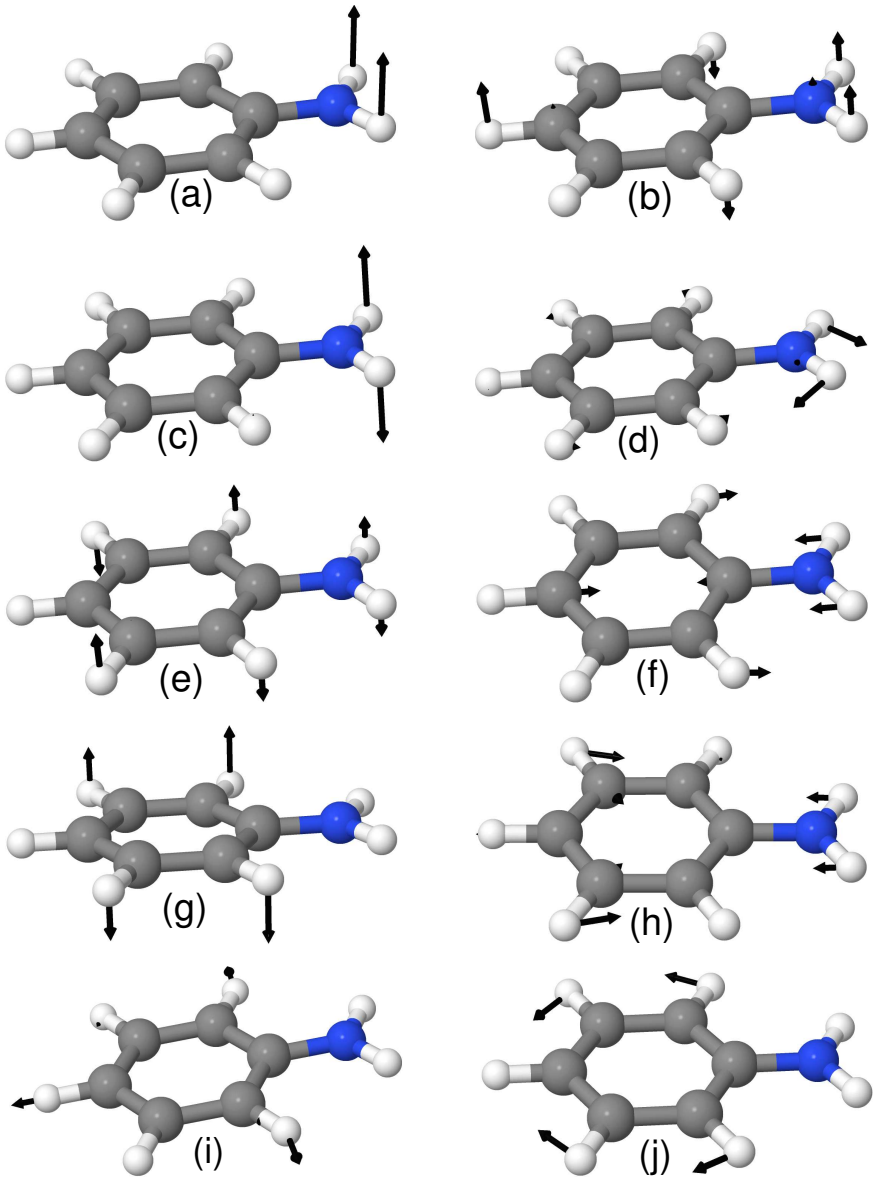

Fig. 7.3: Normal modes important for the description of the dynamics of aniline following excitation to the $\tilde{A}(\pi\pi^*)$ and $\tilde{E}(\pi\pi^*)$ states: (a) $\tilde{Q}_1$ (NH_2 inversion), (b) $\tilde{Q}_2$ (boat), (c) $\tilde{Q}_3$ (NH_2 torsion), (d) $\tilde{Q}_4$ (NH_2 in-plane bend), (e) $\tilde{Q}_5$ (boat), (f) $\tilde{Q}_7$ (ring stretch), (g) $\tilde{Q}_{11}$ (asymmetric C-H out-of-plane bending), (h) $\tilde{Q}_{12}$ (ring stretch), (i) $\tilde{Q}_{16}$ (ring stretch), and (j) $\tilde{Q}_{18}$ (C_5H_5 breathing).

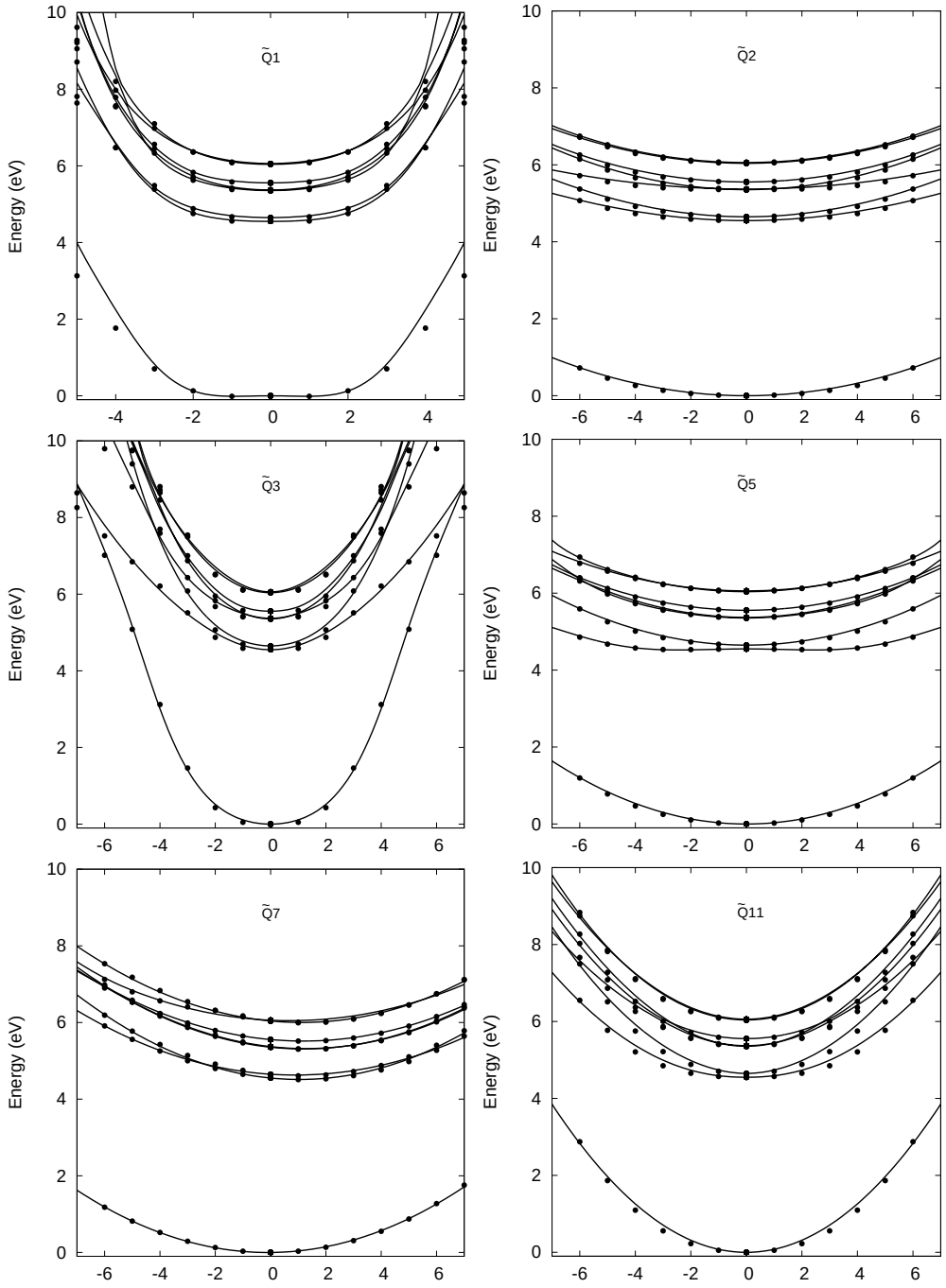

Fig. 7.4: Continued over page.

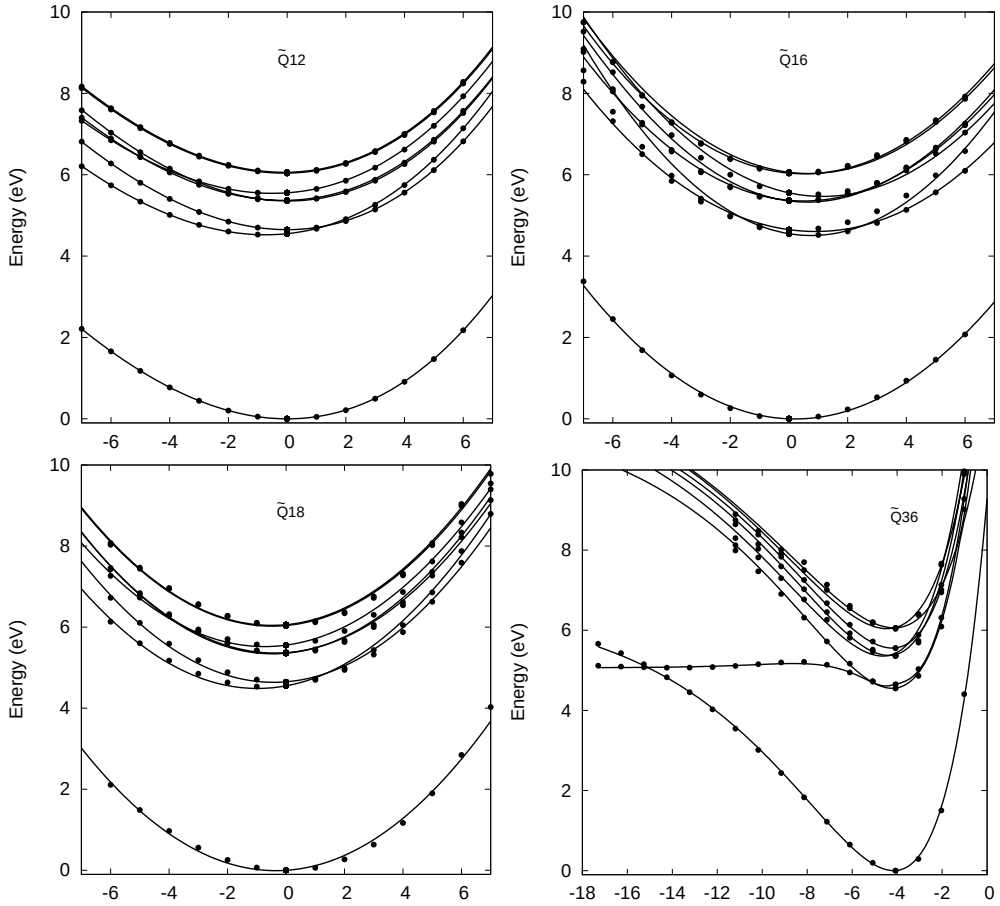

Fig. 7.4: Model (lines) and calculated (points) adiabatic energies along nuclear degrees of freedom important for the description of the dynamics of aniline following excitation to the $\tilde{A}(\pi\pi^*)$ and $\tilde{E}(\pi\pi^*)$ states.

7.3.3 Model Spectra

To reproduce the electronic absorption spectrum in the range 4.0 to 6.0 eV, two wavepacket propagations were performed, corresponding to excitation to the $\tilde{A}(\pi\pi^*)$ and $\tilde{E}(\pi\pi^*)$ states. The total spectrum in this energy range was then produced by summing the two resulting spectra weighted by their calculated oscillator strengths. The details concerning the DVRs and numbers of SPFs used in these calculations are given in Tables 7.5 and 7.6.

To calculate the spectrum corresponding to excitation to the $\tilde{A}(\pi\pi^*)$ state, initial wavepackets were produced by operating on the ground state wavefunction, $|\Psi_{GS}\rangle$, using two different excitation operators,

$$\hat{O}_v = |2\rangle\langle 1| + h.c., \tag{7.16}$$

and

$$\hat{O}_{HT} = \left\{ |2\rangle \left[\boldsymbol{\mu}_{12}(\tilde{\boldsymbol{Q}}_0) + \sum_{\alpha=1}^{3N-6} \frac{\partial \boldsymbol{\mu}_{12}(\tilde{\boldsymbol{Q}}_0)}{\partial \tilde{Q}_\alpha} \tilde{Q}_\alpha \right] \langle 1| \right\} + h.c. \tag{7.17}$$

The first of these operators, $\hat{O}_v$, corresponds to vertical excitation to the $\tilde{A}(\pi\pi^*)$ state, whilst the operator $\hat{O}_{HT}$ is used to take into account the possibility of the Herzberg-Teller effect being operative in this process. Displayed in Figure 7.5 are the calculated and experimental spectra. The spectrum produced using the excitation operator $\hat{O}_{HT}$ is found to yield significantly better agreement with the experimental spectrum, and so only this is shown here. Here, in order to affect homogeneous broadening of the spectra and account for the exclusion of the "bath" of modes not included in the wavepacket propagations, the autocorrelation function is convoluted with an exponential damping function, and short damping times of 18 fs and 38 fs were used in the calculations of the $\tilde{A}(\pi\pi^*)$ and $\tilde{E}(\pi\pi^*)$ state spectra, respectively. Figures 7.6

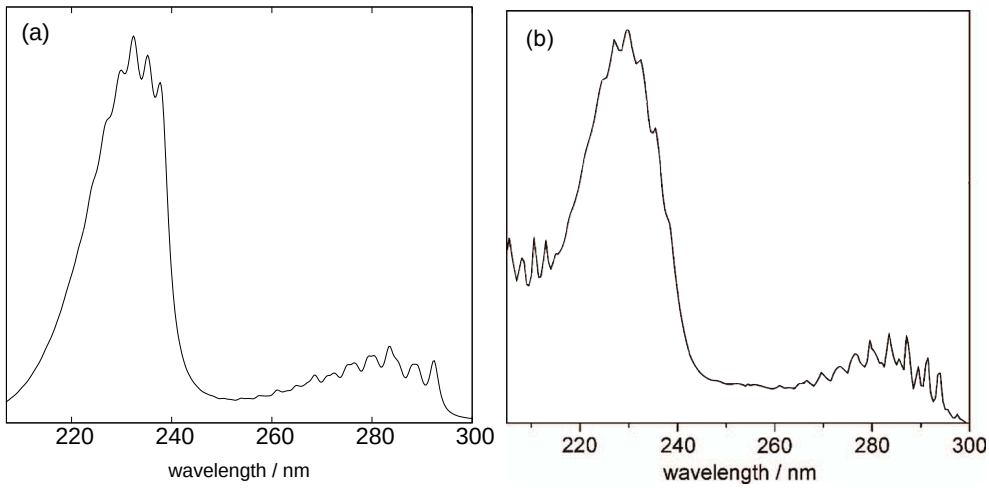

Fig. 7.5: (a) Absorption spectrum calculated using wavepacket propagations over model potential surfaces representing the sub-Hilbert space spanned by the first six electronic states of aniline. The upper band corresponds to vertical excitation to the $\tilde{E}(\pi\pi^*)$ state and was produced using a fourteen-dimensional model potential. The lower band corresponds to excitation to the $\tilde{A}(\pi\pi^*)$ state, was produced using a twelve-dimensional model including Herzberg-Teller terms. Damping functions have been included in the Fourier transforms of the autocorrelation functions to model the homogeneous broadening due to excluded modes. (b) Experimental spectrum, adapted from Ref 116.

and 7.7 show individually the two spectra calculated using a longer damping time (100 fs), which renders transparent their vibrational structures.

Shown in Figure 7.6 (a) and Figure 7.6 (b) are the spectra calculated using the excitation operators $\hat{O}_v$ and $\hat{O}_{HT}$, respectively. The spectrum corresponding to vertical excitation contains progressions due to six modes: $\tilde{Q}_3$, $\tilde{Q}_5$, $\tilde{Q}_7$, $\tilde{Q}_{12}$, $\tilde{Q}_{16}$ and $\tilde{Q}_{18}$. Within the quadratic vibronic coupling model, a mode $\tilde{Q}_\alpha$ with a ground state frequency ω_α possesses a frequency $\omega_\alpha^{(i)}$ in the state indexed by i given by

$$\omega_\alpha^{(i)} = \left(\omega_\alpha^2 + \gamma_{\alpha\alpha}^{(i)}\omega_\alpha\right)^{\frac{1}{2}}, \tag{7.18}$$

and it is the modified frequencies $\omega_\alpha^{(2)}$ that are used in the analysis of the $\tilde{A}(\pi\pi^*)$ state spectrum. Specifically, we have $\omega_3^{(2)} = 0.1130$ eV, $\omega_5^{(2)} = 0.0343$ eV, $\omega_7^{(2)} = 0.0666$ eV, $\omega_{12}^{(2)} = 0.1004$ eV, $\omega_{16}^{(2)} = 0.1384$ eV and $\omega_{18}^{(2)} = 0.1321$

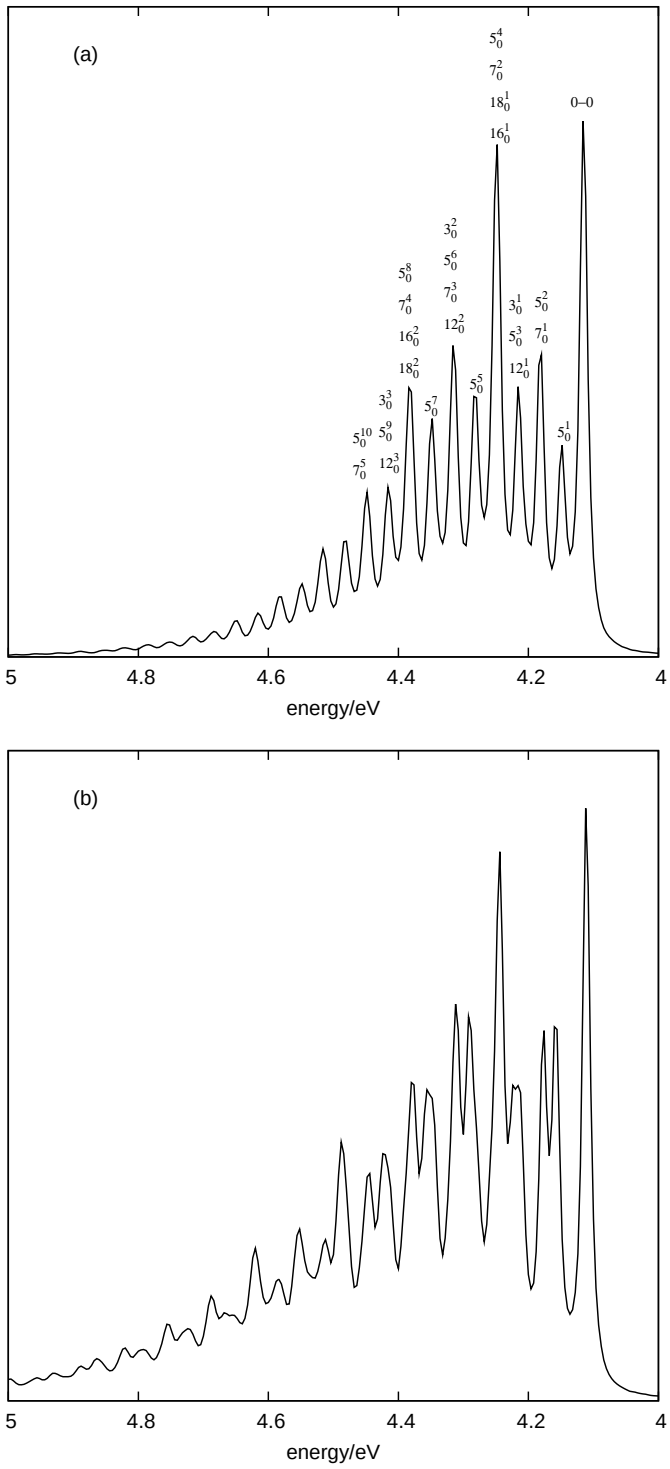

Fig. 7.6: Spectra corresponding to excitation to the $\tilde{A}(\pi\pi^*)$ state, calculated using twelve-dimensional, six-state wavepacket propagations. (a) Spectrum calculated using vertical excitation to the $\tilde{A}(\pi\pi^*)$ state, with assignments of the vibrational progressions given for the first eleven peaks. (b) Spectrum calculated using the linear dipole excitation operator $\hat{O}_{HT}$ to model the Herzberg-Teller effect.

eV. As such, the progressions in the modes $\tilde{Q}_3$ and $\tilde{Q}_{12}$ are found to overlap, as are those in the modes $\tilde{Q}_{16}$ and $\tilde{Q}_{18}$. We note that the non-totally symmetric modes $\tilde{Q}_3$ and $\tilde{Q}_5$ become spectroscopically active due to the strong coupling of the $\tilde{A}(\pi\pi^*)$ and $\tilde{C}(3p_z)$ states that exists with respect to these degrees of freedom. The gradient of transition dipole moment component $\mu_{12,x}$ with respect to the mode $\tilde{Q}_5$ is calculated to be rather large (-1.13). As a result, when the initial wavepacket is produced by operation on $|\Psi_{GS}\rangle$ with $\hat{O}_{HT}$, the intensities of the peaks corresponding to the progression in $\tilde{Q}_5$ are significantly increased, as is illustrated in Figure 7.6 (b). We note that both the inclusion of the $\tilde{C}(3p_z)$ state and the use of the excitation operator $\hat{O}_{HT}$, used to account for the Herzberg-Teller effect, were required in order to adequately reproduce the $\tilde{A}(\pi\pi^*)$ state spectrum.

The calculated spectrum corresponding to vertical excitation to the $\tilde{E}(\pi\pi^*)$ state is shown in Figure 7.7. The spectrum is found to be dominated by progressions in the three modes $\tilde{Q}_7$, $\tilde{Q}_{16}$ and $\tilde{Q}_{18}$. Again the progressions in the modes $\tilde{Q}_{16}$ and $\tilde{Q}_{18}$ are found to overlap due to the almost identical modified frequencies $\omega_\alpha^{(6)}$ of these modes.

7.3.4 Dynamics

The diabatic state populations following excitation to the $\tilde{A}(\pi\pi^*)$ state are shown in Figure 7.8. The system is found to remain predominantly in the initially excited state, with significant population transfer only occurring to the $\tilde{C}(3p_z)$ state. Only a small amount of population is found to cross into the $\tilde{B}(\pi\sigma^*/3s)$ state, with the probability of population of this state growing steadily to reach a value of 0.055 at 300 fs. Although the N-H dissociation coordinate $\tilde{Q}_{36}$ is included in the calculation, only negligible N-H dissociation is found to occur throughout the propagation, with a time-cumulated probability of dissociation of 0.017 after 300 fs. This may be

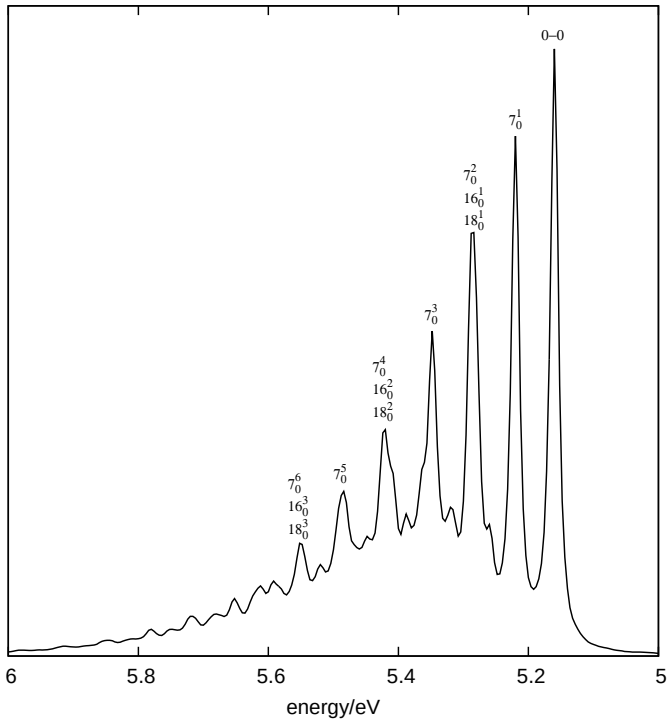

Fig. 7.7: Spectrum corresponding to vertical excitation to the $\tilde{E}(\pi\pi^*)$ state, calculated using a fourteen-dimensional, six-state wavepacket propagation, with assignments of the three dominant vibrational progressions.

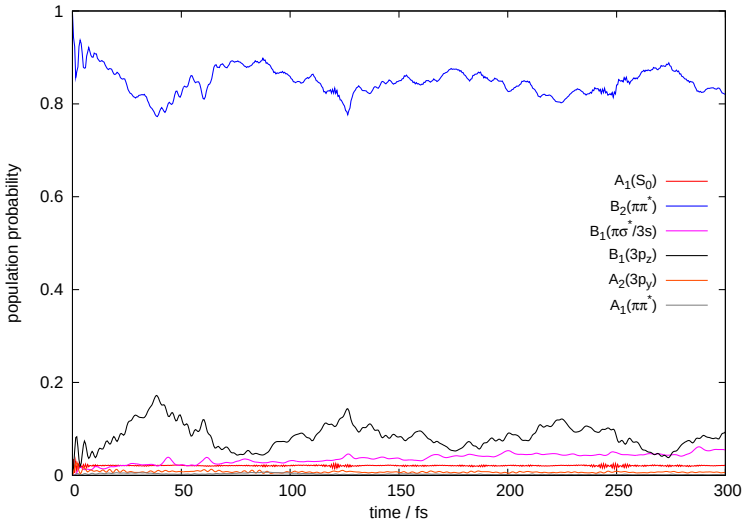

Fig. 7.8: Diabatic state population probabilities following excitation to the $\tilde{A}(\pi\pi^*)$ state, calculated using a twelve-dimensional, six-state wavepacket propagation. The corresponding initial state was produced by operation on the ground state wavefunction with the linear dipole excitation operator $\hat{O}_{HT}$.

attributed to two factors: (i) the barrier to N-H dissociation is found to be rather large (∼0.5 eV at the EOM-CCSD/aug-cc-pVDZ level), and; (ii) there exists only relatively small vibronic coupling of the states $\tilde{A}(\pi\pi^*)$ and $\tilde{B}(\pi\sigma^*/3s)$. We note that a negligible probability of N-H dissociation on the $\tilde{B}(\pi\sigma^*/3s)$ state surface is consistent with the results of the time-resolved velocity map imaging studies performed by Stavros *et al.* [118].

The diabatic state population probabilities following excitation to the $\tilde{E}(\pi\pi^*)$ state are shown in Figure 7.9. Strong vibronic coupling of the energetically proximate $\tilde{D}(3p_y)$ and $\tilde{C}(3p_z)$ states to the $\tilde{E}(\pi\pi^*)$ state results in an in-phase, oscillatory transfer of population between the initially excited state and the two $3p$ Rydberg states throughout the duration of the wavepacket propagation. Further coupling of the $3p$ Rydberg states to the $\tilde{A}(\pi\pi^*)$ and $\tilde{B}(\pi\sigma^*/3s)$ states results in the monotonic rise in the populations of these states. By 300 fs the population probabilities of the five states $\tilde{A}(\pi\pi^*)$, $\tilde{B}(\pi\sigma^*/3s)$, $\tilde{C}(3p_z)$, $\tilde{D}(3p_y)$ and $\tilde{E}(\pi\pi^*)$ are 0.083, 0.173, 0.058,

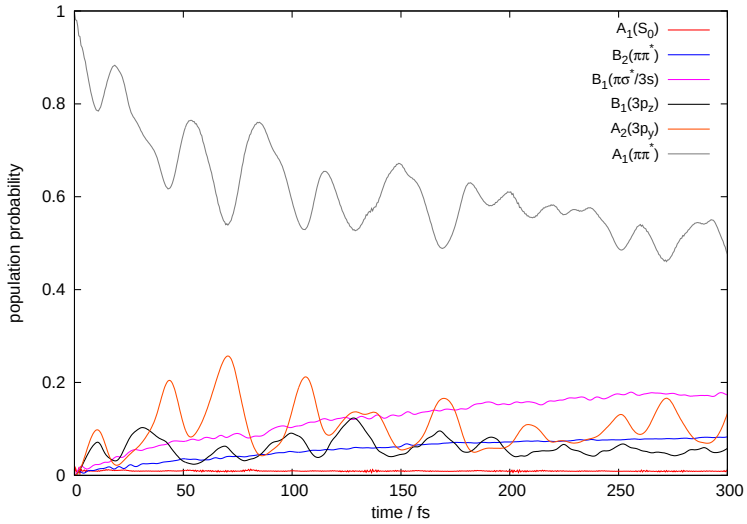

Fig. 7.9: Diabatic state population probabilities following excitation to the $\tilde{E}(\pi\pi^*)$ state, calculated using a fourteen-dimensional, six-state wavepacket propagation and a vertical excitation of the ground state wavefunction.

0.133, and 0.476, respectively. The population that reaches the $\tilde{B}(\pi\sigma^*/3s)$ remains mainly in the interaction region, with the calculated probability of dissociation after 300 fs being 0.068.

We note that only a negligible amount of population is transferred to the ground state. This is in stark disagreement with the time-resolved photoelectron imaging (TRPEI) studies of Fielding *et al.* [119,120], in which transfer of population to the ground state was observed to occur on a timescale of <100 fs. This transfer of population is undoubtedly mediated by an accessible pathway to a conical intersection between the two states that is not included in our model potential. Indeed, the recent CASSF calculations of Paterson and co-workers [118] point to a very likely candidate: a prefulvenic geometry distinctly reminiscent of the geometry of the conical intersection known to be responsible for ultrafast S_1/S_0 internal conversion in the 'channel 3' region of benzene [122, 123]. The results presented here, however, do suggest that without the inclusion of this conical intersection population transfer out

of the manifold of states spanned by the energetically proximate $\tilde{E}(\pi\pi^*)$, $\tilde{D}(3p_y)$ and $\tilde{C}(3p_z)$ states is hindered, indicating that there should be little competition with a pathway that directly connects the $\tilde{E}(\pi\pi^*)$ and $\tilde{X}$ states.

We tentatively note that the rapid transfer of population from the $\tilde{E}(\pi\pi^*)$ state to the energetically proximate $\tilde{C}(3p_z)$ and $\tilde{D}(3p_y)$ states that we observe may be consistent with the energetically broad band in the TRPEI spectrum recorded by Fielding *et al.* [119,120] that is taken to correspond to ionisation from the $\tilde{E}(\pi\pi^*)$ state. At excitation wavelengths close to the origin of the second band in the electronic absorption spectrum of aniline, this peak is seen to split into two components which we posit could be consistent with the existence of an electronic state in existence just below the $\tilde{E}(\pi\pi^*)$ state. For reference, the TRPEI spectra under consideration here are reproduced in Figure 7.10.

7.4 Conclusions

In this chapter a model Hamiltonian based on the quadratic vibronic coupling model has been developed for the primary intention of the study of the electronic absorption spectrum of aniline. The parameterisation of the model Hamiltonian is achieved *via* fitting to the results of extensive EOM-CCSD calculations. In contrast to previously reported CASSCF [118] and SAC-CI [114] calculations, the presently reported EOM-CCSD calculations suggest the existence of two $3p$ Rydberg states in the vicinity of the second $^1\pi\pi^*$ state. The results of further, more rigorous, CR-EOM-CCSD(T) calculations are found to be in agreement with this picture.

Using our model Hamiltonian, wavepacket propagations were performed in order to calculate the absorption spectra corresponding to excitation to the $\tilde{A}(\pi\pi^*)$ and $\tilde{E}(\pi\pi^*)$ states. The inclusion of the strong vibronic coupling

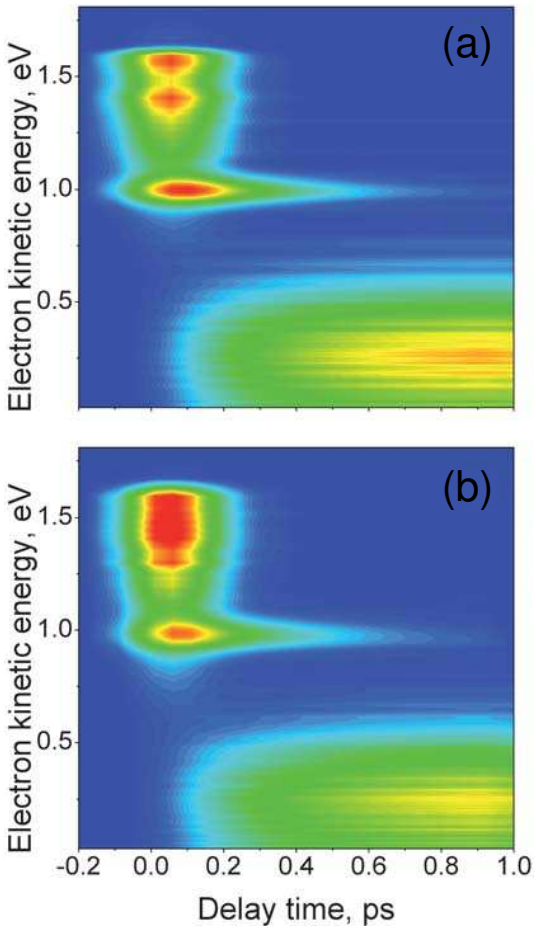

Fig. 7.10: Time-resolved photoelectron spectra recorded following photoexcitation of aniline adapted from Ref. [119]: (a) spectrum recored following excitation at 5.17 eV, and; (b) spectrum recorded following excitation at 5.21 eV. The lower peak at $\sim$ 1 eV is attributable to ionisation from the $B_2(\pi\pi^*)$ state. The broad peak seen at $\sim$ 1.3 eV to $\sim$ 1.6 eV has been taken to correspond to ionisation from the $A_1(\pi\pi^*)$ state [119], but at lower excitation energies is found to be composed of two peaks, the lower of which we propose could be due to ionisation from the $\tilde{D}(3p_y)$ and/or $\tilde{C}(3p_z)$ states.

of the $\tilde{A}(\pi\pi^*)$ and $\tilde{C}(3p_z)$ states is found to be crucial to being able to satisfactorily reproduce the $\tilde{A}(\pi\pi^*)$ spectrum. Further, the inclusion of the Herzberg-Teller effect, through the use of a linear dipole excitation operator, is also found to significantly alter the spectrum and is necessary to capture the features of first band of the experimental spectrum.

The model Hamiltonian used is found to be capable of reproducing the second band in the experimental spectrum, corresponding to excitation the the $\tilde{E}(\pi\pi^*)$ state. The $\tilde{C}(3p_z)$ and $\tilde{D}(3p_y)$ Rydberg states are found to be active in the short-time dynamics following excitation of this state. A major deficiency of the current model, however, is it's inability to account for the experimentally observed ultrafast internal conversion to the ground state following excitation to the $\tilde{E}(\pi\pi^*)$ state. This is almost certainly due to the inaccuracy of the model potential in the regions connecting the FC point to a prefulvenic S_1/S_0 conical intersection known to exist [118]. Given this, further work to extend the current model potential to describe accurately regions further away from the reference geometry is desirable.

Chapter 8

Conclusions

In this thesis the results of the quantum dynamics simulations of a number of molecular systems have been presented. A common feature unifying the systems studied is the presence of one or more low-lying, quasi-bound singlet $3s/\pi\sigma^*$ states in each. Until now the identity of the vibronic coupling responsible for the formation of the quasi-bound topologies of these states has not been sought, nor an evaluation of its effect on the dynamics that ensue following excitation to these states attempted.

Ammonia represents a prototype for systems containing quasi-bound $3s/\pi\sigma^*$ states. All previous theoretical studies of the photodissociation of ammonia have considered only the roles played by its S_0 and $S_1(3s/\pi\sigma^*)$ states. Given the likelihood of the quasi-bound topology of the $S_1(3s/\pi\sigma^*)$ state arising as a result of vibronic coupling to higher-lying states, a pertinent question to ask is whether S_0 and $S_1(3s/\pi\sigma^*)$ states of ammonia constitute a Hilbert subspace, and if not what the effect of the coupling of these two states to their orthogonal complement will have on ammonia's photodissociation dynamics in its $S_1(3s/\pi\sigma^*)$ state. In Chapter 4, through the evaluation of the extended Curl equation for these two states, it was shown in a quantitative manner that the states in question do not form to a satisfactory extent a Hilbert subspace at either the Franck-Condon point or the $S_1(3s/\pi\sigma^*)$ D_{3h}

minimum. Further, the estimated order of magnitude of the non-adiabatic coupling of these states to their orthogonal complement was determined to be large, prompting the construction of two eight-state model Hamiltonians for use in quantum dynamics simulations of the photodissociation of ammonia in its $S_1(3s/\pi\sigma^*)$ state. From simple symmetry arguments and NACT calculations, the strong vibronic coupling of the $\tilde{A}(3s)$ and $\tilde{D}(4s)$ states was identified as possibly providing the origin to the barrier to dissociation on the $S_1(3s/\pi\sigma^*)$ state surface, and this coupling scheme incorporated into the construction of the model Hamiltonians. The validity of the Hamiltonians constructed (differing in their dimensionality and the choice of nuclear coordinates used in their parameterisation) was confirmed by their ability to reproduce well the $S_1(3s/\pi\sigma^*) \leftarrow S_0$ electronic absorption spectrum. In order to assess the effect of the coupling of the S_0 and $S_1(3s/\pi\sigma^*)$ states to their orthogonal complement on the dissociation of ammonia in the latter state, a transformation of the model Hamiltonians used was devised based upon a block-diagonalisation of the model potentials such that the coupling by the electronic Hamiltonian of $\tilde{X}$ and $\tilde{A}(3s)$ diabatic states to their orthogonal complement was removed. By ignoring the coupling terms introduced into the off-diagonal elements of the matrix representation of the kinetic energy operator by this transformation, the effect of this coupling of the dynamics of ammonia following excitation to the $\tilde{A}(3s)$ state was evaluated. It is found that the strong coupling of the $\tilde{A}(3s)$ and $\tilde{D}(4s)$ states, that in both models used is responsible for the barrier to dissociation in the $S_1(3s/\pi\sigma^*)$ state, has an almost negligible effect on the rates of dissociation, and a minor effect on the calculated branching ratios between the two adiabatic dissociation channels. The coupling of the $\tilde{A}(3s)$ state to the and $\tilde{B}(3p)$ states by the planar angular degrees of freedom was found to have a more pronounced ef-

fect on the dissociation dynamics, with the inclusion of the coupling leading to a decrease by 10% of the probability of dissociation by 750 fs. The fact that the inclusion in the model Hamiltonians used of the vibronic coupling that is responsible for the formation of the barrier to dissociation appears to have little effect on the dissociation dynamics of ammonia is of use with regards to the construction of model Hamiltonians for larger systems: the incorporation of this coupling complicates significantly the construction of the model Hamiltonian, a complication that will be amplified for larger systems with higher densities of states, and the demonstration here of its negligibility with regards to the dynamics in the $\tilde{A}(3s)$ state of ammonia provides a more rigorous argument for the neglect of analogous coupling in other systems.

The simulation of the dynamics of ammonia following excitation to both components of its doubly-degenerate $\tilde{B}(3p)$ state was performed using an eight-state, four-mode model. Sub-picosecond timescales for the transfer of population from both components to the $\tilde{A}(3s)$ state were found, whereupon dissociation was found to proceed almost entirely diabatically. Hindrance of a meaningful comparison with experimentally determined timescales for relaxation from the $\tilde{B}(3p)$ state is brought about by the excitation of specific vibrational levels (and the reporting of a high degree of sensitivity of rate of relaxation with the initial vibrational state excited) in the only existing time-resolved experimental study [71], in contrast to the vertical excitation used in the present work. It would thus be desirable to repeat these calculations to include the preparation of initial states corresponding to specific vibrational levels of the $\tilde{B}(3p)$ state.

In Chapter 5 a model Hamiltonian based on the vibronic coupling Hamiltonian, but extended to allow the description of the breaking of a bond, was developed and used to model the excited state dynamics of 3-pyrroline. Us-

ing the method of improved relaxation, wavefunctions corresponding to the axial and equatorial conformers of 3-pyrroline were calculated. A conformer-resolved study of dissociation dynamics of 3-pyrroline was performed by using as initial wavepackets these wavefunctions vertically displaced to each of the $\tilde{A}(3s)$ and $\tilde{B}(3p_x)$ states. Comparable branching ratios and rates of dissociation were found for both conformers, a consequence of the existence of shared quasi-planar minima in both the $\tilde{A}(3s)$ and $\tilde{B}(3p_x)$ states. In analogy with the dissociation of ammonia in its first excited state, the dynamics of 3-pyrroline following excitation to its $\tilde{A}(3s)$ state is found to be dominated by the requirement of quasi-planarisation for the unhindered dissociation of the N-H bond to occur. This is found to be reflected in the calculated $\tilde{A}(3s) \leftarrow \tilde{X}$ and $\tilde{B}(3p_x) \leftarrow \tilde{X}$ absorption spectra, which are both dominated by progressions in the C-N-C and N-H out-of-plane modes, which together describe the planarisation of the C-NH-C unit. Again, this can be seen to be analogous to the case of ammonia, whose electronic absorption spectrum is dominated by progressions in the umbrella mode, corresponding to the planarisation of the molecule in its electronically excited states.

Using the methodology developed in Chapter 5, an eight-state model Hamiltonian for use in the description of the excited state dynamics of pyrrole was presented in Chapter 6. The parameterisation of the model Hamiltonian was achieved through fitting to the results of a large number of CASPT2 calculation. Using this model Hamiltonian, and an 'auxiliary' single-state vibronic coupling Hamiltonian parameterised to describe the $B_1(3p_y)$ state, the first band in the electronic absorption spectrum of pyrrole was calculated. The three spectra corresponding to vertical excitation to the $A_1(\pi\pi^*)$, $B_1(3p_y)$ and $B_2(\pi\pi^*)$ states were found to account for the majority of the intensity in this band, with the spectrum being dominated

by the $B_2(\pi\pi^*)$ state spectrum, as has previously been postulated. However, it is found that much of the calculated spectrum arises due to intensity borrowing from the $A_1(\pi\pi^*) \leftarrow A_1(S_0)$ and $B_2(\pi\pi^*) \leftarrow A_1(S_0)$ transitions by the the $B_1(3s) \leftarrow A_1(S_0)$ and $A_2(3p_z) \leftarrow A_1(S_0)$ transitions. The effect of this intensity borrowing is starkest for the $B_2(\pi\pi^*)$ spectrum, the majority of whose intensity below 6.15 eV is found to result from coupling to the $B_1(3s)$ and $A_2(3p_z)$ states. Interestingly, the calculations performed suggest that the peak appearing at ∼5.7 eV in the experimental spectrum does not correspond, as has previously been postulated [95, 103], to the origin of the $B_2(\pi\pi^*)$ band, but instead to excitation to the $B_1(3s)$ and $A_2(3p_z)$ states, rendered non-negligible *via* coupling, respectively, to the $A_1(\pi\pi^*)$ and $B_2(\pi\pi^*)$ states.

Using a seven-mode, six-state model, the dissociation dynamics of pyrrole following excitation to its $A_2(3s)$ state was modelled. Two timescales for the dissociation of the vertically excited wavepacket were found to exist. The first, of ∼30 fs corresponds to direct dissociation of those components of the initial wavepacket that lie above the barrier to dissociation, whilst the second timescale of ∼340 fs was found to correspond to tunnelling of the low-energy components of the wavepacket through the barrier to dissociation. By varying in the model potential the height of the barrier to dissociation on the $A_2(3s)$ state surface, an extreme sensitivity of the calculated timescale for tunnelling through the barrier to dissociation was revealed. This serves to highlight the need for accurate electronic structure calculations to underlie the parameterisation of a model Hamiltonian, with a variation of the barrier height by only ±0.1 eV being found to change the rate of tunnelling by an order of magnitude.

Using a ten-mode, six-state model, the dynamics of pyrrole following ex-

citation to the $B_2(\pi\pi^*)$ state was modelled. Approximately 60% of the population is found to relax efficiently *via* the $A_2(3p_z)$ state to the $A_2(3s)$ and $B_1(3s)$ states, whereupon diabatic dissociation was found to proceed unhindered. Diabatic trapping of the remaining population in the initially excited $B_2(\pi\pi^*)$ state was found to occur as a consequence of the C-N-C out-of-plane bending mode Q_2. This result is not in accord with the generally held view that relaxation of pyrrole following excitation to the $B_2(\pi\pi^*)$ state occurs at least in part by internal conversion to the ground state mediated by the so-called ring-puckered conical intersection [86–89]. The evolving wavepacket does, however, appear to sample regions of nuclear configuration space corresponding to geometries for which distinct similarities with the geometry of the ring-puckered conical intersection exist. This serves to highlight the limitations of the vibronic coupling Hamiltonian, the model on which the Hamiltonian used here is based. Although able to reproduce well spectra and describe relaxation pathways that are dominated by single nuclear coordinates, the use of a model potential based on a low-order Taylor expansion makes the accurate description of the potential along pathways corresponding to linear combinations of possibly strongly correlated nuclear degrees of freedom difficult task to achieve.

In Chapter 7, a study of the dynamics of aniline following excitation to its first two $\pi\pi^*$ states was presented. The parameterisation of the model potential was achieved *via* fitting to the results of extensive EOM-CCSD calculations. The results of these, and further, more rigorous CR-EOM-CCSD(T) calculations, suggest that two 3*p*-type Rydberg states, labelled the $\tilde{C}(3p_z)$ and $\tilde{D}(3p_y)$ states, should exist between the $\tilde{B}(3s/\pi\sigma^*)$ and $\tilde{E}(\pi\pi^*)$ states. These two states have previously been ignored, presumably as previous, less accurate, calculations have placed them significantly higher in energy [114].

In order to bring into agreement the calculated and experimental first bands in aniline's electronic absorption spectrum, both the inclusion of the coupling of the $\tilde{A}(\pi\pi^*)$ and $\tilde{C}(3p_z)$ states and the use of a linear dipole excitation operator were found to be necessary. The latter highlights the role played by the Hertzberg-Teller effect in the excitation to the $\tilde{A}(\pi\pi^*)$, with, in particular, the gradient of the transition dipole moment $\boldsymbol{\mu}_{12}$ with respect to the 'boat' mode $\tilde{Q}_5$ being responsible for important aspects of the vibrational structure seen in the $\tilde{A}(\pi\pi^*)$ spectrum.

The $\tilde{C}(3p_z)$ state, as well as the $\tilde{D}(3p_y)$ state, is found to play a role also in the dynamics of aniline following excitation to its $\tilde{E}(\pi\pi^*)$ state, with population being found to cascade through both states into the lower-lying $\tilde{A}(\pi\pi^*)$ and $\tilde{B}(3s/\pi\sigma^*)$ states. Analogous to the case of pyrrole, there is known to exist an efficient mechanism for internal conversion of aniline excited to its $\tilde{E}(\pi\pi^*)$ state to its ground state, thought to involve a prefulvenic-type conical intersection [118]. The model used in this work, however, is found to not describe the potential well enough along the pathway to this conical intersection to be able to describe this relaxation pathway. Again, as in the case of pyrrole, this is due to a lack of correlation in the model potential of the nuclear degrees of freedom involved in the transition to this conical intersection. Future work in which this pathway is included in the model potential is thus motivated.

Finally, we comment on the roles found to be played by usually neglected $3p$ Rydberg states in the excited states dynamics of both pyrrole and aniline. In both systems, states of this character were found to play important roles in relaxation following excitation to bright $\pi\pi^*$ states. The activity of the $3p$ Rydberg states in these systems raises important questions with regards to the choice of method used in the calculations of adiabatic energies for

such systems. Multireference methods based on a CASSCF wavefunction are the only currently available means of being able to describe bond-breaking consistently well over a large range of systems, and as such are undoubtedly of much value. However, for systems such as the heteroaromatic species studied here, the high density of low-lying electronic states poses significant problems for CASSCF-based methods, for which an active space must be selected. The requirement of choosing a tractable active space will almost always result in the inability of a single CASSCF calculation to be able to describe all states in existence within an energy range of interest. Hence, an *a priori* evaluation of the importance of an electronic state with regards to a system's excited state dynamics must be made, even though such an importance may only truly be evaluated *a posteriori*, following the execution of a quantum dynamics simulation. Active-space-free methods such as the EOM-CCSD method obviate this problem and require no effective user-made pre-selection of electronic states. Such single-reference methods, however, are prone to failure when, for example, when far into a dissociation limit.

Bibliography

[1] R. Schoenlein, L. Peteanu, R. Mathies, and C. Shank. Science **254**, 412 (1991).

[2] C. E. Crespo-Hernandez, B. Cohen, P. M. Hare, and B. Kohler. Chem. Rev. **104**, 1977 (2004).

[3] D. Creed. Photochem. Photobiol. **39**, 537 (1984).

[4] P. Callis. Annu. Rev. Phys. Chem. **34**, 329 (1983).

[5] M. N. R. Ashfold, B. Cronin, A. L. Devine, R. N. Dixon, and M. G. D. Nix. Science **312**, 1637 (2006).

[6] A. L. Sobolewski and W. Domcke. Chem. Phys. **259**, 181 (2000).

[7] A. Iqbal and V. G. Stavros. J. Phys. Chem. A **114**, 68 (2010).

[8] M. N. R. Ashfold, A. L. Devine, R. N. Dixon, G. A. King, M. G. D. Nix, and T. A. A. Oliver. Proc. Natl. Acad. Sci. **105**, 12701 (2008).

[9] M. N. R. Ashfold, G. A. King, D. Murdock, M. G. D. Nix, T. A. A. Oliver, and A. G. Sage. Phys. Chem. Chem. Phys. **12**, 1218 (2010).

[10] A. Alijah and M. Baer. J. Phys. Chem. A **104**, 389 (2000).

[11] M. Baer. *Beyond Born-Oppenheimer: Electronic Nonadiabatic Coupling Terms and Conical Intersections*, Wiley (2006).

[12] T. S. Venkatesan, S. G. Ramesh, Z. Lan, and W. Domcke. J. Chem. Phys. **136**, 174312 (2012).

[13] J. Jornet-Somoza, B. Lasorne, M. A. Robb, H. D. Meyer, D. Lauvergnat, and F. Gatti. J. Chem. Phys. **137**, 084304 (2012).

[14] T. Helgaker, P. Jørgensen, and J. Olsen. *Molecular Electronic Structure Theory*, Wiley (2000).

[15] B. O. Roos and K. Andersson. Chem. Phys. Lett. **245**, 215 (1995).

[16] R. Kosloff and H. Tal-Ezer. Chem. Phys. Lett **127**, 223 (1986).

[17] H. D. Meyer, F. L. Quéré, C. Léonard, and F. Gatti. Chem. Phys. **329**, 179 (2006).

[18] M. H. Beck, A. Jäckle, G. A. Worth, and H. D. Meyer. Physics Reports **324**, 1 (2000).

[19] H. Köppel, W. Domcke, and L. S. Cederbaum. Adv. Chem. Phys. **57**, 59 (1984).

[20] L. S. Cederbaum, H. Köppel, and W. Domcke. Int. J. Quantum Chem. **15**, 251 (1981).

[21] D. M. Bishop. *Group Theory and Chemistry*, Oxford University Press (1973).

[22] M. N. R. Ashfold, C. L. Mennett, and R. N. Dixon. Chem. Phys. **93**, 293 (1985).

[23] L. D. Zeigler. J. Chem. Phys. **82**, 664 (1985).

[24] M. N. R. Ashfold, C. L. Mennett, and R. N. Dixon. Farady Discuss. Chem. Soc. **82**, 163 (1986).

[25] V. Vaida, M. I. McCarthy, P. C. Engelking, P. Rosmus, H.-J. Werner, and P. Botschwina. J. Chem. Phys. **86**, 669 (1987).

[26] P. Rosmus, P. Botschwina, H.-J. Werner, V. Vaida, P. C. Engelking, and M. I. McCarthy. J. Chem. Phys. **86**, 6677 (1987).

[27] M. I. McCarthy, P. Rosmus, H.-J. Werner, P. Botschwina, and V. Vaida. J. Chem. Phys. **86**, 6693 (1987).

[28] J. Biesner, L. Schnieder, J. Schmeer, G. Ahlers, X. Xie, K. H. Welge, M. N. R. Ashfold, and R. N. Dixon. J. Chem. Phys. **88**, 3607 (1988).

[29] J. Biesner, L. Schnieder, G. Ahlers, X. Xie, , K. H. Welge, M. N. R. Ashfold, and R. N. Dixon. J. Chem. Phys. **91**, 2901 (1989).

[30] E. L. Woodbridge, M. N. R. Ashfold, and S. R. Leone. J. Chem. Phys. **94**, 4195 (1991).

[31] U. Manz, E.-A. Reinsch, P. Rosmus, H.-J. Werner, and S. V. O'Neil. J. Chem. Soc. Fraraday Trans. **87**, 1809 (1991).

[32] F. F. Crim. Ann. Rev. Phys. Chem. **44**, 397 (1993).

[33] A. P. Baronavski and J. C. Owrutsky. J. Phys. Chem. **99**, 10077 (1995).

[34] S. A. Henck, M. A. Mason, W.-B. Yan, K. K. Lehmann, and S. L. Coy. J. Chem. Phys. **102**, 4772 (1995).

[35] S. A. Henck, M. A. Mason, W.-B. Yan, K. K. Lehmann, and S. L. Coy. J. Chem. Phys. **102**, 4783 (1995).

[36] D. H. Mordaunt, M. N. R. Ashfold, and R. N. Dixon. J. Chem. Phys. **104**, 6460 (1996).

[37] D. H. Mordaunt, M. N. R. Ashfold, and R. N. Dixon. J. Chem. Phys. **104**, 6472 (1996).

[38] D. H. Mordaunt, M. N. R. Ashfold, and R. N. Dixon. J. Chem. Phys. **109**, 7659 (1998).

[39] R. A. Loomis, J. P. Reid, and S. R. Leone. J. Chem. Phys. **112**, 658 (2000).

[40] J. P. Reid, R. A. Loomis, and S. R. Leone. J. Chem. Phys. **112**, 3181 (2000).

[41] J. P. Reid, R. A. Loomis, and S. R. Leone. J. Phys. Chem. A **104**, 10139 (2000).

[42] J. P. Reid, R. A. Loomis, and S. R. Leone. Chem. Phys. Lett. **324**, 240 (2000).

[43] A. Bach, J. M. Hutchinson, R. J. Holiday, and F. F. Crim. J. Chem. Phys. **116**, 9315 (2002).

[44] A. Bach, J. M. Hutchinson, R. J. Holiday, and F. F. Crim. J. Phys. Chem. A **107**, 10490 (2003).

[45] M. L. Hause, Y. H. Yoon, and F. F. Crim. J. Chem. Phys **125**, 174309 (2006).

[46] K. L. Wells, G. Perriam, and V. G. Stavros. J. Chem. Phys. **130**, 074308 (2009).

[47] P. Avouris, A. R. Rossi, and A. C. Albrecht. J. Chem. Phys. **74**, 5516 (1981).

[48] R. N. Dixon. Chem. Phys. Lett. **147**, 377 (1988).

[49] R. N. Dixon. Mol. Phys. **68**, 263 (1989).

[50] S. L. Tang, E. H. Abramson, and D. G. Imre. J. Phys. Chem. **95**, 4969 (1991).

[51] T. Seideman. J. Chem. Phys. **103**, 10556 (1995).

[52] R. N. Dixon. Mol. Phys. **88**, 949 (1996).

[53] R. N. Dixon and T. W. R. Hancock. J. Phys. Chem. A **101**, 7567 (1997).

[54] D. R. Yarkony. J. Chem. Phys. **121**, 628 (2004).

[55] W. Lai, S. Y. Lin, D. Xie, and H. Guo. J. Chem. Phys. **129**, 154311 (2008).

[56] D. Bonhommeau and D. G. Truhlar. J. Chem. Phys. **129**, 014302 (2008).

[57] D. Bonhommeau, R. Valero, D. G. Truhlar, and A. W. Jasper. J. Chem. Phys. **130**, 234303 (2009).

[58] W. Lai, S. Y. Lin, D. Xie, and H. Guo. J. Phys. Chem. A **114**, 3121 (2010).

[59] K. Giri, E. Chapman, C. S. Sanz, and G. Worth. J. Chem. Phys. **135**, 044311 (2011).

[60] J. Ma, X. Zhu, H. Guo, and D. R. Yarkony. J. Chem. Phys. **137**, 22A541 (2012).

[61] S. Nangia and D. G. Truhlar. J. Chem. Phys. **124**, 124309 (2006).

[62] M. Baer. Phys. Rep. **358**, 75 (2002).

[63] H.-J. Werner, P. J. Knowles, R. Lindh, F. R. Manby, M. Schütz, P. Celani, T. Korona, A. Mitrushenkov, G. Rauhut, T. B. Adler, R. D. Amos, A. Bernhardsson, A. Berning, D. L. Cooper, M. J. O. Deegan, A. J. Dobbyn, F. Eckert, E. Goll, C. Hampel, G. Hetzer, T. Hrenar, G. Knizia, C. Köppl, Y. Liu, A. W. Lloyd, R. A. Mata, A. J. May, S. J. McNicholas, W. Meyer, M. E. Mura, A. Nicklass, P. Palmieri, K. Pflüger, R. Pitzer, M. Reiher, U. Schumann, H. Stoll, A. J. Stone, R. Tarroni, T. Thorsteinsson, M. Wang, and A. Wolf, *Molpro, version 2009.1, a package of ab initio programs* (2009), see.

[64] W. Eisfeld and A. Viel. J. Chem. Phys. **122**, 204317 (2005).

[65] A. Jäckle and H. D. Meyer. J. Chem. Phys. **104**, 7974 (1996).

[66] H. Nakano. J. Chem. Phys. **99**, 7983 (1993).

[67] M. Schmidt, K. Baldridge, J. Boatz, S. Elbert, M. Gordon, J. Jensen, S. Kosecki, N. Matsunaga, K. Nguyen, S.J.Su, T. Windus, M. Dupuis, and J. Montgomery. J. Comput. Chem. **14**, 1347 (1993).

[68] L. S. Cederbaum, J. Schirmer, and H. D. Meyer. J. Phys. A **22**, 2427 (1989).

[69] V. Vallet, Z. G. Lan, S. Mahapatra, A. L. Sobolewski, and W. Domcke. Faraday Discuss. **127**, 283 (2004).

[70] S. G. Ramesh and W. Domcke. Faraday Discuss. **163**, 1 (2013).

[71] H. H. Ritze, W. Radloff, and I. V. Hertel. Chem. Phys. Lett. **289**, 46 (1998).

[72] E. Tannenbaum, E. M. Coffin, and A. J. Harrison. J. Chem. Phys. **21**, 311 (1953).

[73] M. N. R. Ashfold, R. N. Dixon, N. Little, R. J. Stickland, and C. M. Western. J. Chem. Phys. **89**, 1754 (1988).

[74] S. R. Langford, A. J. Orr-Ewing, R. A. Morgan, C. M. Western, and M. N. R. Ashfold. J. Chem. Phys. **108**, 6667 (1988).

[75] T. A. A. Oliver, G. A. King, and M. N. R. Ashfold. J. Chem. Phys. **133**, 194303 (2010).

[76] C. R. Nave and K. P. Pullen. Chem. Phys. Lett. **12**, 499 (1972).

[77] J. Dommen, W. Caminati, H. Hollenstein, T. K. Ha, R. Meyer, and A. Bauder. J. Mol. Spectrosc. **180**, 369 (1996).

[78] K. Aarset, E. M. Page, and D. A. Rice. J. Phys. Chem. A **109**, 4961 (2005).

[79] R. J. Bartlett and M. Musiał. Rev. Mod. Phys. **79**, 291 (2007).

[80] M. N. R. Ashfold, G. A. King, D. Murdock, M. G. D. Nix, T. A. A. Oliver, and A. G. Sage. Phys. Chem. Chem. Phys. (2010).

[81] A. L. Sobolewski, W. Domcke, C. Dedonder-Lardeux, and C. Jouvet. Phys. Chem. Chem. Phys. **4**, 1093 (2002).

[82] V. Vallet, Z. Lan, S. Mahapatra, A. L. Sobolewski, and W. Domcke. J. Chem. Phys. **123**, 144307 (2005).

[83] Z. Lan, A. Dupays, V. Vallet, S. Mahapatra, and W. Domcke. J. Photochem. Photobiol. A **190**, 177 (2007).

[84] Z. Lan and W. Domcke. Chem. Phys. **350**, 125 (2008).

[85] S. Faraji, M. Vazdar, V. S. Reddy, M. Eckert-Maksic, H. Lischka, and H. Köppel. J. Chem. Phys. **135**, 154310 (2011).

[86] M. Vazdar, M. Eckert-Maksić, M. Barbatti, and H. Lishka. Mol. Phys. **107**, 845 (2009).

[87] B. Sellner, M. Barbatti, and H. Lishka. J. Chem. Phys. **131** (2009).

[88] M. Barbatti, M. Vazdar, Adélia, M. Eckert-Maksić, and H. Lischka. J. Chem. Phys. **125**, 164323 (2006).

[89] M. Barbatti, J. Pittner, M. Pederzoli, U. Werner, R. Mitrić, V. B. Koutecký, and H. Lischka. Chem. Phys. **375**, 26 (2010).

[90] B. Cronin, M. G. D. Nix, R. H. Qadiri, and M. N. R. Ashfold. Phys. Chem. Chem. Phys. **6**, 5031 (2004).

[91] B. Cronin, A. L. Devine, M. G. D. Nix, and N. R. Ashfold. Phys. Chem. Chem. Phys **8**, 3440 (2006).

[92] J. Wei, J. Riedel, A. Kuczmann, F. Renth, and F. Temps. Faraday Discuss. **127**, 267 (2004).

[93] H. Lippert, H. H. Ritzel, I. V. Hertel, and W. Radloff. ChemPhysChem **5**, 1423 (2004).

[94] M. H. Palmer, I. C. Walker, and M. F. Guest. Chem. Phys. **238**, 179 (1998).

[95] B. O. Roos, P. A. Malmqvist, V. Molina, L. Serrano-Andrés, and M. Merchán. J. Chem. Phys **116**, 7526 (2002).

[96] G. M. Roberts, C. A. Williams, H. Yu, A. S. Chatterly, J. D. Young, S. Ulrich, and V. G. Stavros. Farraday Discuss. **163**, 1 (2012).

[97] M. J. Frisch, G. W. Trucks, H. B. Schlegel, G. E. Scuseria, M. A. Robb, J. R. Cheeseman, J. A. Montgomery, Jr., T. Vreven, K. N. Kudin,

J. C. Burant, J. M. Millam, S. S. Iyengar, J. Tomasi, V. Barone, B. Mennucci, M. Cossi, G. Scalmani, N. Rega, G. A. Petersson, H. Nakatsuji, M. Hada, M. Ehara, K. Toyota, R. Fukuda, J. Hasegawa, M. Ishida, T. Nakajima, Y. Honda, O. Kitao, H. Nakai, M. Klene, X. Li, J. E. Knox, H. P. Hratchian, J. B. Cross, V. Bakken, C. Adamo, J. Jaramillo, R. Gomperts, R. E. Stratmann, O. Yazyev, A. J. Austin, R. Cammi, C. Pomelli, J. W. Ochterski, P. Y. Ayala, K. Morokuma, G. A. Voth, P. Salvador, J. J. Dannenberg, V. G. Zakrzewski, S. Dapprich, A. D. Daniels, M. C. Strain, O. Farkas, D. K. Malick, A. D. Rabuck, K. Raghavachari, J. B. Foresman, J. V. Ortiz, Q. Cui, A. G. Baboul, S. Clifford, J. Cioslowski, B. B. Stefanov, G. Liu, A. Liashenko, P. Piskorz, I. Komaromi, R. L. Martin, D. J. Fox, T. Keith, M. A. Al-Laham, C. Y. Peng, A. Nanayakkara, M. Challacombe, P. M. W. Gill, B. Johnson, W. Chen, M. W. Wong, C. Gonzalez, and J. A. Pople, *Gaussian 03, Revision B.05* (), Gaussian, Inc., Wallingford, CT, 2004.

[98] P. Celani and H. J. Werner. J. Chem. Phys **119**, 5044 (2003).

[99] X. Li and J. Paldus. J. Phys. Chem. A **114** (2010).

[100] O. Christiansen, J. Gauss, J. F. Stanton, and P. Jorgensen. J. Chem. Phys. **111**, 525 (1999).

[101] M. H. Palmer and P. J. Wilson. Mol. Phys. **101**, 2391 (2003).

[102] P. J. Derrick, L. Asbrink, O. Edqvist, B. O. Jonsson, and E. Lindholm. Int. J. Mass. Spectrom. Ion Phys. **6**, 161 (1971).

[103] M. Bavia, F. Bertinelli, C. Taliani, and C. Zauli. Mol. Phys. **31**, 479 (1976).

[104] M. Barbatti and H. Lischka. J. Am. Chem. Soc. **130**, 6831 (2008).

[105] W. M. I. Hassan, W. C. Chung, N. Shimakura, S. Koseki, H. Kono, and Y. Fujimura. Phys. Chem. Chem. Phys. **12**, 5317 (2010).

[106] K. L. Wells, D. J. Hadden, M. G. D. Nix, and V. G. Stavros. J. Phys. Chem. Lett. **1**, 993 (2010).

[107] M. Barbatti, J. J. Szymczak, A. J. A. Aquino, D. Nachtigallova, and H. Lischka. J. Chem. Phys. **134**, 014301 (2011).

[108] H. Chen and S. Li. J. Chem. Phys. **124**, 154315 (2006).

[109] Z. Lan, E. Fabiano, and W. Thiel. Chem. Phys. Chem. **10**, 1225 (2009).

[110] H. R. Hudock and T. J. Martinez. Chem. Phys. Chem. **9**, 2486 (2008).

[111] M. Merchán and L. Serrano-Andrés. J. Am. Chem. Soc. **125**, 8108 (2003).

[112] K. Kimura, H. Tsubomura, and S. Nagakura. Bull. Chem. Soc. Jpn. **37**, 1337 (1964).

[113] K. Kimura and S. Nagakura. Mol. Phys. **9**, 117 (1965).

[114] Y. Honda, M. Hada, M. Ehara, and H. Nakatsuji. J. Chem. Phys. **117**, 2045 (2002).

[115] T. Ebata, C. Minejima, and N. Mikami. J. Phys. Chem. A **106**, 11070 (2002).

[116] G. A. King, T. A. A. Oliver, and M. N. R. Ashfold. J. Chem. Phys. **132**, 214307 (2010).

[117] R. Montero, A. P. Conde, V. Ovejas, R. Martínez, F. C. no, and A. Longarte. J. Chem. Phys. **135**, 054308 (2011).

[118] G. M. Roberts, C. A. Williams, J. D. Young, S. Ulrich, M. J. Paterson, and V. G. Stavros. J. Am. Chem. Soc. **134**, 12578 (2012).

[119] R. Spesyvtsev, O. M. Kirkby, and H. H. Fielding. Faraday Discuss. **157**, 165 (2012).

[120] R. Spesyvtsev, O. M. Kirkby, M. Vacher, and H. H. Fielding. Phys. Chem. Chem. Phys. **14**, 9942 (2012).

[121] K. Kowalski and P. Piecuch. J. Chem. Phys. **120**, 1715 (2004).

[122] T. J. Penfold and G. A. Worth. J. Chem. Phys. **131**, 064303 (2009).

[123] R. S. Mins, D. S. N. Parker, T. J. Penfold, G. A. Worth, and H. H. Fielding. Phys. Chem. Chem. Phys. (2010).